# *Advances in* Quantum Chemistry

Volume 53

# CONTRIBUTORS

Numbers in parentheses indicate the pages where the authors' contributions can be found.

D.F. Anagnostopoulos (217)
Department of Material Science and Engineering, University of Ioannina, Ioannina, GR-45110, Greece

Dilip Angom (177)
Physical Research Laboratory, Navarangpura-380 009, Gujarat, India

T. Beier (83)
Gesellschaft für Schwerionenforschung, D-64291 Darmstadt, Germany

I. Bergström (67)
Atomic Physics, FYSIKUM, AlbaNova, Stockholm University, SE-106 91, Stockholm, Sweden

K. Blaum (83)
Gesellschaft für Schwerionenforschung, D-64291 Darmstadt, Germany and Johannes Gutenberg-Universität Mainz, D-55099 Mainz, Germany

G. Borchert (217)
Institut für Kernphysik, Forschungszentrum Jülich, D-52425 Jülich, Germany

S. Boucard (217)
Laboratoire Kastler Brossel, École Normale Supérieure, CNRS, Université Pierre et Marie Curie-Paris 6, Case 74, 4 place Jussieu, F-75252 Paris, Cedex 05, France

D.S. Covita (217)
Department of Physics, Coimbra University, P-3000 Coimbra, Portugal

L. Dahl (83)
Gesellschaft für Schwerionenforschung, D-64291 Darmstadt, Germany

A. Dax (217)
Paul Scherrer Institut, Villigen PSI, CH5232 Villigen, Switzerland

G.W.F. Drake (37)
Department of Physics, University of Windsor, Windsor, Ontario, Canada N9B 3P4

J.P. Egger (217)
Institut de Physique de l' Université de Neuchâtel, CH-2000 Neuchâtel, Switzerland

S. Eliseev (83)
Gesellschaft für Schwerionenforschung, D-64291 Darmstadt, Germany

Jesus R. Flores (151)
Departamento de Química Física Universidad de Vigo, 36-200 Vigo, Spain

T. Fritioff (67)
Atomic Physics, FYSIKUM, AlbaNova, Stockholm University, SE-106 91, Stockholm, Sweden

Stephan Fritzsche (177)
Institut für Physik, Universität Kassel, D-34132 Kassel, Germany

H. Fuhrmann (217)
Stefan Meyer Institut für subatomare Physik, Austrian Acad. of Sci., A-1090 Vienna, Austria

D. Gotta (217)
Institut für Kernphysik, Forschungszentrum Jülich, D-52425 Jülich, Germany

Walter Greiner (99)
Frankfurt Institute for Advanced Studies, Johann Wolfgang Goethe University, Max-von-Laue-Str. 1, 60438 Frankfurt am Main, Germany

A. Gruber (217)
Stefan Meyer Institut für subatomare Physik, Austrian Acad. of Sci., A-1090 Vienna, Austria

A. Gumberidze (57)
Gesellschaft für Schwerionenforschung, D-64291 Darmstadt, Germany

M. Hennebach (217)
Institut für Kernphysik, Forschungszentrum Jülich, D-52425 Jülich, Germany

F. Herfurth (83)
Gesellschaft für Schwerionenforschung, D-64291 Darmstadt, Germany

A. Hirtl (217)
Stefan Meyer Institut für subatomare Physik, Austrian Acad. of Sci., A-1090 Vienna, Austria

B. Hofmann (83)
Gesellschaft für Schwerionenforschung, D-64291 Darmstadt, Germany

P. Indelicato (217)
Laboratoire Kastler Brossel, École Normale Supérieure, CNRS, Université Pierre et Marie Curie-Paris 6, Case 74, 4 place Jussieu, F-75252 Paris, Cedex 05, France

Karol Jankowski (151)
Institute of Physics, Nicholas Copernicus University, 87-100 Toruń, Poland

Ulrich D. Jentschura (253)
Max-Planck-Institut für Kernphysik, Saupfercheckweg 1, 69117 Heidelberg, Germany

Savely G. Karshenboim (237)
D.I. Mendeleev Institute for Metrology (VNIIM), St. Petersburg 190005, Russia and Max-Planck-Institut für Quantenoptik, 85748 Garching, Germany

O. Kester (83)
Gesellschaft für Schwerionenforschung, D-64291 Darmstadt, Germany

H.-J. Kluge (83)
Gesellschaft für Schwerionenforschung, D-64291 Darmstadt, Germany and Universität Heidelberg, Physikalisches Institut, D-69120 Heidelberg, Germany

S. Koszudowski (83)
Gesellschaft für Schwerionenforschung, D-64291 Darmstadt, Germany

Svetlana Kotochigova (253)
National Institute of Standards and Technology, Mail Stop 8401, Gaithersburg, MD 20899-8401, USA

C. Kozhuharov (83)
Gesellschaft für Schwerionenforschung, D-64291 Darmstadt, Germany

A. Kumar (57)
Gesellschaft für Schwerionenforschung, D-64291 Darmstadt, Germany

Eric-Olivier Le Bigot (217, 253)
Laboratoire Kastler Brossel, École Normale Supérieure, CNRS, Université Pierre et Marie Curie-Paris 6, Case 74, 4 place Jussieu, F-75252 Paris, Cedex 05, France

Y.-W. Liu (217)
Paul Scherrer Institut, Villigen PSI, CH5232 Villigen, Switzerland

G. Maero (83)
Gesellschaft für Schwerionenforschung, D-64291 Darmstadt, Germany

Brajesh K. Mani (177)
Physical Research Laboratory, Navarangpura-380 009, Gujarat, India

B. Manil (217)
Laboratoire Kastler Brossel, École Normale Supérieure, CNRS, Université Pierre et Marie Curie-Paris 6, Case 74, 4 place Jussieu, F-75252 Paris, Cedex 05, France and CIRIL, GANIL, BP 5133, 14070 Caen Cedex 5, France

Peter J. Mohr (27, 253)
National Institute of Standards and Technology, Gaithersburg, MD 20899-8420, USA

Sz. Nagy (67)
Atomic Physics, FYSIKUM, AlbaNova, Stockholm University, SE-106 91, Stockholm, Sweden

N. Nelms (217)
Department of Physics and Astronomy, University of Leicester, Leicester LEI7RH, England, UK

W. Nörtershäuser (83)
Gesellschaft für Schwerionenforschung, D-64291 Darmstadt, Germany and Johannes Gutenberg-Universität Mainz, D-55099 Mainz, Germany

J. Pfister (83)
Gesellschaft für Schwerionenforschung, D-64291 Darmstadt, Germany and Johann Wolfgang Goethe-Universität Frankfurt, D-60438 Frankfurt, Germany

W. Quint (83)
Gesellschaft für Schwerionenforschung, D-64291 Darmstadt, Germany

Norman F. Ramsey (1)
Lyman Physics Laboratory, Harvard University, Cambridge, MA 02138, USA

U. Ratzinger (83)
Johann Wolfgang Goethe-Universität Frankfurt, D-60438 Frankfurt, Germany

R. Reuschl (57)
Gesellschaft für Schwerionenforschung, D-64291 Darmstadt, Germany

J.M.F. dos Santos (217)
Department of Physics, Coimbra University, P-3000 Coimbra, Portugal

A. Schempp (83)
Johann Wolfgang Goethe-Universität Frankfurt, D-60438 Frankfurt, Germany

S. Schlesser (217)
Laboratoire Kastler Brossel, École Normale Supérieure, CNRS, Université Pierre et Marie Curie-Paris 6, Case 74, 4 place Jussieu, F-75252 Paris, Cedex 05, France

R. Schuch (67, 83)
Atomic Physics, FYSIKUM, AlbaNova, Stockholm University, SE-106 91, Stockholm, Sweden

L.M. Simons (217)
Paul Scherrer Institut, Villigen PSI, CH5232 Villigen, Switzerland

Romuald Słupski (151)
Computing Centre, Nicholas Copernicus University, 87-100 Toruń, Poland

A. Solders (67)
Atomic Physics, FYSIKUM, AlbaNova, Stockholm University, SE-106 91, Stockholm, Sweden

L. Stingelin (217)
Paul Scherrer Institut, Villigen PSI, CH5232 Villigen, Switzerland

Th. Stöhlker (57, 83)
Gesellschaft für Schwerionenforschung, D-64291 Darmstadt, Germany

M. Suhonen (67)
Atomic Physics, FYSIKUM, AlbaNova, Stockholm University, SE-106 91, Stockholm, Sweden

Barry N. Taylor (253)
National Institute of Standards and Technology, Mail Stop 8401, Gaithersburg, MD 20899-8401, USA

R.C. Thompson (83)
Imperial College London, SW7 2AZ London, United Kingdom

Peter E. Toschek (7)
Institut für Laser-Physik, Universität Hamburg, D-22761 Hamburg, Germany

M. Trassinelli (57)
Gesellschaft für Schwerionenforschung, D-64291 Darmstadt, Germany

M. Trassinelli (217)
Laboratoire Kastler Brossel, École Normale Supérieure, CNRS, Université Pierre et Marie Curie-Paris 6, Case 74, 4 place Jussieu, F-75252 Paris, Cedex 05, France and GSI, Plankstr. 1, D-64291, Darmstadt, Germany

J. Veloso (217)
Department of Physics, Coimbra University, P-3000 Coimbra, Portugal

M. Vogel (83)
Gesellschaft für Schwerionenforschung, D-64291 Darmstadt, Germany

G. Vorobjev (83)
Gesellschaft für Schwerionenforschung, D-64291 Darmstadt, Germany

A. Wasser (217)
Paul Scherrer Institut, Villigen PSI, CH5232 Villigen, Switzerland

A. Wells (217)
Department of Physics and Astronomy, University of Leicester, Leicester LEI7RH, England, UK

G. Werth (83)
Johannes Gutenberg-Universität Mainz, D-55099 Mainz, Germany

D.F.A. Winters (83)
Gesellschaft für Schwerionenforschung, D-64291 Darmstadt, Germany

Z.-C. Yan (37)
Department of Physics, University of New Brunswick, Fredericton, New Brunswick, Canada E3B 5A3

J. Zmeskal (217)
Stefan Meyer Institut für subatomare Physik, Austrian Acad. of Sci., A-1090 Vienna, Austria

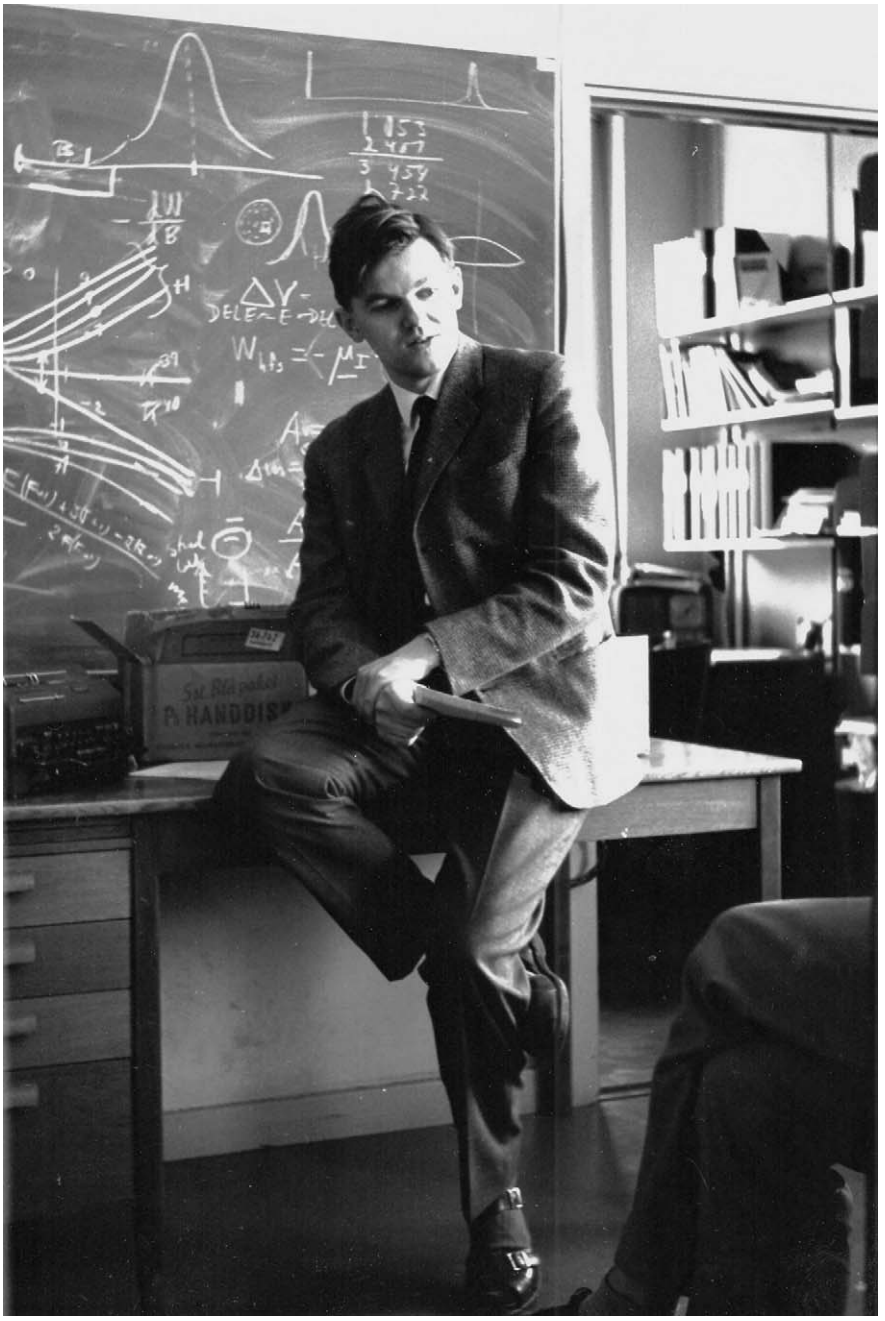

Ingvar Lindgren at Fysicum in Uppsala around 1960.

# PREFACE

Throughout a long and highly productive career, Ingvar Lindgren has pursued with unwavering fidelity a scientific goal that is beset with formidable obstacles. His goal has been to understand many-body effects and relativistic phenomena in atoms, and in this he has enjoyed many successes. In pursuing his goal Ingvar has been the devoted leader of an outstanding research group that has trained generations of physicists. He has also given generously to the governance of Chalmers University of Technology and Göteborg University, and he has played a major role in guiding science policy in Sweden. Following in the great tradition of eminent physicists speaking out on public affairs, Ingvar has become *de facto* an international statesman for science. For all these reasons, plus his exceptional human qualities of friendship and good humor, to his many friends and admirers, Ingvar is an icon for the best in physics. To put it simply: knowing Ingvar Lindgren makes one proud to be a physicist.

In celebration of Ingvar's 75th birthday, many of his friends and admirers gathered for a Symposium in his honor, held at Chalmers University of Technology on June 2nd and 3rd, 2006. The symposium was organized by Berit Augustsson, Eleanor Campbell, Daniel Hedendahl, Eva Lindroth and Sten Salomonson, to whom I express a deep gratitude that I know is shared by everyone who attended. The Symposium was followed by a weekend outing to Ingvar's home in Ljungskile where Ingvar revealed yet another of his extraordinary qualities: in addition to being a great host, he is a great cook.

This volume of the proceedings is offered to Ingvar with affection by the authors and by all who attended, as well as his many friends who could attend only in spirit.

Daniel Kleppner
Cambridge, Massachusetts

Group photo of the participants.

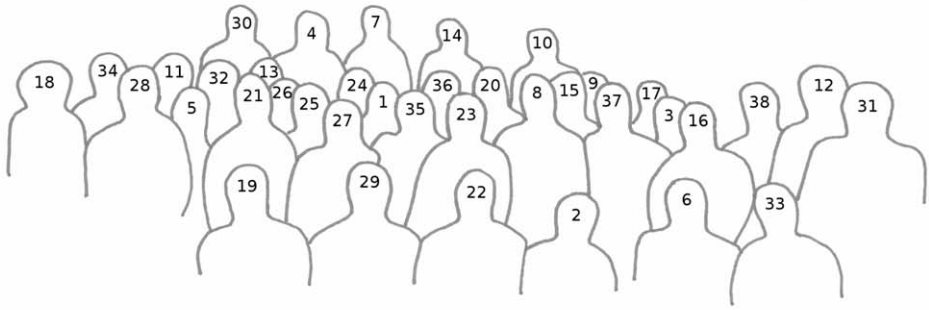


1. Thomas Beier
2. Ingmar Bergström
3. Raymond Bishop
4. Erkki Brändas
5. Eleanor Campbell
6. Gordon Drake
7. Curt Ekström
8. Burkhard Fricke
9. Stephan Fritzsche
10. Walter Greiner
11. Dag Hanstorp
12. Daniel Hedendahl
13. Jean-Louis Heully
14. Wim Hogervorst
15. Paul Indelicato
16. Massimo Inguscio
17. Karol Jankowski
18. Savely Karshenboim
19. Daniel Kleppner
20. Jürgen Kluge
21. Eric-Olivier Le Bigot
22. Ingvar Lindgren
23. Eva Lindroth
24. Peter Mohr
25. John Morrison
26. David Pegg
27. Ann-Marie Pendrill
28. Leslie Pendrill
29. Norman Ramsey
30. Lennart Robertsson
31. Arne Rosén
32. Reinhold Schuch
33. Sten Salomonson
34. Thomas Stöhlker
35. Joeseph Sucher
36. Sune Svanberg
37. Peter Toschek
38. Anders Ynnerman

CHAPTER 1

# Magnetic Resonance Contributions to Other Sciences

**Norman F. Ramsey***

Contents



Abstract

In 1947, I.I. Rabi invented the molecular beam magnetic resonance method for the important, but limited purpose, of measuring nuclear magnetic moments and five of us working in his laboratory immediately began such experiments. The first experiments with LiCl gave the expected single resonance for each nucleus, but we were surprised to discover six resonances for the proton in $H_2$, which we soon showed was due to the magnetic effects of the other proton and the rotating charged molecule: from these measurements we could also obtain new information on molecular structure. We had another shock when we studied $D_2$ and found the resonance curves were spread more widely for $D_2$ than $H_2$ even though the magnetic interactions should have been much smaller. We found we could explain this by assuming that the deuteron had an electric quadrupole moment and J. Schwinger pointed out that this would require the existence of a previously unsuspected electric tensor force between the neutron and the proton. With this, the resonance method was giving new fundamental information about nuclear forces. In 1944, Rabi and I pointed out that it should be

* Lyman Physics Laboratory, Harvard University, Cambridge, MA 02138, USA

Advances in Quantum Chemistry, Vol. 53
ISSN 0065-3276, DOI:10.1016/S0065-3276(07)53001-7

possible by the Dirac theory and our past resonance experiments to calculate exactly the hyperfine interaction between the electron and the proton in the hydrogen atom and we had two graduate students, Nafe and Nelson do the experiment and they found a disagreement which led J. Schwinger to develop the first successful relativistic quantum field theory and QED. In 1964, Purcell, Bloch and others detected magnetic resonance transitions by the effect of the transition on the oscillator, called NMR, making possible measurements on liquids, solids and gases and giving information on chemical shifts and thermal relaxation times T1 and T2. I developed a magnetic resonance method for setting a limit to the EDM of a neutron in a beam and with others for neutrons stored in a suitably coated bottle. Magnetic resonance measurements provide high stability atomic clocks. Both the second and the meter are now defined in terms of atomic clocks. Lauterbuhr, Mansfield, Damadian and others developed the important methods of using inhomogeneous magnetic fields to localize the magnetic resonance in a tissue sample producing beautiful and valuable magnetic resonance images, MRI's, and fMRI's.

## 1. INTRODUCTION

It is a pleasure and an honor to speak at this celebration for Ingvar and his important relativistic atomic calculations, for his work with the Nobel Foundation and for his contributions to the international community of atomic physics where he has been a wonderful friend to all of us.

A delightful feature of fundamental scientific research is the frequency with which a study started in one limited field of research eventually contributes to other scientific and applied fields and often leads to the creation of new research fields. This has been markedly true of magnetic resonance.

I shall initially discuss the scientific basis of magnetic resonance, the first successful experiments and then the subsequent discoveries and inventions which led to other disciplines.

## 2. MAGNETIC RESONANCE AND NUCLEAR MAGNETIC MOMENTS

I.I. Rabi invented the molecular beam magnetic resonance method in 1937, just two months after I began working for my Ph.D. with him at Columbia University. Immediately, six of us in his laboratory dropped all other activities to adapt two of our apparatuses to his new invention. Magnetic resonance depends on the facts that electrons and most nuclei spin like tops with angular momentum $J$ and are magnetized like compass needles with magnetic moments $\boldsymbol{\mu}$. Just as a tilted top in the earth's gravity field will precess about a vertical axis, the $J$ of a nucleus or electron in a magnetic field $B$ will precess about that field with a frequency $\nu_0$. Rabi's proposed experiment [1,2] was to apply an oscillatory magnetic field at frequency $\nu$ and to vary $\nu$ in hopes of finding a resonant change in the orientation of $\boldsymbol{\mu}$ when at resonance $\nu = \nu_0$. Initially this was with $^7$Li [2] in LiCl and with the proton [3]

in molecular $H_2$. The experiment with $^7$Li worked as expected and gave the hoped for change in orientation at the resonance frequency $\nu = \nu_0$, from which $\boldsymbol{\mu}$ could be calculated. In subsequent years many nuclear magnetic moments were measured in this way.

## 3. MAGNETIC INTERACTIONS IN MOLECULES

In contrast to the success of the first $^7$Li measurements of nuclear magnetic moments, the experiment with $H_2$ was initially very disappointing. Instead of the expected sharp resonance we obtained a broad pattern looking like noise. However when we greatly reduced the strength of the oscillatory field we found [3] that we had six separate resonances, due to the proton magnetic moment also interacting with the magnetic field from the other proton and from the electric charges of the rotating molecule. In other words we were observing the radio-frequency spectrum of the molecule. This extended the contributions of magnetic resonance to the fields of molecular structure and chemistry. From these measurements we could also obtain molecular structure parameters of interest to chemists, such as the value of $\langle 1/R^3 \rangle$ for the $H_2$ molecule.

At the time of these measurements we knew that our nuclear magnetic moment measurements had to be corrected for magnetic shielding from the circulation of the electrons in the molecule induced by the external magnetic field. W. Lamb calculated this correction for single atoms but not for molecules. After WWII, I developed a method for calculating the magnetic shielding correction for polyatomic molecules and discovered that the corrections were different for the same atom in different locations in the same molecule [4]. At about the same time this chemical shift was independently discovered experimentally by N. Bloembergen, F. Bloch and others. The magnetic resonance chemical shifts are now powerful methods in chemical analysis and studies of molecular structure.

## 4. NUCLEAR ELECTRIC INTERACTIONS IN MOLECULES

When we studied the radio-frequency spectrum of $D_2$ we hit another surprise [5]. The separation of the spectral lines in $D_2$ were greater than in $H_2$ even though the nuclear spin–spin interaction and the nuclear spin molecular rotation interaction should be much less. We found a similar anomaly for HD. We finally interpreted this as due the deuterium nucleus having a quadrupole moment (being ellipsoidal in shape) which gave rise to a spin dependent electrical interaction. The existence of the quadrupole moment, in turn, implied the existence of a new elementary particle force called a tensor force. In this way, magnetic resonance made a fundamental contribution to particle physics.

## 5. ATOMIC HYPERFINE STRUCTURE, SEPARATED OSCILLATORY FIELDS AND ATOMIC CLOCKS

The magnetic resonance method was extended to atomic physics to measure the magnetic interaction between the atom and electron which in atomic spectroscopy is called the hyperfine separation frequency, $\Delta\nu_{\rm hfs}$. Since $\Delta\nu_{\rm hfs}$ is dependent only on interactions internal to the atom, it could be used as a standard for frequency and time, but atomic clocks at that time would have been no more accurate than clocks based on vibrating crystals. The magnetic resonance methods then in use had the great problem that for high accuracy the oscillatory field region should be as long as possible and the wave length of the radiation should be as short as possible, but these two requirements were mutually incompatible since the oscillatory field region had to be less than one-half a wave length long to avoid cancellations by opposite phases. In 1949 I invented the separated oscillatory fields method [6] which overcomes this problem by confining the phase coherent oscillatory fields to two separate regions, each of which is shorter than one half a wave length, but with their separation being many wave lengths apart, the resonance width is correspondingly narrow. This greatly increased the accuracy of all radiofrequency spectroscopy measurements and made it possible for atomic clocks to be much more stable than any other time or frequency standard. In addition to their high stability, atomic clocks had the advantage over all previous time standards of being determined by internal atomic properties which, by the quantum mechanical identity principle, were the same for all atoms in the same state. As a result the international definitions of both the second and the meter are now based on magnetic resonance atomic Cs clocks. Atomic clocks are now extensively used in many different disciplines. If one counts all these disciplines, the list of sciences would be very long indeed, including radio-astronomy, metrology, precision navigation in outer space and on the earth, the Global Positioning System (GPS), tests of relativity, tests of the constancy of fundamental constants, etc.

## 6. ATOMIC HYPERFINE STRUCTURE AND QED

In 1947 it was thought that for atomic hydrogen the value of $\Delta\nu_{\rm hfs}$ could be calculated precisely because magnetic resonance experiments had measured the ratio of the electron and proton magnetic moments and the Dirac theory gave the wave function of the atom and the magnetic moment of the electron. Rabi and I therefore started our graduate students, J.E. Nafe and E.B. Nelson, on an experiment to measure $\Delta\nu_{\rm hfs}$ for H. They found [7] a slight disagreement with the Dirac theory, which led J. Schwinger to develop a successful new relativistic quantum field theory of electromagnetism (QED). This theory showed that the magnetic moment of the electron was slightly different from that used in the Dirac theory. This was the first accurate relativistic quantum field theory and it stimulated the later development of other field theories in particle physics. The anomalous magnetic moment was quickly confirmed by an experiment of P. Kusch.

## 7. NMR

Shortly after WWII, E.M. Purcell, F. Bloch and their associates invented methods, called NMR, for detecting magnetic resonance by the effect of the resonance absorption on the oscillator inducing the resonance transition, which enabled them to study liquid, gaseous and solid samples. The molecules in these substances were subject to frequent collisions which averaged out most of the nuclear interactions in molecules. This collision narrowing had the advantage of producing strong narrow resonances, but the disadvantage of losing much molecular information. However, the relaxation time T1 for the nuclear spin system to reach thermal equilibrium with the sample and T2 for the precessing nuclear spin system to lose phase coherency can be measured. T1, T2, the observed chemical shifts and the electron coupled nuclear spin–spin interaction provide sufficient information to be a guide in determining the location of atoms in a molecule and information about the surroundings of an atom in a molecule. Improved procedures for measuring the relevant NMR parameters have been developed, such as the spin-echo techniques of E. Hahn for measuring relaxation times and the pulse and Fourier transform methods developed by R.R. Ernst and others for obtaining magnetic resonance spectra. As a result, NMR has become an immensely valuable research tool.

## 8. MAGNETIC RESONANCE IMAGING

Although NMR provided valuable information about the materials being studied, the observations suffered by not being able to localize the signals in the sample. P.C. Lauterbur, P. Mansfield and R.V. Damadian developed different methods for using inhomogeneous magnet fields to localize the NMR signals in the sample, leading to the present beautifully detailed magnetic resonance images (MRI). A typical modern MRI apparatus includes a very strong and stable homogeneous magnetic field of approximately 20,000 Gauss (2 Tesla), usually produced by a large super-conducting magnet. In addition there are three variable gradient magnets at 180 to 270 Gauss each of which can produce an inhomogeneous magnetic field such that there are magnetic resonances only along a line, so the observed signal is the result of all of these resonances. When the gradient field is changed similar results are obtained for a different line. When a different gradient magnet is used the resonance lines lie in different planes. These results are then analyzed in a computer using Fourier transforms and programs similar to those used in X-ray CAT scans to give two dimensional pictures in arbitrary planes and in remarkably fine detail. The early MRI scans were of great value in biological and medical research and treatments, but the technology and applications of MRI's have been and are being greatly improved and extended by the development of even sharper images, of images showing blood circulation, of injectable contrast materials, of functional MRI (fMRI) which shows which portion of the brain responds to different stimuli, etc. The illustration in Figure 1.1 shows an MRI of a

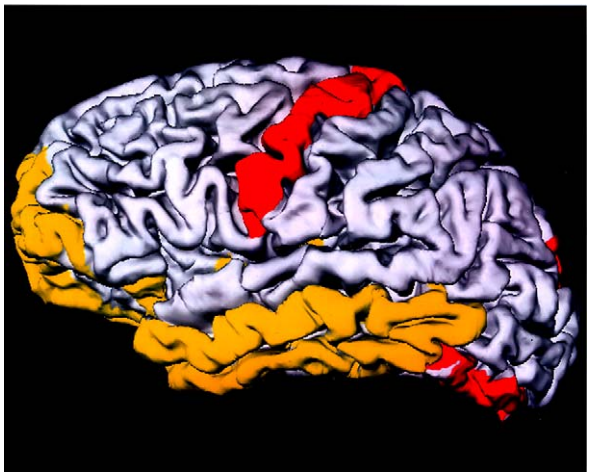

**FIGURE 1.1** An MRI of a human brain, when the subject is asked to think hard about a particular problem. For a colour reproduction of this figure see the colour plate section, near the end of this book.

human brain, when the subject is asked to think hard about a particular problem.

## 9. CONCLUSIONS

Magnetic Resonance has greatly contributed to the fields of Nuclear Magnetic Moments, Molecular Structure, Quantum Field Theory, Particle Physics, QED, Chemical Analysis, Chemistry, Navigation on Earth and in Space, Biology, Time, Frequency, Astronomy, Seismology, Metrology, Tests of Relativity, Medicine, MRI and fMRI. There is every reason in the future to expect even better contributions.

## REFERENCES

[1] I.I. Rabi, *Phys. Rev.* **51** (1937) 652.
[2] I.I. Rabi, J.R. Zacharias, S. Millman, P. Kusch, *Phys. Rev.* **53** (1938) 318.
[3] J.M.B. Kellogg, I.I. Rabi, N.F. Ramsey, J.R. Zacharias, *Phys. Rev.* **55** (1939) 318.
[4] N.F. Ramsey, *Phys. Rev.* **78** (1950) 699;
N.F. Ramsey, *Phys. Rev.* **89** (1953) 527.
[5] J.M.B. Kellogg, I.I. Rabi, N.F. Ramsey, J.R. Zacharias, *Phys. Rev.* **57** (1940) 677.
[6] N.F. Ramsey, *Phys. Rev.* **76** (1949) 996;
N.F. Ramsey, *Phys. Rev.* **78** (1950) 695.
[7] J.E. Nafe, E.B. Nelson, I.I. Rabi, *Phys. Rev.* **71** (1947) 914;
J.E. Nafe, E.B. Nelson, *Phys. Rev.* **73** (1948) 718;
E.B. Nelson, J.E. Nafe, *Phys. Rev.* **76** (1949) 1858.

CHAPTER 2

# A Single Quantum System: Evolution, Prediction, Observation

**Peter E. Toschek** *

Contents



Abstract

The evolution of quantum mechanics has followed the critical analysis of "gedanken" experiments. Many of these concrete speculations can become implemented today in the laboratory—thanks to now available techniques. A key experiment is concerned with the time evolution of a quantum system under repeated or continuing observation. Here, three problems overlap: (1) The microphysical measurement by a macroscopic device, (2) the system's temporal evolution, and (3) the emergence of macroscopic reality out of the microcosmos. A well-known calculation shows the evolution of a quantum system being slowed down, or even obstructed, when the system is merely *observed*. An experiment designed to demonstrate this "quantum Zeno effect" and performed in the late eighties on an ensemble of identical atomic ions confirmed its quantum description, but turned out inconclusive with respect to the very origin of the impediment of evolution. During the past years, experiments on *individual* electrodynamically stored and laser-cooled ions have been performed that unequivocally demonstrate the observed system's quantum evolution being impeded. Strategy and results exclude any physical reaction on the measured object, but reveal the effect of the gain of information as put forward by the particular correlation of the ion state with the detected signal. They shed light on the

* Institut für Laser-Physik, Universität Hamburg, D-22761 Hamburg, Germany
E-mail address: toschek@physnet.uni-hamburg.de

Advances in Quantum Chemistry, Vol. 53
ISSN 0065-3276, DOI:10.1016/S0065-3276(07)53002-9

process of measurement as well as on the quantum evolution and allow an epistemological interpretation.

## 1. FROM "GEDANKEN" EXPERIMENTS TO QUANTUM MEASUREMENT

The exceedingly successful modelling of the microscopic world by quantum mechanics has been achieved on the expense of non-intuitive peculiarities that are associated with this description. In spite of this dilemma—or, perhaps, because of it—the historic evolution of quantum mechanics has proceeded in step with the critical analysis of "gedanken" experiments. At the very heart of these concrete speculations resided Erwin Schrödinger's concept of "entanglement": the non-separability of the wave function of a composite system that quantitatively models this system. To a large extent, the debate encircled the problem of knowing what can be known *in principle*, and what not—which is, after all, the fundamental epistemological problem. A particularly acute embodiment is the plot of Einstein, Podolsky, and Rosen [1], in the version of D. Bohm [2], which has the inevitable consequence: Of a bipartite quantum system with zero total spin, that is, being in the singlet state, let only one part be detected, and its spin component measured in an arbitrary direction. Then, the result of this measurement determines the corresponding component of the remote other part—irrespective of the selected direction and of the distance!

Einstein commented on this consequence which points to the intrinsic nonlocality of quantum mechanics: "... it is spooky action on a distance ..."

Another kind of entanglement refers to different features of an individual atomic particle, say, to its internal and external degrees of freedom (Figure 2.1). Such a concept was inaccessible to experimental scrutiny at Einstein's time. The very idea of experimenting with single atoms has been ridiculed by Schrödinger even in 1952 as a proposal of "... raising ichthyosauria in the zoo ..." [3], but today it does no longer remain the mere basis of lofty gedanken experiments. Rather it is solid experimentation, since we have learnt, more than 25 years ago, the manipulation of individual atomic particles [4–6]. That this concept seems less "spooky" to us is only because the distance of the electron from the vibrating centre of mass is so small on a human scale.

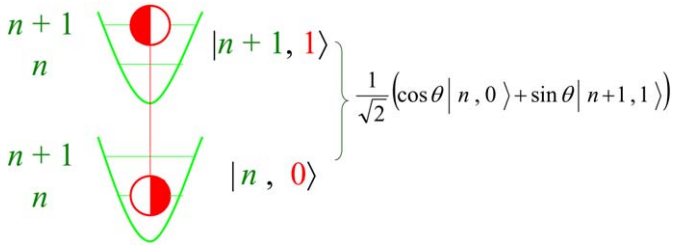


**FIGURE 2.1** Ion vibration in external potential well *correlated* with electronic excitation [39] or spin excitation [48] as described by entangled state with mixing angle $\theta$. Application in quantum information processing [49].

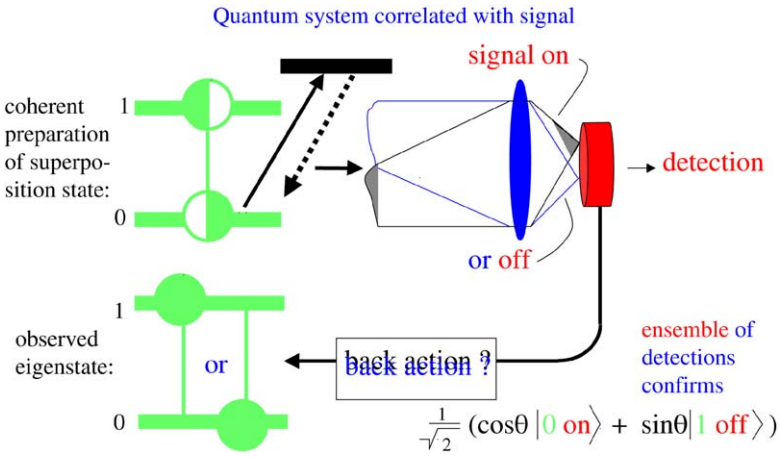


**FIGURE 2.2** A single quantum system, prepared in a superposition of its lower state $|0\rangle$ and upper state $|1\rangle$ by coherent interaction with a resonant radiative pulse of area $\theta$ (top left) does or does not scatter probe light such that signal "*on*" or "*off*" is detected, respectively (top right). A schematically indicated beam of scattered probe light, marked by shaded sectors and "signal *on*", correlates with the quantum system being in state $|0\rangle$. The other schematic beam, marked by "*off*", and indicating null scattering, correlates with the quantum system being in $|1\rangle$. The quantum system is left in one of its eigenstates (bottom left) that is shared (0) or not shared (1) with the probe line. What kind of action, if any, has made the superposition become an eigenstate?

There is another consideration of entanglement needed in the attempt of unravelling an actual observation that is claimed to be a "measurement": namely, when we have to include in the analysis the detector apparatus, or "meter". Let us assume, in another gedanken experiment, an atom being prepared in a *superposition* of its ground state and a metastable state (Figure 2.2). One of these eigenstates, say, the ground state, may become identified by excitation and detection of light scattering on a resonance line: Presence or absence of scattered light makes the atom appear in this "bright" ground state, or in the "dark" excited metastable state, respectively, depending on the scattered-light signal recorded by the detector found "*on*", or "*off*". This is a prototype of what John von Neumann had labelled "state reduction" by a measurement [7]. It was sometimes considered to be caused by the reaction of the meter on the measured system, as suggested in Heisenberg's scheme of microscopically detecting a diffracted electron [8]—which is still another gedanken experiment! Repeated observations of the atom's state via probing by scattered light will provide us with a string of "*on*" or "*off*" results in the shape of a "random telegraph" signal. Its *statistics* certainly will obey the laws of quantum mechanics [9], although the particular, individual trajectory of stochastic data is unpredictable.

Here, obviously, three problems overlap each other:

(1) the temporal evolution of a quantum-mechanical system,
(2) the measurement on such a micro-physical system, and
(3) the emergence of the classical world out of the quantum micro-cosmos.

Attempts to tackle these problems are therefore supposed to benefit from deeper analysing the scenario of an evolving quantum system under repeated or continued measurement, and from an experimental embodiment.

## 2. EVOLUTION FRUSTRATED BY OBSERVATION?

The scenario, at first glance, seems to escape the standard experimental approach, namely comparison of the outcome from a set of observations with predictions based on a fittable model: The control of all degrees of freedom of a quantum object is hard to achieve. Moreover, any measurement requires the interaction of quantum object and classical meter, and the object is supposed to suffer intolerable back action. However, there is a loophole based on "indirect null-result" measurements [10]. Fortunately enough, there are predictions, stated more than half a century ago, that may be matched with the results of measurements on a well-isolated *and available* type of microphysical system. A very counterintuitive prediction proclaims: The evolution of a *measured* quantum system becomes slowed down, or, in the extreme, even completely frustrated [11,12]. This prediction, the "quantum Zeno effect" (QZE) [13], has evoked a wealth of theoretical work [14] but very little, and highly controversial experimental evidence.

A macroscopic and even completely *classical* experiment seems to demonstrate the structure of the Zeno effect: While linearly polarised light propagates in an optically active medium, the concomitant variation of light polarisation turns out impeded by the insertion of analysers [15,16]. A simple implementation is the following one (Figure 2.3): The polarisation of a light beam, set by polariser $P_0$ and probed at distance $L$ by analyser $P_1$, is found rotated by the angle $\theta$. Another analyser $P_2$ inserted at $L/2$ with its direction of transmitted field *parallel* $P_0$ leaves the light polarisation at $P_1$ rotated by $\theta/2$ only. Insertion of $n-1$ of such analysers separated by $L/n$ yields, at the position of $P_1$, the total rotation $\theta/n$. With $n$ growing larger, the rotation at $P_1$ tends to zero, and the original polarisation $P_0$ shows up. Loss from the repetitive projection of the rotated light polarisation on the direction $P_0$ does not invalidate this result: Since the loss per inserted analyser is $(\theta/n)^2$, the total loss is $\theta^2/n$ and vanishes with the rotation.

For a discussion of this scheme, the polarisation of a light beam may be represented by a vector in a three-dimensional configuration space whose symmetry group is SO(3). The apices of all possible polarisation vectors fill the unit sphere, the "Poincaré sphere", whose north and south pole may be chosen as locations of the two eigenstates of linear polarisation, horizontal and vertical (Figure 2.4). States of complete polarisation are placed on the surface, and transformations among these states correspond to rotations of the state vector. In particular, the rotation of linear light polarisation corresponds to the rotation of the state vector along a particular meridian whose plane stands vertically on the plane of the figure. Each increment of propagation along the path length $L/n$ turns the state vector by a finite angle $\theta/n$, but the subsequent transit through the next analyser sets it back. Thus, in the large-$n$ limit, the state vector is left unaltered.

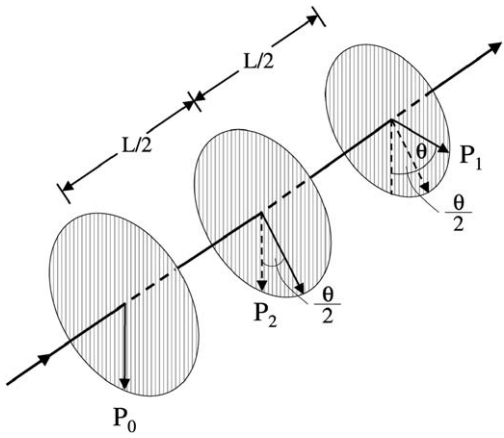


**FIGURE 2.3** A light beam of polarisation $P_0$ propagates through a polarisation-rotating medium. After path length $L$, the polarisation is $P_1$, rotated by the angle $\theta$. With a second analyser ($P_2||P_0$) inserted at $L/2$, the final rotation is $\theta/2$. With $n-1$ analysers (all $||P_0$) inserted at distances $L/n$, the final rotational angle at $P_1$ approaches zero for $n \to \infty$.

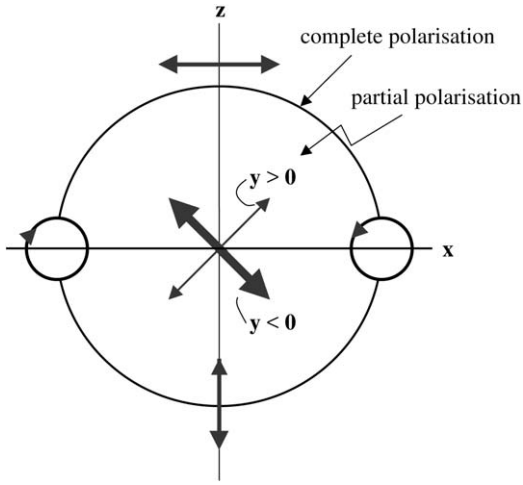


**FIGURE 2.4** Configuration space of light polarisation ("Poincaré sphere"). Thick polarisation arrow in foreground, thin arrow in background.

Although this concept seems convincing, letting it pass as a model of the genuine quantum Zeno effect is questionable: Although an analyser plate is required for measuring the polarisation of light, its mere insertion into a beam may not qualify as a measurement. The inhibition of polarisation may be ascribed, instead, to the filtering action of the set of analysers—not to measurements, understood as acts of gaining information. Moreover, any result of this classical experiment, that a nineteenth-century physicist could have recognized, is deterministic, since every

real measurement on the light polarisation repeated again and again at anyone particular stage of light propagation leads to the same result—within the boundaries set by the standard deviation around the average value. The results are *not* random, as are the results of measurements on a quantum system in a superposition state. This latter restriction does not apply, however, when this experiment makes use of light at the single-photon level.

## 3. OBSERVATIONS ON A DRIVEN QUANTUM SYSTEM

It seems that a better suited approach should make use of a series of actual measurements on an evolving material quantum system. In fact, two-level atoms, equivalent to spin systems, show a formal analogy with light polarisation. Whereas the configuration space of polarisation transforms according to symmetry group SO(3), the symmetry of spin transformation is SU(2), which is a double covering of SO(3), and locally isomorphic with the latter one [17]. Thus, similar visualisations of the dynamics of both systems apply.

In an ensemble of two-level atoms, all of them may be initially prepared in state 0, and driven by a long pulse of radiation resonant with the transition $0 \rightarrow 1$. When we neglect relaxation, for simplicity, the excitation probability for each atom is

$$P_{01}(1) = \sin^2(\theta/2), \tag{1}$$

where $\theta = \Omega\tau$, the pulse duration is $\tau$, and the Rabi frequency $\Omega$ of the driving field varies as the field amplitude at the atomic location [18]. At $\theta = \Omega T = \pi$, all atoms are supposed to be found, after the driving pulse, in state 1 with certainty. Simultaneous irradiation of the ensemble by $n$ short pulses of "probe" light tuned to a resonance line has been considered to interrupt the atoms' coherent evolution, and to make this evolution disintegrate into intervals of length $\tau = T/n$. Then, the final probability of having excited a particular atom during *anyone* of these $n$ intervals is

$$P_{01}(n) \cong n(\Omega\tau/2)^2 = \pi^2/4n, \tag{2}$$

which vanishes in the large-$n$ limit. Recording the amount of scattered light generated by the last probe pulse allows one to measure the chance of *finally finding* the atoms in state 1, i.e. the *net* transition probability [19]

$$P_{01}(n) = \frac{1}{2}\left[1 - \cos^n(\pi/n)\right] \underset{n\rightarrow\infty}{\rightarrow} 0. \tag{3}$$

Along this line, an interesting experiment has been performed on the ground-state hyperfine transition of an ensemble of 5000 beryllium ions in an electromagnetic ion trap [20] (Figure 2.5). The results of this experiment showed complete agreement with the predictions of quantum mechanics as expressed by Eqs. (1) through (3), and this agreement was considered a proof of the QZE.

During the nineties, more and more points of criticism had been raised against the outlined interpretation of this experiment. Arguments that related either acceptance or refusal of the interpretation to the applicability of the postulate of state

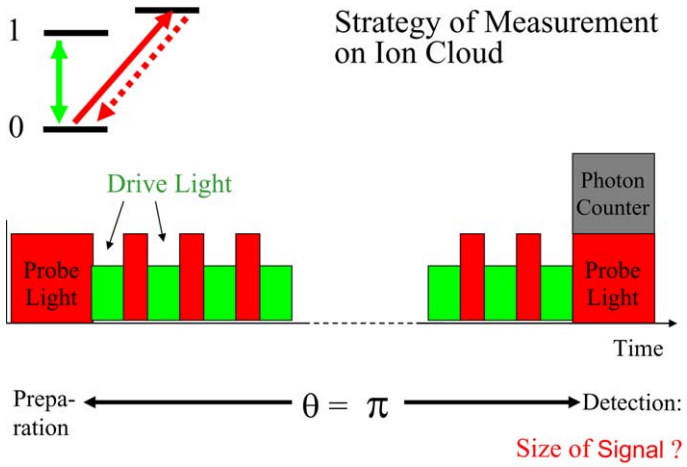


**FIGURE 2.5** Coherent excitation by a long $\pi$-pulse of "driving" radiation, simultaneously irradiated probe pulses, and final detection of ion state [19,20].

reduction have been shown irrelevant [21]. However, more disquieting questions have remained controversial:

1. Recording the *net probability* of finally finding the ions in their excited state was said neither to establish the intermediate probe interactions as measurements, nor to reveal the transition probability: individual transitions, back and forth, may compensate each other and finally leave detectable, at best, the probability of *retrieval* in the ground or excited state [22].
2. The obstruction of the ion's evolution was said comprehensible, at least *in principle*, in terms of physical reaction of the apparatus on the ion ensemble, and as such not being too surprising. Only the *non-local* correlation of system and meter, and a *null result* of the detection, however, would exclude dynamical coupling and qualify as back-action-free measurement. Such a procedure would prove the obstruction of the evolution by *measurement*, that is, by gain of information, and would establish a real QZE, or "quantum Zeno paradox" (QZP) [21].
3. Moreover, measurements on an *ensemble* of quantum systems seem fundamentally unable to discriminate a potentially non-local effect of such a measurement from physical actions of neighbours, environment, or of the measuring device, e.g., the recoil of light on the members of the ensemble [23,24].

The last argument is based on an essential of the quantum description: In a measurement, an ensemble reveals an expectation value that allows the observer to learn about an *average* value of the observable, that characterises the "macro-state" of the system. Any measurement on an individual system, however, yields an *eigen*value, and repeated observations provide a string of information on this system that defines a "micro-state" of the ensemble of the repeated *measurements*. The particular features of measurements on *individual* quantum systems have been

**TABLE 2.1** Preparation and addressing of an individual quantum system

| System | Ensemble | Individual quantum system | Application |
|---|---|---|---|
| Quantity | Expectation value $\langle O \rangle$ | Eigenvalue $O_i$ | |
| Perturbation | Interaction with neighbours | No | Frequency standard |
| Observed | Macro-state average | Micro-state | Quantum information processing |
| Result | Deterministic | Stochastic | Cryptography |

recognized prerequisite for various applications, as time-keeping, quantum information processing, and cryptography (see Table 2.1).

For the unequivocal demonstration of the real QZE, it seems indispensable to address a *single* quantum system. Let us examine in more detail how incomplete information from an ensemble disqualifies an attempted proof.

The quantum states admissible by a two-level atom and a corresponding ensemble may be visualised in the configuration space of SU(2) symmetry, as well as what these objects reveal to their observer. The states of a two-level system [18,25] are placed on the surface of the doubly covered unit sphere, the Bloch sphere (Figure 2.6). On the other hand, an ensemble's Bloch vector can describe mixed states located in the interior of the Bloch sphere. A measurement of the excitation of an ensemble yields an expectation value that corresponds to a particular energy of excitation. This value is *deterministic* save the small variation on the order of its standard deviation—the "projection noise" [26]. The measured value corresponds to a great variety of near-degenerate quantum states, and the actually prepared state cannot be identified from this result. Moreover, the coherent driving should have generated a pure superposition state, but spurious decoherence may have left over a mixed state.

In contrast, a single two-level system is necessarily prepared in a pure state. The result of a measurement on this system is *random*, within the boundaries required by the actual composition of the state, which is determined by the mixing angle $\theta$. However, repeated measurements on the identically prepared system allow the observer to identify $\theta$.

A string of measurements, each of them including reiterated driving the system by pulses of radiation, subsequent probing, and recording scattered probe light, yields a trajectory of results that represents the history of the system's evolution. Any such sequence of results on a single system in the time domain, a particular trajectory, corresponds to a "micro-state" in an ensemble of systems. Whereas the ensemble's micro-state is inaccessible by measurement, the single system's trajectory may become documented. But only the fully documented evolution of the state complies with the requirements for a valid demonstration of the QZE,

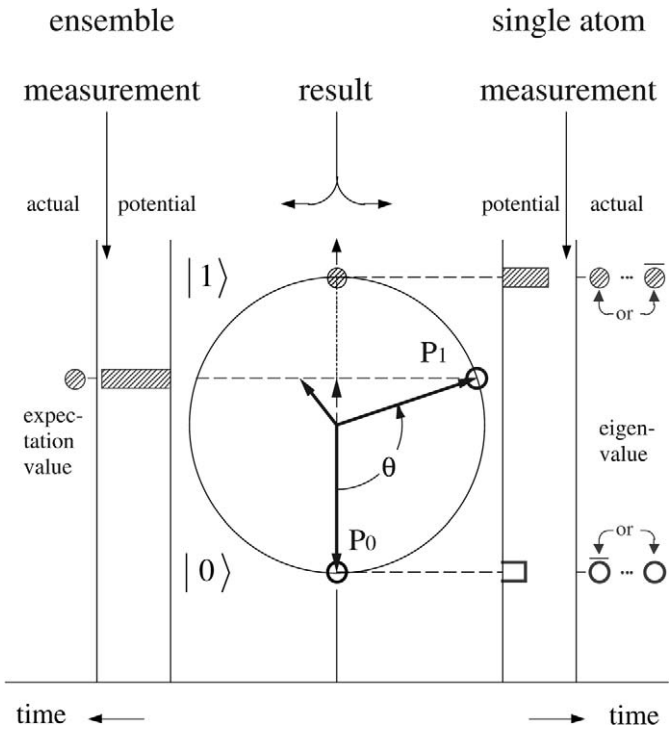


**FIGURE 2.6** Preparation and measurement of two-level quantum system (*SU 2*). $P_0$ initial state vector, $P_1$ after preparation, by pulse with area $\theta$ of *single* quantum system (right). The expectation value from a measurement on an *ensemble* (left) may result from any $P_1$ state located at the horizontal plane indicated by the dashed line. Any such mixed state located inside the Bloch sphere would result from phase decoherence by interaction with measuring device, neighbour atoms, or environment. In contrast, a single-atom measurement makes use of a *pure* state $P_1$, located on the surface of the Bloch sphere, that results from the coherent preparation $P_0 \rightarrow P_1$. The small bars indicate the probabilities of the results of measurement anticipated from $\theta$; they are different, in general, for $|0\rangle$ and $|1\rangle$. The actual result is an eigenvalue: 1 (and not 0), or 0 (and not 1).

since neither non-locality nor the absence of any physical reaction could be taken for granted otherwise. In short, "*... the essence of the quantum Zeno effect is that it is a nonlocal negative-result effect between a microscopic system and a macroscopically separated macroscopic measuring device ...*" [21]. These requirements call for the demonstration of QZE on an *individual* system.

Finally, the complete documentation of the quantum system's evolution entails *recording* the data acquired along each trajectory. Detection of the scattered light in each cycle of probing allows the observer to identify the results of the probing and to distinguish intermediary signals from null signals. On the other hand, recording only the final result after a series of cycles lacks the complete control necessary for the identification and acceptance of a true null-result measurement.

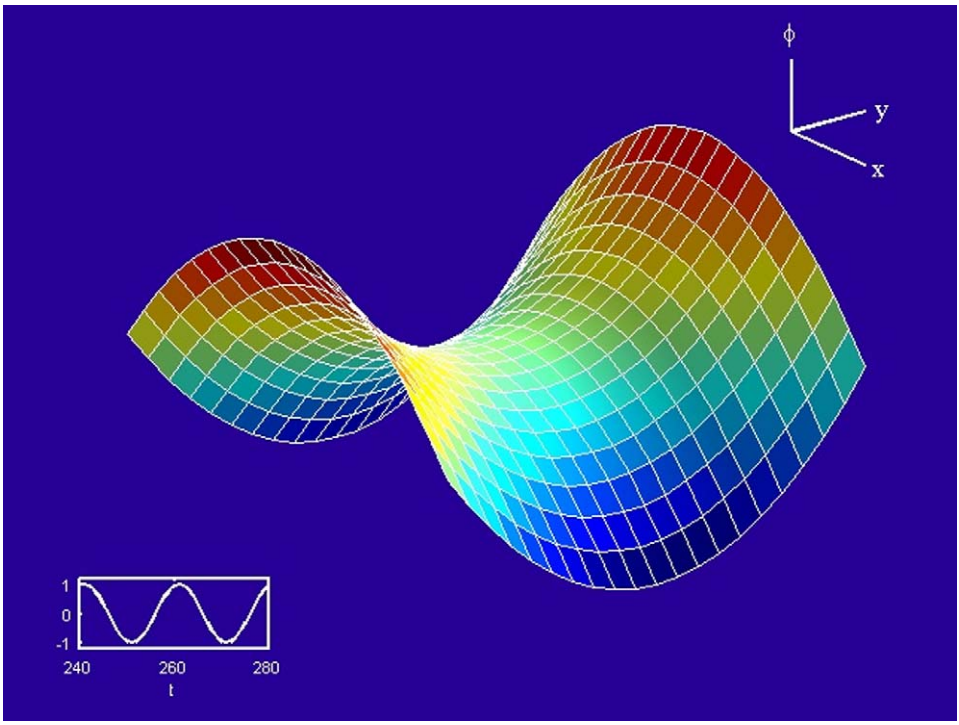


**FIGURE 2.7** Instantaneous electric potential in electrodynamic (Paul) trap. Insert: Temporal variation of the potential. For a colour reproduction of this figure see the colour plate section, near the end of this book.

These preconditions determine a strategy that allows to unequivocally demonstrate the obstruction of a quantum system's evolution as being *caused* by the reiterated acts of measurement.

## 4. MEASUREMENTS ON SINGLE IONS

It is well known how individual atomic ions are singled out, confined *in vacuo*, and cooled as well as controlled by laser light [6,27–30]. Recently, preparation of individual quantum systems has been achieved with neutral atoms and molecules [31–33]. Ions may be stored in a superposition of a homogeneous magnetic field and an electrostatic quadrupole field, the "Penning" ion trap [34], or in an ac electric quadrupole field, the electrodynamic, or "Paul" ion trap [35]. The quadrupole field of a Paul trap is generated inside a ring electrode of 1 mm diameter on whose axis of symmetry ($z$) are placed two grounded cap electrodes facing each other. The ring is loaded by ac voltage of, say, 1 kV and 20 MHz frequency. At any instant of time, a saddle potential extends across any plane ($r$–$z$) containing the trap axis with the caps (Figure 2.7). The direction of the saddle switches back and forth, at the ac frequency, between the $r$- and $z$-directions. Averaging over many ac periods yields

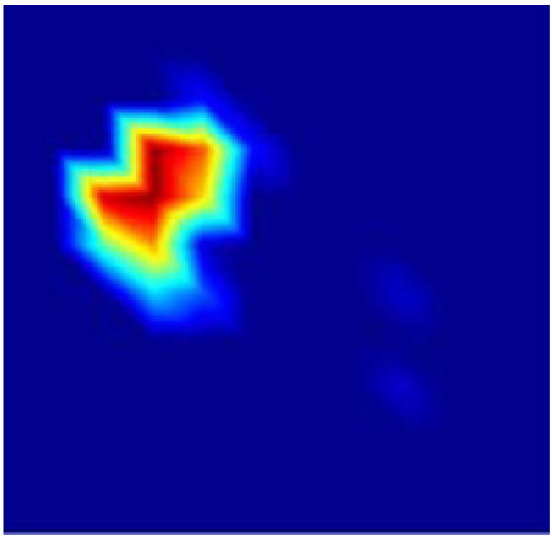

**FIGURE 2.8** An individual trapped barium ion ($^{138}Ba^{+}$). Diffraction-limited image of its laser-induced resonance scattering. False-colour display of scattered intensity. A second ion placed 3 μm apart would show up in the lower right part of the figure, but was temporarily excited into its "dark" metastable state $^{2}D_{5/2}$. For a colour reproduction of this figure see the colour plate section, near the end of this book.

a net dc potential well, on the order of 1 V deep, that derives from the "ponderomotive" electric force. An ion is generated inside the trap volume by impact of an evaporated atom with an electron from a small electron gun. It is retained in this potential well and moves harmonically at about 1 MHz vibrational frequency. In addition, it is driven far off resonance at the ac frequency, with its excursion growing in proportion to its distance from the trap centre, and to the ac amplitude. Since the ac field vanishes at the point of symmetry, a *single* ion at the trap centre is free of this "micro-motion". The ion approaches this location when its "secular" motion in the potential well is laser-cooled [4,5], and by application of small auxiliary dc voltages to the caps. Figure 2.8 shows a single trapped and cooled barium ion ($^{138}Ba^{+}$) in the light of its 492 nm resonance fluorescence, recorded by a CCD camera. The ion may be transferred, either by means of additional laser light from its ground level, or by spontaneous decay, into a metastable state, here $^{2}D_{5/2}$. Such an event is signalled by extinction of the resonance fluorescence [36,37]. In fact, another ion being "dark" resided at the location imaged on the lower right part of the Figure. This ion decayed to the ground state and scattered probe light again a few milliseconds after the image having been recorded.

During the past years, individual ions of barium and ytterbium have been prepared in the outlined way at Hamburg University in order to study the interaction of these ions with light and radio frequency radiation [38–43]. Some of this work was devoted to the very observation of the obstruction of a free ion's evolution by its repeated measurement [41–43]. An experiment on a single ytter-

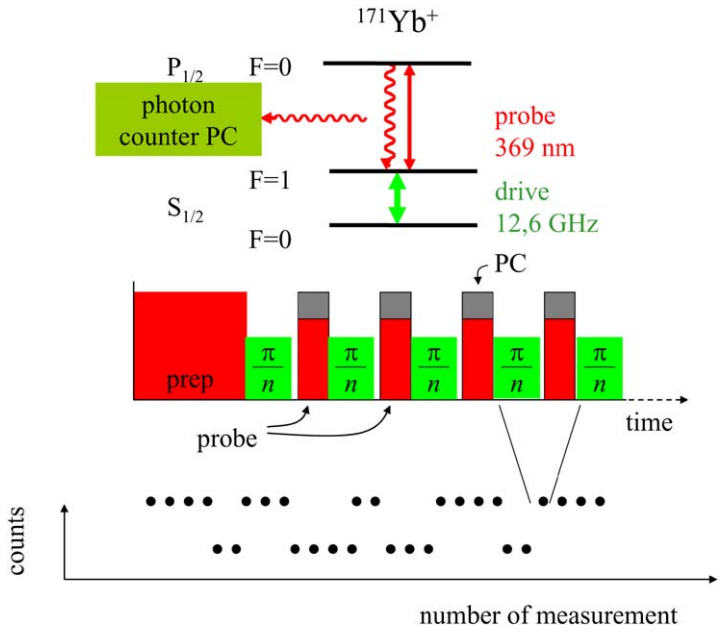


**FIGURE 2.9** Alternating microwave-optical double resonance on individual $^{171}Yb^{+}$ ion: Scheme of excitation and detection (top). Temporal schedule of measurements (middle). Schematic trajectory of results (bottom).

bium ion ($^{171}Yb^{+}$) has been carried out, in principle, as follows (Figure 2.9) [43]: After the ion initially having been prepared in its electronic state 0—the hyperfine level F = 0 of the ground state $^{2}S_{1/2}$—it is irradiated by alternating pulses of microwave radiation (12.6 GHz) and resonant laser light at 369 nm wavelength. The microwave pulses coherently drive the hyperfine resonance, whereas the light probes the F = 1 hyperfine level by attempts of exciting resonance scattering, via the $^{2}S_{1/2}$ (F = 1) − $^{2}P_{1/2}$ line, which succeed *only* if the F = 1 level had been actually populated before. A photon counter, activated synchronously with the probe light, records possibly scattered resonance light. A pair of subsequent drive and probe pulses complete with the activation of the counter represents a single measurement, whose result is one out of the two possible outcomes: scattered light "*on*", or "*off*". These alternatives are strictly correlated with the ion being found in hyperfine level 1, or 0. Reiterated measurements yield a trajectory. Its particular shape is conditionally random, that is, its distribution of the two alternative results depends on the "area" $\theta = \Omega\tau$ of the driving pulses which agrees with the mixing angle of the generated state. The special values $\theta = \pi$ or $2\pi$ would yield deterministic trajectories: alternations of "*on*" or "*off*", or a string of exclusively "*off*" results, respectively. In general, a trajectory is made up of alternating strings of "*on*" and "*off*" results of irregular length. They contain sequences of two, three, four, $\ldots q \ldots$ equal results, whose occurrence may be subject to statistical analysis. The "frequency" $U(q)$ is defined by the number of such a sequence of length $q$

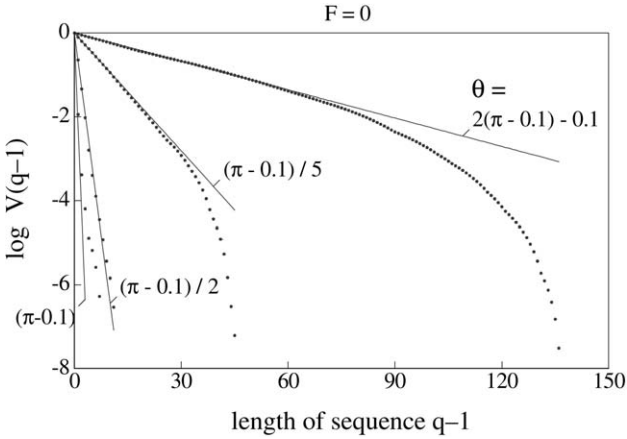


**FIGURE 2.10** Probability $U(q)/U(1)$ of uninterrupted sequences of $q$ results *all* of them "*off*", when the ion was initially prepared in the "*off*" state $F = 0$ (dots; log scale). The lines show the distribution of probability of survival, $V(q-1)$, for the ion *not* undergoing a flip of its spin to the "*on*" state during the entire sequence. Length of trajectories: 2000 measurements of 4.9 ms driving time and 2 ms probing time (see text).

found in the entire trajectory. In a long trajectory containing a large enough number of individual measurements, this normalised frequency is a reliable measure of the *probability* for the appearance of a sequence of specific length. Then, we have

$$U(q) = U(1)V_i(q-1), \tag{4}$$

since the probability of a sequence of $q$ results (all either "*on*", or "*off*") equals the probability for the appearance of one of these results, multiplied by the conditional probability for $(q-1)$-fold survival in this state. This conditional probability is

$$V_i(q-1) = p_i^{q-1} \quad (i = 0 \text{ or } 1) \tag{5}$$

with the simple probability of survival [18,25]

$$p_0 = p_1 = \cos^2(\theta/2), \tag{6}$$

if relaxation can be neglected, as with the hyperfine ground levels. The complement of $p_i$ is the transition probability

$$p_{ij} = 1 - p_i = \sin^2(\theta/2), \tag{7}$$

where $ij = 01$ or 10. Now, the observed normalised numbers of sequences $U(q)/U(1)$ may be compared to the calculated probability of survival from Eq. (5). In Figure 2.10, trajectories, made up of 2000 individual measurements each, and recorded with four different values of pulse area $\theta = \Omega\tau$ have been evaluated. The ratios $U(q)/U(1)$ are shown as dots; the predictions $V_i$ are straight lines in logarithmic scale. The slopes of these lines depend very sensitively on the angle $\theta$ [42]. Thus, fits to the observed data allow a highly precise determination of the area of the actually applied driving pulses, which may somewhat deviate from the

preselected values, for setting the pulse amplitude $\mathcal{E} \propto \Omega$ and duration $\tau$ is liable to deviations. These values were chosen such as to set $\theta$ equal $2\pi - 0.1$, $\pi/5$, $\pi/2$, and $\pi$. The fits almost reproduced these values, but uncovered a systematic error of 0.1 in the settings of the pulse area. The deficiency in the recorded numbers of long sequences ($q \gg 1$) results from the finite length of each trajectory which the more restricts the statistical chance of its occurrence the larger $q$. Eventually, the normalised frequencies $U(q)/U(1)$ cannot anymore be taken for probabilities.

The foremost result of this experiment is the agreement of the empirical distribution $U(q)/U(1)$ with the $(q-1)$-fold conditional survival probability. The latter one has been calculated under the precondition that the coherent evolution of the microwave-driven ion's wave function is broken by just the *possibility* of observation during the intermittent irradiation of probe light. If such breaks were not to happen, the evolution of the ion's wave function should continue during the subsequent intervals of driving. An uninterrupted evolution would require a different calculation of the conditional probabilities of survival [44], namely

$$V''(q-1) = \prod_{n=1}^{q-1} V'(n), \tag{8}$$

where

$$V'(n) = \cos^2(n\theta/2). \tag{9}$$

The step-like function (8) is incompatible with the recorded distributions.

Is the pulse area $\theta$ of the microwave drive small enough, a second measurement will most probably reproduce the result of the first one, since the chance of survival in Eq. (6) deviates from unity only as the *square* of $\theta$. The quantum state we *ascribe* to the ion, based on the previous result, has evolved after the next driving pulse as well as the associated expectation value. This ascribed state could be verified only by a set of observations on the (equally prepared) system. In fact, the equal result of a second measurement makes jump back our *best knowledge* to what we knew after the first measurement, i.e. before the second driving pulse; it is an updating of information, by the measurement. This is why the evolution *ascribed* to the ion is retarded, or frustrated, by reiterated observation even when scattered light, in an "*off*" result, does not show up.

## 5. AN ALTERNATIVE STRATEGY

Still another strategy is capable of divulging the impeding effect of measurement. This alternative approach makes use of effective driving pulses of total pulse area $\theta = \pi$, i.e., of sequences composed out of $n$ fractional pulses (Figure 2.11). Such a composite pulse is expected to transfer the ion from its lower ground level 0 into its upper ground level 1 to a certainty. Any residual population left over in state 0, as brought about by the intermittent irradiation of probe-light pulses, is considered evidence for QZP.

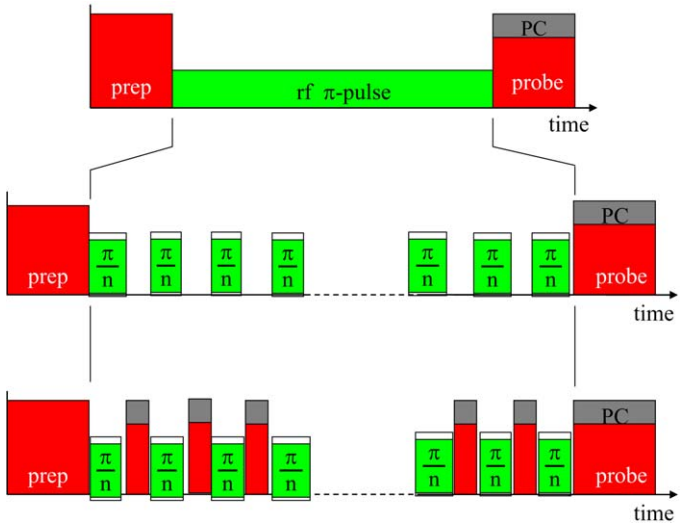


**FIGURE 2.11** Scheme of measurement (*a*) with one driving $\pi$ pulse, (*b*) with fractionated $\pi$ pulse ($n$-times $\pi/n$), no intermediate probing, and (*c*) with $\pi/n$ pulses alternating with probe pulses, *and* simultaneous detection of scattered probe light. PC: photon counting.

So far, this approach recalls the strategy of the experiment on an ensemble of $Be^+$ ions mentioned above [19,20]. However, the present approach is characterised by essential and distinctive features:

1. The quantum object is a *single* ion.
2. The effective pulse of driving is split up in $n$ fractional pulses of area $\pi/n$. During the intermittent intervals, the ion's coherent evolution is supposed to halt.
3. There is no spurious decoherence effect expected to impair the overall coherent evolution, since perturbations that affect the ion's internal state are minimised by its solitary positioning in the trap centre, within ultra-high vacuum.
4. The probe pulses are applied within the intermissions of the coherent driving, not during the driving pulses. Thus, nonlinear interaction of the ion with simultaneously present drive and probe fields is avoided.
5. The photon counter is activated during *all* the probe-light irradiations such that actual *detections* of the scattered light form sequences of $n$ results each. This recording provides control of the ion state whenever probe light examines the ion.

The complete documentation of the ion's history allows one to select sequences that prove the ion to *survive* in state 0, and to discriminate those other sequences that contain some events of transition to state 1. The latter kind of sequences goes unnoticed when merely recording the final result of the sequence. From a large number of recorded sequences, one determines the fraction of histories of $n$-fold *survival* in state 0. This fraction approaches the conditional probability of

survival,

$$P_{00}^{(s)}(n) = \left[p_0(\theta_n)\right]^n = \cos^{2n}(\pi/2n), \tag{10}$$

where $\theta_n = \pi/2n$ [43]. This distribution increases monotonously with $n$.

Ignoring the results of the intermediate recordings by the photon counter makes contribute to the set of data with final result "*off*" many more sequences: those data that reveal one or more intermediate back-and-forth transitions. All these sequences with a final "*off*" form a set of "non-selective" measurements. The compiled results do not approach the survival probability, but rather the probability of *retrieval* in state 0,

$$P_{00}^{(ns)}(n) = \frac{1}{2}\left[1 + \cos^n(\pi/n)\right] \underset{n\to\infty}{\to} 1, \tag{11}$$

which is the complement of (3).

A set of non-selective measurements cannot indicate the survival of the ion. Rather, it conveys information analogous to that from an experiment on an ensemble of quantum systems [19,20]. In both cases, agreement of the observed distributions with (3) or (11) does *not* qualify as proof of measurement-induced survival of the quantum system.

The results of a series of selective measurements are shown in Figure 2.12. The normalised numbers of sequences whose $n$ results *never* showed light scattering have been plotted at five values of $n$. Control measurements lacking the intermediate probing should finally leave the ion in the light-scattering state 1, and they should allow no survival. Indeed, the results of such a test show null survival for $n$ up to 3, in agreement with actual $\pi$-pulse driving. At $n = 9$, there is a 10% chance of survival in the "dark" state 0. This deviation from the strictly coherent ion evolution hints to increasing perturbation of the ion state upon the extended duration of the actual measurement: The area of the fractional driving pulses, $\Omega(n)\tau = \pi/n$, had been set by keeping $\tau$ constant, and varying $\Omega(n) \propto \sqrt{I(n)}$ via the local intensity of the driving radiation $I$, in step with $n$. Therefore, the duration of the complete $\pi$ pulse increased with $n$, and left the ion's state more susceptible to decoherence by thermal radiation from the environment.

In Figure 2.12, also shown are the calculated probabilities of survival in selective measurements ($P_{00}^{(s)}$, black bars), and the probabilities of retrieval in non-selective measurements ($P_{00}^{(ns)}$, white bars). Both types of results agree, within the error limits, with the observed data, which are displayed only for the selective measurements. The agreement of the former data with the corresponding probabilities $P_{00}^{(s)}$ from Eq. (10) indeed proves the frustration of the quantum mechanical evolution by the repeated acts of measurement, that is, of the QZE. An essential feature of the observed data set is its exclusive composition of *null results*. Any reaction to the quantum object by the measuring device cannot account for the corresponding acts of measurement. Measurements of this kind leave the system untouched—they are in fact "quantum non-demolition" measurements [10].

Both reported experiments prove a quantum system's evolution being impeded by a measurement that involves *no physical backaction*. The very existence

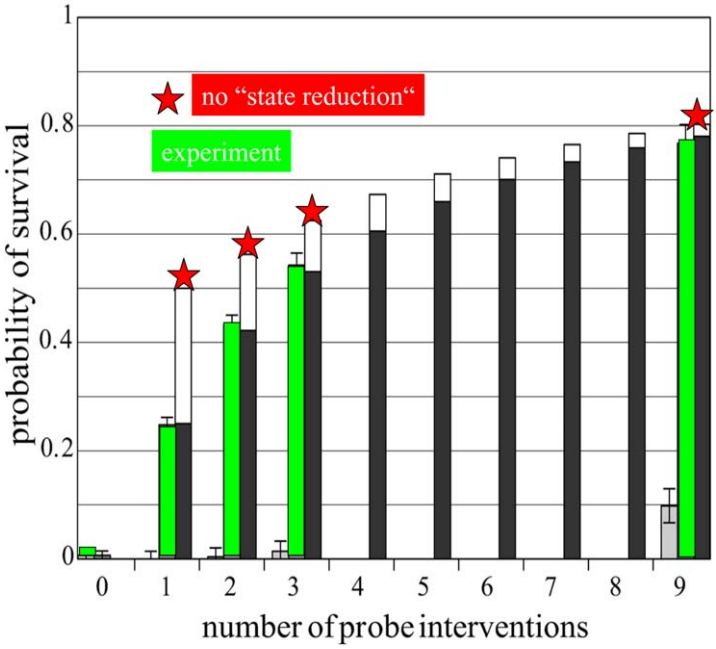


**FIGURE 2.12** Probability of *survival* in the "*off*" state with intermediate probing (green bars, grey in print), and with no probing (light-gray bars close to abscissa line), versus number *n* of $\pi$-pulse partition. The probability is evaluated by counting as favourable those measurements that show only "*off*" results in each of the *n* observations. Driving time 2.9 ms, probing time 3 ms. Probability of *survival* in a selective measurement, calculated after Eq. (8) (black bars). The probability of *retrieval* (stars), evaluated from the *entire* ensemble of results with final "*off*" irrespective intermediate "*on*" results would represent a non-selective measurement and does not prove QZP. This probability is calculated after (11) (white bars behind black bars).

of such an impedance, the QZP, requires reinspection of epistemological positions in the context of quantum-mechanical measurement.

## 6. SUMMARY

The experiments outlined in Sections 4 and 5, as well as corresponding ones that involve a *light*-driven ion [41], have allowed the reiterated detection of the internal state of a free, isolated quantum system without perturbing this quantum state. The results show that mere observation and recognition of the results—the "gain of knowledge"—retards or inhibits the temporal evolution of the system, *as it is predicted* by quantum-mechanical modelling. This effect is the consequence of an intentionally prepared correlation of the system with the detected signal—a particular entanglement of quantum states and meter states [21]. Whereas in most kinds of actual measurement on a quantum system the detected signal in fact physically reacts on the measured system, the above results show that such

a reaction seems irrelevant for both the definition and the comprehension of the measurement process. This situation forbids dynamical explanations of the fundamental uncertainty of micro-physical measurements, as in the early concept of the "Heisenberg microscope" that relied on this very reaction for the vindication of the limitations imposed upon the measurement process by quantum mechanics [8].

The empirical findings seem to support a simple interpretation: The results of measurements convey information on the measured object; they establish an element of reality, embodied in the data strings of the trajectories. Predictions provided by quantum mechanics on the basis of these results represent the *potentiality* of the future evolution of the system, not its reality. The predicted evolution passes a discontinuity when a new result of a measurement is available. The well-known consequences of such a discontinuity are

**(1)** loss of coherence of the quantum system as an intrinsic effect of *potentially* allowed measurements, and
**(2)** the renormalisation of the predictions as an effect of a new factual result of the measurement that updates the initial conditions for the predicted evolution.

On the other hand, if we insist on attributing reality to the predicted quantum mechanical evolution, we have to trade in "real" discontinuities of this evolution, including the acceptance of state reduction as a dynamic effect.

Taking into account the consequences of the two possible alternative positions, it seems more acceptable to restrict the role of quantum modelling to the *potential* future, in the tradition of Wolfgang Pauli [45]. Although state reduction plays an important role as a tool in computational applications [14], it seems to reflect only the stepwise gain of knowledge in the course of subsequent measurements.

Aside from the epistemological notion, there is a more down-to-earth motivation to the reported work: It demonstrates how to achieve, by microwaves and even by light, a crucial manipulation of an individual two-level-atom, equivalent to a spin system, in its configuration space, the deliberate "coherent rotation". This process, fundamental for preparation and application of micro-physical systems, is associated with maximally controlled absorption and emission of radiative energy by an atom. A spin system is the physical representation of a "qubit", the smallest unit of quantum information. Thus, the demonstration of coherent rotation in configuration space, especially in the optical domain is a small but essential step in the progress towards technical applications of manipulations on individual quantum systems [46,47]. These techniques promise to put into reality, in a not too distant future, the long-proclaimed quantum computer that will herald a new age of quantum information processing.

## REFERENCES

[1] A. Einstein, B. Podolsky, N. Rosen, *Phys. Rev.* **47** (1935) 777.
[2] D. Bohm, *Quantum Theory*, Prentice–Hall, Englewood, Cliffs, NJ, 1951;
See: J.S. Bell, *Speakable and Unspeakable in Quantum Mechanics*, Cambridge Univ. Press, Cambridge, UK, 1987.
[3] E. Schrödinger, *Br. J. Philos. Sci.* **3** (1952) 109.

[4] W. Neuhauser, M. Hohenstatt, P.E. Toschek, H.G. Dehmelt, *Phys. Rev. Lett.* **41** (1978) 233.
[5] W. Neuhauser, M. Hohenstatt, P.E. Toschek, H.G. Dehmelt, *Appl. Phys.* **17** (1978) 123.
[6] W. Neuhauser, M. Hohenstatt, P.E. Toschek, H. Dehmelt, *Phys. Rev. A* **22** (1980) 1137.
[7] J. von Neumann, *Mathematische Grundlagen der Quantenmechanik*, Springer, Berlin, 1932.
[8] W. Heisenberg, *Z. Phys.* **43** (1927) 172.
[9] Trajectories may be described by sets of quantum correlation functions whose required number increases with the length of the trajectory.
See, e.g., A. Schenzle, R.G. Brewer, *Phys. Rev. A* **34** (1986) 3127.
[10] V.B. Braginsky, F.Ya. Khalili, *Quantum Measurement*, Cambridge Univ. Press, Cambridge, England, 1992.
[11] L.A. Khalfin, *Pis'ma Zh. Eksp. Teor. Fiz.* **8** (1968) 106 [*JETP Lett.* **8** (1968) 65].
[12] L. Fonda, G.C. Ghirardi, A. Rimini, T. Weber, *Nuovo Cimento A* **15** (1973) 689.
[13] B. Misra, E.C.G. Sudarshan, *J. Math. Phys. (N.Y.)* **18** (1977) 756.
[14] A. Beige, G.C. Hegerfeldt, *Phys. Rev. A* **53** (1996) 53.
[15] A. Peres, *Am. J. Phys.* **48** (1990) 11.
[16] P. Kwiat, H. Weinfurter, Th. Herzog, A. Zeilinger, *Phys. Rev. Lett.* **74** (1995) 4763.
[17] J.J. Sakurai, *Modern Quantum Mechanics*, Addison–Wesley, Reading, MA, 1994.
[18] L. Allen, J.H. Eberly, Optical Resonance & Two Level Atoms, Wiley, New York, 1975.
[19] R. Cook, *Phys. Scr. T* **21** (1988) 49.
[20] W.M. Itano, D.J. Heinzen, J.J. Bollinger, D.J. Wineland, *Phys. Rev. A* **41** (1990) 2295; *Phys. Rev. A* **43** (1991) 5168.
[21] D. Home, M.A.B. Whitaker, *Ann. Phys. (NY)* **258** (1997) 237.
[22] H. Nakazato, M. Namiki, S. Pascazio, H. Rauch, *Phys. Lett. A* **217** (1996) 203.
[23] T.P. Spiller, *Phys. Lett. A* **192** (1994) 163.
[24] O. Alter, Y. Yamamoto, *Phys. Rev. A* **55** (1997) 2499.
[25] P. Meystre, M. Sargent III, *Elements of Quantum Optics*, Springer-Verlag, Berlin, Heidelberg, 1990.
[26] W.M. Itano, J.C. Bergquist, J.J. Bollinger, J.M. Gilligan, D.J. Heinzen, F.L. Moore, M.G. Raizen, D.J. Wineland, *Phys. Rev. A* **47** (1993) 3554.
[27] P.E. Toschek, Atomic particles in traps, in: G. Grynberg, R. Stora (Eds.), *New Trends in Atomic Physics (Les Houches Session 1982)*, North-Holland, Amsterdam, 1982, p. 283.
[28] Th. Sauter, R. Blatt, W. Neuhauser, P.E. Toschek, *Opt. Commun.* **60** (1986) 287.
[29] Th. Sauter, H. Gilhaus, I. Siemers, R. Blatt, W. Neuhauser, P.E. Toschek, *Z. Phys. D* **10** (1988) 153.
[30] I. Siemers, M. Schubert, R. Blatt, W. Neuhauser, P.E. Toschek, *Europhys. Lett.* **18** (1992) 139.
[31] S. Kuhr, W. Alt, D. Schrader, M. Müller, V. Gomer, D. Meschede, *Science* **293** (2001) 278.
[32] I. Dotsenko, W. Alt, M. Khudaverdyan, S. Kuhr, D. Meschede, Y. Miroshnychenko, D. Schrader, A. Rauschenbeutel, *Phys. Rev. Lett.* **95** (2005) 033002.
[33] U. Kubitscheck, U. Fischer (Eds.), *Single Mol.* **3** (2002) 253ff.
[34] F.M. Penning, *Physica* **3** (1936) 873.
[35] W. Paul, O. Osberghaus, E. Fischer, Forschungsber. d. Wirtsch., u. Verkehrsministerium NRW, Nr. **415** (1955).
[36] W. Nagourney, J. Sandberg, H. Dehmelt, *Phys. Rev. Lett.* **56** (1986) 2797.
[37] Th. Sauter, W. Neuhauser, R. Blatt, P.E. Toschek, *Phys. Rev. Lett.* **57** (1986) 1696.
[38] B. Appasamy, J. Eschner, Y. Stalgies, I. Siemers, *Phys. Scr. T* **59** (1995) 278.
[39] B. Appasamy, Y. Stalgies, P.E. Toschek, *Phys. Rev. Lett.* **80** (1998) 2805.
[40] R. Huesmann, Chr. Balzer, Ph. Courteille, W. Neuhauser, P.E. Toschek, *Phys. Rev. Lett.* **82** (1999) 1611.
[41] Chr. Balzer, R. Huesmann, W. Neuhauser, P.E. Toschek, *Opt. Commun.* **180** (2000) 115.
[42] P.E. Toschek, Ch. Wunderlich, *Eur. Phys. J. D* **14** (2001) 387.
[43] Chr. Balzer, Th. Hannemann, R. Huesmann, D. Reiß, Chr. Wunderlich, W. Neuhauser, P.E. Toschek, *Opt. Commun.* **211** (2002) 235.
[44] P.E. Toschek, Chr. Balzer, *J. Opt. B: Quantum Semiclass. Opt.* **4** (2002) S450.
[45] W. Pauli, *Wahrscheinlichkeit und Physik, Dialectica* **8** (2) (1954);
W. Pauli, *Phänomen und physikalische Realität, Dialectica* **11** (1/2) (1957);
Quoted after: W. Pauli, *Physik und Erkenntnistheorie*, Vieweg, Braunschweig, 1984.

[46] D.P. DiVincenzo, *Fortschr. Phys.* **48** (2000) 771.
[47] A.M. Steane, D.M. Lucas, *Fortschr. Phys.* **48** (2000) 839.
[48] C. Monroe, D.M. Meekhof, B.E. King, W.M. Itano, D.J. Wineland, *Phys. Rev. Lett.* **75** (1995) 4714.
[49] J.I. Cirac, P. Zoller, *Phys. Rev. Lett.* **74** (1995) 4091.

CHAPTER 3

# The Quantum SI: A Possible New International System of Units

**Peter J. Mohr***

Contents



Abstract

The International System of Units is a widely used system of measurement standards that provide the basis for expressing physical quantities, such as the kilogram for mass. This paper will describe a proposed modernization of some of the unit definitions that would provide a system that is more stable over time and more suitable for expressing the values of many fundamental constants.

## 1. INTRODUCTION

It is generally recognized that it is in the interests of science, technology, and commerce to have a universally agreed to set of measurement standards. In fact, efforts in unification and standardization of measurements date back thousands of years.

* National Institute of Standards and Technology, Gaithersburg, MD 20899-8420, USA

Advances in Quantum Chemistry, Vol. 53
ISSN 0065-3276, DOI:10.1016/S0065-3276(07)53003-0
Published by
Elsevier Inc. (2008)

Currently, the International System of Units (SI) provides standards that are officially used by many countries.

As science and technology have advanced, standards have also advanced. A recent change in the SI was made in 1983, when the definition of the meter was revised to be the distance that light travels in a specified time interval. Also, for some time it has been recognized that, after more than 100 years of use, the definition of the kilogram to be the mass of the prototype located near Paris at the International Bureau of Weights and Measures (BIPM), is no longer satisfactory. Moreover, the definition of the ampere has not been used as a practical current standard since 1990. To deal with these shortcomings, redefinitions of the kilogram and ampere are being considered by the metrology community; redefinitions of the kelvin for temperature and the mole for amount of substance are also being discussed [1].

In this paper, the relevant issues and the proposed redefinitions are reviewed. One of the consequences of these possible redefinitions is that values of many of the fundamental constants, when expressed in the new units, would be exact and many others would have reduced uncertainties. Another possibly surprising result is that the new definitions could be made in such a way that the distinction between base units and derived units, presently specified in the SI, would become unnecessary and could be eliminated. This might be called unit democracy, in which all SI units have equal status. In principle, this scheme could be extended to include an analogous redefinition of the second, but this would have to await improved accuracy in the relevant experiments and theory. Constraints on timing of the proposed redefinitions, which could take effect as early as 2011, will be described.

## 2. INTERNATIONAL SYSTEM OF UNITS

The International System of Units is presently defined in terms of seven base units, various coherent derived units, and units that are defined to be in other categories.

The seven base units and symbols are:

- **meter** m (length),
- **kilogram** kg (mass),
- **second** s (time),
- **ampere** A (electric current),
- **kelvin** K (thermodynamic temperature),
- **mole** mol (amount of substance),
- **candela** cd (luminous intensity).

A few of the many SI derived units and symbols are:

- **hertz** Hz (frequency),
- **newton** N (force),
- **joule** J (energy),
- **coulomb** C (electric charge),
- **volt** V (electric potential difference).

The derived units are coherent with the base units and each other, which means that relations between equivalent ways of expressing units have unit coefficients. As an example $1\ \mathrm{J} = 1\ \mathrm{kg\,m^2\,s^{-2}}$.

Non-SI units and symbols are also recognized in the SI. Two examples are:

- **electron volt** eV (energy),
- **unified atomic mass unit** u (mass).

In general, the non-SI units are not coherent with the SI units; for example, $1\ \mathrm{eV} \approx 1.6 \times 10^{-19}$ J, where the coefficient is not unity, and in this case depends on measured quantities.

The SI system of units provides the international basis for expressing physical quantities that is officially recognized by the 51 states that are members of the Convention of the Meter.

## 3. THE KILOGRAM AND THE AMPERE

In the SI system, the unit of mass is the kilogram, which is defined to be the mass of the prototype kilogram kept at the International Bureau of Weights and Measures (BIPM) near Paris. This definition was adopted by the 3rd General Conference on Weights and Measures (CGPM) in 1901, with some minor subsequent modifications. Figure 3.1 shows a replica of the international prototype of the kilogram. Although it is kept under glass covers, it is not in vacuum. This way of defining the kilogram has a number of limitations:

- The prototype definition is not linked to an unchanging property of nature.
- The mass of the international prototype appears to be changing relative to the mass of its copies.
- The drift of the kilogram prototype together with its copies (relative to an unchanging standard) could be as large as $20 \times 10^{-9}$ kg per year [2,3].
- The prototype and its copies appear to gain mass over time and lose mass when washed for use in comparisons.
- The kilogram mass definition cannot be realized independently of the international prototype.

It is also of interest to consider the definition of the ampere adopted by the 9th CGPM in 1948: *The ampere is that constant current which, if maintained in two straight parallel conductors of infinite length, of negligible circular cross-section, and placed one meter apart in vacuum, would produce between these conductors a force equal to* $2 \times 10^{-7}$ *newton per meter of length.* For the precision that is possible with present day technology, this definition is not useful, because it does not provide a measurement standard with comparable precision. In general, it has not been used since 1990, when a conventional electrical system of units was adopted. This modified system is based on the fact that modern voltage measurements are based on the Josephson effect and modern resistance measurements are based on the quantum Hall effect. In this case, voltage and resistance measurements are made in terms of the Josephson constant $K_J$ and von Klitzing constant $R_K$, respectively. The theoretical

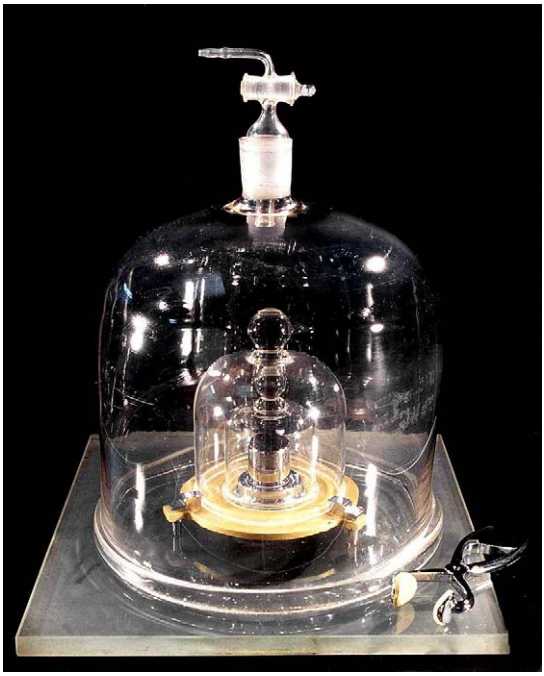

**FIGURE 3.1** A replica of the international prototype of the kilogram.

relations,

$$K_{\mathrm{J}} = \frac{2e}{h}, \tag{1}$$

$$R_{\mathrm{K}} = \frac{h}{e^2}, \tag{2}$$

which are often assumed to be exact, relate these constants to the elementary charge $e$ and the Planck constant $h$. However, the values of $e$ and $h$ in SI units are of a limited accuracy that is well below the measurement precision that can be achieved. Therefore, in the conventional electrical system, the SI values are replaced by the exact values

$$K_{\text{J-90}} = 483\,597.9\ \text{GHz/V}, \tag{3}$$

$$R_{\text{K-90}} = 25\,812.807\ \Omega, \tag{4}$$

which provide an arbitrary, but precise definition of voltage and resistance.

## 4. POSSIBLE REDEFINITIONS OF THE KILOGRAM

The limitations on the stability of the kilogram defined in terms of the international prototype could be eliminated if the kilogram were defined in terms of a

fundamental constant in analogy with the definition of the meter. This definition of the meter, adopted by the 17th CGPM in 1983, is: *The meter is the length of the path traveled by light in vacuum during a time interval of 1/299 792 458 of a second.* As a consequence, the velocity of light $c$ is given by:

$$c = \frac{1\ \mathrm{m}}{1/299\,792\,458\ \mathrm{s}} = 299\,792\,458\ \mathrm{m/s}. \tag{5}$$

An alternative statement of the definition of the meter could be: *The meter is the unit of length scaled such that the velocity of light is* 299 792 458 m/s.

An analogous definition of the kilogram, based on a certain value of a fundamental constant, can be made by specifying the value of the Planck constant. Such a definition could be used to determine the mass of an object by means of the watt-balance experiment [3–5] which is sketched as follows.

In a recent version of the experiment [5], a horizontal circular coil is suspended in a radial magnetic field produced by superconducting magnets. In the first phase of the experiment, the current in the coil is adjusted so that the net magnetic forces on the coil equal the force of gravity on a 1 kilogram mass. In the second phase of the experiment, the coil is slowly moved through the magnetic field and the induced voltage on the coil and the velocity of the coil are measured to calibrate the magnetic field and geometry factors. The electrical measurements are done in terms of the Josephson and von Klitzing constants, which results in a determination of the combination

$$K_{\mathrm{J}}^2 R_{\mathrm{K}} = \frac{4}{h}, \tag{6}$$

assuming the relations in Eqs. (1) and (2) are exact. The present-day interpretation of this experiment is that the precise kilogram mass together with the watt-balance experiment determine the value of the Planck constant $h$.

On the other hand, if the value of the Planck constant were specified in advance, then that value, together with the watt-balance experiment, would determine the mass used in the first phase of the experiment in kilograms. This means that instead of using the example of an object that has the mass of one kilogram in order to define the unit, one could specify a value of the Planck constant and use the watt-balance experiment to determine the mass of a given object in the resulting kilogram units. Of course, the value for the Planck constant would be selected so that the new kilogram unit would be as close as possible to the current artifact based kilogram. In this way, a possible new definition of the kilogram might be: *The kilogram is the unit of mass scaled such that the Planck constant is exactly* $6.626\,069\,3 \times 10^{-34}$ J s.

An alternative definition of the kilogram could be made in terms of an assigned value of the Avogadro constant. In this case the relevant experiment could be the Avogadro Project [6], which is an international effort to measure the Avogadro constant by determining the number of atoms in a kilogram of silicon, along the lines of Ref. [7].

In this experiment, the volume and lattice spacing of a crystalline silicon sphere with a precisely known mass is measured to determine the number of atoms it

contains. This result, together with the relative atomic mass of silicon isotopes and the isotopic composition of the sphere, determines a value of the Avogadro constant.

On the other hand, if a value of the Avogadro constant were specified in advance, then that value, together with the Avogadro Project experiment, would determine the mass of the sphere in kilograms. The corresponding definition of the kilogram would be: *The kilogram is the unit of mass scaled such that the Avogadro constant is exactly* $6.022\,141\,5 \times 10^{23}\ \mathrm{mol}^{-1}$.

## 5. RELATION BETWEEN THE AVOGADRO CONSTANT AND THE PLANCK CONSTANT

Although the experiments to measure the Planck constant and the Avogadro constant are completely independent, the values of the two constants are closely related theoretically. An expression for the mass of the electron in kilograms can be obtained from the definition of the Rydberg constant $R_\infty$:

$$R_\infty = \frac{\alpha^2 m_\mathrm{e} c}{2h} \quad \Rightarrow \quad \frac{1}{m_\mathrm{e}} = \frac{\alpha^2 c}{2hR_\infty}, \tag{7}$$

where $\alpha$ is the fine-structure constant and $m_\mathrm{e}$ is the mass of the electron, which taken together with the expression for the electron mass in terms of the unified atomic mass unit u:

$$m_\mathrm{e} = A_\mathrm{r}(\mathrm{e})\mathrm{u} \quad \Rightarrow \quad \frac{1}{\mathrm{u}} = \frac{A_\mathrm{r}(\mathrm{e})}{m_\mathrm{e}}, \tag{8}$$

yields a relation between the Avogadro constant and the Planck constant given by

$$N_\mathrm{A} = \frac{10^{-3}\ \mathrm{kg/mol}}{1\ \mathrm{u}} = A_\mathrm{r}(\mathrm{e})\left(\frac{\alpha^2 c}{2hR_\infty}\right) \times 10^{-3}\ \mathrm{kg/mol}. \tag{9}$$

This relation contains other constants, but the uncertainties of those constants are much smaller than the uncertainty of either $N_\mathrm{A}$ or $h$ [8]. The result of this relationship is that in principle, either of the constants could be specified to define the kilogram, and either experiment could be used to realize the definition.

At present, the relation can be used to calculate a value of the Planck constant determined by the Avogadro Project experiment to be compared to the value obtained from watt-balance experiments. Figure 3.2 shows values of the Planck constant determined by various experiments, including watt-balance experiments, labeled $K_\mathrm{J}^2 R_\mathrm{K}$, and the Avogadro Project experiment, labeled $V_\mathrm{m}$(Si) (see Ref. [8] for an explanation of the other entries). As is evident from the figure, there is disagreement between the two methods of determining the Planck constant. Presumably, this disagreement will be resolved by further work on the experiments.

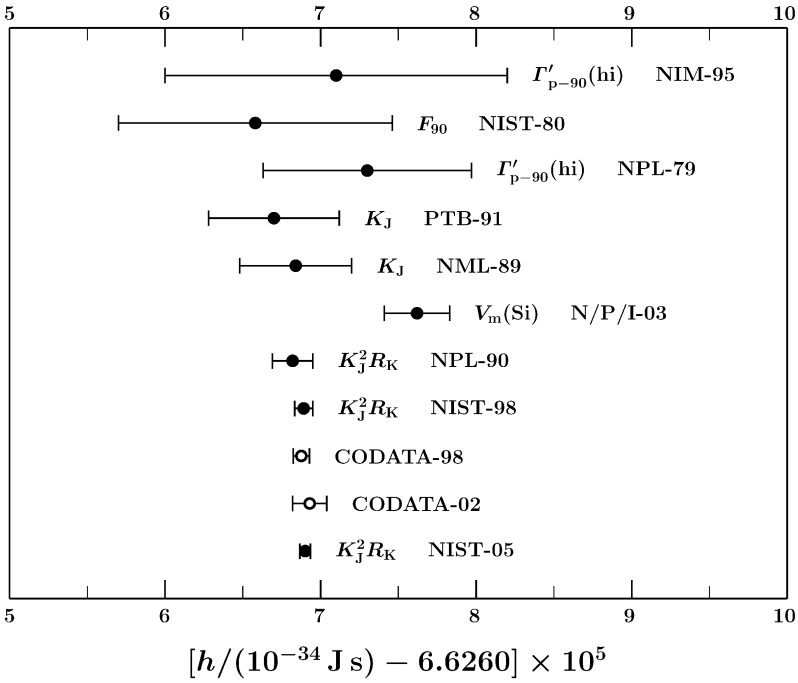


**FIGURE 3.2** Values of the Planck constant determined by various experiments.

## 6. OTHER REDEFINITIONS

Redefinitions in terms of fundamental constants are also being considered for the ampere, kelvin, and mole [1].

Such a definition of the ampere could be: *The ampere, unit of electric current, is such that the elementary charge is* $1.602\,176\,53 \times 10^{-19}$ *coulomb.* This definition determines the ampere, because in principle at least, one could count the number of electrons passing through a surface, and since the amount of charge carried by each electron would be known, the current would also be known. One of the consequences of this definition is that the electric constant $\epsilon_0$ and the magnetic constant $\mu_0$ would no longer be exact quantities, but would be defined by experiment through the expressions

$$\alpha = \frac{e^2}{4\pi\epsilon_0 \hbar c} \tag{10}$$

and $\epsilon_0\mu_0 = c^{-2}$, for example. Thus, the value of $\epsilon_0$ would follow directly from the value of $\alpha$, since $e$, $\hbar$, and $c$ would have exact values. Another consequence would be that the Josephson constant and the von Klitzing constant, as given in Eqs. (1) and (2) would be exact quantities. This would be valuable for electrical metrology, because voltage and resistance are measured in terms of these constants, and they would have exact values in the new SI. As a result, precise electrical measure-

ments could be made in terms of SI units rather than the arbitrary units defined by Eqs. (3) and (4), as they presently are.

The kelvin temperature unit could be defined in terms of an exact value of the Boltzmann constant $k$ by the statement: *The kelvin, the unit of thermodynamic temperature, is scaled such that the Boltzmann constant is exactly* $1.380\,650\,5 \times 10^{-23}$ *joule per kelvin.*

Similarly, the mole could be defined in terms of an exact value of the Avogadro constant $N_A$ through the statement: *The mole, the unit of amount of substance, is scaled such that the Avogadro constant is exactly* $6.022\,141\,5 \times 10^{23}$ *per mole.*

## 7. CONSEQUENCES FOR OTHER FUNDAMENTAL CONSTANTS

If the SI units were redefined as described above, other fundamental constants, which are functions of the constants used in the new definitions, would also be exact. A partial list is:

- Faraday constant $\mathcal{F}$
- molar gas constant $R$
- Stefan–Boltzmann constant $\sigma$
- eV–joule conversion factor
- Hz–joule conversion factor
- kelvin–joule conversion factor

The effect of these new SI definitions would be to decrease the uncertainties of many other fundamental constants not used in the new definitions. For example, the relative uncertainty of the mass of the electron in kilograms $m_e$ would change from $2 \times 10^{-7}$ to $2 \times 10^{-9}$. Of course, the mass of the current kilogram artifact mass would no longer be exactly one kilogram, but rather would be determined by experiment, with its uncertainty being of the order of a few parts in $10^8$.

## 8. THE QUANTUM SI

The SI system defined in terms of fundamental constants as discussed above is more closely related to atomic scale phenomena than to macroscopic scale standards, as is presently the case. Hence, the name Quantum SI might be appropriate for the new system. It is quantum in the sense that it uses the Planck constant, the quantum of action and angular momentum; the elementary charge, which is quantized; the Boltzmann constant, which appears in the Planck radiation formula; and the mole directly defined as a number of entities, rather than in terms of mass, which emphasizes the role of atoms and molecules. The present day definitions of the kilogram, ampere, and kelvin, and mole are independent of quantum phenomena, since they are based on concepts that predate such knowledge.

In the Quantum SI, the fundamental constants, $c$, $h$, $e$, $k$, and $N_A$, and at least for the moment, the hyperfine frequency of cesium $\nu_{Cs}$, would have exact values. The SI redefinitions have been described in terms of the base units, such as

the kilogram and ampere to make contact with the present-day system. However, a moment's reflection reveals that associating particular constants with particular units is unnecessary. For example, specifying that the hyperfine frequency of cesium has a particular value and that the speed of light (in meters/second) has a particular value assures that the meter will be a particular length without stating that specification of the speed of light defines the meter. Similarly, the specification of the elementary charge determines the ampere without specifically stating that fact. It is sufficient to define the Coulomb by relating it to the elementary charge, and from that current, which is charge divided by time, follows from the fact that the SI units are coherent. In fact, charge is a derived unit that is defined by specifying the value of the electron charge in coulombs. An explicit association with current is not necessary.

The conclusion that can be drawn from these considerations is that the separation of units into base units and derived units is not necessary in the Quantum SI. This would eliminate the arbitrary selection of base units.

## 9. THE SECOND

Evidently, the present definition of the second is out of character with the rest of the definitions based on constants which could be called universal (with the possible exception of the Avogadro constant). In contrast, the hyperfine frequency of cesium is a property of a specific atom.

A definition of the second that is consistent with those made in terms of universal constants could, in principle at least, be based on specifying a value for the Rydberg constant, which is also a universal constant. If the value of the Rydberg constant in inverse meters were specified, then since the speed of light $c$ is exact, the corresponding frequency would be fixed. From this, the observed frequencies of particular atomic transitions could be known and used as time standards.

The drawback, at the moment, is that the theory needed to relate the Rydberg constant to observable frequencies is not sufficiently accurate to make this modification without introducing an excessively large uncertainty. This could change in the future, but for now, such a redefinition would not be practical.

## 10. TIME SCALE FOR REDEFINITIONS

At its meeting in October 2004, the International Committee on Weights and Measures (CIPM) asked the Consultative Committee on Units (CCU) to study the possibility of a fundamental constant-based definition of the kilogram. In June, 2005, the CCU requested that the CIPM approve preparation of possible new definitions of the kilogram, ampere, and kelvin in terms of fundamental constants, and also consider redefining the mole at the same time. At its meeting in October, 2005, the CIPM approved, in principle, preparation of the new definitions, as requested by the CCU, for possible adoption by the General Conference on Weights and Measures (CGPM) in 2011, provided the results of experiments over the next few years make this acceptable.

## 11. CONCLUSION

The SI can be improved by modernizing the way units are defined. In particular, the definitions of the kilogram, ampere, kelvin and mole are based on 19th century science and technology and can be replaced by ones that take into account subsequent progress in physics.

If an update of the SI were done by specifying values of fundamental constants, the concepts of base units and derived units would not be necessary.

If there are no persistent problems with experiments, the changes could be made in 2011.

## REFERENCES

[1] I.M. Mills, P.J. Mohr, T.J. Quinn, B.N. Taylor, E.R. Williams, *Metrologia* **43** (2006) 227.
[2] R. Davis, *Metrologia* **40** (2003) 299.
[3] E.R. Williams, R.L. Steiner, D.B. Newell, P.T. Olsen, *Phys. Rev. Lett.* **81** (1998) 2404.
[4] B.P. Kibble, I.A. Robinson, J.H. Belliss, *Metrologia* **27** (1990) 173.
[5] R.L. Steiner, E.R. Williams, D.B. Newell, R. Liu, *Metrologia* **42** (2005) 431.
[6] P. Becker, H. Bettin, H.-U. Danzebrink, M. Gläser, U. Kuetgens, A. Nicolaus, D. Schiel, P. De Bièvre, S. Valkiers, P. Taylor, *Metrologia* **40** (2003) 271.
[7] R.D. Deslattes, A. Henins, H.A. Bowman, R.M. Schoonover, C.L. Carroll, I.L. Barnes, L.A. Machlan, L.J. Moore, W.R. Shields, *Phys. Rev. Lett.* **33** (1974) 463.
[8] P.J. Mohr, B.N. Taylor, *Rev. Mod. Phys.* **77** (2005) 1.

CHAPTER 4

# Studies of Light Halo Nuclei from Atomic Isotope Shifts

**G.W.F. Drake*** and **Z.-C. Yan****

Contents



Abstract

This paper reviews progress in the application of atomic isotope shift measurements, together with high precision atomic theory, to the determination of nuclear radii from the nuclear volume effect. The theory involves obtaining essentially exact solutions to the nonrelativistic three- and four-body problems for helium and lithium by variational methods. The calculation of relativistic and quantum electrodynamic corrections by perturbation theory is discussed, and in particular, methods for the accurate calculation of the Bethe logarithm part of the electron self energy are presented. The results are applied to the calculation of isotope shifts for the short-

* Department of Physics, University of Windsor, Windsor, Ontario, Canada N9B 3P4
E-mail: GDrake@uwindsor.ca
** Department of Physics, University of New Brunswick, Fredericton, New Brunswick, Canada E3B 5A3
E-mail: zyan@unb.ca

Advances in Quantum Chemistry, Vol. 53
ISSN 0065-3276, DOI:10.1016/S0065-3276(07)53004-2

lived 'halo' nuclei $^6$He and $^{11}$Li in order to determine their nuclear charge radii from high precision spectroscopic measurements. It is shown that the results provide a unique measurement tool that is capable of discriminating amongst a variety of theoretical models for nuclear structure. In view of the high precision that is now obtainable, helium and lithium, along with hydrogen, can be regarded as fundamental atomic systems whose spectra are well understood for all practical purposes.

## 1. INTRODUCTION

More than 20 years ago, Tanihata *et al.* [1,2] discovered that certain neutron-rich nuclei such as $^6$He and $^{11}$Li have a halo-like structure in which a pair of neutrons orbits a more tightly bound core. Since the neutrons are electrically neutral, one would expect the nuclear mass radius to be substantially larger than the charge radius, and this is in fact the hallmark of a halo nucleus. A comparison between the two radii provides a sensitive test of nuclear structure models, and especially of correlation effects between the two neutrons in the presence of the core. However, the nuclear charge radius has been notoriously difficult to measure in a model-independent way. This paper provides an overview of recent advances in both theory and experiment that open the way to a new method for accurate determinations of the nuclear charge radius. The key idea is that the isotope shift in atomic transition frequencies depends on the nuclear charge radius, as well as a large number of other effects that depend on the mass difference between the two isotopes, such as $^6$He and $^4$He. The nuclear charge radius can thus be determined if the other mass-dependent effects can be calculated to sufficient accuracy and subtracted from high-precision laser-resonance measurements of the isotope shift. Accuracies of the order of 100 kHz or better are required.

The basic idea of using the isotope shift to determine the nuclear charge radius has been in use for many years for heavy nuclei [3,4] where the field shift is proportionately much bigger. For such cases, relativistic coupled cluster methods are sufficiently accurate. However, for light nuclei, the necessary accuracies of $\pm 100$ kHz have not been available until recently. The achievement of this goal requires accurate nonrelativistic eigenvalues, relativistic corrections of order $\alpha^2$ Ry, and quantum electrodynamic corrections of order $\alpha^3$ Ry, where $\alpha \simeq 1/137.035\,999\,11(46)$ is the fine structure constant. Recent advances over the past several years [5–10] now make it possible to obtain solutions to the quantum mechanical three- and four-body problem that are essentially exact for all practical purposes, at least in the nonrelativistic limit. The calculation of the lowest order $\alpha^2$ Ry relativistic corrections is then straight-forward, but the calculation of the QED corrections (especially the Bethe logarithm) has remained a long- standing problem in atomic physics. This last problem has also now been solved [11], thereby opening the way to complete calculations up to order $\alpha^3$ Ry. Even these terms by themselves would introduce uncertainties much larger than the required $\pm 100$ kHz. However, it is only the finite mass corrections to these terms that contribute to the isotope shift, and so the uncertainties are suppressed by a factor of the electron-nucleus mass ratio of $\mu/M \simeq 10^{-4}$ for $^6$He or $^{11}$Li.

**TABLE 4.1** Contributions to the energy and their orders of magnitude in terms of $Z$, $\mu/M = 1.370\,745\,624 \times 10^{-4}$ (for $^4$He), and $\alpha^2 = 0.532\,513\,5450 \times 10^{-4}$

| Contribution | Magnitude |
|---|---|
| Nonrelativistic energy | $Z^2$ |
| Mass polarization | $Z^2\mu/M$ |
| Second-order mass polarization | $Z^2(\mu/M)^2$ |
| Relativistic corrections | $Z^4\alpha^2$ |
| Relativistic recoil | $Z^4\alpha^2\mu/M$ |
| Anomalous magnetic moment | $Z^4\alpha^3$ |
| Hyperfine structure | $Z^3 g_1 \mu_0^2$ |
| Lamb shift | $Z^4\alpha^3 \ln\alpha + \cdots$ |
| Radiative recoil | $Z^4\alpha^3(\ln\alpha)\mu/M$ |
| Finite nuclear size | $Z^4\langle \bar{r}_c/a_0\rangle^2$ |

On the experimental side, there is a large body of high precision data available for comparison. The particular significance in relation to the present work is that the theoretical uncertainty in the D-states for helium is now so small that their energies can be taken as absolute points of reference. The measured transition frequencies to the lower-lying S- and P-states can then be used to determine the absolute ionization energies of these states (see Drake and Martin [12], and Morton *et al.* [13]), and from this the QED energy shifts can be determined.

## 2. THEORETICAL BACKGROUND

Table 4.1 summarizes the various contributions to the energy, expressed as a double expansion in powers of $\alpha \simeq 1/137.036$ and the electron reduced mass ratio $\mu/M \simeq 10^{-4}$. Since all the lower-order terms can now be calculated to very high accuracy, including the QED terms of order $\alpha^3$ Ry, the dominant source of uncertainty comes from the QED corrections of order $\alpha^4$ Ry or higher. The comparison between theory and experiment is therefore sensitive to these terms. For the isotope shift, the QED terms independent of $\mu/M$ cancel out, and so it is only the radiative recoil terms of order $\alpha^4\mu/M \simeq 10^{-12}$Ry ($\sim$10 kHz) that contribute to the uncertainty. Since this is much less than the finite nuclear size correction of about 1 MHz, the comparison between theory and experiment clearly provides a means to determine the nuclear size.

## 3. SOLUTION TO THE NONRELATIVISTIC SCHRÖDINGER EQUATION

### 3.1 Variational basis sets for helium

Considering first the case of helium, the starting point for the calculation is to find accurate solutions to the nonrelativistic Schrödinger equation. The effects of finite

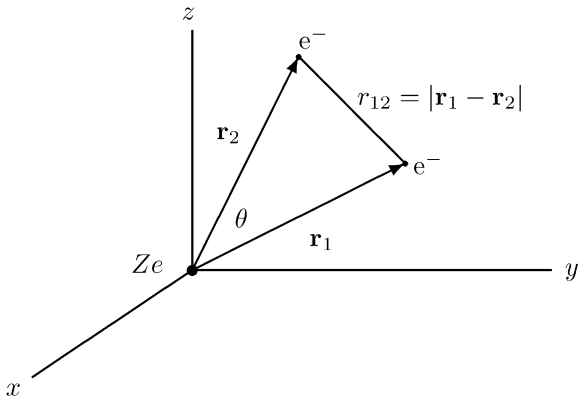


**FIGURE 4.1** Coordinate system for a helium atom with the nucleus at the origin.

nuclear mass will play a key role in studies of the isotope shift, but we begin with the case of infinite nuclear mass, in which case the nucleus can be taken as a fixed point of reference. The Schrödinger equation is then given by (in atomic units)

$$\left(-\frac{1}{2}\nabla_1^2 - \frac{1}{2}\nabla_2^2 - \frac{Z}{r_1} - \frac{Z}{r_2} + \frac{1}{r_{12}}\right)\Psi(\mathbf{r}_1, \mathbf{r}_2) = E\Psi(\mathbf{r}_1, \mathbf{r}_2). \tag{1}$$

The usual methods of theoretical atomic physics, such as the Hartree–Fock approximation or configuration interaction methods, are not capable of yielding results of spectroscopic accuracy. For this reason, specialized methods have been developed. As long ago as 1929, Hylleraas suggested expanding the wave function in an explicitly correlated variational basis set of the form

$$\Psi(\mathbf{r}_1, \mathbf{r}_2) = \sum_{i,j,k} a_{ijk} r_1^i r_2^j r_{12}^k e^{-\alpha r_1 - \beta r_2} \mathcal{Y}^M_{l_1 l_2 L}(\hat{\mathbf{r}}_1, \hat{\mathbf{r}}_2) \tag{2}$$

where $r_{12} = |\mathbf{r}_1 - \mathbf{r}_2|$ is the interelectronic separation (see Figure 4.1). The coefficients $a_{ijk}$ are linear variational parameters, and $\alpha$ and $\beta$ are nonlinear variational coefficients that set the distance scale for the wave function. The usual strategy is to include all powers such that $i + j + k \leqslant \Omega$ (a so-called Pekeris shell), where $\Omega$ is an integer. The inclusion of powers of $r_{12}$, and especially the odd powers, makes the basis set rapidly convergent as $\Omega$ increases. The basis set is provably complete in the limit $\Omega \to \infty$ [14].

For states of higher angular momentum $L$, the quantity $\mathcal{Y}^M_{l_1 l_2 L}(\hat{\mathbf{r}}_1, \hat{\mathbf{r}}_2)$ denotes a vector-coupled product of spherical harmonics, and the basis set includes a summation over the possible integer values of $l_1$ and $l_2$ (with $l_2$ constrained to be $l_2 = L - l_1$) such that $l_1 \leqslant L/2$. In addition, the nonlinear parameters $\alpha$ and $\beta$ are separately optimized for each set of angular momentum terms, and, as discussed in Refs. [5–7], it is desirable further to 'double' the basis set so that each set of powers $\{i, j, k\}$ is included two (or more [15]) times with different values of $\alpha$ and $\beta$. For sufficiently large basis sets, the doubling is very important because it

helps to preserve the numerical stability of the wave function, it gives improved accuracy for a given total size of basis set, and it avoids the disastrous loss of accuracy that normally sets in for variational calculations involving the higher-lying Rydberg states [5–7].

The principal computational steps are first to orthogonalize the $\chi_{ijk}$ basis set, and then to diagonalize the Hamiltonian matrix **H** in the orthogonalized basis set so as to satisfy the Rayleigh–Schrödinger variational principle

$$\delta \int \Psi (H - E)\Psi \, d\tau = 0. \tag{3}$$

Finally, a complete optimization is performed with respect to variations in the $\alpha$s and $\beta$s so as to minimize the energy.

For high precision calculations, and especially for the isotope shift, it is necessary to include also the motion of the nucleus in the center-of-mass (CM) frame. A transformation to CM plus relative coordinates yields the additional $-(\mu/M)\nabla_1 \cdot \nabla_2$ mass polarization term in the modified Hamiltonian

$$H = -\frac{1}{2}\nabla_1^2 - \frac{1}{2}\nabla_2^2 - \frac{Z}{r_1} - \frac{Z}{r_2} + \frac{1}{r_{12}} - \frac{\mu}{M}\nabla_1 \cdot \nabla_2 \tag{4}$$

in reduced mass atomic units $e^2/a_\mu$, where $a_\mu = (m/\mu)a_0$ is the reduced mass Bohr radius, and $\mu = mM/(m+M)$ is the electron reduced mass, $M$ is the nuclear mass, and $a_0 = \hbar^2/me^2$ is the Bohr radius. The mass polarization term can be treated either by including it as a perturbation (up to second-order), or by including it explicitly in the Hamiltonian. The latter procedure is simpler and more direct, and the coefficient of the second-order term can still be extracted by differencing [5,7]. A general method for the decomposition of this equation was developed many years ago by Bhatia and Temkin [16], and the effects of mass polarization studied by Bhatia and Drachman [17] for a range of values of $\mu/M$. These authors have also extended the calculation of the second-order mass polarization term for several low-lying states to the He-like ions [18].

As an example, Table 4.2 shows a convergence study for the very well studied case of the ground state of helium [15]. The quantity $R$ in the last column is the ratio of successive differences between the energies. A constant or slowly changing value of $R$ indicates smooth convergence, and allows a reliable extrapolation to $\Omega \to \infty$. The results clearly indicate that convergence to 20 or more figures can be readily obtained, using conventional quadruple precision (32 decimal digit) arithmetic in FORTRAN. The very large calculation by Schwartz [20], using 104-digit arithmetic, provides a benchmark for comparison.

## 3.2 Variational basis sets for lithium

The same variational techniques can be applied to lithium and other three-electron atomic systems. In this case, the terms in the Hylleraas correlated basis set have the form

$$r_1^{j_1} r_2^{j_2} r_3^{j_3} r_{12}^{j_{12}} r_{23}^{j_{23}} r_{31}^{j_{31}} e^{-\alpha r_1 - \beta r_2 - \gamma r_3} \mathcal{Y}^{LM}_{(\ell_1\ell_2)\ell_{12},\ell_3}(\mathbf{r}_1, \mathbf{r}_2, \mathbf{r}_3)\chi_1, \tag{5}$$

**TABLE 4.2** Convergence study for the ground state of helium (infinite nuclear mass case) [15]. $N$ is the number of terms in the 'triple' basis set

| $\Omega$ | $N$ | $E(\Omega)$ | $R(\Omega)$ |
|---|---|---|---|
| 8 | 269 | −2.903 724 377 029 560 058 400 | |
| 9 | 347 | −2.903 724 377 033 543 320 480 | |
| 10 | 443 | −2.903 724 377 034 047 783 838 | 7.90 |
| 11 | 549 | −2.903 724 377 034 104 634 696 | 8.87 |
| 12 | 676 | −2.903 724 377 034 116 928 328 | 4.62 |
| 13 | 814 | −2.903 724 377 034 119 224 401 | 5.35 |
| 14 | 976 | −2.903 724 377 034 119 539 797 | 7.28 |
| 15 | 1150 | −2.903 724 377 034 119 585 888 | 6.84 |
| 16 | 1351 | −2.903 724 377 034 119 596 137 | 4.50 |
| 17 | 1565 | −2.903 724 377 034 119 597 856 | 5.96 |
| 18 | 1809 | −2.903 724 377 034 119 598 206 | 4.90 |
| 19 | 2067 | −2.903 724 377 034 119 598 286 | 4.44 |
| 20 | 2358 | −2.903 724 377 034 119 598 305 | 4.02 |
| Extrapolation | $\infty$ | −2.903 724 377 034 119 598 311(1) | |
| Korobov [19] | 5200 | −2.903 724 377 034 119 598 311 158 7 | |
| Korobov extrap. | $\infty$ | −2.903 724 377 034 119 598 311 159 4(4) | |
| Schwartz [20] | 10259 | −2.903 724 377 034 119 598 311 159 245 194 404 4400 | |
| Schwartz extrap. | $\infty$ | −2.903 724 377 034 119 598 311 159 245 194 404 446 | |
| Goldman [21] | 8066 | −2.903 724 377 034 119 593 82 | |
| Bürgers *et al.* [22] | 24 497 | −2.903 724 377 034 119 589(5) | |
| Baker *et al.* [23] | 476 | −2.903 724 377 034 118 4 | |

where $\mathcal{Y}^{LM}_{(\ell_1\ell_2)\ell_{12},\ell_3}$ is again a vector-coupled product of spherical harmonics, and $\chi_1$ is a spin function with spin angular momentum 1/2. As for helium, the usual strategy is to include all terms from (5) such that

$$j_1 + j_2 + j_3 + j_{12} + j_{23} + j_{31} \leqslant \Omega, \tag{6}$$

and study the eigenvalue convergence as $\Omega$ is progressively increased. The lithium problem is much more difficult than helium both because the integrals over fully correlated wave functions are more difficult, and because the basis set grows much more rapidly with increasing $\Omega$. Nevertheless, there has been important progress in recent years [24–26], and results of spectroscopic accuracy can be obtained for the low-lying states.

Bhatia and Drachman have also made important progress in applying the asymptotic expansion methods to the Rydberg states of lithium [27–29]. The calculations in this case are more difficult because the 'polarizable core' now consists of the nucleus and two 1s electrons, and so its multipole moments cannot be calculated analytically.

## 4. RELATIVISTIC CORRECTIONS

This section briefly summarizes the lowest-order relativistic corrections of order $\alpha^2$ Ry, and the relativistic recoil corrections of order $\alpha^2\mu/M$ Ry. The well-known terms in the Breit interaction [30] (including for convenience the anomalous magnetic moment terms of order $\alpha^3$ Ry) give rise to the first-order perturbation correction

$$\Delta E_{\rm rel} = \langle \Psi_J | H_{\rm rel} | \Psi_J \rangle, \tag{7}$$

where $\Psi_J$ is a nonrelativistic wave function for total angular momentum $\mathbf{J} = \mathbf{L} + \mathbf{S}$ and $H_{\rm rel}$ is defined by (in atomic units)

$$H_{\rm rel} = \left(\frac{\mu}{m_{\rm e}}\right)^4 B_1 + \left(\frac{\mu}{m_{\rm e}}\right)^3 \left[ B_2 + B_4 + B_{\rm so} + B_{\rm soo} + B_{\rm ss} + \frac{m_{\rm e}}{M}\left(\tilde{\Delta}_2 + \tilde{\Delta}_{\rm so}\right) + \gamma\left(2B_{\rm so} + \frac{4}{3}B_{\rm soo} + \frac{2}{3}B_{3{\rm e}}^{(1)} + 2B_5\right) + \gamma\frac{m_{\rm e}}{M}\tilde{\Delta}_{\rm so}\right] \tag{8}$$

with $\gamma = \alpha/(2\pi)$. The factors of $(\mu/m_{\rm e})^4 = (1-\mu/M)^4$ and $(\mu/m_{\rm e})^3 = (1-\mu/M)^3$ arise from the mass scaling of each term in the Breit interaction, while the terms $\tilde{\Delta}_2$ and $\tilde{\Delta}_{\rm so}$ are dynamical corrections arising from the transformation of the Breit interaction to CM plus relative coordinates [31]. These latter terms are often not included in atomic structure calculations, but they make an important contribution to the isotope shift. The explicit expressions for the spin-independent operators are

$$B_1 = \frac{\alpha^2}{8}\left(p_1^4 + p_2^4\right), \tag{9}$$

$$B_2 = -\frac{\alpha^2}{2}\left(\frac{1}{r_{12}}\mathbf{p}_1\cdot\mathbf{p}_2 + \frac{1}{r_{12}^3}\mathbf{r}_{12}\cdot(\mathbf{r}_{12}\cdot\mathbf{p}_1)\mathbf{p}_2\right), \tag{10}$$

$$B_4 = \alpha^2\pi\left(\frac{Z}{2}\delta(\mathbf{r}_1) + \frac{Z}{2}\delta(\mathbf{r}_2) - \delta(\mathbf{r}_{12})\right) \tag{11}$$

and the spin-dependent terms are

$$B_{\rm so} = \frac{Z\alpha^2}{4}\left[\frac{1}{r_1^3}(\mathbf{r}_1\times\mathbf{p}_1)\cdot\boldsymbol{\sigma}_1 + \frac{1}{r_2^3}(\mathbf{r}_2\times\mathbf{p}_2)\cdot\boldsymbol{\sigma}_2\right], \tag{12}$$

$$B_{\rm soo} = \frac{\alpha^2}{4}\left[\frac{1}{r_{12}^3}\mathbf{r}_{12}\times\mathbf{p}_2\cdot(2\boldsymbol{\sigma}_1+\boldsymbol{\sigma}_2) - \frac{1}{r_{12}^3}\mathbf{r}_{12}\times\mathbf{p}_1\cdot(2\boldsymbol{\sigma}_2+\boldsymbol{\sigma}_1)\right], \tag{13}$$

$$B_{\rm ss} = \frac{\alpha^2}{4}\left[-\frac{8}{3}\pi\delta(\mathbf{r}_{12}) + \frac{1}{r_{12}^3}\boldsymbol{\sigma}_1\cdot\boldsymbol{\sigma}_2 - \frac{3}{r_{12}^3}(\boldsymbol{\sigma}_1\cdot\mathbf{r}_{12})(\boldsymbol{\sigma}_2\cdot\mathbf{r}_{12})\right]. \tag{14}$$

Finally, the relativistic recoil terms are [31]

$$\tilde{\Delta}_2 = -\frac{Z\alpha^2}{2}\left\{\frac{1}{r_1}(\mathbf{p}_1+\mathbf{p}_2)\cdot\mathbf{p}_1 + \frac{1}{r_1^3}\mathbf{r}_1\cdot\left[\mathbf{r}_1\cdot(\mathbf{p}_1+\mathbf{p}_2)\right]\mathbf{p}_1 + \frac{1}{r_2}(\mathbf{p}_1+\mathbf{p}_2)\cdot\mathbf{p}_2 + \frac{1}{r_2^3}\mathbf{r}_2\cdot\left[\mathbf{r}_2\cdot(\mathbf{p}_1+\mathbf{p}_2)\right]\mathbf{p}_2\right\}, \tag{15}$$

$$\tilde{\Delta}_{\rm so} = \frac{Z\alpha^2}{2}\left(\frac{1}{r_1^3}\mathbf{r}_1 \times \mathbf{p}_2 \cdot \boldsymbol{\sigma}_1 + \frac{1}{r_2^3}\mathbf{r}_2 \times \mathbf{p}_1 \cdot \boldsymbol{\sigma}_2\right). \tag{16}$$

It is then a relatively straight forward matter to calculate accurate expectation values for these operators. Also, asymptotic expansions have been derived for the matrix elements and compared with the direct variational calculations, as discussed in Ref. [7].

## 5. QED CORRECTIONS

For a many-electron atom, the total QED shift of order $\alpha^3\,\mathrm{Ry}$ consists of two parts—an electron-nucleus part $E_{\mathrm{L},1}$ (the Kabir–Salpeter term [32]), and an electron–electron term $E_{\mathrm{L},2}$ originally obtained by Araki [33] and Sucher [34]. The $E_{\mathrm{L},2}$ term is relatively small and stright-forward to calculate. The principal computational challenges come from the $E_{\mathrm{L},1}$ term given by (in atomic units)

$$E_{L,1} = \frac{4}{3}Z\alpha^3\langle\delta(\mathbf{r}_1) + \delta(\mathbf{r}_2)\rangle\left[\ln\alpha^{-2} - \beta(1s n\ell) + \frac{19}{30}\right], \tag{17}$$

where $\beta(1s n\ell)$ is the two-electron Bethe logarithm arising from the emission and re-absorption of a virtual photon (see Figure 4.2). It is the logarithmic remainder after mass renormalization, and is defined by

$$\beta(1s n\ell) = \frac{\mathcal{N}}{\mathcal{D}} = \frac{\sum_i |\langle\Psi_0|\mathbf{p}_1 + \mathbf{p}_2|i\rangle|^2(E_i - E_0)\ln|E_i - E_0|}{\sum_i |\langle\Psi_0|\mathbf{p}_1 + \mathbf{p}_2|i\rangle|^2(E_i - E_0)}. \tag{18}$$

The foregoing equations are virtually identical to the corresponding one-electron (hydrogenic) case, except that there the $\delta$-function matrix elements can be replaced by their hydrogenic value

$$\langle\delta(\mathbf{r}_1) + \delta(\mathbf{r}_2)\rangle \to Z^3/(\pi n^3). \tag{19}$$

The sum in the denominator of (18) can be completed by closure with the result

$$\mathcal{D} = \langle\Psi_0|\mathbf{p}(H - E_0)\mathbf{p}|\Psi_0\rangle = 2\pi Z\langle\delta(\mathbf{r}_1) + \delta(\mathbf{r}_2)\rangle, \tag{20}$$

where $\mathbf{p} = \mathbf{p}_1 + \mathbf{p}_2$. The numerator is much more difficult to calculate because the sum over intermediate states (including an integration over the continuum)

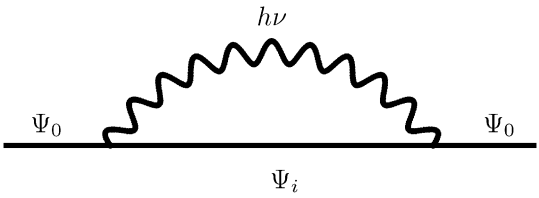


**FIGURE 4.2** Feynman diagram for the electron self energy.

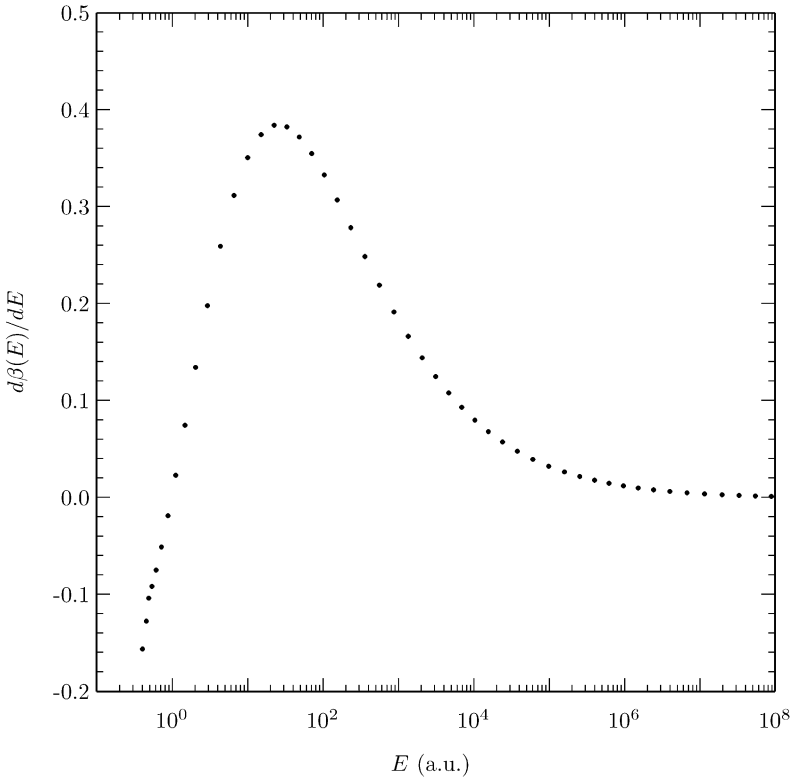


**FIGURE 4.3** Differential contributions to the Bethe logarithm for the ground state of hydrogen. Each point represents the contribution from one pseudostate.

cannot be performed analytically, and a sum over pseudostates nearly diverges at high energies. Schwartz [35] transformed the numerator to read

$$\mathcal{N} = \lim_{K\to\infty}\left(-K\langle\Psi_0|\mathbf{p}\cdot\mathbf{p}|\Psi_0\rangle + \mathcal{D}\ln(K) + \int_0^K k\,dk\langle\Psi_0|\mathbf{p}(H-E_0+k)^{-1}\mathbf{p}|\Psi_0\rangle\right). \tag{21}$$

However, this is slowly convergent, and expensive in computer time since a matrix diagonalization must be performed at each integration point. Despite this, results of useful accuracy for the lowest-lying S- and P-states have been obtained by this method in Refs. [36–38].

An alternative method based on a discrete variational representation of the continuum in terms of pseudostates has been developed by Drake and Goldman [11]. The method is simplest to explain for the case of hydrogen. The key idea is to define a variational basis set containing a huge range of distance scales according to:

$$\chi_{i,j} = r^i \exp(-\alpha_j r)\cos(\theta), \tag{22}$$

**TABLE 4.3** Convergence of the Bethe logarithm $\beta(1s) = \ln(k_0/Ry)$ for hydrogen

| $\Omega$ | $N$ | $\beta(1s)$ | Differences | Ratios |
|---|---|---|---|---|
| 2 | 3 | 2.73448191727230174149 | | |
| 3 | 6 | 2.94877219077044909822 | 0.21429027349814735672 | |
| 4 | 10 | 2.97975301862169611861 | 0.03098082785124702039 | 6.917 |
| 5 | 15 | 2.98361449929795351803 | 0.00386148067625739942 | 8.023 |
| 6 | 21 | 2.98407183714911362800 | 0.00045733785116010997 | 8.443 |
| 7 | 28 | 2.98412247036420809592 | 0.00005063321509446792 | 9.032 |
| 8 | 36 | 2.98412792735460886871 | 0.00000545699040077279 | 9.279 |
| 9 | 45 | 2.98412849201006208099 | 0.00000056465545321228 | 9.664 |
| 10 | 55 | 2.98412854946585020174 | 0.00000005745578812075 | 9.828 |
| 11 | 66 | 2.98412855514977775545 | 0.00000000568392755370 | 10.108 |
| 12 | 78 | 2.98412855570645173753 | 0.00000000055667398208 | 10.211 |
| 13 | 91 | 2.98412855575986426711 | 0.00000000005341252957 | 10.422 |
| 14 | 105 | 2.98412855576496736061 | 0.00000000000510309350 | 10.467 |
| 15 | 120 | 2.98412855576544766988 | 0.00000000000048030928 | 10.625 |
| 16 | 136 | 2.98412855576549294823 | 0.00000000000004527834 | 10.608 |
| 17 | 153 | 2.98412855576549717245 | 0.00000000000000422422 | 10.719 |
| 18 | 171 | 2.98412855576549756974 | 0.00000000000000039729 | 10.633 |
| 19 | 190 | 2.98412855576549760688 | 0.00000000000000003714 | 10.697 |
| 20 | 210 | 2.98412855576549761038 | 0.00000000000000000351 | 10.594 |
| Extrap. | | 2.98412855576549761075 | | |

with $j = 0, 1, \ldots, \Omega - 1$, $i = 0, 1, \ldots, \Omega - j - 1$, and

$$\alpha_j = \alpha_0 \times g^j, \quad g \simeq 10, \quad \alpha_0 \simeq 1. \tag{23}$$

Thus, each increase in $\Omega$ introduces another set of terms containing different powers of $r$, but with a distance scale $1/\alpha_j$ that is approximately a factor of 10 smaller than the previous one (a number close to 10 happens to be the variational optimum). For example, for $p$-states $\chi_{0,20} \simeq \exp(-10^{20}r)\cos\theta$. As shown in Figure 4.3, this has the effect of pushing the eigenvalue spectrum up to enormously high energies far above the few tens of atomic units that one would normally expect for a variational basis set. The number of elements is $N = \Omega(\Omega + 1)/2$. One then follows the usual procedure of orthogonalizing the basis set, and then diagonalizing the Hamiltonian to generate a set of $N$ pseudostates that can be summed over to calculate the Bethe logarithm.

As an example, for the ground 1s state of hydrogen, one would generate a set of pseudostates with $p$-symmetry, and then calculate the dipole transition integrals in Eq. (18). An additional trick to speed convergence is to include in the basis set terms that behave as $r^{l-1}$ at the origin for pseudostates of angular momentum $l$. Such terms of course do not contribute to the exact wave functions of angular momentum $l$, but they do contribute to the effective Green's function that the sum over intermediate states represents (see Ref. [11] for further details). The results in Table 4.3 demonstrate that the Bethe logarithm calculated in this way

converges to the known result for the 1s ground state of hydrogen to 20 figure accuracy. Figure 4.3 shows the differential contributions to the Bethe logarithm from each pseudostate. It is clear that extremely high energies are needed to capture the majority of the Bethe logarithm. The basis set has good numerical stability, and standard quadruple precision (32 decimal digit) arithmetic is sufficient for the example shown.

## 5.1 Bethe logarithms for helium and lithium

The basis sets for helium and lithium are more complicated in detail but the principles are the same. In each case the Bethe logarithm comes almost entirely from virtual excitations of the inner 1s electron to p-states lying high in the photoionization continuum, and so the basis set must be extended to very short distances for this particle. The outer electrons are to a good approximation just spectators to these virtual excitations.

Results for the low-lying states of helium and the He-like ions are listed in Table 4.4 (see also Korobov [39]). In order to make the connection with the hydrogenic Bethe logarithm more obvious, the quantity tabulated is $\ln(k_0/Z^2\mathrm{Ry})$. The effect of dividing by a factor of $Z^2$ is to reduce all the Bethe logarithms to approximately the same number $\beta(1s) = 2.984\,128\,556$ for the ground state of hydrogen. It is convenient to express the results in the form $\beta(1snL) = \beta(1s) + \Delta\beta(nL)/n^3$, where $\Delta\beta(nL)$ is a small number that tends to a constant at the series limit.

**TABLE 4.4** Bethe logarithms $\ln(k_0/Z^2\mathrm{Ry})$ for He-like atoms, from Ref. [11] (see also Ref. [39])

| State | $Z = 2$ | $Z = 3$ | $Z = 4$ | $Z = 5$ | $Z = 6$ |
|---|---|---|---|---|---|
| $1\,^1S$ | 2.983 865 9(1) | 2.982 624 558(1) | 2.982 503 05(4) | 2.982 591 383(7) | 2.982 716 949(1) |
| $2\,^1S$ | 2.980 118 275(4) | 2.976 363 09(2) | 2.973 976 98(4) | 2.972 388 16(3) | 2.971 266 29(2) |
| $2\,^3S$ | 2.977 742 36(1) | 2.973 851 679(2) | 2.971 735 560(4) | 2.970 424 952(5) | 2.969 537 065(5) |
| $2\,^1P$ | 2.983 803 49(3) | 2.983 186 10(2) | 2.982 698 29(1) | 2.982 340 18(7) | 2.982 072 79(6) |
| $2\,^3P$ | 2.983 690 84(2) | 2.982 958 68(7) | 2.982 443 5(1) | 2.982 089 5(1) | 2.981 835 91(5) |
| $3\,^1S$ | 2.982 870 512(3) | 2.981 436 5(3) | 2.980 455 81(7) | 2.979 778 086(4) | 2.979 289 8(9) |
| $3\,^3S$ | 2.982 372 554(8) | 2.980 849 595(7) | 2.979 904 876(3) | 2.979 282 037 | 2.978 844 34(6) |
| $3\,^1P$ | 2.984 001 37(2) | 2.983 768 943(8) | 2.983 584 906(6) | 2.983 449 763(6) | 2.983 348 89(1) |
| $3\,^3P$ | 2.983 939 8(3) | 2.983 666 36(4) | 2.983 479 30(2) | 2.983 350 844(8) | 2.983 258 40(4) |
| $4\,^1S$ | 2.983 596 31(1) | 2.982 944 6(3) | 2.982 486 3(1) | 2.982 166 154(3) | 2.981 932 94(5) |
| $4\,^3S$ | 2.983 429 12(5) | 2.982 740 35(4) | 2.982 291 37(7) | 2.981 988 21(2) | 2.981 772 015(7) |
| $4\,^1P$ | 2.984 068 766(9) | 2.983 961 0(2) | 2.983 875 8(1) | 2.983 813 2(1) | 2.983 766 6(2) |
| $4\,^3P$ | 2.984 039 84(5) | 2.983 913 45(9) | 2.983 828 9(1) | 2.983 770 1(2) | 2.983 727 5(2) |
| $5\,^1S$ | 2.983 857 4(1) | 2.983 513 01(2) | 2.983 267 901(6) | 2.983 094 85(5) | 2.982 968 66(2) |
| $5\,^3S$ | 2.983 784 02(8) | 2.983 422 50(2) | 2.983 180 677(6) | 2.983 015 17(3) | 2.982 896 13(2) |
| $5\,^1P$ | 2.984 096 174(9) | 2.984 038 03(5) | 2.983 992 23(1) | 2.983 958 67(5) | 2.983 933 65(5) |
| $5\,^3P$ | 2.984 080 3(2) | 2.984 014 4(4) | 2.983 968 9(4) | 2.983 937 2(4) | 2.983 914 07(6) |

**TABLE 4.5** Residual two-electron Bethe logs $\Delta_{\rm ho}\beta$(1snl)

| State | $n^3\Delta\beta_{\rm ho}$(1snl) | Least squares fit | Difference |
|---|---|---|---|
| $3\,^1$D | −0.000 001 08(4) | | |
| $3\,^3$D | 0.000 181 74(5) | | |
| $4\,^1$D | −0.000 018 4(3) | | |
| $4\,^3$D | 0.000 231 18(7) | | |
| $5\,^1$D | −0.000 026 84(9) | | |
| $5\,^3$D | 0.000 249 73(12)[a] | | |
| $4\,^1$F | 0.000 006 58(2) | 0.000 006 60 | −0.000 000 02(2) |
| $4\,^3$F | 0.000 007 63(2) | 0.000 007 64 | −0.000 000 01(2) |
| $5\,^1$F | 0.000 008 70(3) | 0.000 008 69 | 0.000 000 01(3) |
| $5\,^3$F | 0.000 010 42(3) | 0.000 010 41 | 0.000 000 01(3) |
| $6\,^1$F | 0.000 009 8(1) | 0.000 009 83 | 0.000 000 0(1) |
| $6\,^3$F | 0.000 011 9(3) | 0.000 011 98 | −0.000 000 1(3) |
| $5\,^1$G | 0.000 000 770(3) | 0.000 000 770 | 0.000 000 000(3) |
| $5\,^3$G | 0.000 000 771(3) | 0.000 000 771 | 0.000 000 000(3) |
| $6\,^1$G | 0.000 001 043(3) | 0.000 001 042 | 0.000 000 001(3) |
| $6\,^3$G | 0.000 001 050(8) | 0.000 001 047 | 0.000 000 003(8) |
| $6\,^1$H | 0.000 000 127(2) | 0.000 000 127 | 0.000 000 000(2) |
| $6\,^3$H | 0.000 000 127(2) | 0.000 000 127 | 0.000 000 000(2) |

*a* Corresponds to an energy uncertainty of ±14 Hz.

For high-L, the dependence of the quantity $\Delta\beta$(nL) on n and L can be understood in terms of the core polarization model originally developed by Drachman [40,41] and extended by Drake [6,7] for the energies of Rydberg states. Just as for the energy, the Rydberg electron induces corrections to the Bethe logarithm for the 1s electron corresponding to the various multipole moments of the core, with the leading term being the dipole term $0.316\,205(6)\langle x^{-4}\rangle/Z^6$ [42,43]. The complete expression is

$$\beta(1\text{snl}) = \beta(1\text{s}) + \left(\frac{Z-1}{Z}\right)^4 \frac{\beta(\text{nl})}{n^3} + \frac{0.316\,205(6)}{Z^6}\langle x^{-4}\rangle + \Delta_{\rm ho}\beta(1\text{snl}), \qquad (24)$$

where the $\beta$(nl) are hydrogenic Bethe logarithms [44,45], and $\Delta_{\rm ho}\beta$(1snl) takes into account contributions from the higher-order multipole moments. A least squares fit to direct calculations up to $L = 6$ and $n = 6$ for helium yields the results [46]

$$\Delta_{\rm ho}\beta\left(1\text{snl}\,^1\text{L}\right) = 95.8(8)\langle r^{-6}\rangle - 845(19)\langle r^{-7}\rangle + 1406(50)\langle r^{-8}\rangle, \qquad (25)$$

$$\Delta_{\rm ho}\beta\left(1\text{snl}\,^3\text{L}\right) = 95.1(9)\langle r^{-6}\rangle - 841(23)\langle r^{-7}\rangle + 1584(60)\langle r^{-8}\rangle. \qquad (26)$$

For example, for the 1s4f $^1$F state, $\beta(4\,^1\text{F}) = 2.984\,127\,1493(3)$. As can be seen from the comparison in Table 4.5, for higher $L$ the asymptotic expansions reproduce the direct calculations to within the accuracy of the calculations.

**TABLE 4.6** Comparison of Bethe logarithms for lithium and its ions

| Atom | $Li(1s^22s)$ | $Li(1s^23s)$ | $Li^+(1s^2)$ | $Li^{++}(1s)$ |
|---|---|---|---|---|
| $\ln(k_0/Z^2\mathrm{Ry})$ | 2.981 06(1) | 2.982 36(6) | 2.982 624 | 2.984 128 |

Table 4.6 compares the Bethe logarithms for the two lowest S-states of lithium with those for the Li-like ions $Li^+(1s^2\ ^1S)$ and $Li^{++}(1s\ ^2S)$. The comparison emphasizes again that the Bethe logarithm is determined almost entirely by the hydrogenic value for the 1s electron, and is almost independent of the state of excitation of the outer electrons, or the degree of ionization.

## 6. APPLICATIONS TO NUCLEAR SIZE MEASUREMENTS

As stated in Section 1, one of the goals of this work is to use the comparison between theory and experiment for the isotope shift to determine the nuclear charge radius for various isotopes of helium and other atoms. One of the most interesting and important examples is the charge radius of the 'halo' nucleus $^6$He. For a light atom such as helium, the energy shift due to the finite nuclear size is given to an excellent approximation by

$$\Delta E_{\mathrm{nuc}} = \frac{2\pi Ze^2}{3}\bar{r}_{\mathrm{c}}^2\left\langle\sum_{i=1}^{2}\delta(\mathbf{r}_i)\right\rangle, \tag{27}$$

where $\bar{r}_{\mathrm{c}}$ is the rms nuclear charge radius. If all other contributions to the isotope shift can be calculated to sufficient accuracy (about 100 kHz) and subtracted, then the residual shift due to the change in $\bar{r}_{\mathrm{c}}$ between the two isotopes can be determined from the measured isotope shift. Specific results for helium and lithium isotopes (especially the halo isotopes) are discussed in the following two subsections.

### 6.1 Results for helium

The theory of isotope shifts, including relativistic recoil and radiative recoil contributions, is discussed in detail in Ref. [47], and will not be repeated here. Instead, we show as an example in Table 4.7 the various calculated contributions to the isotope shift for the 1s2s $^3S_1$–1s3p $^3P_2$ transition of $^6$He relative to $^4$He. The corresponding experimental value was obtained in a remarkable experiment performed at the Argonne National Laboratory by Z.-T. Lu and collaborators [48], using the techniques of single-atom spectroscopy to trap the short-lived $^6$He nuclei ($t_{1/2} = 0.8$ s) in the metastable 1s2s $^3S_1$ electronic state. Each term in the table represents the energy difference between $^6$He and $^4$He with nuclear masses of 6.018 8880(11) u and 4.002 603 250(1) u respectively (see Table 4.8). The first entry denoted $\mu/M$ represents the sum of the 'normal' isotope shift due to the common mass scaling of all the nonrelativistic energies in proportion to $\mu/m_{\mathrm{e}} = 1 - \mu/M$,

**TABLE 4.7** Contributions to the $^6$He–$^4$He isotope shift (MHz)

| Contribution | $2\,^3S_1$ | $3\,^3P_2$ | $2\,^3S_1$–$3\,^3P_2$ |
|---|---|---|---|
| $\mu/M$ | 55 195.526(19) | 12 000.673(4) | 43 194.853(16) |
| $(\mu/M)^2$ | −3.964 | −4.847 | 0.883 |
| $\alpha^2\mu/M$ | 1.435 | 0.724 | 0.711 |
| $r_c^2$[a] | −1.264 | 0.110 | −1.374 |
| $\alpha^3\mu/M$, electron–nucleus | −0.285 | −0.037 | −0.248 |
| $\alpha^3\mu/M$, electron–electron | 0.005 | 0.001 | 0.004 |
| Total | 55 191.453(19) | 11 996.625(4) | 43 194.828(16) |
| Experiment[b] | | | 43 194.772(56) |
| Difference | | | 0.046(56) |

*a* Nuclear size correction for an assumed nuclear charge radius of $\bar{r}_c r(^6\text{He}) = 2.04$ fm.

*b* Wang *et al.* [48].

**TABLE 4.8** Table of nuclear masses used in the calculations. Units are atomic mass units

| Isotope | Mass |
|---|---|
| $^3$He | 3.016029310(1) |
| $^4$He | 4.002603250(1) |
| $^6$He | 6.0188881(11) |
| $^6$Li | 6.015122794(16) |
| $^7$Li | 7.0160034256(45) |
| $^8$Li | 8.02248736(10) |
| $^9$Li | 9.0267895(21) |
| $^{11}$Li | 11.0437157(68) |

and the 'specific' isotope shift due to mass polarization, calculated as a first-order perturbation. The remaining entries represent important corrections to these dominant terms. The second entry of order $(\mu/M)^2$ comes from second-order mass polarization, and the next term of order $\alpha^2\mu/M$ Ry is the relativistic recoil term. It contains contributions from the mass scaling of the terms in the Breit interaction, as well as cross-terms with the mass polarization operator, and the mass dependent Stone terms $(m_e/M)(\tilde{\Delta}_2 + \tilde{\Delta}_{so})$ in Eq. (8). The term denoted $r_c^2$ is the finite nuclear size correction for an assumed nuclear charge radius $\bar{r}_c = 2.04$ fm for $^6$He, relative to the reference value $\bar{r}_c = 1.673(1)$ fm for $^4$He [49].[1] Finally, the two terms of order $\alpha^3\mu/M$ Ry denote the mass-dependent parts of the electron–nucleus and electron–electron QED shift, including recoil [52] and mass polarization correc-

[1] This value is based on measurements of the Lamb shift in muonic helium, but attempts to reproduce the measurement have not proved successful, as discussed by Bracci and Zavattini [50]. The consistent, but less accurate value 1.676(8) fm has been obtained from electron scattering [51]. If the electron scattering value is used for $^4$He, then the size of the error bars for the other helium isotopes increases in proportion, but the results do not otherwise change significantly.

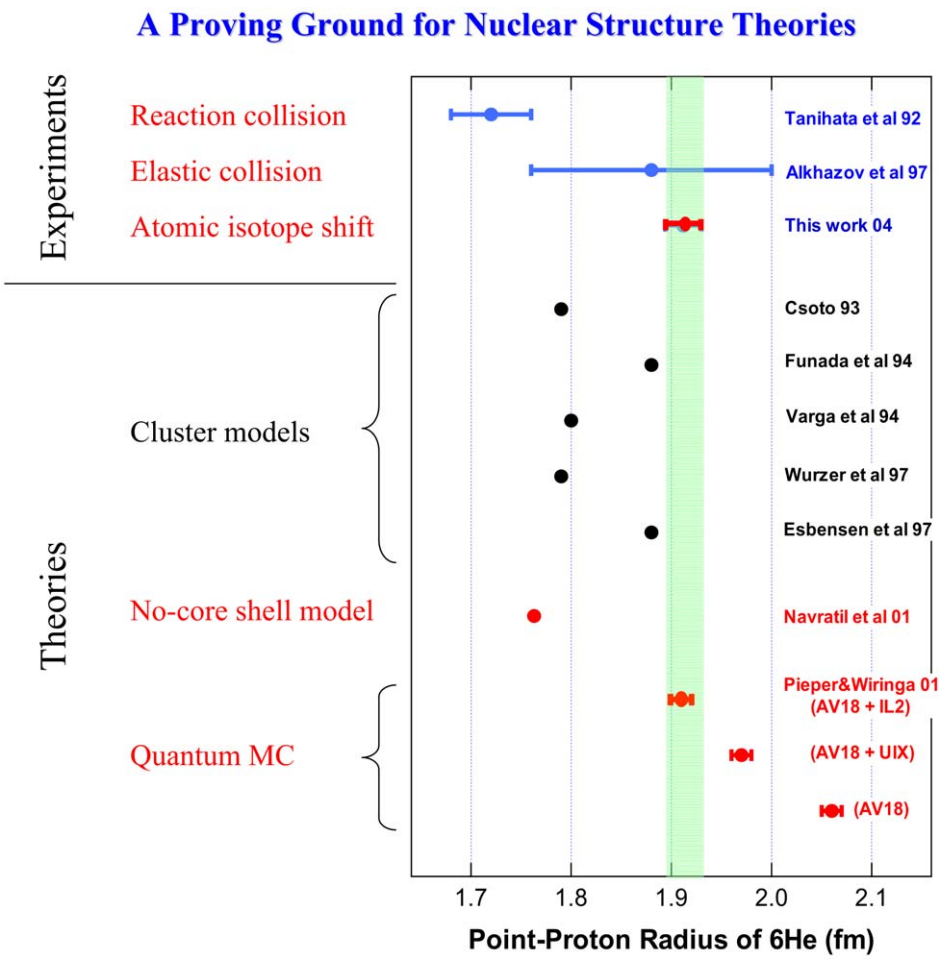


**FIGURE 4.4** Comparison of the point-proton nuclear charge radius $\bar{r}_p$ for $^6$He with other measurements and theoretical values.

tions. The key point is that the uncertainty in the much larger mass-independent part of the QED shift (tens of MHz) cancels when the isotope shift is calculated. The residual uncertainty of only 16 kHz shown in Table 4.7 is then determined primarily by the uncertainty in the nuclear mass of $^6$He, rather than the atomic physics calculations.

Since the goal of the experiment is to determine the nuclear charge radius for $^6$He, the final step is to adjust $\bar{r}_c$ so as to eliminate the small discrepancy of 0.046(56) MHz shown in Table 4.7. The various contributions to the isotope shift in Table 4.7 can be collected together and expressed in the form

$$\mathrm{IS}(2\,^3\mathrm{S}\text{–}3\,^3\mathrm{P}) = 43\,196.202(16) + 1.008\big[\bar{r}_c^2(^4\mathrm{He}) - \bar{r}_c^2(^6\mathrm{He})\big]. \qquad (28)$$

The adjusted nuclear charge radius is then $\bar{r}_c(^6\mathrm{He}) = 2.054(14)$ fm.

**TABLE 4.9** Contributions to the $^6$Li–$^7$Li isotope shift for the $1s^2\ 3s\ ^2S$–$1s^2\ 2s\ ^2S$ transition. Units are MHz

| Contribution | $3\ ^2S$–$2\ ^2S$ |
|---|---|
| $\mu/M$ | 11 454.656 |
| $(\mu/M)^2$ | −1.794 |
| $\alpha^2\mu/M$ | 0.010(5) |
| $\alpha^3\mu/M$, electron–nucleus | −0.066(2) |
| $\alpha^3\mu/M$, electron–electron | 0.011(2) |
| $r_c^2$ | $1.24 \pm 0.39$ |
| $r_c^2\mu/M$ | −0.000 677(98) |
| Total | $11\,454.056(5) \pm 0.39$ |
| Sanchez *et al.* [65] (Expt.) | 11 453.983(20) |
| Difference | 0.073(20) |

The significance of this result in comparison with other measurements and calculations is illustrated in Figure 4.4.[2] The first important point is that no other method of measurement is both independent of nuclear structure models, and capable of yielding sufficient accuracy to provide a meaningful test of theory. Ref. [55] was obtained from nuclear reaction cross sections, and Ref. [56] was extracted from elastic scattering from protons (in water). Second, the accuracy is sufficient to rule out all but two of the cluster calculations. Refs. [57–59] describe $^6$He in terms of a single $(\alpha + n + n)$ channel, but inclusion of the additional $(t + t)$ channel in Refs. [60,61] produces a substantial disagreement. Also, the *ab initio* calculation based on the no-core shell model [62] is in poor agreement. The best agreement is with the *ab initio* quantum Monte Carlo calculations of Pieper and Wiringa [63,64] based on the AV18 two-body potential and the IL2 three-body potential, while other versions of the model potentials do not agree. The comparison with our value of $\bar{r}_c$ obtained by the isotope shift method is therefore capable of distinguishing amongst the various possible candidates for the effective low-energy nucleon–nucleon interaction potential.

## 6.2 Results for lithium

Isotope shifts for the various isotopes of lithium $^6$Li to $^{11}$Li have been measured by the group of Kluge *et al.* at GSI (including a collaboration with TRIUMF for $^{11}$Li) and the results reported in Refs. [66,65]. The result for $^{11}$Li is of special interest because, like $^6$He, it is a halo nucleus with a $^9$Li core, and so the nuclear radius is very sensitive to the details of nuclear structure. All the experiments involve measurements of the isotope shift for the $2\ ^2S_{1/2}$–$3\ ^2S_{1/2}$ two-photon transition. As an interesting test of the method, Table 4.9 compares theory and

[2] For comparison with theory, it is customary to express the calculated values in terms of an effective rms radius $\bar{r}_p$ corresponding to a point-like proton and neutron, which is related to the rms charge radius $\bar{r}_c$ by $\bar{r}_c^2 = \bar{r}_p^2 + \bar{R}_p^2 + (N/Z)\bar{R}_n^2$, where $\bar{R}_p = 0.895(18)$ fm [53] is the rms charge radius of the proton, $\bar{R}_n^2 = -0.116(5)$ fm$^2$ [54] is the mean-square charge radius of the neutron, and $N$ and $Z$ are the neutron and proton numbers.

**TABLE 4.10** Contributions to the $^{11}$Li–$^{7}$Li isotope shift for the $1s^2\ 3s\ ^2S$–$1s^2\ 2s\ ^2S$ transition. Units are MHz

| Contribution | $3\ ^2S$–$2\ ^2S$ |
|---|---|
| $\mu/M$ | 25 104.490(21)[a] |
| $(\mu/M)^2$ | −2.967 9(1) |
| $\alpha^2\mu/M$ | 0.023(10) |
| $\alpha^3\mu/M$, electron–nucleus | −0.145(4) |
| $\alpha^3\mu/M$, electron–electron | 0.026(5) |
| Nuclear polarization [10] | 0.039(4) |
| Total | 25 101.462(24)[a] |
| Sanchez *et al.* [65] (expt.) | 25 101.226(125) |
| Difference | 0.236(125) |

*a* Uncertainty from the atomic mass determination for $^{11}$Li. See Table 4.8.

experiment for the isotope shift of $^6$Li relative to $^7$Li. The assumed nuclear radii are $r_c(^6\text{Li}) = 2.55 \pm 0.04$ fm and $r_c(^7\text{Li}) = 2.39 \pm 0.03$ fm. The theoretical uncertainty of $\pm 0.39$ MHz is completely dominated by the uncertainty in the nuclear radii. The difference between theory and experiment is only $0.073 \pm 0.020$ MHz, and this can be removed by a slight adjustment to the assumed nuclear radii. Using the theoretical results in Table 4.9, the isotope shift can be written in the form

$$\text{IS}(2\ ^2S - 3\ ^2S) = 11{,}452.816(5) + 1.566\left[\bar{r}_c^2(^6\text{Li}) - \bar{r}_c^2(^7\text{Li})\right] \qquad (29)$$

(cf. Eq. (28)), and so, for example, an adjustment to $r_c(^6\text{Li}) = 2.54 \pm 0.04$ fm instead of $2.55 \pm 0.04$ fm would be sufficient to resolve the discrepancy. Thus the experimental accuracy of $\pm 20$ kHz is sufficient to determine the nuclear charge radius to $\pm 0.01$ fm.

The corresponding results for $^{11}$Li are shown in Table 4.10, and compared with the experiment of Sanchez *et al.* [65]. The difference of $0.236 \pm 0.125$ MHz is due entirely to the nuclear volume effect, and so the difference in squared nuclear radii is $0.236(125)/1.566 = 0.151(80)$ fm$^2$. Thus, relative to $r_c(^7\text{Li}) = 2.39 \pm 0.03$, the nuclear charge radius for $^{11}$Li is $2.421 \pm 0.040$ fm.

The significance of this result has recently been discussed by Drake *et al.* [67]. The overall pattern is as follows. The nuclear charge radii progressively decrease from $^6$Li to $^9$Li, where they reach a minimum of $r_c(^9\text{Li}) = 2.185 \pm 0.033$ fm, and then dramatically increase to $2.42 \pm 0.04$ for $^{11}$Li. Of the various models of nuclear structure, only the stochastic variational multi-cluster (SVMC) model [68,69] gives a meaningful result for $^{11}$Li. By chance, their calculated value of 2.43 fm for the assumed point-proton case is in excellent agreement, but when this value is corrected for the finite proton and neutron sizes (see footnote 2), it increases to 2.529 fm. The corresponding value for an assumed frozen $^9$Li core (i.e. neglecting core excitations) is 2.261 fm. The measured value therefore lies between these two extremes, but agrees with neither. Several other calculations of nuclear structure are also available, such as the Greens-Function Monte Carlo method [70,64], fermi-

onic molecular dynamics [71], the dynamic correlation model [72,73], and the *ab initio* no-core shell model [74,75]. It is particularly significant that most of these agree well with the measured values for the stable nuclei $^3$He, $^4$He, $^6$Li, and $^7$Li, and also for $^8$Li and $^9$Li [66], but not for the halo nuclei $^6$He and $^{11}$Li. The measurements of halo nuclear radii therefore play an important role in distinguishing one theory from another.

## 7. SUMMARY AND CONCLUSIONS

The principle message of this paper is that few-body atomic systems such as helium and lithium can be solved essentially exactly for all practical purposes in the nonrelativistic limit, and there is a systematic procedure for calculating the relativistic and other higher-order QED corrections as perturbations. The solution of the problem of calculating Bethe logarithms means that the theoretical energy levels are complete up to and including terms of order $\alpha^3$ Ry.

As a consequence of these advances, helium and lithium now join the ranks of hydrogen and other two-body systems as examples of fundamental atomic systems. The high precision theory that is now available creates new opportunities to develop measurement tools that would otherwise not exist. One such example discussed here is the determination of the nuclear charge radius for the halo nuclei $^6$He and $^{11}$Li. This opens up a new area of study at the interface between atomic physics and nuclear physics, and it provides important input data for the determination of effective nuclear forces. Other similar experiments have been performed on the lithium isotopes [66], including the halo nucleus $^{11}$Li [65], and further work is in progress on $^8$He at Argonne and $^{11}$Be at GSI/TRIUMF.

## ACKNOWLEDGEMENTS

I would like to thank Wilfried Nörtershäuser at GSI and Z.-T. Lu at the Argonne National Laboratory for their hospitality and inspiration on the experimental side. This work was supported by the Natural Sciences and Engineering Research Council of Canada.

## REFERENCES

[1] I. Tanihata, *et al.*, *Phys. Rev. Lett.* **55** (1985) 2676.
[2] I. Tanihata, *Nucl. Phys. A* **522** (1991) C275.
[3] F. Le Blanc, *et al.*, Isolde Collaboration, *Eur. Phys. J.* **15** (2002) 49.
[4] A.M. Martensson-Pendrill, *Mol. Phys.* **98** (2000) 1201, and earlier references therein.
[5] G.W.F. Drake, Z.-C. Yan, *Phys. Rev. A* **46** (1992) 2378.
[6] G.W.F. Drake, in: F.S. Levin, D.A. Micha (Eds.), *Long-Range Casimir Forces: Theory and Recent Experiments on Atomic Systems*, Plenum, New York, 1993, pp. 107–217.
[7] G.W.F. Drake, *Adv. At. Mol. Opt. Phys.* **31** (1993) 1.
[8] K. Pachucki, J. Sapirstein, *J. Phys. B At. Mol. Opt. Phys.* **36** (2003) 803.
[9] M. Puchalski, K. Pachucki, *Phys. Rev. A* **73** (2006) 022503.

[10] M. Puchalski, A.M. Moro, K. Pachucki, *Phys. Rev. Lett.* **97** (2006) 133001.
[11] G.W.F. Drake, S.P. Goldman, *Can. J. Phys.* **77** (1999) 835.
[12] G.W.F. Drake, W.C. Martin, *Can. J. Phys.* **76** (1998) 597.
[13] D.C. Morton, Q.X. Wu, G.W.F. Drake, *Can. J. Phys.* **84** (2006) 83, and earlier references therein.
[14] B. Klahn, W.A. Bingel, *Theor. Chem. Acta* **44** (1977) 27;
B. Klahn, W.A. Bingel, *Int. J. Quantum Chem.* **11** (1978) 943.
[15] G.W.F. Drake, M.M. Cassar, R.A. Nistor, *Phys. Rev. A* **65** (2002) 054501.
[16] A.K. Bhatia, A. Temkin, *Phys. Rev.* **137** (1965) 1335.
[17] A.K. Bhatia, R.J. Drachman, *Phys. Rev. A* **35** (1987) 4051.
[18] A.K. Bhatia, R.J. Drachman, *J. Phys. B: At. Mol. Opt. Phys.* **36** (2003) 1957.
[19] V.I. Korobov, *Phys. Rev. A* **66** (2002) 024501.
[20] C. Schwartz, *Int. J. Mod. Phys. E Nucl. Phys.* **15** (2006) 877.
[21] S.P. Goldman, *Phys. Rev. A* **57** (1998) R677.
[22] A. Bürgers, D. Wintgen, J.-M. Rost, *J. Phys. B: At. Mol. Opt. Phys.* **28** (1995) 3163.
[23] J.D. Baker, D.E. Freund, R.N. Hill, J.D. Morgan III, *Phys. Rev. A* **41** (1990) 1247.
[24] Z.-C. Yan, G.W.F. Drake, *Phys. Rev. Lett.* **81** (1998) 774.
[25] Z.-C. Yan, G.W.F. Drake, *Phys. Rev. A* **66** (2002) 042504.
[26] Z.-C. Yan, G.W.F. Drake, *Phys. Rev. Lett.* **91** (2003) 113004.
[27] A.K. Bhatia, R.J. Drachman, *Phys. Rev. A* **45** (1992) 7752.
[28] R.J. Drachman, A.K. Bhatia, *Phys. Rev. A* **51** (1995) 2926.
[29] A.K. Bhatia, R.J. Drachman, *Phys. Rev. A* **55** (1997) 1842.
[30] H.A. Bethe, E.E. Salpeter, *Quantum Mechanics of One- and Two-Electron Atoms*, Springer-Verlag, New York, 1957.
[31] A.P. Stone, *Proc. Phys. Soc. (London)* **77** (1961) 786;
A.P. Stone, *Proc. Phys. Soc. (London)* **81** (1963) 868.
[32] P.K. Kabir, E.E. Salpeter, *Phys. Rev.* **108** (1957) 1256.
[33] H. Araki, *Prog. Theor. Phys.* **17** (1957) 619.
[34] J. Sucher, *Phys. Rev.* **109** (1958) 1010.
[35] C. Schwartz, *Phys. Rev.* **123** (1961) 1700.
[36] J.D. Baker, R.C. Forrey, J.D. Morgan III, R.N. Hill, M. Jeziorska, J. Schertzer, *Bull. Am. Phys. Soc.* **38** (1993) 1127;
J.D. Baker, R.C. Forrey, M. Jeziorska, J.D. Morgan III, private communication.
[37] V.I. Korobov, S.V. Korobov, *Phys. Rev. A* **59** (1999) 3394.
[38] K. Pachucki, J. Sapirstein, *J. Phys. B: At. Mol. Opt. Phys.* **33** (2000) 455.
[39] V.I. Korobov, *Phys. Rev. A* **69** (2004) 054501.
[40] R.J. Drachman, *Phys. Rev. A* **47** (1993) 694.
[41] R.J. Drachman, in: F.S. Levin, D. Micha (Eds.), *Long-Range Casimir Forces: Theory and Recent Experiments on Atomic Systems*, Plenum Press, New York, 1993, pp. 219–272, and earlier references therein.
[42] S.P. Goldman, G.W.F. Drake, *Phys. Rev. Lett.* **68** (1992) 1683.
[43] S.P. Goldman, *Phys. Rev. A* **50** (1994) 3039.
[44] G.W.F. Drake, R.A. Swainson, *Phys. Rev. A* **41** (1990) 1243.
[45] U.D. Jentschura, P.J. Mohr, *Phys. Rev. A* **72** (2005) 012110.
[46] G.W.F. Drake, *Phys. Scr.* **T95** (2001) 22.
[47] G.W.F. Drake, W. Nörtershäuser, Z.-C. Yan, *Can. J. Phys.* **83** (2005) 311.
[48] L.-B. Wang, P. Mueller, K. Bailey, *et al.*, *Phys. Rev. Lett.* **93** (2004) 142501.
[49] E. Borie, G.A. Rinker, *Phys. Rev. A* **18** (1978) 324.
[50] L. Bracci, E. Zavattini, *Phys. Rev. A* **41** (1990) 2352.
[51] I. Sick, *Phys. Lett. B* **116** (1982) 212.
[52] K. Pachucki, J. Sapirstein, *J. Phys. B* **33** (2000) 455.
[53] I. Sick, *Phys. Lett. B* **576** (2003) 62.
[54] S. Kopecky, P. Riehs, J.A. Harvey, N.W. Hill, *Phys. Rev. Lett.* **74** (1995) 2427;
S. Kopecky, J.A. Harvey, N.W. Hill, M. Krenn, M. Pernicka, P. Riehs, S. Steiner, *Phys. Rev. C* **56** (1997) 2229.
[55] I. Tanihata, *et al.*, *Phys. Lett. B* **289** (1992) 261.

[56] G.D. Alkhazov, *et al.*, *Phys. Rev. Lett.* **78** (1997) 2313.
[57] S. Funada, H. Kameyama, Y. Sakruagi, *Nucl. Phys. A* **575** (1994) 93.
[58] K. Varga, Y. Suzuki, Y. Ohbayasi, *Phys. Rev. C* **50** (1994) 189.
[59] H. Esbensen, G.F. Bertsch, K. Hencken, *Phys. Rev. C* **56** (1997) 3054.
[60] A. Csoto, *Phys. Rev. C* **48** (1993) 165.
[61] J. Wurzer, H.M. Hofmann, *Phys. Rev. C* **55** (1997) 688.
[62] P. Navrátil, J.P. Vary, W.E. Ormand, B.R. Barrett, *Phys. Rev. Lett.* **87** (2001) 172502.
[63] S.C. Pieper, V.R. Pandharipande, R.B. Wiringa, J. Carlson, *Phys. Rev. C* **64** (2001) 014001.
[64] S.C. Pieper, R.B. Wiringa, *Ann. Rev. Nucl. Part. Sci.* **51** (2001) 53.
[65] R. Sanchez, W. Nörtershäuser, G. Ewald, D. Albers, J. Behr, P. Bricault, B.A. Bushaw, A. Dax, J. Dilling, M. Dombsky, G.W.F. Drake, S. Gotte, R. Kirchner, H.J. Kluge, T. Kühl, J. Lassen, C.D.P. Levy, M.R. Pearson, E.J. Prime, V. Ryjkov, A. Wojtaszek, Z.-C. Yan, C. Zimmermann, *Phys. Rev. Lett.* **96** (2006) 033002.
[66] G. Ewald, W. Nörtershäuser, A. Dax, S. Göte, R. Kirchner, H.-J. Kluge, Th. Kühl, R. Sanchez, A. Wojtaszek, B.A. Bushaw, G.W.F. Drake, Z.-C. Yan, C. Zimmermann, *Phys. Rev. Lett.* **93** (2004) 113002; Z.-C. Yan, C. Zimmermann, *Phys. Rev. Lett.* **94** (2005) 039901.
[67] G.W.F. Drake, Z.-T. Lu, W. Nörtershäuser, Z.-C. Yan, in: S. Karshenboim (Ed.), *Precision Physics of Simple Atoms and Molecules*, Springer, Berlin, 2007, to be published.
[68] K. Varga, Y. Suzuki, I. Tanihata, *Phys. Rev. C* **52** (1995) 3013.
[69] K. Varga, Y. Suzuki, R.G. Lovas, *Phys. Rev. C* **66** (2002) 041302.
[70] S.C. Pieper, K. Varga, R.B. Wiringa, *Phys. Rev. C* **66** (2002) 044310.
[71] T. Neff, H. Feldmeier, R. Roth, in: *21st Winter Workshop on Nuclear Dynamics*, Breckenridge, Colorado, USA, 2005.
[72] M. Tomaselli, *et al.*, *Nucl. Phys. A* **690** (2001) 298c.
[73] M. Tomaselli, *et al.*, *Hyperf. Int.* (online first), http://dx.doi.org/10.1007/s10751-006-9484-1, 2007.
[74] P. Navrátil, W.E. Ormand, *Phys. Rev. C* **68** (2003) 034305.
[75] P. Navrátil, B.R. Barrett, *Phys. Rev. C* **57** (1998) 3119.

CHAPTER 5

# Quantum Electrodynamics in One- and Two-Electron High-*Z* Ions

**Th. Stöhlker*, A. Gumberidze*, A. Kumar*, R. Reuschl*** and **M. Trassinelli***

Contents



Abstract

One- and two-electron ions traditionally serve as an important testing ground for fundamental atomic structure theories and for investigation of QED, relativistic and correlation effects. In the domain of high nuclear charges, new opportunities open up for precise testing and consolidating of the present understanding of the atomic structure, in the regime of extreme electromagnetic fields. In this article, the current progress in experimental investigations of the heaviest H- and He-like systems at GSI Darmstadt is presented. In addition, the planned future experimental studies and developments devoted in particular to high-resolution spectroscopy of excited states in heavy He-like ions as well as of the 1s state in hydrogen-like systems, are reviewed.

* Gesellschaft für Schwerionenforschung, D-64291 Darmstadt, Germany

Advances in Quantum Chemistry, Vol. 53
ISSN 0065-3276, DOI:10.1016/S0065-3276(07)53005-4

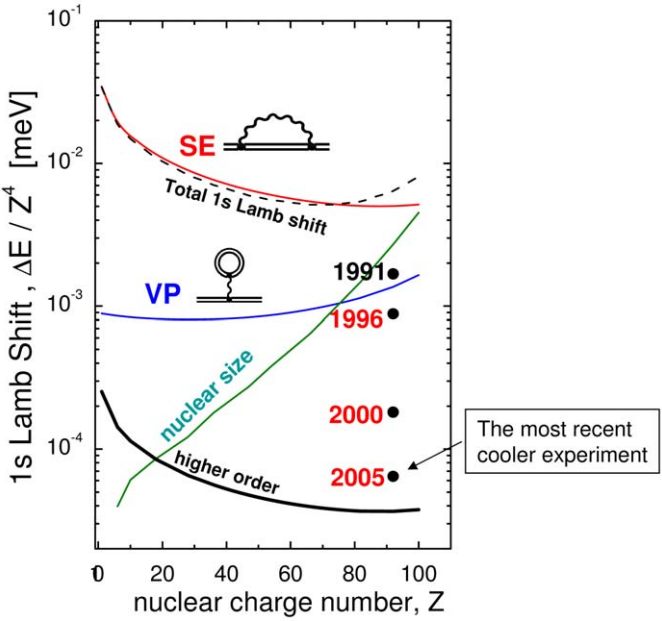


**FIGURE 5.1** Various individual contributions to the ground-state Lamb shift in H-like uranium together with the experimental accuracies achieved so far [13–16]. SE and VP denote the self energy and the vacuum polarisation contributions, respectively.

## 1. THE GROUND-STATE BINDING ENERGY IN H-LIKE URANIUM

One-electron high-$Z$ ions represent the most fundamental atomic systems providing unique opportunities to bring our present understanding of atomic structure under critical tests. In particular, the bound-state Quantum Electrodynamics (QED) which up to now has been extremely successful in describing simple atomic systems in the low-$Z$ domain, can be probed in the nonperturbative regime of extremely strong Coulomb fields (as provided by the heavy nuclei) in the absence of many-electron effects. Besides, in combination with accurate measurements for high-$Z$ Li-like systems, precise results for the 1s binding energy in H-like ions may help to disentangle between nuclear, one- and multielectron contributions to the 2s binding energy in Li-like species where very accurate experimental results have been obtained already [1–3]. Experimental studies at the Experimental Storage Ring (ESR) (at GSI) devoted to precise measurements of the ground-state Lamb shift in high-$Z$ heavy H-like systems have experienced substantial improvements of accuracy over the last decade. In Figure 5.1, this is shown for the example of the 1s Lamb shift in H-like uranium ($U^{91+}$) where an increase of precision by more than order of magnitude has been achieved (the various theoretical contributions displayed in the figure are taken from [4]). Furthermore, very recently all $\alpha^2$-order QED contributions have been evaluated (see Figure 5.1) [5,6], thus providing opportunities for probing higher-order QED effects in the strongest electromagnetic

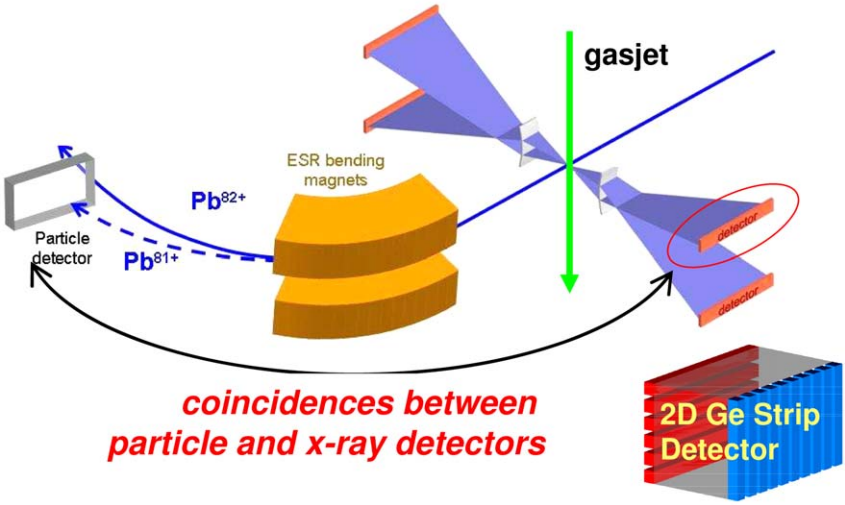


**FIGURE 5.2** The experimental arrangement used in the first beam-time dedicated to measure ground-state Lamb-shift in H-like Pb exploiting high-resolution X-ray spectrometers in combination with position-sensitive Ge(i) detectors.

fields. For the next generation experiments devoted to the ground-state Lamb shift in high-Z H-like systems, novel high-resolution X-ray detection devices namely, crystal spectrometers [7], in combination with position sensitive solid-state detectors [8,9] and bolometers will be exploited [11,12]. Successful commissioning and test experiments with such devices at the gasjet target of the ESR storage ring [7, 8,10–12] has already been followed by a first data-taking beam-time devoted to a measurement of the ground-state Lamb-shift in H-like Pb (see Figure 5.2). The data are currently being evaluated.

## 2. STRONG FIELD QED IN HE-LIKE HEAVY IONS

Helium-like ions, being the simplest among few-electron atomic systems are very important for gaining insights into relativistic many-body, quantum electrodynamical and correlation phenomena and into their impact on the atomic structure. Here, in contrast to hydrogen-like systems, even for light (low-Z) ions there are still considerable disagreements between state-of-the-art theoretical calculations and experimental results [17,18] challenging both experimental as well as theoretical investigations of these fundamental atomic systems. Of particular importance are investigations of high-Z He-like ions, because here the fundamental atomic-structure theories can be tested in the domain of strongest electromagnetic fields as provided by the heavy nuclei. In these strong external fields, the influence of relativistic and QED effects on the bound electrons is significantly enhanced and as a consequence the correlation (many-body) and the specific QED corrections for the electron–electron interaction are of the same order of magnitude providing

a challenge for theoretical description. A further important aspect which makes studies of high-$Z$ He-like ions extremely interesting is the possibility of testing the standard model by means of parity nonconservation (PNC) [19,20].

Theoretical investigations of He-like ions in the high-$Z$ domain have experienced considerable progress during the last decade where a new generation of relativistic many-body calculations (RMBT), the multiconfigurational Dirac–Fock (MCDF) and the configuration interaction (CI) methods have established improved benchmarks for the non-QED part of the electron–electron interaction [21–24]. This was followed by calculations of the ground-state two-electron QED contributions: the so called two-electron Lamb shift, including all corrections of order $\alpha^2$ [25,26]. Moreover, very recently, calculations of various contributions to the two-electron Lamb shift has been completed for L-shell excited states [27].

In the following, we report the first measurement of the two-electron contribution to the ionisation potential for the heaviest stable ion available to experiments, i.e., He-like uranium. The ground state of high-$Z$ He-like ions is of particular relevance for probing bound-state QED in strong fields since to date, the two-electron contribution to the ionisation potential in He-like systems is one of very few measurable values which have been calculated completely to second order in $\alpha$ [25]. In addition, the value for the two-electron contribution is known to be negligibly affected by nuclear size uncertainties, in contrast to the situation in high-$Z$ hydrogen- or lithium-like systems.

## 2.1 The two-electron contribution in $U^{90+}$: experiment at the ESR electron cooler

In order to obtain the two-electron contribution to the ground-state binding-energy in He-like uranium, we have performed a relative measurement of radiative recombination (RR) transitions into the K-shell of initially bare and H-like ions. This experimental technique was first introduced at the Super-EBIT device at the Lawrence Livermore National Laboratory (LLNL) and successfully applied to series of He-like ions up to bismuth [28]. However, at very high-$Z$ there have been difficulties in producing bare species and results were limited by counting statistics. We have extended these earlier studies to the higher $Z$ regime at the electron cooler of the ESR storage ring at GSI by profiting from brilliant-quality beams of heaviest bare and H-like ions.

For the experiment bare and H-like uranium ions were injected into the ESR, in alternate order, at the initial (production) energy of close to 360 MeV/u and subsequently decelerated to the final (measurement) beam energy of 43.6 MeV/u. Meanwhile, the deceleration technique is routinely available at the ESR. There are several advantages resulting from the deceleration: most importantly, the uncertainties stemming from the Doppler effect are considerably reduced. Furthermore, background due to Bremsstrahlung of the cooler electrons is strongly suppressed due to lower cooler current and voltage applied. Besides, the chosen energy allowed us to place the RR-lines in spectrum very close to the calibration $\gamma$-line of $^{169}$Yb, enabling for a precise determination of the line centroid energies. For the detection of the RR photons, the 0 deg X-ray detection apparatus at the ESR

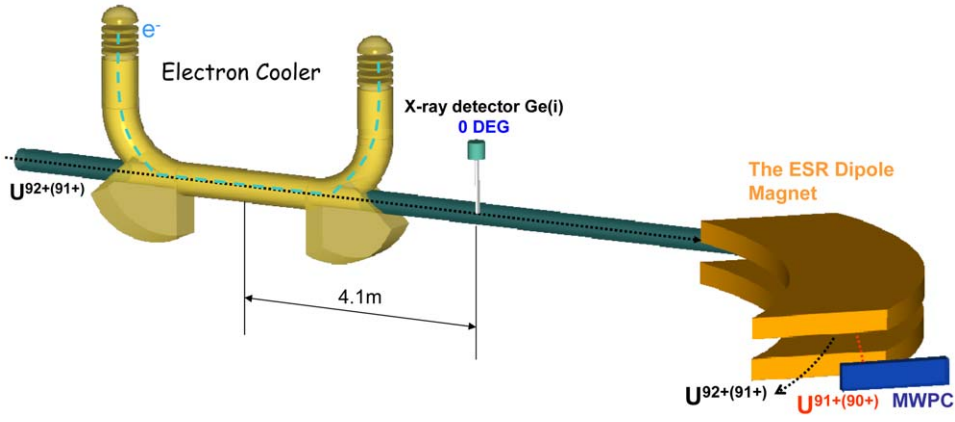


**FIGURE 5.3** Scheme of the experimental setup at the electron-cooler device of the ESR storage ring. X-rays are observed at almost 0 deg with respect to the beam axis and recorded in coincidence with the down-charged ions ($U^{91+}$, $U^{90+}$).

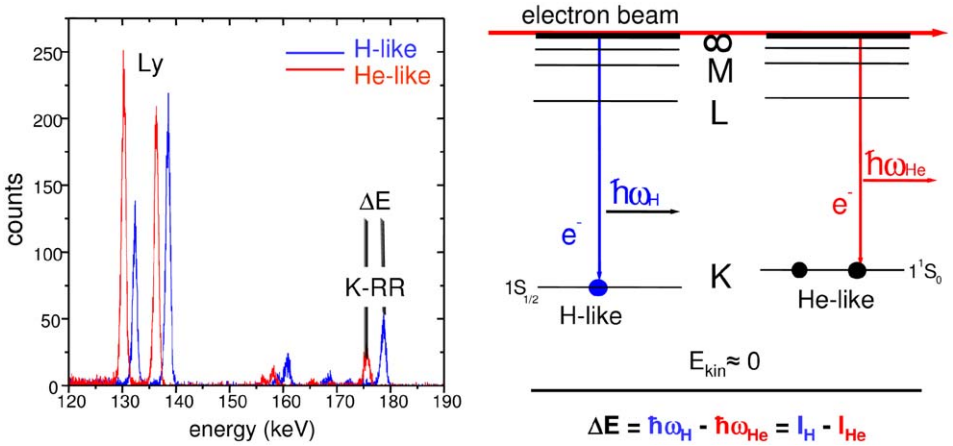


**FIGURE 5.4** Left side: X-ray spectra for capture into bare and H-like uranium (forming H- and He-like uranium, respectively) as measured at ESR electron cooler. Right side: Schematic presentation of the RR process of free electrons into the initially bare and H-like ions. The energy difference $\Delta E = \hbar\omega_{\mathrm{H}} - \hbar\omega_{\mathrm{He}}$ gives exactly the two-electron contribution to the ionisation potential in He-like ions.

cooler section was used, an environment which was already exploited in first Lamb shift experiments at high-$Z$ by Beyer *et al.* [14]. The experimental setup is displayed in Figure 5.3. For details of the experimental arrangement please refer to [14,16]. In Figure 5.4, the X-ray spectra for RR into initially bare- and H-like uranium recorded in coincidence with the ions which have captured an electron is shown.

**TABLE 5.1** Comparison of our experimental result for $Z = 92$ with the RMBPT calculations of Persson [25]. 2eSE and 2eVP denote two-electron self-energy and vacuum polarisation contributions, respectively. All values are in eV

| Nuclear charge | 1st order RMBPT | $\geqslant$2nd order RMBPT | 2eSE | 2eVP | Total theory | Experiment |
|---|---|---|---|---|---|---|
| 92 | 2265.87 | −14.11 | −9.7 | 2.6 | 2246.0 | $2248 \pm 9$ |

The difference between the K-RR centroid energies transformed into the emitter frame gives directly the two-electron contribution to the ground-state binding-energy in He-like uranium (compare Figure 5.4 right side). For the determination of the K-RR line centroid positions, least-squares fits using a Gaussian peak shape with a shelf on the low energy side were done. This model-function is known to describe well response of Ge(i) detectors [29]. Following this method, we obtained a value of $3047.91 \pm 12.6$ eV (as a weighted mean of values for the three strips) for the difference between the K-RR centroid energies ($\Delta = \text{K-RR}_\text{H} - \text{K-RR}_\text{He}$). Finally, using the cooler-voltage value of 23913(5) V (corresponding to the ion beam velocity $\beta = 0.29565 \pm 2.9 \cdot 10^{-5}$) and the X-ray detector observation angles of 0.35(2)°, 0.53(2)°, 0.71(2)° for the three strips, the difference $\Delta$ was transformed into the emitted frame yielding a value of $2248 \pm 9$ eV for two-electron contribution in He-like uranium. Here, one has to emphasise that due to the combination of the 0 deg detection geometry and the deceleration technique the Doppler uncertainties introduced by the observation angle as well as by the beam velocity do not affect the final accuracy. Therefore, our uncertainty is of purely statistical nature.

In Table 5.1 a comparison of the present experimental result with state-of-the-art theoretical calculations is shown. The theory is based on the relativistic Many-Body Perturbation Theory (MBPT) approach and incorporates in addition all of the second order ($\alpha^2$) QED contributions. The comparison shows a very good agreement between our experimental result and the calculations. Our result is sensitive to the second-order MBPT contribution, moreover, the accuracy is of the same size as the two-electron $\alpha^2$-order self-energy. Another theoretical approach by Yerokhin *et al.* [26], which takes into account the electron–electron interaction in a complete manner to second order in $\alpha$ is also in excellent agreement with the present experimental result. Here, we like to emphasise that the relative contribution of the second-order QED effects in the total value of two-electron contribution is quite high (as compared, for example, to the 1s binding energy in H-like system), in addition, the influence of uncertainty introduced by poorly known extended size of the nucleus is negligible for the theoretical value of the two-electron contribution. These distinctive features make this particular kind of QED study unique among other tests for high-$Z$ ions such as 1s Lamb shift (in one-electron systems), $g$-factor of bound electrons, or hyperfine splitting.

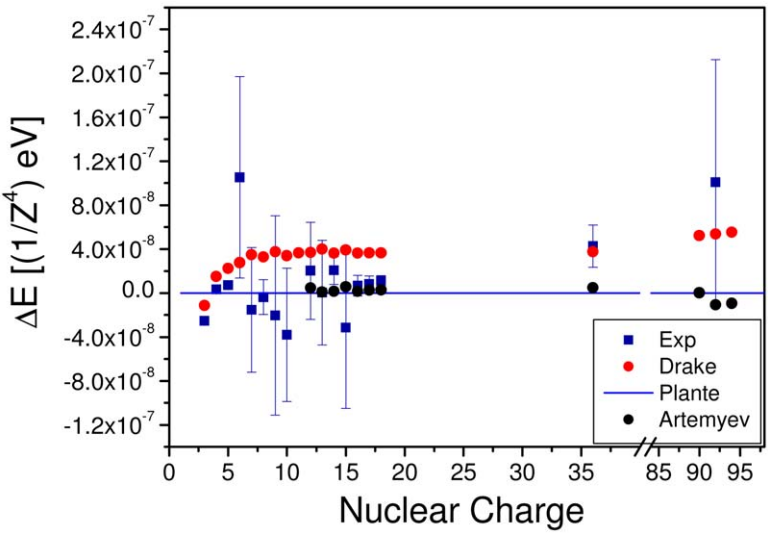


**FIGURE 5.5** $^3P_0$–$^3S_1$ transition in He-like systems as a function of the nuclear charge (relative to the values of Plante *et al.* [24]). The theoretical results are from Plante *et al.* [24], Drake [21] and Artemyev *et al.* [27]. For the experimental data see [30] and references therein.

## 2.2 L-shell excited states in two-electron high-*Z* ions

Recently there has been a significant progress in theoretical investigation of $n = 2$ levels of high-*Z* two-electron systems manifested in evaluation of binding energies of all the L-shell states including all two-electron QED contributions in a complete manner [27]. On the experimental side, there exist numerous data for the low-*Z* domain (see Figure 5.5) providing precise test of the state-of-art QED calculations. However, as mentioned above, there is a significant disagreement between the theory [18] and the recent experimental results [17] for the fine structure in helium, indicating the need for further investigations from theoretical as well as experimental sides. The situation is very different in the high-*Z* regime, where very few experimental data are available up to now (see Figure 5.5). Therefore, a precise test of the fundamental theories as well as probing the higher-order QED contributions for excited states are still awaiting. Besides, an accurate determination of the L-shell binding energies in high-*Z* He-like ions is of importance for PNC investigations [19,20]. In particular, as shown in Figure 5.6, the $^3P_0$–$^1S_0$ interval has still to be determined accurately in order to allow for choosing of a best candidate for the PNC observation.

In high-*Z* ions, the excited levels can be efficiently populated via electron capture into initially H-like species [35]. This is in contrast to the excitation process, which has been a limiting factor for former investigations at the Super-EBIT [31]. Therefore, for future studies at GSI, a production of the excited states in He-like uranium via ion-atom collisions (at the ESR gasjet target) is planned which will be complemented by precise spectroscopy of the $\Delta n = 0$ transition energies. Here,

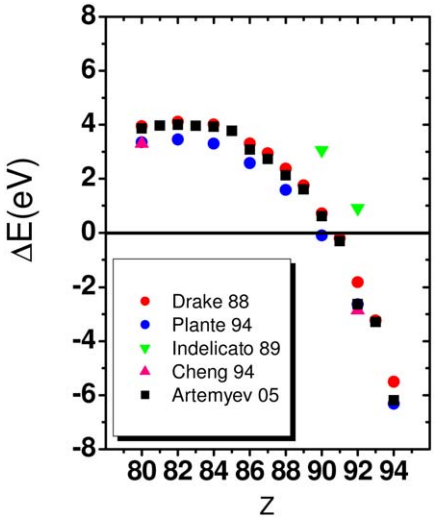


**FIGURE 5.6** $^3P_0$–$^1S_0$ interval (theoretical results) in high-$Z$ two-electron ions. The values are from Drake [21], Plante *et al.* [24], Schäfer *et al.* [32], Cheng *et al.* [23,33], Artemyev *et al.* [27] and Indelicato *et al.* [34].

a novel high-resolution X-ray detection devices, namely crystal spectrometers and microcalorimeters will be utilised.

## 3. SUMMARY

We reviewed the current status of the experimental investigations devoted to precise study of the bound-state QED effects and their impact on atomic structure in one- and two-electron heavy ions. The recent improvements in experimental accuracy for the ground-state binding-energies in H- and He-like heavy systems are accompanied by increase of accuracy in theoretical predictions by evaluating higher-order QED contributions. Comparison of the most recent experimental results with the corresponding theoretical values manifests a good agreement and provides test of the dominant QED contributions on a percent level; even reaching the scale of the higher-order QED effects for the case of two-electron contribution in He-like uranium.

The future experimental investigations will target in particular the accurate spectroscopy of the excited states in heavy He-like systems. In contrast to the ground-state properties, this topic has almost not been addressed up to now experimentally. In addition, very recently, there has been a considerable progress in developments for the next generation Lamb shift experiments on H-like heavy ions. Here, the first beam-time has already been conducted utilising the high-resolution X-ray spectrometers (in combination with novel position-sensitive solid-state detectors) as well as the X-ray microcalorimeter.

## ACKNOWLEDGEMENT

The close collaboration and support by the members of the ESR team is gratefully acknowledged. This work was supported by I3 EURONS under EC Contract No. 506065.

## REFERENCES

[1] J. Schweppe, *et al.*, *Phys. Rev. Lett.* **66** (1991) 1434.
[2] C. Brandau, *et al.*, *Phys. Rev. Lett.* **89** (2002) 053201.
[3] P. Beiersdorfer, H. Chen, D.B. Thorn, E. Träbert, *Phys. Rev. Lett.* **95** (2005) 233003.
[4] W. Johnson, G. Soff, *Adv. Data Nucl. Data Tables* **33** (1985) 405.
[5] V.A. Yerokhin, *et al.*, *Phys. Rev. A* **64** (2001) 062507.
[6] V.A. Yerokhin, *et al.*, *Phys. Rev. Lett.* **91** (2003) 073001.
[7] H.F. Beyer, *et al.*, *Spectrochim. Acta Part B* **59** (2004) 1535.
[8] Th. Stöhlker, *et al.*, *Nucl. Instrum. Methods B* **205** (2003) 210.
[9] D. Protic, *et al.*, *IEEE Trans. Nucl. Sci.* **52** (6) (2005) 3194.
[10] S. Chatterjee, *et al.*, *Nucl. Instrum. Methods Phys. Res. Sect. B* **245** (2006) 67.
[11] A. Bleile, *et al.*, *Nucl. Instrum. Methods Phys. Res. Sect. B* **444** (2000) 488.
[12] E. Silver, *et al.*, *Nucl. Instrum. Methods Phys. Res. Sect. A* **520** (2004) 60.
[13] Th. Stöhlker, *et al.*, *Phys. Rev. Lett.* **71** (1993) 2184.
[14] H.F. Beyer, *et al.*, *Z. Phys. D* **35** (1995) 169.
[15] Th. Stöhlker, *et al.*, *Phys. Rev. Lett.* **85** (2000) 3109.
[16] A. Gumberidze, *et al.*, *Phys. Rev. Lett.* **94** (2005) 223001.
[17] T. Zelevinsky, D. Farkas, G. Gabrielse, *Phys. Rev. Lett.* **95** (2005) 203001.
[18] K. Pachucki, *Phys. Rev. Lett.* **97** (2006) 013002.
[19] R.W. Dunford, Th. Stöhlker, in: E. Zavattini, D. Bakalov, C. Rizzo (Eds.), *Frontier Tests of Quantum Electrodynamics and Physics of the Vacuum*, Heron Press, Sofia, 1998.
[20] L.N. Labzowsky, *et al.*, *Phys. Rev. A* **63** (2001) 054105.
[21] G.W. Drake, *Can. J. Phys.* **66** (1988) 586.
[22] W.R. Johnson, J. Sapirstein, *Phys. Rev. A* **46** (1992) 2197.
[23] M.H. Chen, K.T. Cheng, W.R. Johnson, *Phys. Rev. A* **47** (1993) 3692.
[24] D.R. Plante, W.R. Johnson, J. Sapirstein, *Phys. Rev. A* **49** (1994) 3519.
[25] H. Persson, *et al.*, *Phys. Rev. Lett.* **76** (1996) 204.
[26] V.A. Yerokhin, A.N. Artemyev, V.M. Shabaev, *Phys. Lett. A* **234** (1997) 361.
[27] A.N. Artemyev, *et al.*, *Phys. Rev. A* **71** (2005) 062104.
[28] R.E. Marrs, S.R. Elliott, Th. Stöhlker, *Phys. Rev. A* **52** (1995) 3577.
[29] R.G. Helmer, R.C. Greenwood, R.C. Gehrke, *Nucl. Instrum. Methods* **124** (1975) 107.
[30] K.W. Kukla, *et al.*, *Phys. Rev. A* **51** (1995) 1905.
[31] P. Beiersdorfer, S.R. Elliott, A. Osterheld, Th. Stöhlker, J. Autrey, G.V. Brown, A.J. Smith, K. Widmann, *Phys. Rev. A* **53** (1996) 4000.
[32] A. Schäfer, G. Soff, P. Indelicato, B. Müller, W. Greiner, *Phys. Rev. A* **40** (1989) 7362.
[33] K.T. Cheng, M.H. Chen, W.R. Johnson, J. Sapirstein, *Phys. Rev. A* **50** (1994) 247.
[34] P. Indelicato, F. Parente, R. Marrus, *Phys. Rev. A* **40** (1989) 3505.
[35] Th. Stöhlker, *Phys. Scr. T* **80** (1999) 165.

CHAPTER 6

# Precise Atomic Masses for Fundamental Physics Determined at SMILETRAP

**R. Schuch**[1*], **I. Bergström**[*], **T. Fritioff**[*], **Sz. Nagy**[2*], **A. Solders**[*] and **M. Suhonen**[*]

Contents



Abstract

In this paper we describe the features of the SMILETRAP Penning trap mass spectrometer and give examples of recently performed precision mass measurements. SMILETRAP is designed for precision mass measurements using the merits of highly-charged ions. We emphasize here the importance of accurate masses of hydrogen-like and lithium-like ions for the evaluation of $g$-factor measurements of electrons bound to even–even nuclei and test quantum electrodynamics (QED). For these experiments the ion masses of $^{40}Ca^{17+}$ and $^{40}Ca^{19+}$ were measured at SMILETRAP with $5 \times 10^{-10}$ precision. Highly precise mass measurements can also be used for testing atomic structure calculations and determination of atomic and nuclear binding energies. Some $Q$-values are of fundamental interest, for example, the beta-decay of tritium and the double beta-decay with no neutrinos of several

* Atomic Physics, FYSIKUM, AlbaNova, Stockholm University, SE-106 91, Stockholm, Sweden
1 Corresponding author. E-mail: Reinhold.Schuch@physto.se; url: http://www.atom.physto.se
2 Present address: Physics Department, Johannes Gutenberg University, Staudinerweg 7, D5128 Mainz, Germany

Advances in Quantum Chemistry, Vol. 53
ISSN 0065-3276, DOI:10.1016/S0065-3276(07)53006-6

nuclei, in particular $^{76}$Ge. These decays are related to properties of the electron neutrino mass and whether this neutrino is a Majorana particle. The reason that Penning traps are so reliable for the determinations of accurate decay $Q$-values is due to the fact that systematic errors to a great deal cancel in the mass difference between the two atoms defining the $Q$-value. In this paper we report the most accurate $Q$-values of these two beta decays namely 18589.8(12) eV for the tritium decay, and 2038.997(46) keV for the neutrinoless double beta-decay of $^{76}$Ge.

## 1. INTRODUCTION

Atomic masses are related to fundamental questions in current physics, particularly when they can be measured with extremely high accuracy. Beside their fundamental importance as new information in the atomic mass table [1], high-precision masses have wide ranging applications in modern physics, including the determination of fundamental constants, verification of nuclear models, test of the Standard Model, test of QED, metrology and many more [2]. The Penning trap mass spectrometer SMILETRAP is connected to the electron beam ion source CRYSIS [3,4] which produces Highly-Charged Ions (HCI). High charge is required for high precision mass measurements since the precision ($\delta m/m$) increases linearly with the ion charge state [5]. Furthermore, mass measurements using different charge states of the same element offer a check of certain systematic errors.

In the Penning trap, where an ion with charge $qe$ and mass $m$ is confined by static electric fields and a strong magnetic field $B$ for a certain time $\Delta t$, the cyclotron frequency $\omega_c = (qe/m)B$ of the ion motion is determined. The ratio of cyclotron frequencies of two different ions in the same magnetic field gives directly their mass ratio. Due to the long observation time and the well understood dynamics of the ion motion in a trap, Penning trap mass spectrometers are the leading devices in the field of high-accuracy mass spectrometry today. It is evident that the precision in the mass $m$ increases linearly with $q$, since $m/\Delta m = \nu/\Delta\nu$ grows with $\nu$, for a resonance width $\Delta\nu$ at a fixed observation time $\Delta t$ (as $\Delta\nu \approx 1/\Delta t$). SMILETRAP is the first Penning trap mass spectrometer that is designed for exploiting the mass precision increase by using highly-charged ions.

The acronym SMILETRAP is an abbreviation of Stockholm–Mainz-Ion-Levitation-TRAP, reflecting the close cooperation between the Physics Department of the Johannes Gutenberg University in Mainz and the Atomic Physics group at Stockholm University, a successful cooperation that still is vital. The Penning trap part of SMILETRAP was built in Mainz by German and Swedish undergraduate and graduate students. This work started in the summer of 1990 and finished in the beginning of 1993 when the device was shipped to Stockholm.

During this time the question was raised whether a crystal of $^{28}$Si could be used as an atomic definition of the kilogram. Therefore a measurement of the mass of this atom was made using singly charged silicon ions and $^{12}C^+$ and $^{12}C_3^+$ ions as mass references [6]. Though we reached a statistical uncertainty of $10^{-9}$ we had to face the large $q/A$ asymmetry which resulted in a systematic uncertainty of $10^{-8}$.

This was a clear warning that in future mass measurements we should use ions which, as close as possible, are $q/A$ doublets. Nevertheless, at that time, it was a tenfold improvement of the Si mass. Later in Stockholm, using fully stripped $^{28}$Si ions, we could reach a mass uncertainty of $3.5 \times 10^{-10}$ [7], a compatible value, with a somewhat higher accuracy, had been obtained by the MIT-group [8].

In this contribution we describe measurements with the Penning trap mass spectrometer over a wide span of mass values, from masses of hydrogen and tritium to $^{76}Se^{25+}$ ions. This fact shows also the versatility of SMILETRAP, being able to cover a wide mass range with an accuracy of below $10^{-9}$. So far, mass measurements involving ions of about 30 isotopes in the mass range of up to 200 u and charges of up to 52+ have been performed at SMILETRAP. By measuring the mass of $^{198}$Hg and $^{204}$Hg, a problem in the atomic mass table has been solved [9]. In the following we show examples of accurate mass measurements of heavy HCI for determining the $g$-factor of the bound electron and their electron binding energies. We shall also discuss the possibility of using these measurements for testing QED-effects of strongly bound electrons [10]. We report about the measurement of the cyclotron frequency of atomic tritium ions as well as singly and doubly charged $^3$He ions which gave the atomic masses of $^3$H and $^3$He and thus the $Q$-value of the tritium beta-decay. This $Q$-value is of interest for experiments aiming at finding a finite rest mass for the electron antineutrino.

A further highlight from SMILETRAP is the determination of the $^{76}$Ge double $\beta$-decay $Q$-value [11,12]. This is important to identify the energy where one could observe possible events of neutrinoless double $\beta$-decay that can occur if the neutrino is a Majorana particle.

## 2. THE SMILETRAP FACILITY

In a preceding paper [13] we have described in details the method of mass measurements with SMILETRAP. Here we want to outline the most essential procedures to produce, trap, excite, and detect highly charged ions for mass measurement using the time-of-flight ion cyclotron resonance technique. Most elements have a large number of isotopes. We therefore use an isotope separator after the CHORDIS ion source (see Figure 6.1) in order to be able to inject mass separated beams of singly charged ions into CRYSIS. Figure 6.2a shows the mercury mass spectrum recorded about 50 cm from the entrance to CRYSIS obtained by sweeping the selection magnet current. The mercury isotopes are well resolved and the background is low (Figure 6.2a). A low isotopic abundance can be compensated by a longer accumulation time.

In the charge breeding procedure in CRYSIS it is found that the ions with the highest charges have the largest emittance due to heating by electron–ion collisions when creating highly-charged ions. The large emittance causes problems when trying to inject the ions into the Penning trap. It is therefore necessary to cool the ions with e.g. $^4He^{2+}$ ions during charge breeding. With a typical electron current of 100 mA the number of trapped charges in CRYSIS is about $10^8$, corresponding to about $10^6$ ions with 50+ charge, that are extracted in a 100 μs long pulse.

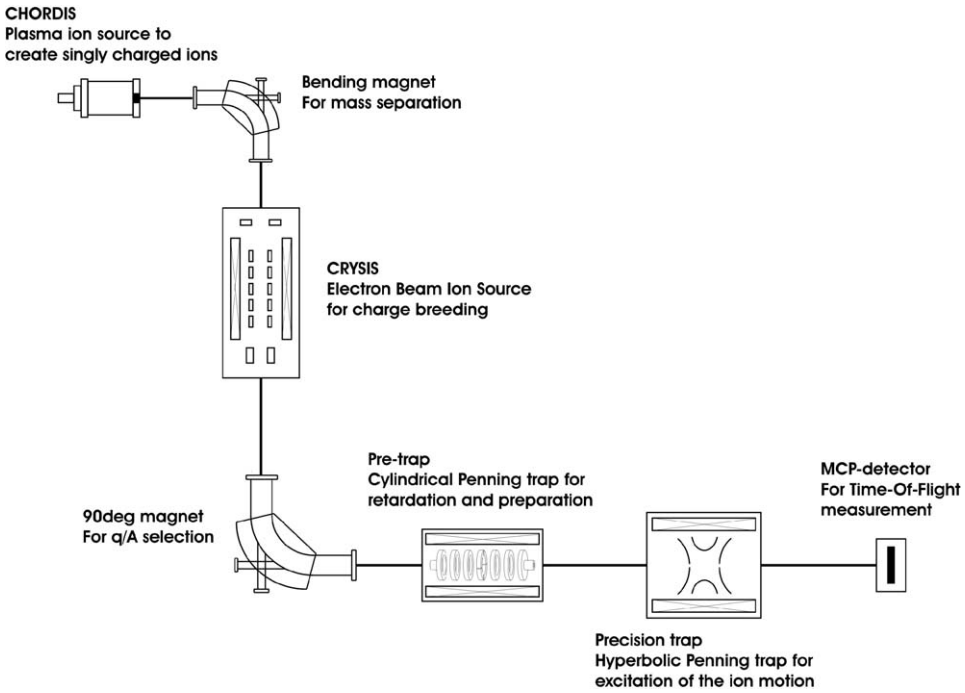


**FIGURE 6.1** Schematic layout of the SMILETRAP facility.

The ions are charge state analysed in a 90 deg magnet so that only ions of a certain isotope in a certain well defined charge state can reach the pre-trap (see Figure 6.1). Figure 6.2b shows a charge state spectrum measured with $^{40}$Ca ions [14]. Only about 1000 ions from the pulse are then caught in the pre-trap. When released from the pre-trap the ions are accelerated by $-1$ kV. Before entering the precision trap the ions are again retarded and forced to pass an aperture with a diameter of 1 mm. About 30 ions are cold enough to enter the precision trap and are trapped by a voltage of about 5 V. The ions used are located in a cylinder with a diameter of less than 1 mm. This volume thus occupies a small part of the trap center where the field is homogeneous to at least $10^{-9}$. The trap voltage is then lowered to about 0.1 V, whereby the hottest ions are boiled away. Usually, in average, 1–2 ions are then left in the precision trap and are exposed to a quadrupole radio frequency field for 1 s [15]. The frequency of the excitation signal is scanned and the flight time to a micro-channel plate detector located at a distance of about 50 cm from the trap centre is recorded. The cyclotron resonance is detectable as a pronounced minimum (see Figure 6.3) in the ion time-of-flight spectrum [16,17]. The cyclotron frequency of a reference ion with well known mass is measured in a similar way. The ions are used in a destructive way since they are lost every detection cycle. After each measuring cycle new ions are loaded.

This procedure has some advantages. We can quickly alternate between the measured ion and the reference ion or between different charge states. Each exper-

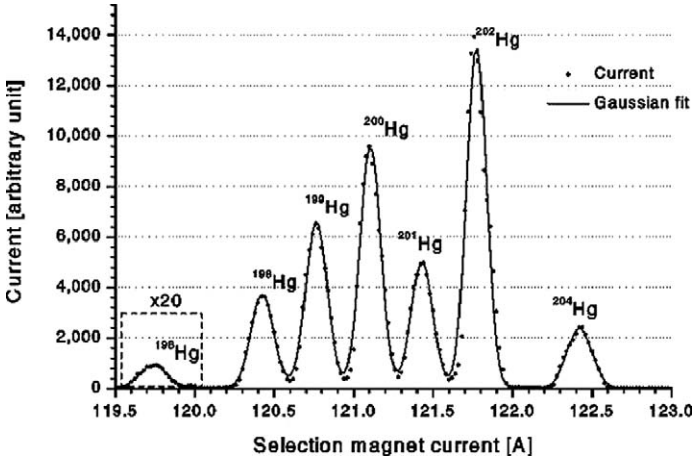


(a)

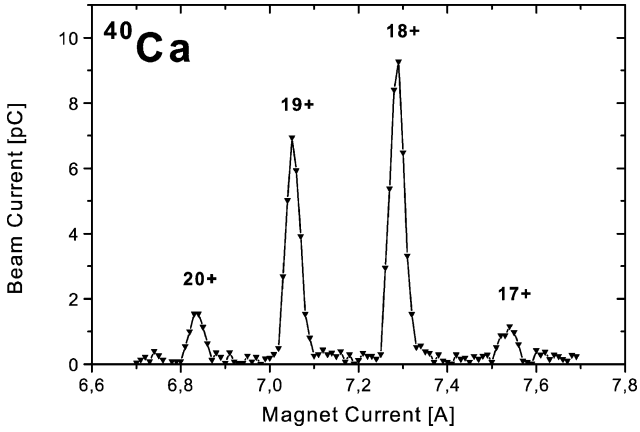


(b)

**FIGURE 6.2** (a) The mass spectrum of singly charged Hg ions [9], (b) the charge spectrum of Ca-ions [14]. As illustrated the mass and charge selection in SMILETRAP is very good.

iment is then based on several thousand injection, excitation, and measurement cycles. Figure 6.4 shows an example of a TOF spectrum measured with $^{76}Ge^{25+}$ ions.

From the resonance curve of flight time versus frequency (see Figure 6.3 for the example of $Se^{25+}$), the cyclotron frequency $\omega_c$ for a particle with mass $m_1$ and charge $q_1$ in the magnetic field $B$ is determined. However, there is not any method to measure $B$ with high precision. Therefore a mass reference $m_2$ is needed, preferably carbon ions in a proper charge state $q_2$. The mass is then

$$m_1 = m_2 \frac{\nu_2}{\nu_1} \frac{q_1}{q_2}. \tag{1}$$

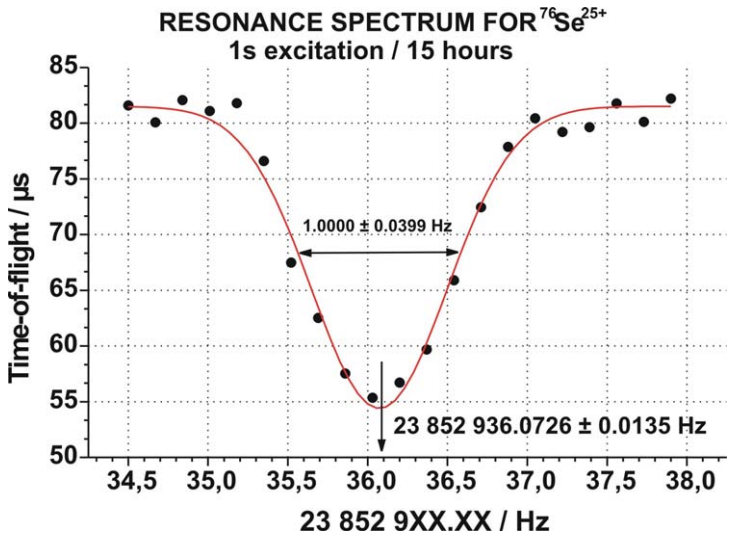


**FIGURE 6.3** The time-of-flight of the ions versus the quadrupolar excitation frequency. The cyclotron resonance frequency is determined from the position of the dip.

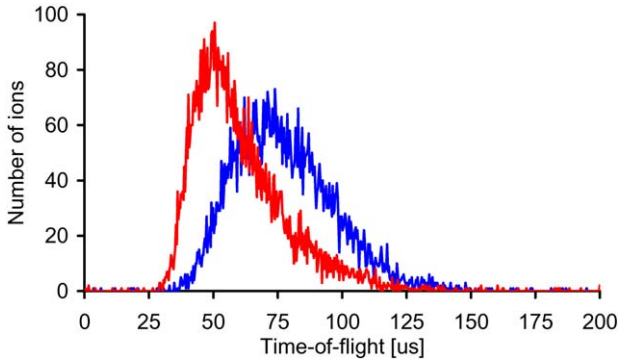


**FIGURE 6.4** Time-of-flight spectrum of $^{76}Ge^{25+}$ ions in resonance (shifted to short times) and off resonance (shifted to long times).

We have frequently used the $H_2^+$ ion as $m_2$ because it can conveniently be produced in the pre-trap by bombarding the rest gas with 3.4 keV electrons. The mass of $H_2^+$ is 2.015 101 497 03 (27) u with an uncertainty of $1.8 \times 10^{-10}$ a detailed evaluation of the $H_2^+$ ion mass is found in [13].

The relation (1) only holds if the magnetic field does not change between the cyclotron frequency measurements of the two ion species. Searching for the cyclotron frequency we therefore scan the frequency interval near the resonance using 21 different frequencies. We do that for $m_1$ and $m_2$ one after the other. A full measuring cycle thus takes about three minutes during which the natural decay of the superconducting coil, as well as faster changes in $B$ depending on temperature de-

pendent changes due to the susceptibility of the trap material, can be neglected. Still, in order to keep the uncertainties due to possible field variations below $10^{-10}$, a temperature stability of 0.01 °C is required.

In case one wants to have the atomic mass $m_{at}$ it is then necessary to add the mass $qm_e$ of the missing electrons and to subtract their binding energy $E_B$: $m_{at} = m_1 + qm_e - E_B$. Most Penning-trap mass spectrometers [2] are using singly charged ions, in which case the electron binding energy is close to 10 eV and experimentally known. Here the uncertainties due to binding energy are so small that they can be neglected even in the most accurate measurements. Using multiply charged ions the involved binding energies can introduce uncertainties which can not be neglected. For higher charge and $Z$-values (typically above $Z = 18$) one has to rely upon calculations [18]. One can turn this around and, by measuring the mass of the same isotope using different ion charges, the binding energy of a number of electrons in the atom can be obtained as a mass difference. This is especially the case when the precision reaches 2–10 eV or better so that the influence from correlation, relativistic, Breit and QED corrections can be directly measured in heavy ions [5]. This will be discussed further in Section 3.

Until recently we have excited the ion using a single continuous radio frequency pulse. This excitation mode is a Fourier limited process that is manifested in a resonance shape similar to a Gaussian (see Figure 6.3). One can, however, drive the excitation in a different way, by applying the so called Ramsey method, where the excitation pulse is applied in time separated intervals. The first group to apply this method was the Mainz collaboration using singly charged $Cs^+$ ions [19]. However, at that time there was no algorithm available for evaluating the fringe pattern that results from the quadrupolar Ramsey excitation mode. Recently, M. Kretzschmar has given a mathematical tool for the fringe pattern evaluation [20]. New experiments in Mainz [21] with singly charged $^{39}K^+$ ions and in Stockholm [12] using $H_2^+$ ions have convincingly shown that the two-pulse mode is the best choice, resulting in a precision gain of up to a factor 3. This is very important since it means a ten times shorter data collection time for equal statistics. Earlier we applied a three-pulse excitation mode to $Se^{25+}$ ions. This has now been evaluated, confirming our previous single-pulse results and our previously obtained $^{76}Ge$ $Q$-value (see Section 3).

The main systematic uncertainties in our mass measurements are due to the following [13]:

1. The mass of the reference ion
2. The number of trapped ions
3. The relativistic mass increase
4. $q/A$ asymmetry
5. Impurity ions having a similar $q/A$ as the ion of interest
6. Magnetic field fluctuations

These uncertainties, in each frequency measurement, lie in the region 0.1–1 ppb or less. The uncertainty coming from $q/A$ asymmetry between the main ion and reference ion of course vanishes when using $q/A$ doublets since our observable is the ratio of the frequencies.

## 3. RESULTS AND DISCUSSIONS

### 3.1 Mass measurements for QED tests

The ionic mass is an essential ingredient when evaluating the $g$-factor experiments of the bound electron in hydrogen-like and lithium-like ions [10] which aim to test and benchmark theoretical QED calculations. Investigations of high $Z$ hydrogen-like systems are strongly restricted by an uncertainty due to nuclear size effects. In the case of the bound electron $g$-factor the role of the nuclear effects is not as crucial as in the case of the hyperfine structure splitting. Furthermore, in a certain combination involving differences of the $g$-factor of the hydrogen-like and lithium-like ions this can be significantly reduced [5]. The value of $g$ can be obtained from

$$g = 2\frac{\omega_L}{\omega_c}\frac{qm_e}{M}, \tag{2}$$

where the Larmor precession frequency, $\omega_L$, and the cyclotron frequency, $\omega_c$, can be accurately measured at the $g$-factor experiment, $m_e$ is the mass of the electron and $M$ is the mass of the ion under investigation. So far the hydrogen-like $^{12}C^{5+}$ and $^{16}O^{7+}$ are the heaviest ions used in the $g$-factor experiment. In both cases the ionic mass was accurately known and the dominant part of the uncertainty in $g$ was due to the uncertainty in the electron mass. Since that time a new value was accepted for the electron mass with 4 times smaller uncertainty. The present relative standard uncertainty in the electron mass is 0.44 ppb [22]. The proposed new $g$-factor experiments involving medium heavy ions like $^{40}$Ca [23] therefore require ion masses with uncertainties similar to that of the electron mass.

Considering the ratio of $g$-factors of hydrogen-like ions of different isotopes of the same element the dependence on the electron mass can be eliminated. An isotope effect in the $g$-factor $\Delta g = g_1/g_2 - 1$ can thus be introduced to characterize this effect. It was shown in [24] that an isotope effect in the $g$-factor would be measurable already between $^{24}Mg^{11+}$ and $^{26}Mg^{11+}$ thanks to the high precision mass values measured with SMILETRAP for both isotopes [24]. The size of the isotope effect in the $g$-factor is more pronounced if the difference in the mass is larger e.g. between $^{40}Ca^{19+}$ and $^{48}Ca^{19+}$ or in $^{36}Ar^{17+}$ and $^{40}Ar^{17+}$. The masses of the hydrogen-like and lithium-like $^{40}$Ca ions were measured recently at SMILETRAP, see Figure 6.5 and Ref. [14].

The atomic structure calculations are experimentally tested with transition energies and ionization potentials for low degrees of ionization. In [25] calculations for highly-charged ions with different methods were tested in their consistency. From there the error limit is derived. These calculations were for closed shell systems on a level of accuracy of 10 eV for medium $Z$ ions. The uncertainty comes mostly from correlation effects (which are typically around 50–60 eV for Ar-like ions) and from QED effects (in particular the many-body QED contributions). In Figure 6.6 the difference of calculated binding energies by Scofield and Rodrigues *et al.* in units relative to the total mass are plotted for different ions ($Cl^{q+}$, $Se^{q+}$, $Cs^{q+}$, $W^{q+}$, and $U^{q+}$) versus the number of electrons left in the ion. One sees that for certain ionic systems the difference (which is so far the uncertainty) is relatively

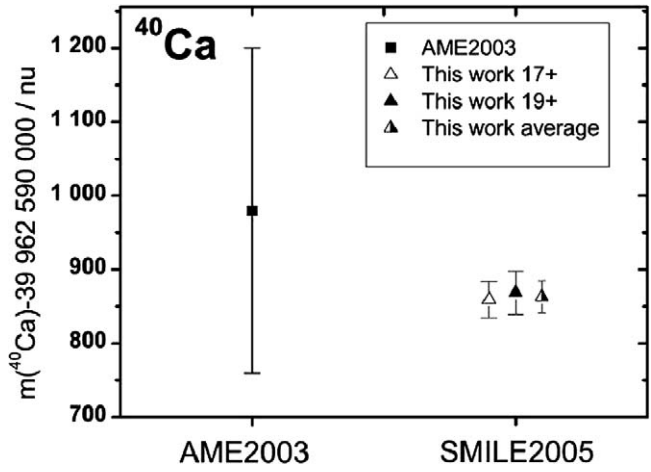


**FIGURE 6.5** The mass of $^{40}$Ca derived from measurements of hydrogen-like and lithium-like $^{40}$Ca ions compared to the previous best values [14].

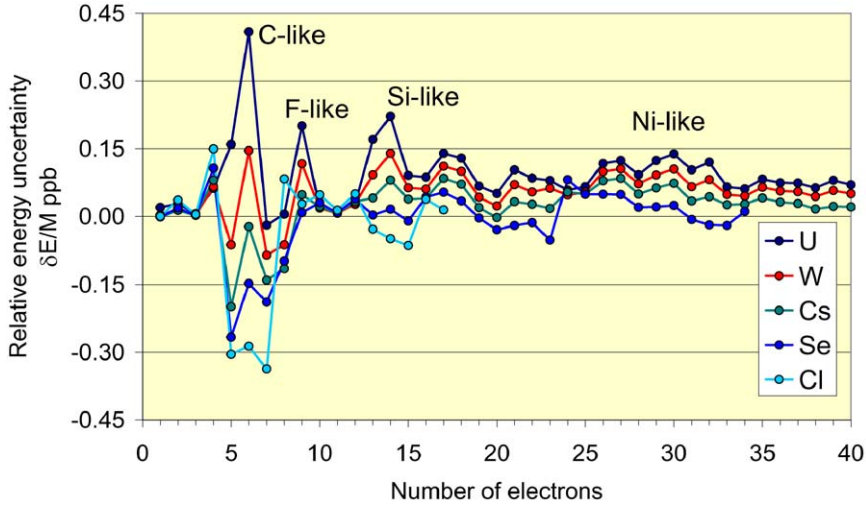


**FIGURE 6.6** The differences of calculated sum of binding energies by Scofield [26] and Rodrigues et al. [27] in units relative to the total mass are plotted versus the number of electrons left in the ion. For a colour reproduction of this figure see the colour plate section, near the end of this book.

large, reaching a few times $10^{-10}$. It should be noticed that QED contributions get large when coming to alkali-like ions as s-shell electrons are added. To first order the QED contributions get negligible when one comes to p-shell electrons. The typical contributions to the atomic masses from the total binding energies, $E_B$, are

(in some examples):

$$\begin{aligned} H_2^+: &\quad E_B = -15.4\ \text{eV} = 8.3\ \text{ppb}, \\ {}^{208}Pb^{50+}: &\quad E_B = -50.372\ \text{keV} = 260\ \text{ppb}, \\ {}^{208}Pb^{72+}: &\quad E_B = -172.177\ \text{keV} = 889\ \text{ppb}. \end{aligned}$$

Some simple $Z$-scaling rules help to pick the ions of interest. Correlation is rather independent of $Z$. To first order the binding energy scales with $Z^2$ and QED with $Z^4$ and $n^{-3}$. The absolute precision decreases linear with the ion mass. Correlation effects are most dominant in lighter ions ($A \sim 50$) and medium charges, where a precision of $10^{-10}$ already gives 5 eV. To measure QED effects a precision better then $10^{-10}$ for $A \cong 200$ and highest charge states, which has not been demonstrated yet, is needed. In particular when measuring charge state sequences such a precision should be achievable in a relative comparison between the ion masses in different charge states.

For example one has in the mass difference from Cu-like to Ni-like Pb a QED effect in the order of 2 eV [28], corresponding to around $10^{-11}$ of the ion mass difference. For the Li-like to He-like Pb mass difference it is around 30 eV [29] and already $1.5 \times 10^{-10}$. For H-like Pb one calculates around 245 eV [30] QED effect in the 1s state, which makes a mass contribution of 1 ppb. In $U^{91+}$ the 1s Lamb shift is ≈500 eV which corresponds to a relative mass shift of $\delta E/M \approx 2$ ppb. So, measuring the relative mass difference between $U^{92+}$ and $U^{91+}$ and between $U^{91+}$ and $U^{90+}$ to $10^{-11}$, which should not be too difficult, one would have the one- and two-electron Lamb-shift to ≈2 eV, i.e. a higher accuracy then present day X-ray spectroscopic measurements.

## 3.2 The *Q*-value of the tritium beta decay

In 2005 we reported about experiments in which CRYSIS has been used to disassociate tritium molecules to ions and to produce singly as well as doubly charge ions of $^3$He. The masses of these ions have been measured by SMILETRAP and from the mass values the $Q$-value of the tritium beta decay has been deduced [31]. The scientific motivation for these measurements is the possibility to use this $Q$-value in the search of the electron neutrino rest mass [32]. This method of determining $m(\nu_e)$ benefits from a very accurate $Q$-value. The use of a Penning trap for accurate determinations of the relevant atomic masses is obvious. A difficulty, but also a challenge for us, was that a relatively strong tritium source had to be used and we had no experience of running our Penning trap spectrometer or the connected electron beam ion source CRYSIS with a long-lived radioactive gas like tritium.

The first Penning trap measurement of this $Q$-value was reported already in 1993 [33]. However, in 2001 we found a discrepancy in the $^4$He mass in an attempt to measure the proton mass. As is evident from Figure 6.7, all mass reference ions except the $^4$He ions gave the same proton mass. It took a long time of chasing systematic errors before we realized that the accepted value of the $^4$He mass was wrong by a large amount. We later found similar errors in the accepted masses of $^3$He and $^3$H reported by the Seattle group.

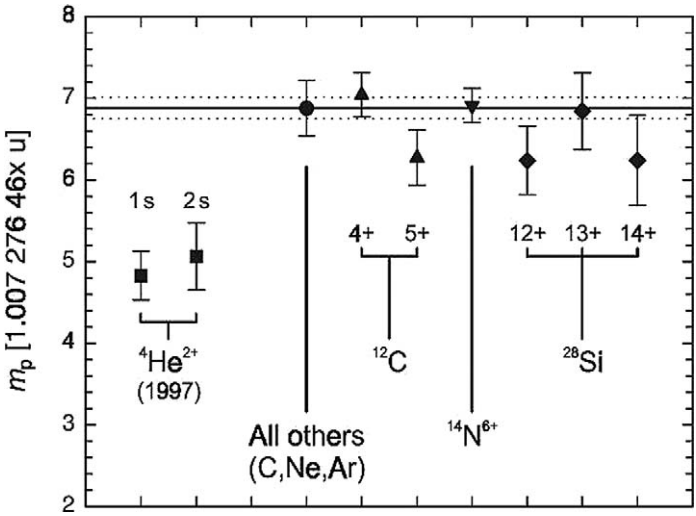


**FIGURE 6.7** The proton masses obtained in 1997 [34] using the ions indicated as mass references (with the ion $^4He^{2+}$ we used excitation times 1 and 2 s).

Since the Seattle group used the wrong masses in their measurement of the tritium beta decay $Q$-value we decided to measure this $Q$-value. In the first measurement, reported at a conference in Oulu in Finland in 2002, we reported a value of 18.587 9(3) keV. The uncertainty was hampered by the use of doubly charged $^3$He ions. However, in 2005 we learned how to run CRYSIS in a mode that essentially singly charged $^3$He ions were produced and the new $Q$-value, thus not being associated with $q/A$ asymmetry errors, became 18.5898(12) keV [31]. Our value happens to agree with the Seattle value based on wrong mass values (see Figure 6.8). Evidently these errors canceled in the mass difference, since they had the same origin. The Seattle group now has a new, very stable, superconducting magnet with drift <0.010 ppb/h [35].

They have already a very accurate mass value of $^3$He and are soon likely to have an as accurate mass value of $^3$H. These mass measurements will improve the Tritium beta-decay $Q$-value by at least a factor 5. The Tallahassee group with their two ion method is likely to provide an even more accurate $Q$-value.

## 3.3 The $Q$-value of the neutrinoless double beta-decay of $^{76}$Ge

In the year 2000 we measured the $^{76}$Ge double beta-decay value [11]. The measurement was motivated by the fact that there were two, seemingly conflicting, $Q$-values, both measured with a classical mass spectrometer by the Manitoba group, see reference [36,37] and Figure 6.9.

It took us 10 years to develop the technology for such a measurement. Singly charged ions of germanium were produced by xenon sputtering of metallic germanium in the CHORDIS ion source, whereas for selenium the ion-source oven was loaded with metallic selenium. An isotopically pure beam was achieved us-

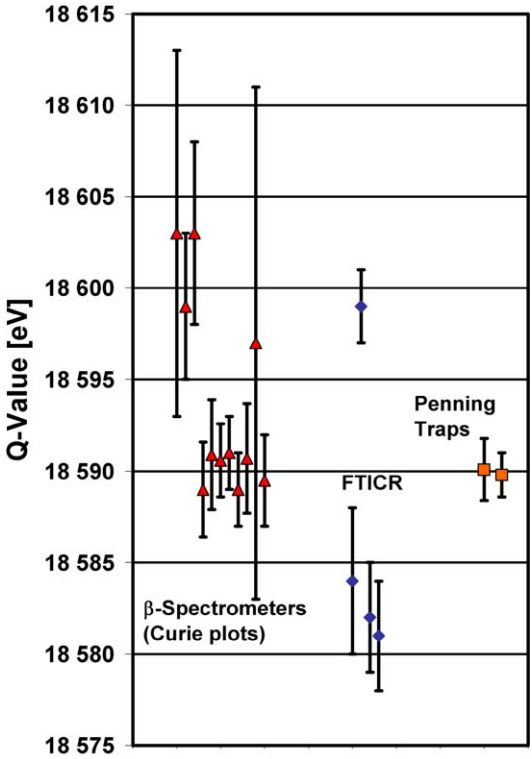


**FIGURE 6.8** Tritium *Q*-values from beta spectra (triangles), Fourier transform ion cyclotron resonance (FTICR) measurements (diamonds) and trap measurements (squares). To the left the Seattle value and to the right our recent value based on singly charged ions of $^3$H and $^3$He. The Seattle value is based on wrong values of the atomic mass of $^3$He and $^3$H which seem to cancel in the mass difference. The Stockholm value is the most precise value with an uncertainty of 1.2 eV.

ing a magnet before injection into CRYSIS where the charge state was increased up to 25+ by intense electron bombardment. In the experiment we used $H_2^+$ ions as mass reference for both ion species. The excitation of the ions in the precision trap was done using of a single continuous pulse with the time length of 1 s. The resulting *Q*-value was 2039.006(50) keV. A comparison between our value and the Manitoba experiment is given in Figure 6.9.

During these experiments we also made a three-pulse Ramsey excitation experiment using 25+ selenium ions, i.e. the excitation pulse is split into three short excitation pulses separated by a waiting times. During the waiting time no excitation is applied. In this experiment the excitation pulses were 100 ms long and the total excitation cycle time was 1 s. The evaluation of this measurement has been pending since we were lacking the theoretical understanding of how the energy absorption profile looks like after a quadrupole Ramsey excitation. Today we have the mathematical formulation needed thanks to M. Kretzschmar [20].

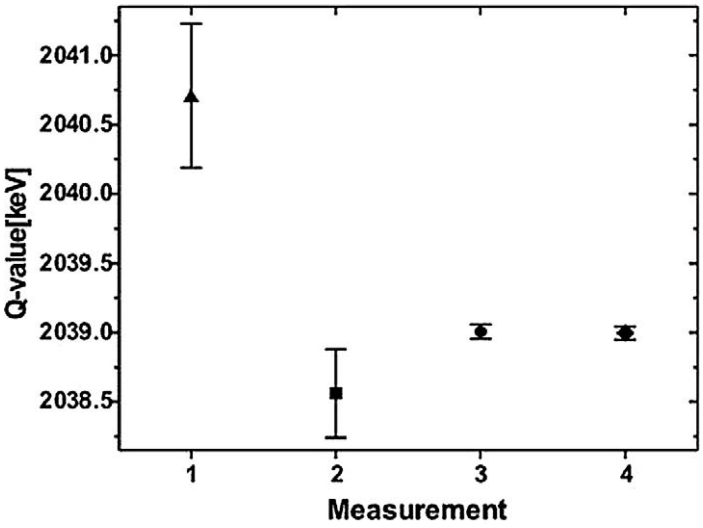


**FIGURE 6.9** $^{76}$Ge double beta-decay *Q*-value deduced from: Up triangle: Ellis *et al.* [36], Square: Hykawy *et al.* [37], Circle: G. Douysset *et al.* [11], Diamond: M. Suhonen *et al.* [12].

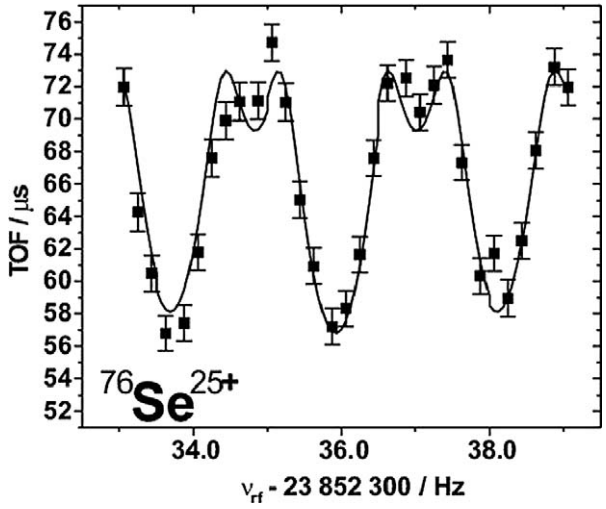


**FIGURE 6.10** Time-of-flight distribution of the $^{76}Se^{25+}$ resonance excited with a three-pulse Ramsey scheme. The fitting has been done using an algorithm [20] that describes the time-of-flight resonance profile for the ions when excited with such a scheme.

Figure 6.10 shows the time-of-flight resonance spectrum with the typical Ramsey fringe pattern fitted with the Kretzschmar algorithm for a three-pulse excitation.

This evaluation gave a mass value of selenium with a smaller statistical uncertainty than the single-pulse mode.

| | |
|---|---|
| Mass of $^{76}$Se, single-pulse | 75.919 213 789(41) (74) u, |
| Mass of $^{76}$Se, three-pulse | 75.919 213 816(31) (74) u, |
| Mass of $^{76}$Se, average | 75.919 213 804(21) (76) u. |

The masses, using single-pulse and three-pulse excitation, are calculated from measurements done on 25+ ions. The average $^{76}$Se mass is then the weighted average from measurements using 24+ and 25+ ions, the SMILETRAP value from 2001 is 75.919 213 795(28)(76) [11]. The impressive fact is that the statistical uncertainty in the $^{76}$Se mass using the three-pulse Ramsey mode is reduced by 25% compared to the single-pulse mode, although having approximately half the amount of statistics.

The new $Q$-value is 2038.997(46) keV, an improvement by almost 10% in the error. More importantly the calculation agrees with the old value.

## 4. CONCLUSION AND OUTLOOK

For high precision mass measurements Penning trap mass spectrometers using highly charged ions, e.g. SMILETRRAP, play an important role, especially when one aims at measuring the $g$-factor of bound electrons in heavy, highly charged ions like $^{238}U^{91+}$. SMILETAP is in fact so far the only facility in the world where ions with $q > 8+$ have been used for mass measurements in a Penning trap. Since, in our experiment, the mass of the hydrogen-like ion is directly obtained this is an obvious advantage compared to mass measurements involving singly charged ions. We report the mass measurements for tritium ions as well as singly and doubly charged $^3$He ions which gave the presently best $Q$-value of the tritium beta-decay. This $Q$-value is of interest for experiments aiming at finding a finite rest mass for electron antineutrino.

Another highlight from SMILETRAP is the determination of the $^{76}$Ge double $\beta$-decay $Q$-value. This is important for the energy where one could identify possible events of neutrinoless double $\beta$-decay that can occur if the neutrino is a Majorana particle.

Our Penning trap mass spectrometer will soon be relocated to an electron beam ion trap (EBIT) ion source to have access to low energy, heavy, highly-charged ions. At present this source can produce up to Neon-like ions of any element. Already now an upgrade of the source is planned after which fully stripped ions up to $U^{92+}$ can be produced. To further improve our mass measurements we will apply longer excitation times and the Ramsey method together with ion cooling in a new preparation Penning trap of our experimental setup.

## ACKNOWLEDGEMENTS

We gratefully acknowledge support from the Knut and Alice Wallenberg Foundation, from the European R&D network HITRAP (contract No. HPRI CT 2001

50036), from the Manne Siegbahn Laboratory, and from the Swedish research council VR.

## REFERENCES

[1] G. Audi, *Int. J. Mass Spectrom.* **251** (2006) 85.
[2] K. Blaum, *Phys. Rep.* **425** (2006) 1.
[3] E. Beebe, L. Liljeby, A. Engström, M. Björkhage, *Phys. Scr.* **47** (1993) 470.
[4] I. Bergström, M. Björkhage, L. Liljeby, *Proceedings of the EBIT/2000* **20** (2001).
[5] T. Fritioff, *et al.*, *Int. J. Mass Spectrom.* **251** (2006) 281.
[6] R. Jertz, *et al.*, *Phys. Scr.* **48** (1993) 399.
[7] I. Bergström, *et al.*, *Phys. Scr.* **66** (2002) 201.
[8] F. DiFilippo, *et al.*, *Phys. Rev. Lett.* **73** (1994) 1481.
[9] T. Fritioff, *et al.*, *Nucl. Phys. A* **723** (2003) 3.
[10] G. Werth, *et al.*, *Int. J. Mass Spectrom.* **251** (2006) 152.
[11] G. Douysset, T. Fritioff, C. Carlberg, I. Bergström, M. Björkhage, *Phys. Rev. Lett.* **86** (2001) 4259.
[12] M. Suhonen, *et al.*, *JINST* **2** (2007) P06003.
[13] I. Bergström, *et al.*, *Nucl. Instrum. Methods Phys. Res. A* **487** (2002) 618.
[14] Sz. Nagy, *et al.*, *Eur. Phys. J. D* **39** (2006) 1.
[15] M. König, *et al.*, *Int. J. Mass Spectrom.* **142** (1995) 95.
[16] F. Bloch, *Physica* **19** (1953) 821.
[17] G. Gräff, H. Kalinowsky, J. Traut, *Z. Phys. A* **297** (1980) 35.
[18] G.C. Rodrigues, P. Indelicato, J.P. Santos, P. Patté, F. Parente, *At. Data Nucl. Data Tables* **86** (2004) 117.
[19] G. Bollen, *et al.*, *Nucl. Instrum. Methods B* **70** (1992) 490.
[20] M. Kretzschmar, *Int. J. Mass Spectrom.* **264** (2007) 122.
[21] S. George, *et al.*, *Int. J. Mass Spectrom.* **264** (2007) 110.
[22] P.J. Mohr, B.N. Taylor, *Rev. Mod. Phys.* **77** (2005) 1.
[23] M. Vogel, J. Alonso, S. Djekic, H.-J. Kluge, W. Quint, S. Stahl, J. Verdu, G. Werth, *Nucl. Instrum. Methods B* **235** (2005) 7.
[24] I. Bergström, M. Björkhage, K. Blaum, H. Bluhme, T. Fritioff, Sz. Nagy, R. Schuch, *Eur. Phys. J. D* **22** (2003) 41.
[25] G.C. Rodrigues, M.A. Ourdane, J. Bieron, P. Indelicato, E. Lindroth, *Phys. Rev. A* **63** (2001) 012510.
[26] J. Scofield, *Ionisation Energies*, LLNL internal report, Livermore, California 94550, USA (1986).
[27] G.C. Rodrigues, P. Indelicato, J.P. Santos, P. Patte, F. Parente, *At. Data Nucl. Data Tables* **86** (2004) 117.
[28] E. Lindroth, M. Tokman, P. Glans, Z. Pesic, G. Vikor, H. Danared, M. Pajek, R. Schuch, *Phys. Rev. Lett.* **86** (2001) 5027.
[29] S.A. Blundell, *Phys. Rev. A* **47** (1993) 1790.
[30] W.R. Johnson, G. Soff, *At. Data Nucl. Data Tables* **33** (1985) 405.
[31] Sz. Nagy, *et al.*, *Europhys. Lett.* **74** (2006) 404.
[32] J. Angrik, *et al.*, *FZKA Sci. Rep.* **7090** (2004) 1.
[33] R.S. Van Dyck, *et al.*, *Phys. Rev. Lett.* **70** (1993) 2888.
[34] C. Carlberg, *Hyperfine Interact.* **114** (1998) 177.
[35] R.S. Van Dyck, *et al.*, *Hyperfine Interact.* **132** (2001) 163.
[36] R.J. Ellis, *et al.*, *Nucl. Phys. A* **435** (1985) 34.
[37] J.G. Hykawy, *et al.*, *Phys. Rev. Lett.* **67** (1991) 1708.

CHAPTER 7

# HITRAP: A Facility at GSI for Highly Charged Ions☆

**H.-J. Kluge[a,b], T. Beier[a], K. Blaum[a,c], L. Dahl[a], S. Eliseev[a], F. Herfurth[a], B. Hofmann[a], O. Kester[a], S. Koszudowski[a], C. Kozhuharov[a], G. Maero[a], W. Nörtershäuser[a,c], J. Pfister[a,d], W. Quint[a], U. Ratzinger[d], A. Schempp[d], R. Schuch[e], Th. Stöhlker[a], R.C. Thompson[f], M. Vogel[a], G. Vorobjev[a], D.F.A. Winters[a]** and **G. Werth[c]**

Contents



[a] Gesellschaft für Schwerionenforschung, D-64291 Darmstadt, Germany
E-mail: J.Kluge@gsi.de; url: http://www.gsi.de
[b] Universität Heidelberg, Physikalisches Institut, D-69120 Heidelberg, Germany
[c] Johannes Gutenberg-Universität Mainz, D-55099 Mainz, Germany
[d] Johann Wolfgang Goethe-Universität Frankfurt, D-60438 Frankfurt, Germany
[e] Atomic Physics, FYSIKUM, AlbaNova, Stockholm University, SE-106 91, Stockholm, Sweden
[f] Imperial College London, SW7 2AZ London, United Kingdom
☆ Dedicated to Ingvar Lindgren on the occasion of his 75th birthday

Advances in Quantum Chemistry, Vol. 53
ISSN 0065-3276, DOI:10.1016/S0065-3276(07)53007-8

Abstract An overview and status report of the new trapping facility for highly charged ions at the Gesellschaft für Schwerionenforschung is presented. The construction of this facility started in 2005 and is expected to be completed in 2008. Once operational, highly charged ions will be loaded from the experimental storage ring ESR into the HITRAP facility, where they are decelerated and cooled. The kinetic energy of the initially fast ions is reduced by more than fourteen orders of magnitude and their thermal energy is cooled to cryogenic temperatures. The cold ions are then delivered to a broad range of atomic physics experiments.

## 1. THE PRESENT GSI FACILITY

The UNILAC at the Gesellschaft für Schwerionenforschung (GSI) produced its first heavy-ion beam in 1975. Today, the current GSI facility can provide quasi-continuous or pulsed beams of ions with practically any charge state, ranging up to $U^{92+}$, with kinetic energies of several MeV or GeV per nucleon. Figure 7.1 shows schematically the present GSI accelerator facility. The ions are produced by Penning, electron cyclotron resonance (ECR) and metal vapour vacuum arc (MEVVA) ion sources, and are then accelerated by a linear accelerator (UNILAC), which is roughly 120 m long, to the first range of kinetic energies, i.e., up to several MeV/u. After the first acceleration stage, the ions can be delivered to a series of low-energy experiments. One example is SHIPTRAP, its name originating from the SHIP velocity filter that was used to discover six new elements: $^{264}_{107}$Bh (Bohrium, 1981), $^{269}_{108}$Hs (Hassium, 1984), $^{268}_{109}$Mt (Meitnerium, 1982), $^{271}_{110}$Ds (Darmstadtium, 1994), $^{272}_{111}$Rg (Röntgenium, 1994), and $^{277}_{112}$Uub (Ununbium, 1996). SHIPTRAP is used to perform high-precision mass measurements of trapped (unstable) radionuclides with a relative mass uncertainty of $\delta m/m \approx 10^{-8}$.

In the heavy-ion synchrotron SIS the ions are accelerated to kinetic energies of up to 2 GeV per nucleon for atomic and nuclear physics experiments as well as heavy-ion tumor therapy. When using highly charged ions, ultra-high vacuum (UHV) conditions are crucial in order to avoid charge changing collisions. In the UNILAC, where the ions' charge states are not yet very high, pressures of around $10^{-6}$ mbar are sufficient. However, in the heavy-ion synchrotron SIS (216 m circumference) and in the experimental storage ring ESR (108 m circumference), for which the charge states are increased by shooting the highly-energetic ions through a stripper foil, the pressure is in the $10^{-11}$ mbar regime.

## 2. THE HITRAP PROJECT

As can be seen from Figure 7.1, the new trapping facility, HITRAP, will be inserted into the re-injection channel between the ESR and the SIS. The new facility will broaden the current research field and open up several new ones, as indicated by the list in Figure 7.2. The combination of high charge states and very low kinetic

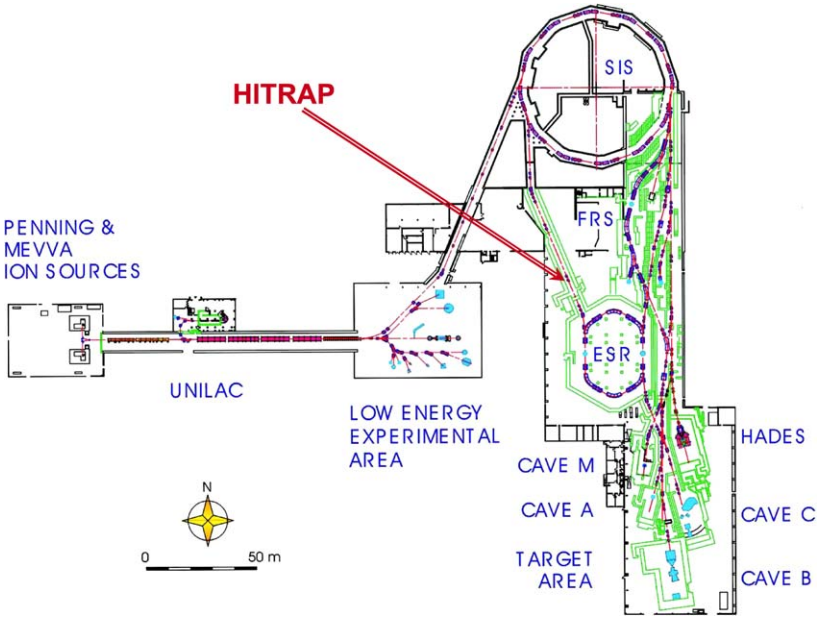


**FIGURE 7.1** The present GSI facility: highly charged ions are produced by a variety of different ion sources and accelerated by the linear accelerator (UNILAC) to several MeV/u. These fast ions can be used for low-energy experiments or can be injected into the heavy-ion synchrotron (SIS) where they are further accelerated. The SIS feeds the fragment separator (FRS), the experimental storage ring (ESR), or the fixed-target experiments in the different caves including that for heavy-ion tumor therapy. The HITRAP facility will be inserted into the re-injection channel, which can be used to feed the SIS with cooled highly charged ions from the ESR.

energies makes it possible to (re)trap the ions in Penning traps, where the ions themselves can be studied with high precision, or to collide them with gases and surfaces, in order to study their interaction with neutral matter [1].

In order to prepare the HITRAP facility itself as well as the different experimental set-ups to be used at the HITRAP facility with low-energy highly charged ions, the HITRAP RTD Network was created, which was funded from 2001 through 2005 by the European Union. Within this project, there were different teams (nine in total) from different countries, each team preparing an experiment (see Table 7.1), or providing theory. The goal of the HITRAP network was *the development of novel instrumentation for a broad spectrum of physics experiments with heavy highly charged ions (up to $U^{92+}$) at low energies (<1 eV/u)*. Within this project, instrumentation was developed for high-precision measurements of atomic and nuclear properties, mass and $g$-factor measurements, and ion–gas and ion–surface interaction studies.

The construction of the HITRAP facility, which is being carried out in close collaboration between the GSI Divisions for Infrastructure, Accelerators and Atomic Physics and the Institute for Applied Physics at the University of Frankfurt, started in the beginning of 2005 when appropriate funds were available. Commissioning

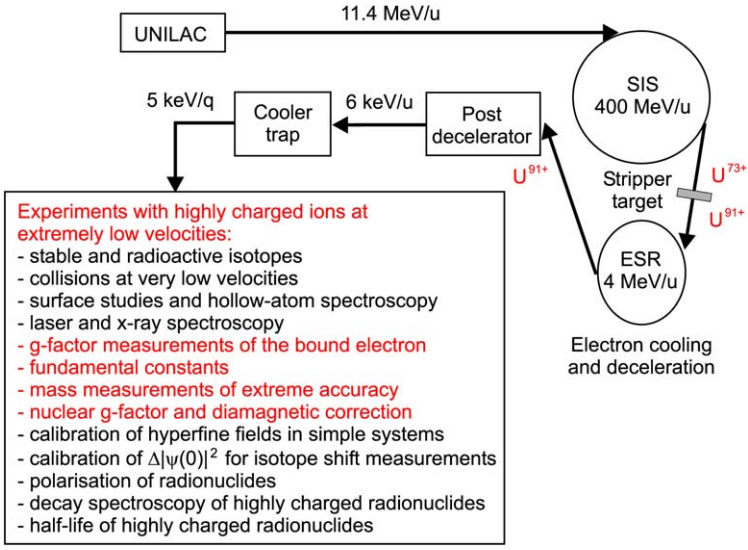


**FIGURE 7.2** Schematic of the HITRAP project: deceleration, trapping, and cooling of highly charged ions for a large variety of atomic physics experiments.

**TABLE 7.1** Participating teams in the HITRAP EU RTD Network (RIMS: Recoil Ion Momentum Spectroscopy, HFS: HyperFine Structure)

| Team | Leader | Task |
|---|---|---|
| Darmstadt, DE | H.-J. Kluge, O. Kester, W. Quint | HITRAP facility |
| Orsay, FR | J.-P. Grandin | RIMS (H1) |
| Groningen, NL | R. Morgenstern, R. Hoekstra | Ion–surface exp. (H2) |
| Mainz, DE | G. Werth, K. Blaum | *g*-Factor, mass (H4, H5) |
| Krakow, PL | A. Warczak | X-ray spectroscopy (H3) |
| Stockholm, SE | R. Schuch | Mass (H5) |
| Heidelberg, DE | J. Ullrich | RIMS (H1) |
| Vienna, AU | J. Burgdörfer | Theory (H2) |
| London, UK | R.C. Thompson | HFS (H6) |

of the HITRAP facility is planned for the first half of 2008 so that the experimental teams can start to perform their experiments in the second half of 2008.

## 3. THE HITRAP FACILITY

The new trapping facility is shown schematically in Figure 7.3. The highly charged ions are accelerated in the SIS to typically 400 MeV/u, almost completely stripped

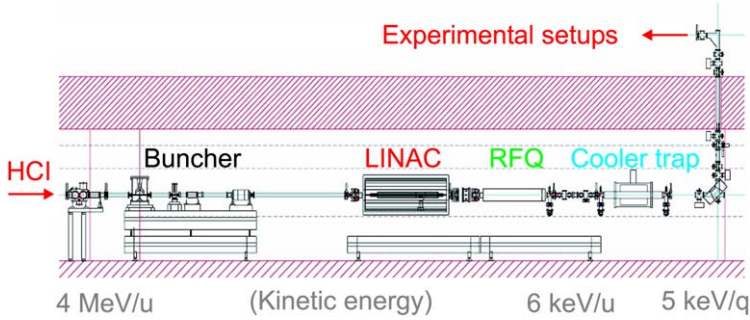


**FIGURE 7.3** Side view of the HITRAP facility. The highly charged ions come from the left and are decelerated by LINAC and RF quadrupole structures. They are injected at an energy of 6 keV/u into the Cooler Penning trap where they are trapped and cooled. After cooling to liquid-helium temperature they are ejected and transported with very low energies to the experiments on top of the platform.

and injected into the ESR. Here they are electron cooled as well as decelerated and a single bunch is created by bunch-merging. At an energy of 4 MeV/u, the ions are ejected out of the ESR as a bunch of about $10^5$ ions, with a pulse length of 1 µs (roughly 1 m long) and enter the linear decelerator of HITRAP. The facility is designed to operate in a pulsed mode, which means that this cycle (filling the ESR, cooling, deceleration and ejection) will be repeated every 10 s. Before the ion bunch enters the LINAC and the radiofrequency quadrupole (RFQ) structure, the ion pulse is reshaped by the buncher (Figure 7.3). After deceleration in the RFQ, the ions enter the Cooler (Penning) trap with only few a keV/u.

The Cooler trap operates in two steps for cooling the highly charged ions to liquid-helium temperature: electron cooling and resistive cooling. For the first step, there are sections with cold electrons that interact with the highly charged ions, thus dissipating the ions' kinetic energy. The electrons themselves cool by synchrotron radiation inside the cold bore of the superconducting magnet within a few seconds [2]. In the case of resistive cooling, the ions induce image charges in the trap electrodes. Connecting a frequency-resonant RLC-circuit to the trap electrodes allows for energy dissipation to this external cryogenic circuit. Resistive cooling is expected to take several seconds [3]. Finally, the trapped highly charged ions will have a thermal energy corresponding to slightly more than 4 K, due to noise in the electronic circuits. The cold ions are then transported, with kinetic energies of only a few keV/q, to the different setups installed on top of the re-injection channel as a high-quality ion beam.

A new platform was built inside the ESR experimental hall at GSI to house huts for electronics for the local control of the HITRAP facility and for the different HITRAP experiments and to provide space for the required infrastructure of the HITRAP facility such as supplies for radiofrequency, electricity and water. A hole was drilled through the concrete above the re-injection channel, which will be used for the beamline to transport the ions from the Cooler trap towards the setups. The construction of this platform is illustrated by the photo series in Figure 7.4.

**FIGURE 7.4** Photographs taken from the same position in the ESR Experimental Hall and showing the construction of the HITRAP platform. Left: situation in 2004 before construction. Middle: situation in 2005 when the platform was erected for the huts housing the electronics of the HITRAP facility and of the HITRAP experiments, for RF power supplies and other devices. Right panel: situation in 2006 when the platform is ready, the huts are in place, and the installations are almost completed.

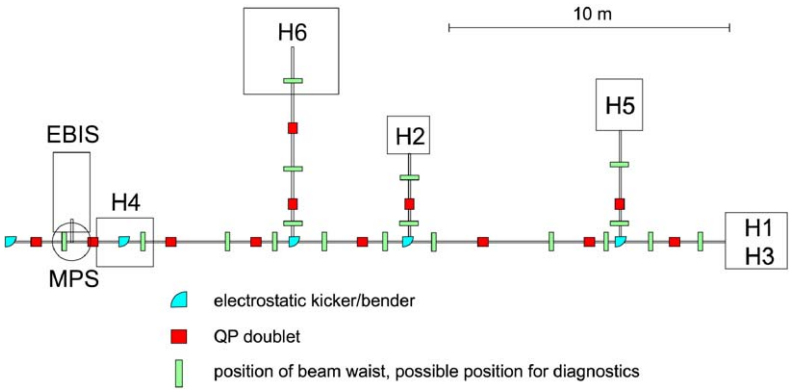


**FIGURE 7.5** Schematic overview of the beamline on the experimental platform. The experiments are indicated by the numbers H1–H6 (see Table 7.1). Beam transport calculations have been performed leading to the arrangement of ion optical elements as shown in the figure. The ion beam enters this section from below and travels from the extreme left-hand side to the right. The EBIS is an off-line ion source for tests of the systems, the MPS (multi-passage spectrometer) will feed the EBIS ion beam into the system when needed.

For the HITRAP experiments, a complete network of beamlines and ion optical elements needs to be developed and constructed. Calculations of these elements and the beam transport have been carried out showing that nearly 100% transmission is possible. A scheme of the current layout of the experiments is shown in Figure 7.5. Most of the ion optical elements are designed. The elements for bending the ion beam, the so-called kicker-benders, are under construction. The beamline towards the experiments needs to have a vacuum of the order of $10^{-11}$ mbar or better to avoid charge exchange with residual gas. This puts severe demands on the materials used for the construction of the ion optical elements almost approaching

**TABLE 7.2** The time schedule for the HITRAP project

| Action | Date |
|---|---|
| Preparation of infrastructure (safety, media supply, controls, RF) | Ongoing |
| Delivery of the Cooler trap magnet | Spring 2007 |
| Test of HITRAP low-energy beam transport and Cooler trap with EBIS | Mid 2007 |
| Installation of buncher cavities in the re-injection channel | Spring 2007 |
| First test of buncher cavities with beam from ESR | May 2007 |
| Installation of LINAC cavities | Fall 2007 |
| Commissioning of the LINAC | Spring 2008 |
| Commissioning of HITRAP first experiments | Spring 2008 |

those encountered when constructing an electrostatic UHV storage ring such as, e.g., ELISA in Aarhus, Denmark [4].

Because the HITRAP facility will not be able to continuously obtain the ESR beam for testing the Cooler trap and the experimental setups, it was decided to install an electron beam ion source (EBIS), which was available from the University of Frankfurt, on the platform for off-line tests. This source (MAXEBIS) is currently being tested and will be used to tune the low-energy beam line (LEBT) towards the Cooler trap, and for tests of the Cooler trap itself. Afterwards, the components will be moved to the HITRAP facility. A more complete overview of the time planning for the construction of the HITRAP facility is presented in Table 7.2.

## 4. EXPERIMENTS AT HITRAP

Since this publication is dedicated to Ingvar Lindgren on the occasion of his 75th birthday, out of the many experiments becoming possible (see inset of Figure 7.2), we discuss here only those which are very close to the heart of Ingvar Lindgren. These are the $g$-factor of the bound electron, the hyperfine structure, and the precision mass measurements. X-ray spectroscopy is discussed in a publication by Th. Stöhlker *et al.* in the same volume [5]. In all these experiments, quantum electrodynamics plays a dominant role, and the progress in atomic theory is essential.

### 4.1 The $g$-factor of the bound electron

The precise measurement of the $g$-factor of the electron bound in a hydrogen-like ion is a sensitive test of bound-state Quantum Electrodynamics (QED) at high fields. Highly charged ions are ideal for such studies, because the electromagnetic

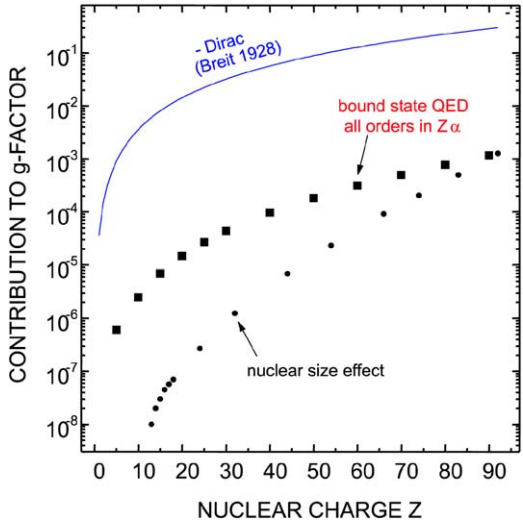


**FIGURE 7.6** Contributions to the *g*-factor versus nuclear charge *Z*. For heavy ions, the situation is more difficult, but also more interesting, since the QED and nuclear size contributions become comparable.

fields existing close to the nucleus are much higher than those which can be created artificially in a laboratory. For example, the electric field strength close to the nucleus of $U^{91+}$ is of the order of $10^{16}$ V/cm, which is higher than those created by the strongest lasers available. At such high electromagnetic fields, perturbative QED calculations are no longer accurate, and higher-order terms need to be evaluated carefully. Unfortunately, in this regime there is little or no experimental data to compare the non-perturbative codes to. This is precisely why *g*-factor experiments are important.

In relativistic Dirac theory, the *g*-factor of an electron bound to a H-like ion is given by [6,7]

$$g = \frac{2}{3}\left(1 + 2\sqrt{1 - (Z\alpha)^2}\right), \tag{1}$$

where $Z$ is the nuclear charge and $\alpha$ the fine structure constant. The ratio of the bound-electron ($g_{\mathrm{bound}}$) to the free-electron *g*-factor ($g_{\mathrm{free}}$) can be expressed, to leading order in $Z\alpha$, as

$$\frac{g_{\mathrm{bound}}}{g_{\mathrm{free}}} \approx 1 - \frac{1}{3}(Z\alpha)^2 + \frac{1}{4\pi}\alpha(Z\alpha)^2. \tag{2}$$

The first two terms in Eq. (2) are dominant and stem from Dirac theory, the third term comes from bound-state QED. Both contributions are indicated in Figure 7.6, and it can be seen that at high $Z$ the QED term is of the same order of magnitude as the nuclear size effects. From Eq. (1) it is clear that for $Z$ larger or equal to $\alpha^{-1}$, $g$ is undefined. Already when $Z \ll \alpha^{-1}$ is no longer valid, non-perturbative calcu-

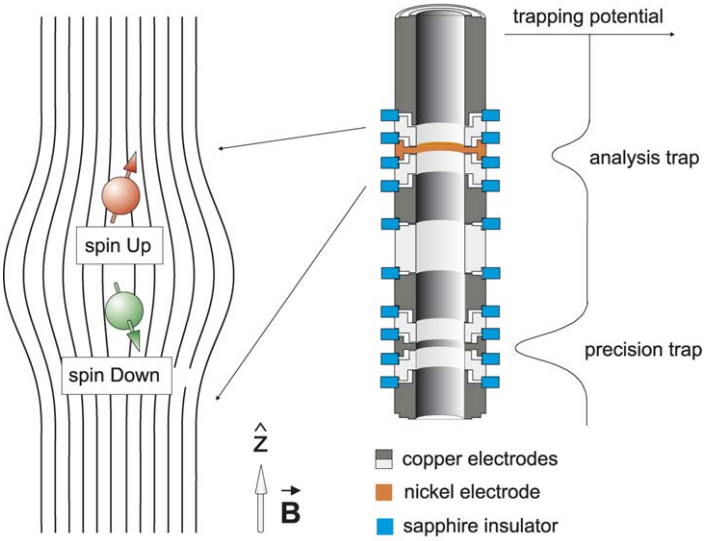


**FIGURE 7.7** Schematic of the double Penning trap setup used for $g$-factor measurements of the bound electron.

lations have to be performed [8,9]. Corresponding first calculations were initiated by I. Lindgren and G. Soff.

The $g$-factor of the bound electron in $^{12}C^{5+}$ [10] and $^{16}O^{7+}$ [11] has been obtained via spin-flip measurements of a single cold (4 K) ion. The setup was constructed in a GSI-Mainz collaboration, and consists of two Penning traps [12], i.e., a 'precision trap' and an 'analysis trap,' placed in one superconducting magnet. A schematic of the trap is shown in Figure 7.7. The $g$-factor can be obtained from measurements of the cyclotron frequency $\omega_c = qB/M_i$ and the Larmor frequency $\omega_L = geB/(2m_e)$, since it can be expressed as

$$g = 2\left(\frac{q}{e}\right)\left(\frac{m_e}{M_i}\right)\left(\frac{\omega_L^e}{\omega_c^i}\right), \tag{3}$$

where $m_e, e$ and $M_i, q$, are the mass and charge of the electron and the ion, respectively. Using high-quality resonant circuits, the oscillation frequencies of an ion inside a Penning trap can be measured independently and with high accuracy. For these measurements, the polarisation of the electron spin is 100%, because only one ion is used. The cyclotron frequency $\omega_c$ is determined inside the precision trap, and a spin–flip may be induced by microwave irradiation at a frequency close to the Larmor frequency $\omega_L$. Detection of a spin–flip takes place after transporting the ion to the analysis trap. Here, a significant inhomogeneity of the magnetic field, produced by a nickel ring, makes the $z$-motion of the ion sensitive to the spin direction. The frequency of the $z$-motion is detected via electronic detection (based on image charges). After analysing the spin direction, the ion is transported back to the precision trap for the next measurement cycle.

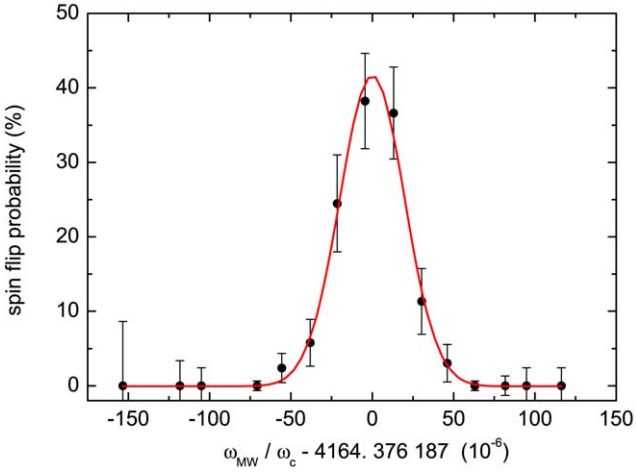


**FIGURE 7.8** Larmor resonance of the *g*-factor measurement of the bound electron in $^{12}C^{5+}$ [10].

The experimental result obtained for a *g*-factor measurement of a single $^{12}C^{5+}$ ion is presented in Figure 7.8. The horizontal axis shows the ratio of the microwave frequency $\omega_{MW}$ to the cyclotron frequency $\omega_c$, from which the *g*-factor of the bound electron can be obtained. The experimental *g*-factors of the hydrogen-like ions $^{12}C^{5+}$ [10] and $^{16}O^{7+}$ [11] agree within the uncertainties, which are dominated by the accuracy of the electron mass, with the calculated values [7,13]. The *g*-factor of the 1s electron thus enabled a test of bound-state QED at a level of 0.25%.

Accurate *g*-factor measurements also provide means to obtain better values for fundamental constants, such as the fine structure constant $\alpha$ (Figure 7.9). For example, because of the good agreement with theory, the *g*-factor data led to a determination of the electron mass with a four times higher accuracy [14]. The relative experimental accuracy $\delta m/m$ of this measurement was as good as $6 \times 10^{-10}$.

From Eq. (1) it can be seen that the *g*-factor is linked to $\alpha$, and it can easily be shown that the relative uncertainty in $\alpha$ is correlated to that in *g* via

$$\frac{\delta\alpha}{\alpha} \propto \frac{1}{(Z\alpha)^2}\frac{\delta g}{g}. \tag{4}$$

It is therefore most interesting to measure *g* at the highest possible *Z*. Succeeding the measurements in $^{12}C^{5+}$ [10] and $^{16}O^{7+}$ [11], a measurement of the electronic *g*-factor in $^{40}Ca^{19+}$ [15] is currently being prepared. When HITRAP is operational, similar experiments on heavy systems like $^{238}U^{91+}$ will be performed. It is expected that, from such a measurement, $\alpha$ (Figure 7.9) can be obtained with an accuracy of $10^{-8}$ [16]. A combination of such measurements in H-like and B-like heavy ions can increase this accuracy significantly [17].

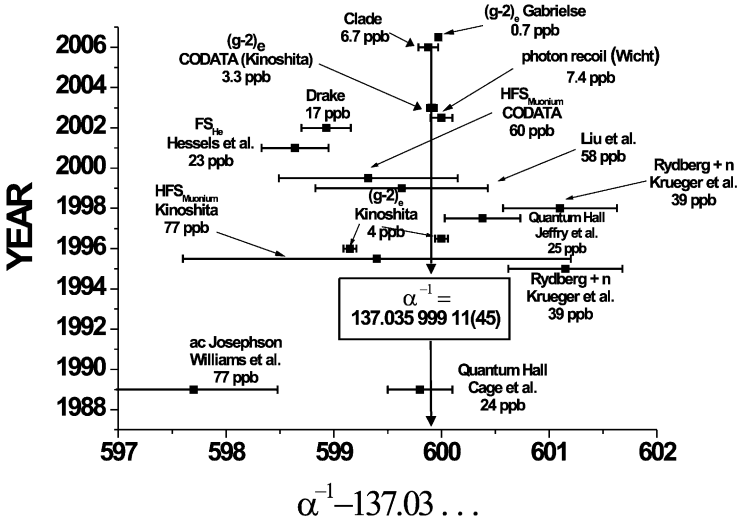


**FIGURE 7.9** Landscape of the fine structure constant $\alpha$: the evolution of the different measurements and their accuracies during the last 20 years is indicated.

## 4.2 Precision mass measurements

Masses of stable or radioactive nuclides can be measured with very high accuracy and single-ion sensitivity, using Penning traps [18,19]. Since the cyclotron frequency of a trapped ion increases with the charge state, highly charged ions provide better resolution and potentially also higher accuracy than singly charged ions. The SMILETRAP group in Stockholm has pioneered the use of highly charged ions in ion traps for mass spectrometry [20–22]. They measured the masses of several ions, which are important for tests of QED or double-beta decay, with an uncertainty close to $10^{-10}$. Using the mass of $^{12}C^{6+}$, Van Dyck *et al.* [23] in Seattle measured the masses of stable singly charged ions with an accuracy of about $10^{-10}$. A similar accuracy was obtained for the proton–antiproton comparison at CERN, measured by the group of Gabrielse [24]. Pritchard *et al.* [25] at MIT even had a mass spectrometer, which is now at Florida State University [26], with an accuracy of about $10^{-11}$. The masses of singly charged radionuclides have been measured with an accuracy of $10^{-7}$ to $10^{-8}$ and better, by Penning trap mass spectrometers installed at ISOLDE/CERN [27,28], Argonne [29], Jyväskylä [30], Michigan State University (MSU) [31], and GSI [32]. Highly charged ions for mass spectrometry will be used at TITAN at ISAC/TRIUMF, Vancouver [33], LEBIT/MSU [34], HITRAP/GSI [35], ISOLTRAP/ISOLDE [36], MAFFTRAP/Munich [37], and at MATS/GSI [19].

Table 7.3 shows a comparison between a mass measurement in a Penning trap with a singly charged ion, and one with a highly charged ion. The numbers show that, for the same isotope, an ion with a charge of $q = 50$ already leads to an improved mass resolution of nearly two orders of magnitude. Longer observation times (for example, $T_{obs} \geqslant 10$ s) and higher charge states (i.e., $q = 92$ for uranium)

**TABLE 7.3** Comparison of the accuracy of mass measurements for a singly and a highly charged ion with mass $A = 100$ in a magnetic field of $B = 6$ T. $\nu_c$ is the cyclotron frequency, $T_{obs}$ the observation time of a measurement, $R$ is the resolving power given by the ratio $\nu_c/\delta\nu_c$, and $\delta m/m$ is the relative mass uncertainty

| Singly charged ion | |
|---|---|
| $q = 1$ | $\nu_c = 1$ MHz |
| $T_{obs} = 1$ s | $\delta\nu_c = 1$ Hz |
| $R = 10^6$ | $\delta m/m \approx 10^{-8}$ |
| **Highly charged ion** | |
| $q = 50$ | $\nu_c = 50$ MHz |
| $T_{obs} = 1$ s | $\delta\nu_c = 1$ Hz |
| $R = 5 \times 10^7$ | $\delta m/m \approx 2 \times 10^{-10}$ |

can further improve the mass resolution. In principle, a mass measurement accuracy of $10^{-11}$ or better can be reached. This would, for example, make it possible to 'weigh' the 1s Lamb shift in $U^{91+}$ with an accuracy better than presently possible by X-ray spectroscopy [38].

## 4.3 Laser spectroscopy of hyperfine structure

An experiment is being prepared to perform laser spectroscopy of ground state hyperfine structure in highly charged ions [39]. Normally, the hyperfine splitting wavelength in atoms and ions is in the microwave region. However, since the hyperfine splitting of hydrogen-like ions scales with the nuclear charge as $Z^3$, the hyperfine structure becomes measurable by laser spectroscopy above $Z \approx 60$. This allows for accurate laser spectroscopy measurements of these hyperfine splittings and, in turn, for sensitive tests of corresponding calculations of transition energies and lifetimes. Previous measurements were carried out for $^{209}Bi^{82+}$ [40], $^{165}Ho^{66+}$ [41], $^{185,187}Re^{74+}$ [42], $^{207}Pb^{81+}$ [43], $^{209}Bi^{80+}$ [44] and $^{203,205}Tl^{80+}$ [45]. These measurements suffered from the Doppler width and shift of the transition, which were due to the relativistic velocities and velocity spreads of the ions in the ESR. In the case of the measurements conducted in the EBIT (electron beam ion trap) at Livermore, resonance transitions were broadened due to the high temperatures of the ions in the EBIT. The new experiments will be performed in a Penning trap with confined and cold highly charged ions at cryogenic temperatures. This strongly reduces the Doppler effects and will lead to a measurement resolution of the order of $10^{-7}$. Hence, these results will allow the determination of hyperfine anomalies which requires high precision. The trapped ions will be laser-excited along the trap axis, and fluorescence detection will take place perpendicular to the trap axis, through the transparent ring electrode (see Figure 7.10). Furthermore, by use of a rotating wall technique [46], which radially compresses the ion cloud via a rotating dipole field applied to the segmented ring electrode, a high ion number

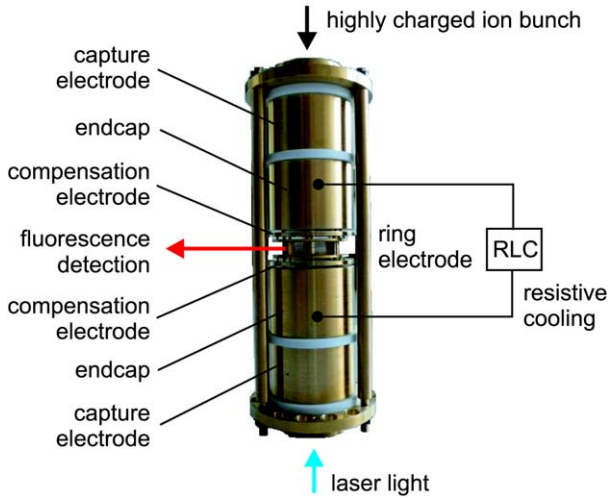


**FIGURE 7.10** Photograph of the spectroscopy trap, which will be used for laser spectroscopy measurements of hyperfine splittings in highly charged ions. The ring electrode is split into four segments, which are covered by highly transparent mesh.

density can be obtained. Together with the localisation, this enhances the intensity of the measured fluorescence. For an ion cloud of $10^5$ highly charged ions at the space charge limit of the trap, we calculated fluorescence rates of several thousand counts per second on a background of a few hundred counts per second ($S/N \approx 50$) [47]. Laser intensities of several tens of $W/m^2$ are required to saturate the 10 $mm^2$ ion cloud, which implies moderate laser powers of just a few mW [39].

Furthermore, measurements of hyperfine structure in H- and Li-like ions can test quantum electrodynamics (QED) at high electromagnetic fields [48]. Such accurate measurements can be compared to corresponding calculations that include nuclear effects, such as the Bohr–Weisskopf and Breit–Schawlow effects, as well as (higher-order) QED effects. From a comparison of the hyperfine splitting in H- and Li-like ions of the same isotope, the nuclear effects cancel to a large extent, thus enabling a stringent test of the QED effects [48]. The necessary experimental resolution for such a comparison is of the order of $10^{-6}$, which can relatively easily be met by laser spectroscopy [49].

## 5. THE NEW GSI FACILITY

In the more distant future, HITRAP will be a component of the new international Facility for Antiproton and Ion Research (FAIR) [50]. HITRAP will thus, in addition to highly charged and radioactive ions, also produce low-energy antiprotons. Furthermore, the FAIR facility will provide the highest intensities of both stable and radioactive ion beams with energies up to 34 GeV per nucleon. At such energies, the highly charged ions generate electric and magnetic fields of exceptional

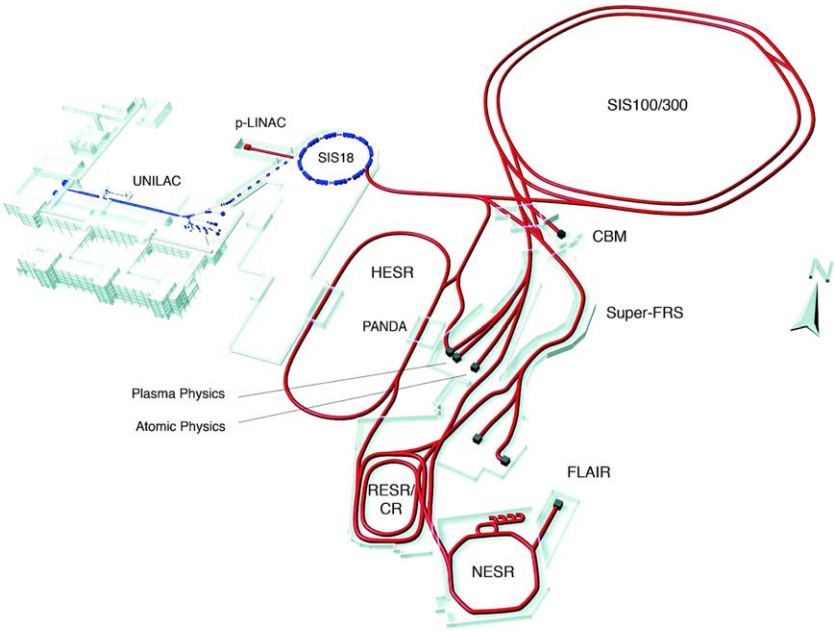


**FIGURE 7.11** The future GSI facility FAIR (Facility for Antiproton and Ion Research) in Darmstadt.

strength and ultra-short duration. The general layout of FAIR is shown in Figure 7.11.

## 5.1 Stored Particle Atomic Research Collaboration (SPARC)

The new FAIR facility has key features that offer a range of new opportunities in atomic physics research and related fields, which will be exploited by the Stored Particle Atomic Research Collaboration (SPARC) [51]. In particular, the Superconducting Fragment Separator (SFRS) will provide a rich spectrum of radionuclides. The high intensity of secondary beams produced at the SFRS will make it possible to extract decelerated radioactive ion beams from the New Experimental Storage Ring (NESR) and to decelerate them for trap experiments with sufficient intensity at HITRAP. Therefore, the physics program of HITRAP can be extended to novel experiments with trapped radioactive ions and, of course, with trapped antiprotons. Trapped radioactive ions in high charge states may reveal a completely new domain for fundamental interaction studies and for experiments on the borderline between atomic and nuclear physics.

Moreover, the manipulation of trapped radioactive ions with laser light opens up possibilities to study questions of the Standard Model. By optical pumping within the hyperfine levels of the ground state, the nuclear spins of radioactive nuclides can be polarised with high efficiency. The detection of the asymmetry of beta decay, for example, will allow one to explore deviations from the vector/axial-

vector (VA)-structure of the weak interaction and to set limits for the masses of heavy bosons, which are not included in the Standard Model.

Direct mass measurements on unstable nuclides with ultra-high accuracy (up to $\delta m/m \approx 10^{-11}$) will also be possible. Such an accuracy would allow one to determine the binding energy of $U^{91+}$ with an accuracy of $\delta mc^2 \approx 2$ eV. If the QED calculations are found to be correct, nuclear charge radii of unstable nuclides can be determined.

For a general exploration of masses in the chart of nuclei, a mass resolution of $\delta m/m \approx 10^{-6}$ to $10^{-7}$ is sufficient. This is also planned by isochronous or Schottky mass spectrometry experiments at the New Experimental Storage Ring (NESR). However, in some cases, like double-beta decay or tests of the unitarity of the Cabibbo–Kobayashi–Maskawa matrix, a much higher accuracy is required, which is possible by using trapped highly charged ions at HITRAP [35] and at MATS, dedicated to precision mass measurements on very short lived nuclei [19].

## 5.2 Facility for Low-Energy Antiproton and Ion Research (FLAIR)

The planned FLAIR facility will be the most intense source of low-energy antiprotons world-wide [52]. The beam intensity of extracted low-energy antiprotons will be two orders of magnitude higher than that of the Antiproton Decelerator (AD) at CERN. We therefore anticipate that experiments with trapped antiprotons, which are currently impossible anywhere else (due to insufficient intensities), will be performed at the FLAIR facility. A possible highlight in the field of low-energy antimatter research would be the first direct experimental investigation of the gravitational interaction of antimatter, which has never been attempted up to now. Such investigations could be performed on ultra-cold antihydrogen atoms [53] which are produced by recombining trapped antiprotons with positrons in a so-called nested Penning trap. The effect of gravity on antimatter is an important issue for the development of quantum theories of gravity.

## ACKNOWLEDGEMENTS

We acknowledge support by the European Union, the German Ministry for Education and Research (BMBF) and the Helmholtz Association (HGF).

## REFERENCES

[1] T. Beier, *et al.*, *Nucl. Instrum. Methods Phys. Res. B* **235** (2005) 473.
[2] J. Bernard, *et al.*, *Nucl. Instrum. Methods Phys. Res. A* **532** (2004) 224.
[3] G. Maero, private communication.
[4] S.P. Møller, *Nucl. Instrum. Methods Phys. Res. A* **394** (1997) 281.
[5] T. Stöhlker, *et al.*, in: S. Salomonson, E. Lindroth (Eds.), *Advances in Quantum Chemistry, vol. 53*, Elsevier, Amsterdam, 2007, pp. 57–65.
[6] G. Breit, *Nature* **122** (1928) 649.
[7] T. Beier, *Phys. Rep.* **339** (2000) 79.
[8] S.A. Blundell, *et al.*, *Phys. Rev. A* **55** (1997) 1857.

[9] H. Persson, *et al.*, *Phys. Rev. A* **56** (1997) R2499.
[10] H. Häffner, *et al.*, *Phys. Rev. Lett.* **85** (2000) 5308.
[11] J. Verdú, *et al.*, *Phys. Rev. Lett.* **92** (2004) 093002.
[12] H. Häffner, *et al.*, *Eur. Phys. J. D* **22** (2003) 163.
[13] T. Beier, *et al.*, *Phys. Rev. A* **62** (2000) 032510.
[14] T. Beier, *et al.*, *Phys. Rev. Lett.* **88** (2002) 011603.
[15] M. Vogel, *et al.*, *Nucl. Instum. Methods B* **235** (2005) 7.
[16] V.M. Shabaev, V.A. Yerokhin, *Phys. Rev. Lett.* **88** (2002) 091801.
[17] V.M. Shabaev, *et al.*, *Phys. Rev. Lett.* **96** (2006) 253002.
[18] D. Lunney, *et al.*, *Rev. Mod. Phys.* **75** (2003) 1021.
[19] K. Blaum, *Phys. Rep.* **425** (2006) 1.
[20] R. Jertz, *et al.*, *Z. Phys. D* **21** (1991) S179.
[21] T. Fritioff, *et al.*, *Int. J. Mass Spectrom.* **251** (2006) 281.
[22] S. Nagy, *et al.*, *Phys. Rev. Lett.* **96** (2006) 163004.
[23] R.S. Van Dyck Jr., *et al.*, *Int. J. Mass Spectrom.* **251** (2006) 231.
[24] G. Gabrielse, *Int. J. Mass Spectrom.* **251** (2006) 273.
[25] J.K. Thompson, *et al.*, *Nature* **430** (2004) 58.
[26] M. Redshaw, *et al.*, *Int. J. Mass Spectrom.* **251** (2006) 125.
[27] F. Herfurth, *et al.*, *Phys. Rev. Lett.* **87** (2001) 142051.
[28] M. Mukherjee, *et al.*, *Phys. Rev. Lett.* **93** (2004) 150801.
[29] G. Savard, *et al.*, *Int. J. Mass Spectrom.* **251** (2006) 252.
[30] T. Eronen, *et al.*, *Phys. Lett. B* **636** (2006) 191.
[31] G. Bollen, *et al.*, *Phys. Rev. Lett.* **96** (2006) 152501.
[32] C. Rauth, *et al.*, *Phys. Rev. Lett.* (2006), submitted.
[33] J. Dilling, *et al.*, *Int. J. Mass Spectrom.* **251** (2006) 198.
[34] G. Bollen, private communication (2006).
[35] F. Herfurth, *et al.*, *Int. J. Mass Spectrom.* **251** (2006) 266.
[36] A. Herlert, *et al.*, *Int. J. Mass Spectrom.* **251** (2006) 131.
[37] D. Habs, private communication (2006).
[38] A. Gumberidze, *et al.*, *Phys. Rev. Lett.* **94** (2005) 223001.
[39] M. Vogel, *et al.*, *Rev. Sci. Instrum.* **76** (2005) 103102.
[40] I. Klaft, *et al.*, *Phys. Rev. Lett.* **73** (1994) 2425.
[41] J.R. Crespo López-Urrutia, *et al.*, *Phys. Rev. Lett.* **77** (1996) 826.
[42] J.R. Crespo López-Urrutia, *et al.*, *Phys. Rev. A* **57** (1998) 879.
[43] P. Seelig, *et al.*, *Phys. Rev. Lett.* **81** (1998) 4824.
[44] P. Beiersdorfer, *et al.*, *Phys. Rev. Lett.* **80** (1998) 3022.
[45] P. Beiersdorfer, *et al.*, *Phys. Rev. A* **64** (2001) 032506.
[46] W.M. Itano, *et al.*, *Science* **279** (1998) 686.
[47] D.F.A. Winters, *et al.*, *Nucl. Instrum. Methods Phys. Res. B* **235** (2005) 201.
[48] V.M. Shabaev, *et al.*, *Phys. Rev. Lett.* **86** (2001) 3959.
[49] D.F.A. Winters, *et al.*, *Can. J. Phys.* **85** (2007) 403.
[50] *An International Accelerator Facility for Beams of Ions and Antiprotons*, Conceptual Design Report, November 2001, http://www.gsi.de/fair/overview/info/index_e.html.
[51] T. Stöhlker, *et al.*, *Nucl. Instrum. Methods B* **235** (2005) 494.
[52] E. Widmann, *Phys. Scr.* **72** (2005) C51–C56.
[53] J. Walz, T.W. Hänsch, *Gen. Rel. Grav.* **36** (2004) 561.

CHAPTER 8

# Structure of Vacuum and Elementary Matter: From Superheavies via Hypermatter to Antimatter—The Vacuum Decay in Supercritical Fields☆

**Walter Greiner***

Contents



* Frankfurt Institute for Advanced Studies, Johann Wolfgang Goethe University, Max-von-Laue-Str. 1, 60438 Frankfurt am Main, Germany

☆ Dedicated to Ingvar Lindgren, great physicist and friend, on occasion of his 75th birthday

Advances in Quantum Chemistry, Vol. 53
ISSN 0065-3276, DOI:10.1016/S0065-3276(07)53008-X

Abstract The extension of the periodic system into various new areas is investigated. Experiments for the synthesis of superheavy elements and the predictions of magic numbers are reviewed. Different ways of nuclear decay are discussed like cluster radioactivity, cold fission and cold multifragmentation, including the recent discovery of the triple fission of $^{252}$Cf. Furtheron, investigations on hypernuclei and the possible production of antimatter-clusters in heavy-ion collisions are reported. Various versions of the meson field theory serve as effective field theories at the basis of modern nuclear structure and suggest structure in the vacuum which might be important for the production of hyper- and antimatter. I also discuss the possibility of producing a new kind of nuclear systems by putting a few antibaryons inside ordinary nuclei. This leads to surprising results: in particular to cold compression of nuclear matter—in contrast to hot compression via nuclear shock waves (Rankine–Hugoniot). Also the basics of the decay of the vacuum in supercritical Coulomb fields is reminded. Connected with that is the time delay in giant nuclear systems like U + Cm, etc. The last chapters are devoted to these questions. A perspective for future research is given.

## 1. INTRODUCTION

There are fundamental questions in science, like, e.g., "how did life emerge" or "how does our brain work" and others. However, the most fundamental of those questions is "how did the world originate?" The material world has to exist before life and thinking can develop. Of particular importance are the substances themselves, i.e., the particles the elements are made of (baryons, mesons, quarks, gluons), i.e., elementary matter. The vacuum and its structure is closely related to that. On this I want to report today. I begin with the discussion of modern issues in nuclear physics. The elements existing in nature are ordered according to their atomic (chemical) properties in the *periodic system* which was developed by Mendeleev and Lothar Meyer. The heaviest element of natural origin is uranium. Its nucleus is composed of $Z = 92$ protons and a certain number of neutrons ($N = 128$–$150$). They are called the different uranium isotopes. The transuranium elements reach from neptunium ($Z = 93$) via californium ($Z = 98$) and fermium ($Z = 100$) up to lawrencium ($Z = 103$). The heavier the elements are, the larger are their radii and their number of protons. Thus, the Coulomb repulsion in their interior increases, and they undergo fission. In other words: the transuranium elements become more instable as they get bigger.

In the late sixties the dream of the superheavy elements arose. Theoretical nuclear physicists around S.G. Nilsson (Lund) [1] and from the Frankfurt school [2–4] predicted that so-called closed proton and neutron shells should counteract the repelling Coulomb forces. Atomic nuclei with these special *"magic" proton and neutron numbers* and their neighbors could again be rather stable. These magic proton ($Z$) and neutron ($N$) numbers were thought to be $Z = 114$ and $N = 184$ or 196. Typical predictions of their life times varied between seconds and many thousand years. Figure 8.1 summarizes the expectations at the time. One can see the islands

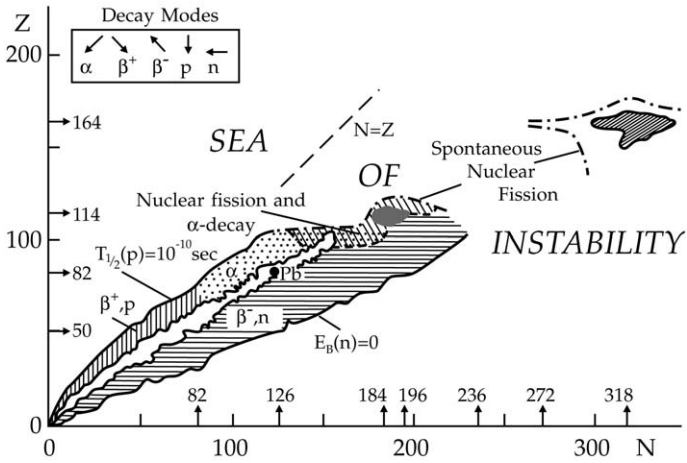


**FIGURE 8.1** The periodic system of elements as conceived by the Frankfurt school in the late sixties. The islands of superheavy elements ($Z = 114$, $N = 184, 196$ and $Z = 164$, $N = 318$) are shown as dark hatched areas.

of superheavy elements around $Z = 114$, $N = 184$ and 196, respectively, and the one around $Z = 164$, $N = 318$.

## 2. COLD VALLEYS IN THE POTENTIAL

The important question was how to produce these superheavy nuclei. There were many attempts, but only little progress was made. It was not until the middle of the seventies that the Frankfurt school of theoretical physics together with foreign guests (R.K. Gupta (India), A. Sandulescu (Romania)) [5] theoretically understood and substantiated the concept of bombarding of double magic lead nuclei with suitable projectiles, which had been proposed intuitively by the Russian nuclear physicist Y. Oganessian [6]. The two-center shell model, which is essential for the description of fission, fusion and nuclear molecules, was developed in 1969–1972 together with my then students U. Mosel and J. Maruhn [7]. It showed that the shell structure of the two final fragments was visible far beyond the barrier into the fusioning nucleus. The collective potential energy surfaces of heavy nuclei, as they were calculated in the framework of the two-center shell model, exhibit pronounced valleys, such that these valleys provide promising doorways to the fusion of superheavy nuclei for certain projectile–target combinations (Figure 8.3). If projectile and target approach each other through those *"cold" valleys*, they get only minimally excited and the barrier which has to be overcome (fusion barrier) is lowest (as compared to neighboring projectile–target combinations). In this way the correct projectile- and target-combinations for fusion were predicted. Indeed, Gottfried Münzenberg and Sigurd Hofmann and their group at GSI [8] have followed this approach. With the help of the SHIP mass-separator and the position

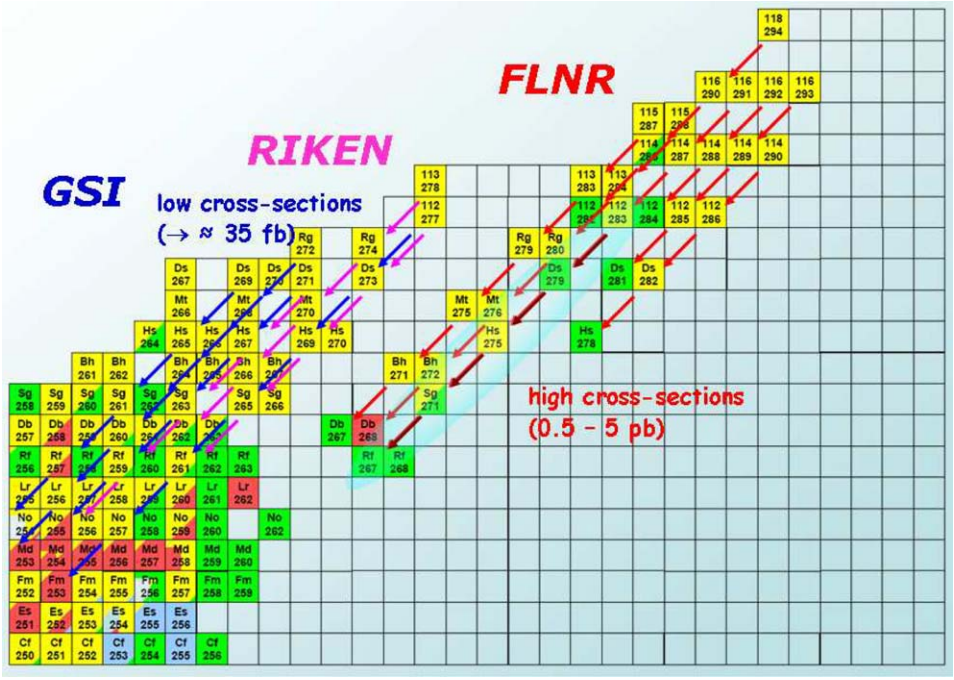


**FIGURE 8.2** The $Z = 106$–$112$ isotopes were fused by the Hofmann–Münzenberg (GSI) group. The $Z = 114$ isotopes were produced by the Dubna–Livermore group under the leadership of Y. Oganessian. It is claimed that three neutrons are evaporated. This indicates more energy loss in the fusion process. Therefore one speaks of "hot" fusion, even though less pronounced valleys for deformed spherical nuclear encounter are possible [9]. Some key elements in these FLNR-discoveries have recently been confirmed by the GSI-group [72]. Obviously the lifetimes of the various decay products are rather long (because they are closer to the stable valley), in crude agreement with early predictions [3,4] and in excellent agreement with the recent calculations of the Sobicevsky group [11]. For a colour reproduction of this figure see the colour plate section, near the end of this book.

sensitive detectors, which were especially developed by them, they produced the pre-superheavy elements $Z = 106, 107, \ldots, 112$, each of them with the theoretically predicted projectile–target combinations, and only with these. Everything else failed. This is an impressing success, which crowned the laborious construction work of many years. The before last example of this success, the discovery of element 112 and its long $\alpha$-decay chain, is shown in Figure 8.5. Very recently the Dubna–Livermore group produced two isotopes of $Z = 114$ element by bombarding $^{244}$Pu with $^{48}$Ca (Figure 8.2). Also this is a cold-valley reaction (in this case due to the combination of a spherical and a deformed nucleus), as predicted by Gupta, Sandulescu and Greiner [9] in 1977. There exist also cold valleys for which both fragments are deformed [10], but these have yet not been verified experimentally.

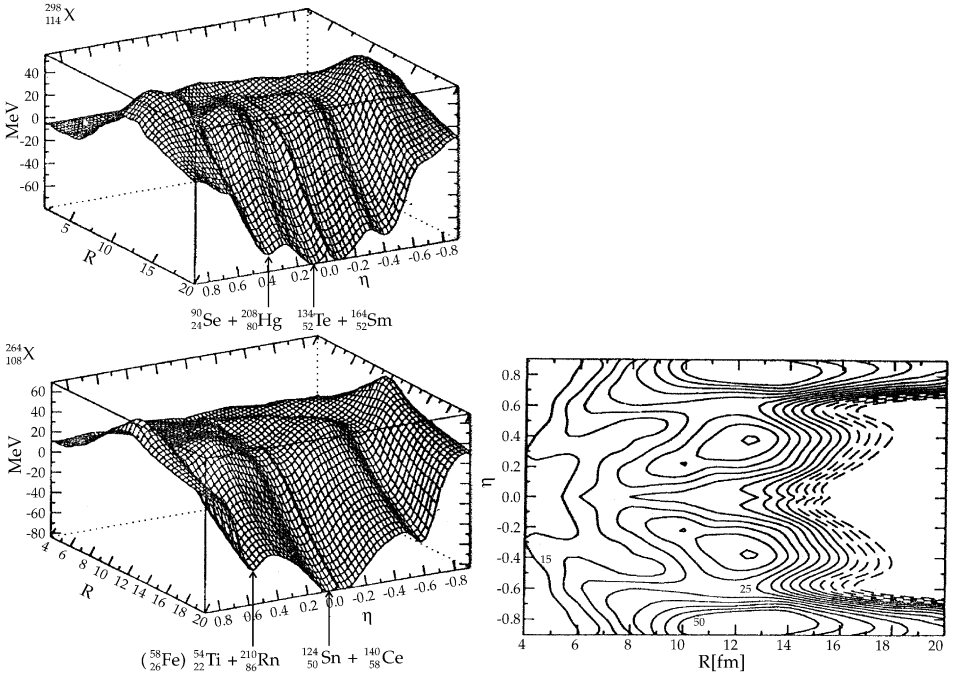


**FIGURE 8.3** The collective potential energy surface of $^{264}108$ and $^{298}114$, calculated within the two-center shell model by J. Maruhn *et al.*, shows clearly the cold valleys which reach up to the barrier and beyond. Here $R$ is the distance between the fragments and $\eta = \frac{A_1 - A_2}{A_1 + A_2}$ denotes the mass asymmetry: $\eta = 0$ corresponds to a symmetric, $\eta = \pm 1$ to an extremely asymmetric division of the nucleus into projectile and target. If projectile and target approach through a cold valley, they do not "constantly slide off" as it would be the case if they approach along the slopes at the sides of the valley. Constant sliding causes heating, so that the compound nucleus heats up and gets unstable. In the cold valley, on the other hand, the created heat is minimized. The colleagues from Freiburg should be familiar with that: they approach Titisee (in the Black Forest) most elegantly through the Höllental and not by climbing its slopes along the sides.

## 3. SHELL STRUCTURE IN THE SUPERHEAVY REGION

Studies of the shell structure of superheavy elements in the framework of the meson field theory and the Skyrme–Hartree–Fock approach have recently shown that the magic shells in the superheavy region are very isotope dependent [12] (see Figure 8.6). *According to these investigations* $Z = 120$ *being a magic proton number seems to be as probable as* $Z = 114$. Additionally, recent investigations in a chirally symmetric mean-field theory (see also below) result also in the prediction of these two magic numbers [13,14]. The corresponding magic neutron numbers are predicted to be $N = 172$ and—as it seems to a lesser extend—$N = 184$. Thus, this region provides an open field of research. R.A. Gherghescu *et al.* have calculated the potential energy surface of the $Z = 120$ nucleus. It utilizes interesting isomeric and valley structures (Figure 8.7). The charge distribution of

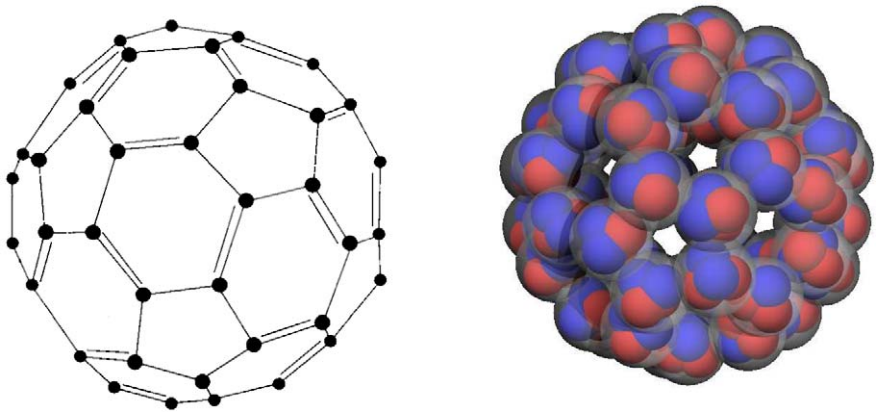

**FIGURE 8.4** Typical structure of the fullerene $^{60}$C. The double bindings are illustrated by double lines. In the nuclear case the Carbon atoms are replaced by $\alpha$ particles and the double bindings by the additional neutrons. Such a structure would immediately explain the semi-hollowness of that superheavy nucleus, which is revealed in the mean-field calculations within meson-field theories. For a colour reproduction of this figure see the colour plate section, near the end of this book.

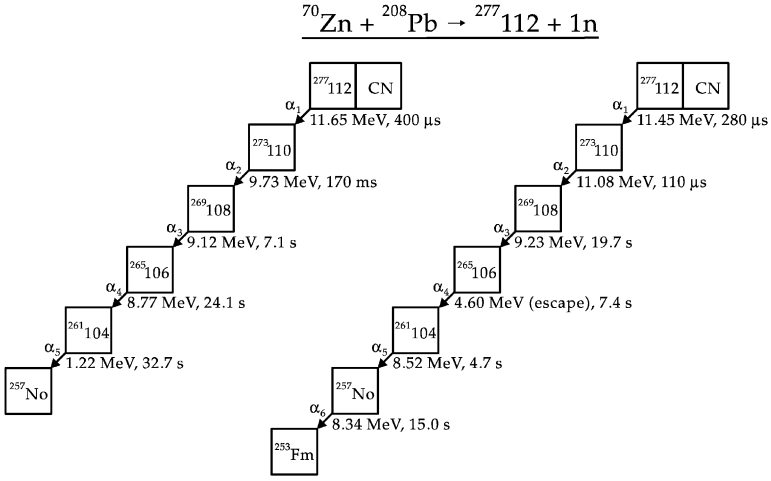


**FIGURE 8.5** The fusion of element 112 with $^{70}$Zn as projectile and $^{208}$Pb as target nucleus has been accomplished for the first time in 1995/96 by S. Hofmann, G. Münzenberg and their collaborators.

the $Z = 120$, $N = 184$ nucleus indicates a hollow inside. This leads us to suggest that it might be essentially a fullerene consisting of 60 $\alpha$-particles and one additional binding neutron per alpha. This is illustrated in Figure 8.4. The protons and neutrons of such a superheavy nucleus are distributed over 60 $\alpha$ particles and 60 neutrons (forgetting the last 4 neutrons). The determination of the chemistry of superheavy elements, i.e., the calculation of the atomic structure—

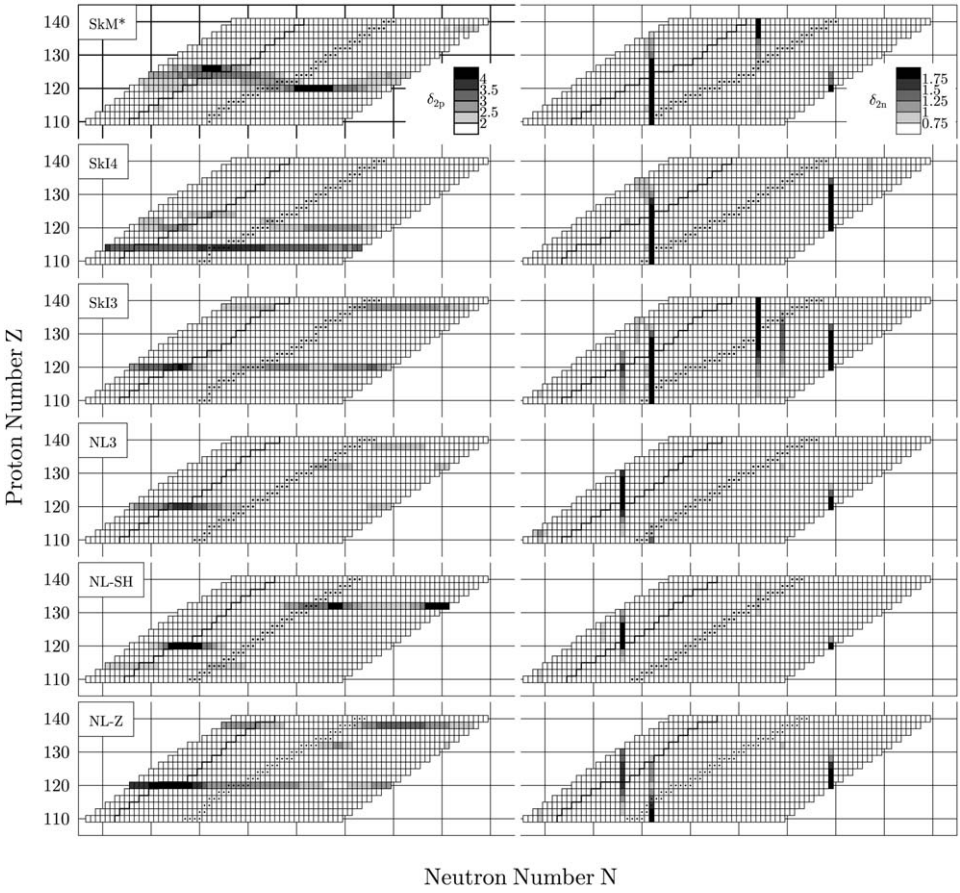


**FIGURE 8.6** Grey scale plots of proton gaps (left column) and neutron gaps (right column) in the $N$–$Z$ plane for spherical calculations with the forces as indicated. The assignment of scales differs for protons and neutrons, see the uppermost boxes where the scales are indicated in units of MeV. Nuclei that are stable with respect to $\beta$ decay and the two-proton dripline are emphasized. The forces with parameter sets SkI4 and NL–Z reproduce the binding energy of $^{264}_{156}108$ (Hassium) best, i.e. $|\delta E/E| < 0.0024$. Thus one might assume that these parameter sets could give the best predictions for the superheavies. Nevertheless, it is noticed that NL–Z predicts only $Z = 120$ as a magic number while SkI4 predicts both $Z = 114$ and $Z = 120$ as magic numbers. The magicity depends—sometimes quite strongly—on the neutron number. These studies are due to Bender, Rutz, Bürvenich, Maruhn, P.G. Reinhard *et al.* [12].

which is in the case of element 112 the shell structure of 112 electrons due to the Coulomb interaction of the electrons and in particular the calculation of the orbitals of the outer (valence) electrons—has been carried out as early as 1970 by B. Fricke and W. Greiner [15]. Hartree–Fock–Dirac calculations yield rather precise results.

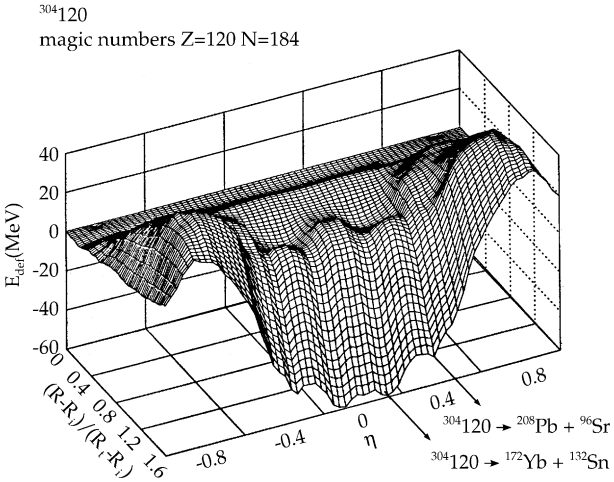


**FIGURE 8.7** Potential energy surface as a function of reduced elongation $(R - R_i)/(R_t - R_i)$ and mass asymmetry $\eta$ for the double magic nucleus $^{304}120$, $^{304}120_{184}$.

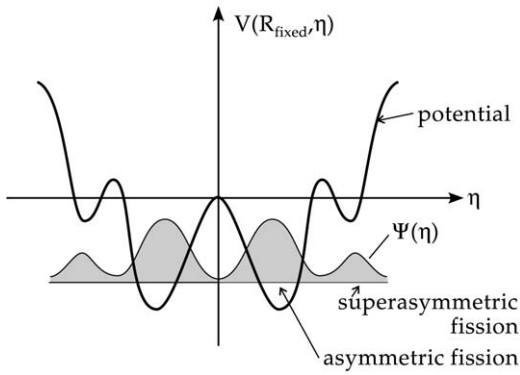


**FIGURE 8.8** The collective potential as a function of the mass asymmetry $\eta = \frac{A_1 - A_2}{A_1 + A_2}$. $A_i$ denotes the nucleon number in fragment $i$. This qualitative potential $V(R_{\text{fixed}}, \eta)$ corresponds to a cut through the potential landscape at $R = R_{\text{fixed}}$ close to the scission configuration. The wave function is drawn schematically. It has maxima where the potential is minimal and vice versa.

## 4. ASYMMETRIC AND SUPERASYMMETRIC FISSION—CLUSTER RADIOACTIVITY

The potential energy surfaces, which are shown prototypically for $Z = 114$ in Figure 8.3, contain even more remarkable information that I want to mention cursorily: if a given nucleus, e.g., uranium, undergoes fission, it moves in its potential mountains from the interior to the outside. Of course, this happens quantum mechanically. The wave function of such a nucleus, which decays by tunneling

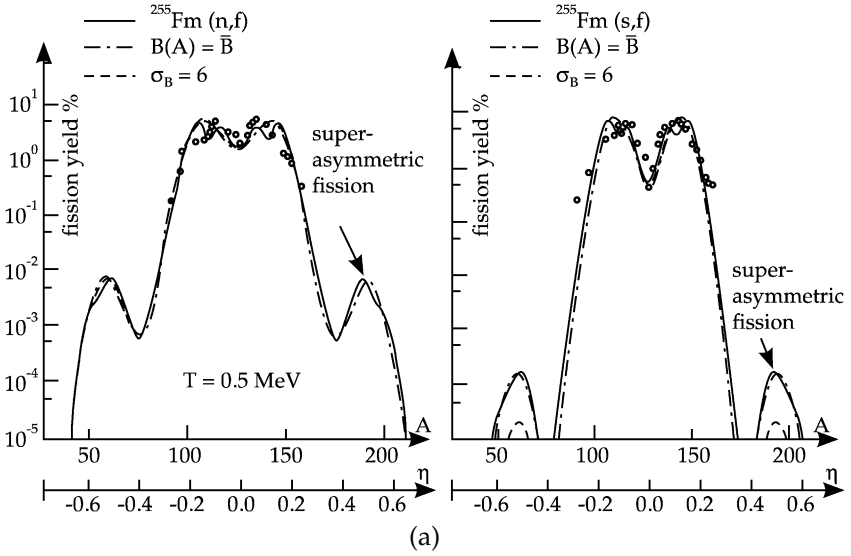


**FIGURE 8.9** Asymmetric (a) and symmetric (b) fission. For the latter, also superasymmetric fission is recognizable, as it has been observed only a few years ago by the Russian physicist Itkis—just as expected theoretically.

through the barrier, has maxima where the potential is minimal and minima where it has maxima. This is depicted in Figure 8.8.

The probability for finding a certain mass asymmetry $\eta = \frac{A_1 - A_2}{A_1 + A_2}$ of the fission is proportional to $\psi^*(\eta)\psi(\eta)\,d\eta$. Generally, this is complemented by a coordinate dependent scale factor for the volume element in this (curved) space, which I omit for the sake of clarity. Now it becomes clear how the so-called *asymmetric* and *superasymmetric* fission processes come into being. They result from the enhancement of the collective wave function in the cold valleys. And that is indeed, what one observes. Figure 8.9 gives an impression of it.

For a large mass asymmetry ($\eta \approx 0.8, 0.9$) there exist very narrow valleys. They are not as clearly visible in Figure 8.3, but they have interesting consequences. Through these narrow valleys nuclei can emit spontaneously not only $\alpha$-particles (Helium nuclei) but also $^{14}$C, $^{20}$O, $^{24}$Ne, $^{28}$Mg, and other nuclei. Thus, we are lead to the *cluster radioactivity* (Poenaru, Sandulescu, Greiner [16]).

By now this process has been verified experimentally by research groups in Oxford, Moscow, Berkeley, Milan and other places. Accordingly, one has to revise what is learned in school: there are not only 3 types of radioactivity ($\alpha$-, $\beta$-, $\gamma$-radioactivity), but many more. Atomic nuclei can also decay through spontaneous cluster emission (that is the "spitting out" of smaller nuclei like carbon, oxygen, ...). Figure 8.10 depicts some nice examples of these processes.

The knowledge of the collective potential energy surface and the collective masses $B_{ij}(R, \eta)$, all calculated within the Two-Center Shell Model (TCSM), allowed H. Klein, D. Schnabel and J.A. Maruhn to calculate lifetimes against fission in an "ab initio" way [17]. Utilizing a WKB-minimization for the penetrability in-

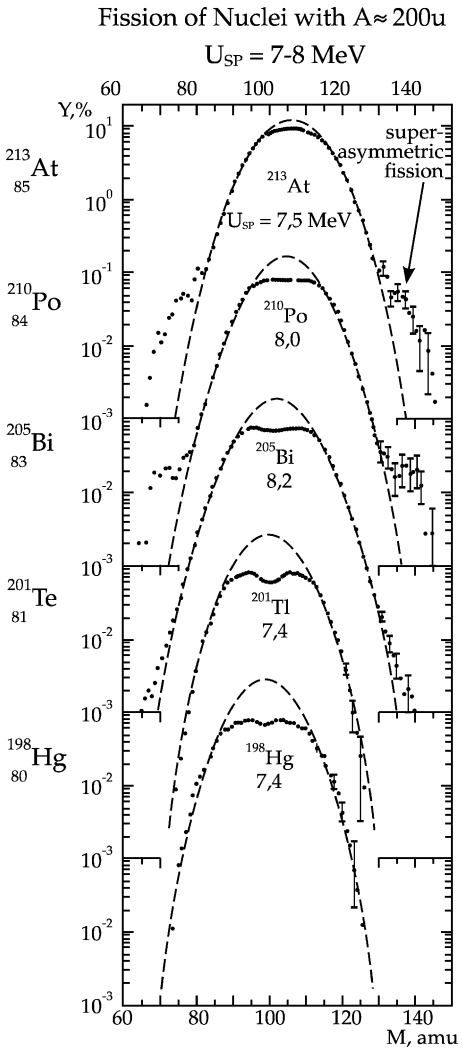


**FIGURE 8.9** (*Continued*)

tegral

$$\mathcal{P} = e^{-\mathrm{I}}, \quad \mathrm{I} = \min_{\forall \text{paths}} \frac{2}{\hbar} \int_S \sqrt{2m\big(V(R,\eta) - E\big)}\, ds$$

$$= \min_{\forall \text{paths}} \frac{2}{\hbar} \int_0^1 \sqrt{\underbrace{2mg_{ij}}_{B_{ij}}\big(V\big(x_i(t) - E\big)\big)\frac{dx_i}{dt}\frac{dx_j}{dt}}\, dt, \tag{1}$$

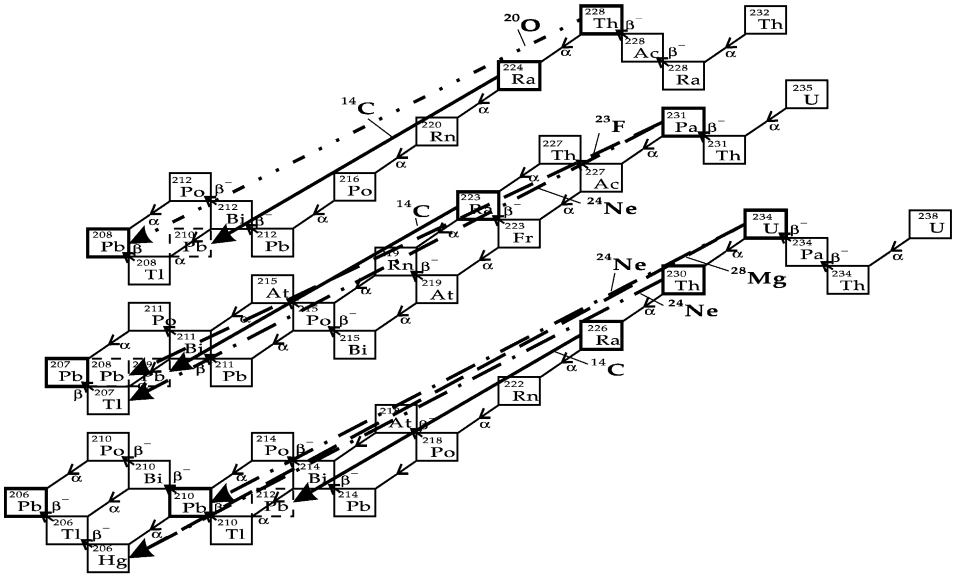


**FIGURE 8.10** Cluster radioactivity of actinide nuclei. By emission of $^{14}$C, $^{20}$O, . . . "big leaps" in the periodic system can occur, just contrary to the known $\alpha$-, $\beta$-, $\gamma$-radioactivities, which are also partly shown in the figure.

where $ds^2 = g_{ij}\, dx_i\, dx_j$ and $g_{ij}$—the metric tensor—is in the well-known fashion related to the collective masses $B_{ij} = 2mg_{ij}$, one explores the minimal paths from the nuclear ground state configuration through the multidimensional fission barrier (see Figure 8.11).

The thus obtained fission half lives are depicted in the lower part of Figure 8.11. Their distribution as a function of the fragment mass $A_2$ resembles quite well the asymmetric mass distribution. Cluster radioactive decays correspond to the broad peaks around $A_2 = 20$, 30 (200, 210). The confrontation of the calculated fission half lives with experiments is depicted in Figure 8.12. One notices "nearly quantitative" agreement over 20 orders of magnitude, which is—for an ab-initio calculation—remarkable!

Finally, in Figure 8.13, we compare the lifetime calculation discussed above with one based on the Preformation Cluster Model by D. Poenaru *et al.* [18] and recognize an amazing degree of similarity and agreement.

The systematics for the average total kinetic energy release for spontaneously fissioning isotopes of Cm and No is following the Viola trend, but $^{258}$Fm and $^{259}$Fm are clearly outside. The situation is similar also for $^{260}$Md, where two components of fission products (one with lower and one with higher kinetic energy) were observed by Hulet *et al.* [19]. The explanation of these interesting observations lies in two different paths through the collective potential.

One reaches the scission point in a stretched neck position (i.e., at a lower point of the Coulomb barrier—thus lower kinetic energy for the fragments) while the other one reaches the scission point practically in a touching-spheres-position (i.e.,

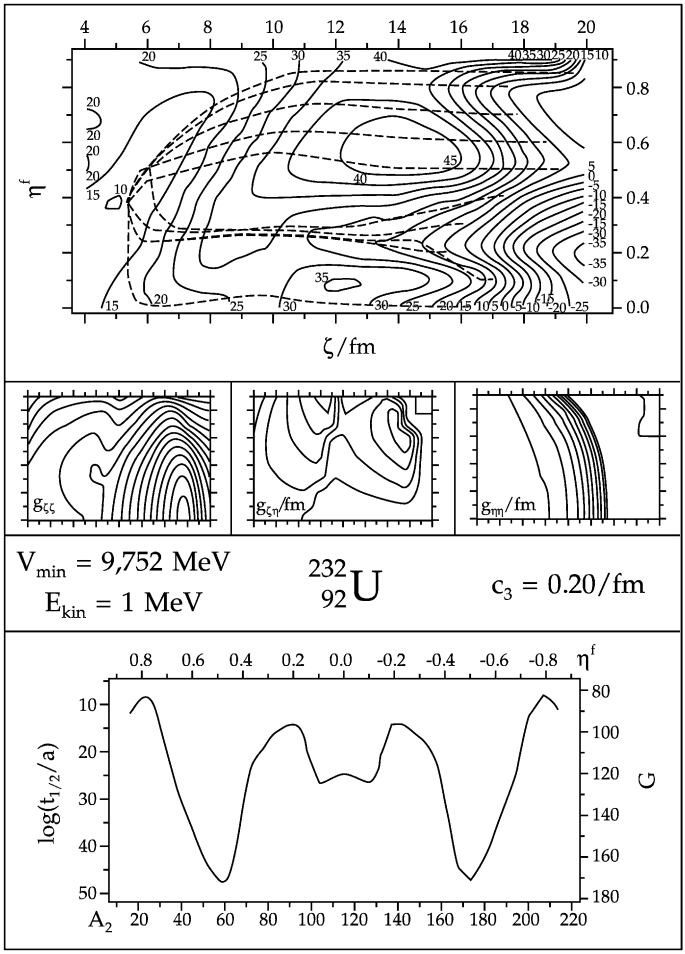


**FIGURE 8.11** The upper part of the figure shows the collective potential energy surface for $^{232}_{92}$U with the ground-state position and various fission paths through the barrier. The middle part shows various collective masses, all calculated in the TCSM. In the lower part the calculated fission half lives are depicted.

higher up on the Coulomb barrier and therefore highly energetic fragments) [20]. The latter process is cold fission; i.e., the fission fragments are in or close to their ground state (cold fragments)and all the available energy is released as kinetic energy. Cold fission is, in fact, typically a cluster decay. The side-by-side occurrence of cold and normal (hot) fission has been named bi-modal fission [20]. There has now been put forward a fantastic idea [21] in order to study cold fission (Cluster decays) and other exotic fission processes (ternary-, multiple fission in general) very elegantly: By measuring with, e.g., the Gamma-sphere characteristic $\gamma$-transitions of individual fragments in coincidence, one can identify all these processes in a direct and simple way (Figure 8.14). First confirmation of this

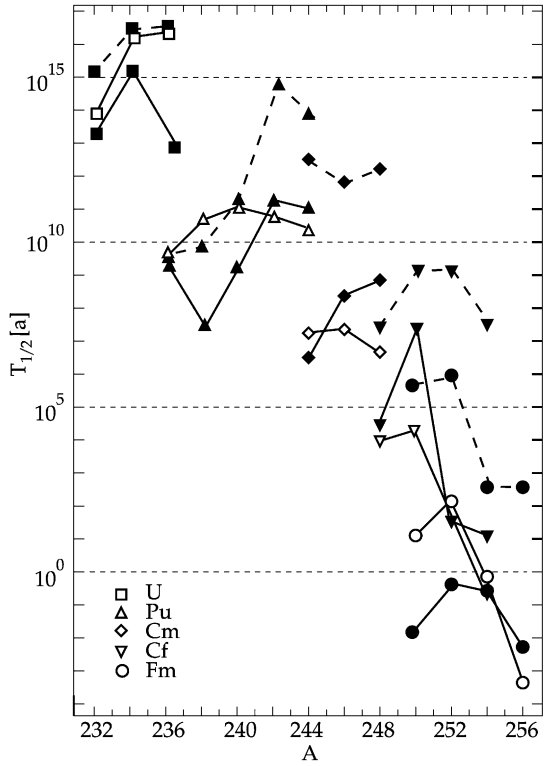


**FIGURE 8.12** Fission half lives for various isotopes of $Z = 92$ (□), $Z = 94$ (△), $Z = 96$ (◇), $Z = 98$ (▽) and $Z = 100$ (○). The black curves represent the experimental values. The calculations drawn with full and dashed lines correspond to a different choice of the barrier parameter in the Two-Center Shell Model ($c_3 \approx 0.2$ and 0.1, respectively).

method by J. Hamilton, V. Ramaya *et al.* worked out excellently [22]. This method has high potential for revolutionizing fission physics! With some physical intuition one can imagine that *triple* and *quadruple* fission processes and even the process of *cold multifragmentation* will be discovered—absolutely fascinating! We have thus seen that fission physics (cold fission, cluster radioactivity, . . .) and fusion physics (especially the production of superheavy elements) are intimately connected.

Indeed, it seems possible that triple fission of the kind

$^{252}\mathrm{Cf} \rightarrow {}^{146}\mathrm{Ba} + {}^{96}\mathrm{Sr} + {}^{10}\mathrm{Be}$,

$^{252}\mathrm{Cf} \rightarrow {}^{112}\mathrm{Ry} + {}^{130}\mathrm{Sn} + {}^{10}\mathrm{Be}$,

$^{252}\mathrm{Cf} \rightarrow \ldots$

could occur. In principle this can be identified by measuring the various $\gamma$-transitions of these nuclei in coincidence (see Figure 8.15). Even though the statistical evidence for the $^{10}$Be line might be small ($\approx$50 events) the various coincidences would proof that spontaneous triple fission out of the ground state of $^{252}$Cf with the heavy cluster $^{10}$Be as a third fragment might exist. The question is whether a triple-nuclear-molecule is formed within the break-up of the initial nucleus, i.e.,

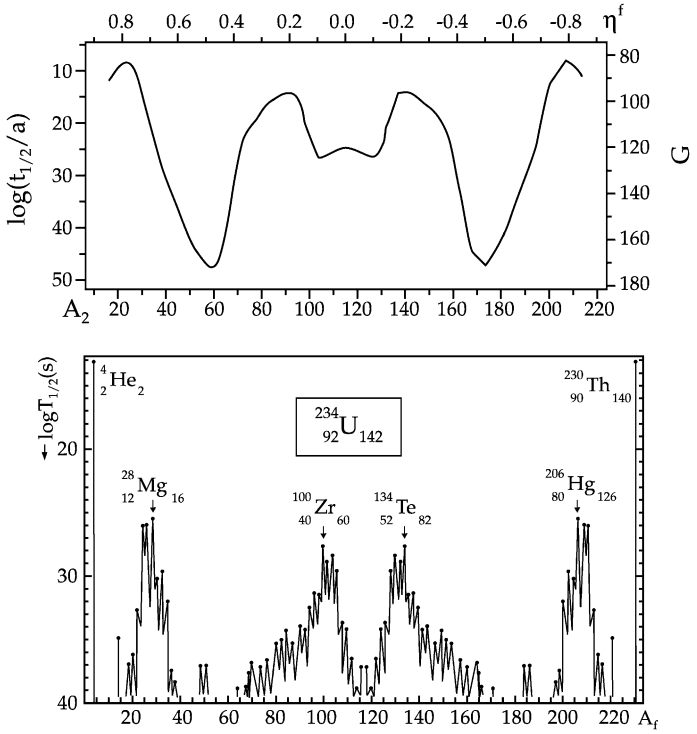


**FIGURE 8.13** Comparison of the fission half lives calculated in the fission model (upper figure—see also Figure 8.11) and in the Preformation Cluster Model [18]. In both models the deformation of the fission fragments is not included completely.

whether a triple-cluster pocket in the potential is formed. Also other triple fragmentations can be expected. One of those is also denoted above. In fact, there were early experimental indications, that such break-ups appear. The most amazing question is, however, the following: The cross coincidences should indicate that one deals with a simultaneous three-body breakup and not with a cascade process. For such case one expects, for example, a configuration as shown in Figure 8.16. Consequently the $^{10}$Be will obtain kinetic energy while running down the combined Coulomb barrier of $^{146}$Ba and $^{96}$Sr and, therefore, the 3368 keV line of $^{10}$Be should be Doppler-broadened. The molecule has to live longer than about $10^{-12}$ s. The nuclear forces from the $^{146}$Ba and $^{96}$Sn cluster to the left and right from $^{10}$Be lead to a softening of its potential and therefore to a somewhat smaller transition energy. This would give evidence for rather long-living nuclear molecules consisting of three fragments. It is by no means clear whether such structures occur. Present day theory is too unprecise to allow for clear predictions.

Of course, I do immediately speculate whether such configurations do eventually also exist in, e.g., U + Cm soft encounters directly at the Coulomb barrier. This would have tremendous importance for the observation of the spontaneous vacuum decay [25], for which "sticking giant molecules" with a lifetime of the

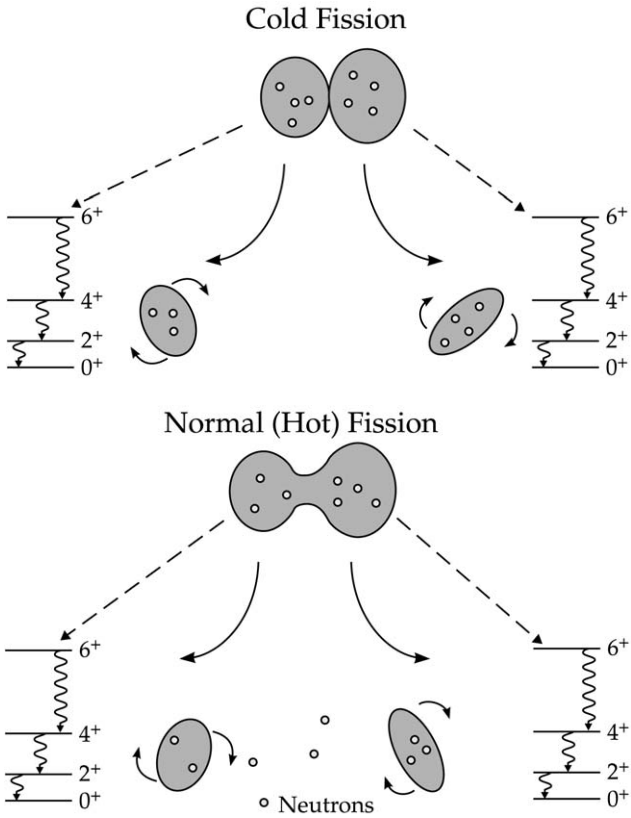


**FIGURE 8.14** Illustration of cold and hot (normal) fission identification through multiple $\gamma$-coincidences of photons from the fragments. The photons serve to identify the fragments.

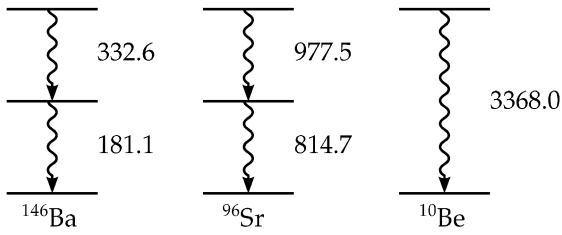


**FIGURE 8.15** The $\gamma$-transitions of the three fission products of $^{252}$Cf measured in coincidence. Various combinations of the coincidences were studied. The free 3368 keV line in $^{10}$Be has recently been remeasured by Burggraf *et al.* [23], confirming the value of the transition energy within 100 eV.

order of $10^{-19}$ s are needed. The nuclear physics of such heavy ion collisions at the Coulomb barrier (giant nuclear molecules) is intriguing. It should indeed be investigated!

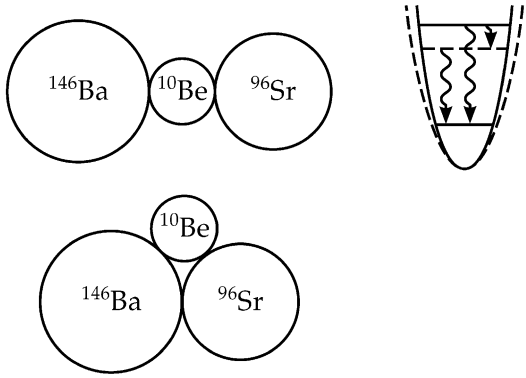


**FIGURE 8.16** Typical linear cluster configurations which might lead to triple fission of $^{252}$Cf. The influence of both clusters leads to a softening of the $^{10}$Be potential and thus to a somewhat smaller transition energy. Some theoretical investigations indicate that the axial symmetry of this configuration might be broken (lower left-hand figure).

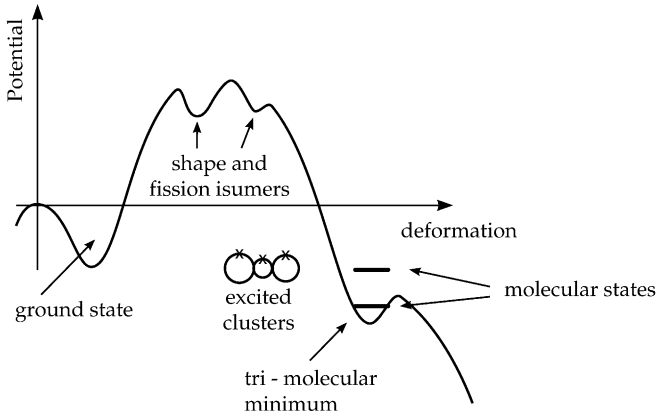


**FIGURE 8.17** Cluster molecules: Potential energy curve of a heavy nucleus showing schematically the location of ground state, shape- and fission-isomeric states and of tri-molecular states.

As mentioned before there are other tri-molecular structures possible; some with $^{10}$Be in the middle and both spherical or deformed clusters on both sides of $^{10}$Be. The energy shift of the $^{10}$Be-line should be smaller, if the outside clusters are deformed (smaller attraction $\Leftrightarrow$ smaller softening of the potential) and bigger, if they are spherical. Also other than $^{10}$Be-clusters are expected to be in the middle. One is lead to the molecular doorway picture. Figure 8.17 gives a schematic impression where within the potential landscape cluster-molecules are expected to appear, i.e., close to the scission configuration. Clearly, I expect not a single tri-molecular configuration, but a variety of three-body fragmentations leading to a spreading width of the tri-molecular state. This is schematically shown

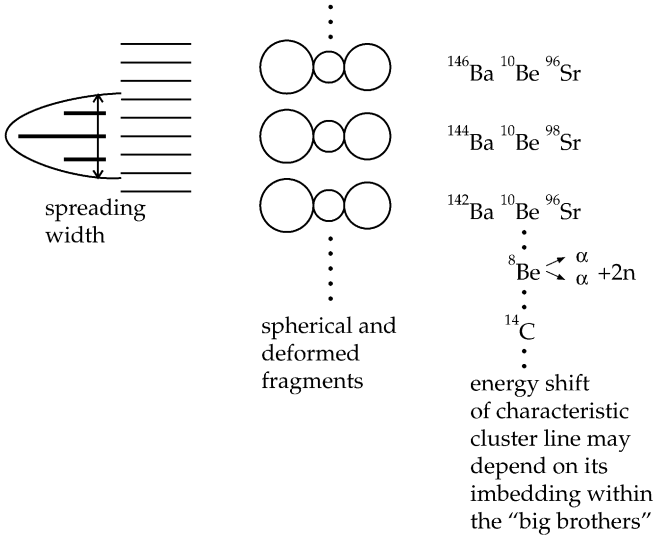


**FIGURE 8.18** Vision of the microstructure of tri-molecular states: Various tri-cluster configurations are spread out and mix with background states. Thus the tri-molecular state obtains a spreading width.

in Figure 8.18. Finally, these tri-body nuclear molecules are expected to perform themselves rotational and vibrational (butterfly, wiggler, $\beta$-, $\gamma$-type) modes. The energies were estimated by P. Hess *et al.* [24]; for example rotational energies typically of the order of a few keV (4 keV, 9 keV, . . .). A new molecular spectroscopy, if possible, would be fantastic!

The "cold valleys" in the collective potential energy surface are basic for understanding this exciting area of nuclear physics! It is a master example for understanding the *structure of elementary matter*, which is so important for other fields, especially astrophysics, but even more so for enriching our "Weltbild," i.e., the status of our understanding of the world around us.

## 5. EXTENSION OF THE PERIODIC SYSTEM INTO THE SECTIONS OF HYPER- AND ANTIMATTER

Nuclei that are found in nature consist of nucleons (protons and neutrons) which themselves are made of u (up) and d (down) quarks. However, there also exist s (strange) quarks and even heavier flavors, called charm, bottom, top. The latter has just recently been discovered. Let us stick to the s quarks. They are found in the 'strange' relatives of the nucleons, the so-called hyperons ($\Lambda$, $\Sigma$, $\Xi$, $\Omega$). The $\Lambda$-particle, e.g., consists of one u, d and s quark, the $\Xi$-particle even of an u and two s quarks, while the $\Omega$ (sss) contains strange quarks only. Figure 8.19 gives an overview of the baryons, which are of interest here, and their quark content.

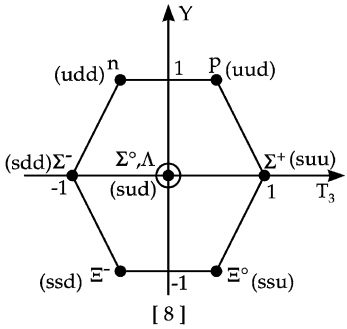


**FIGURE 8.19** Important baryons are ordered in this octet. The quark content is depicted. Protons (p) and neutrons (n), most important for our known world, contain only u and d quarks. Hyperons contain also an s quark. The number of s quarks is a measure for the strangeness.

If such a hyperon is taken up by a nucleus, a *hyper-nucleus* is created. Hypernuclei with one hyperon have been known for 20 years now, and were extensively studied by B. Povh (Heidelberg) [26]. Several years ago, Carsten Greiner, Jürgen Schaffner and Horst Stöcker [27] theoretically investigated nuclei with many hyperons, *hypermatter*, and found that the binding energy per baryon of strange matter is in many cases even higher than that of ordinary matter (composed only of u and d quarks). This leads to the idea of extending the periodic system of elements in the direction of strangeness.

One can also ask for the possibility of building atomic nuclei out of *antimatter*, that means searching e.g. for anti-helium, anti-carbon, anti-oxygen. Figure 8.20 depicts this idea. Due to the charge conjugation symmetry antinuclei should have the same magic numbers and the same spectra as ordinary nuclei. However, as soon as they get in touch with ordinary matter, they annihilate with it and the system explodes. Now the important question arises how these strange matter and antimatter clusters can be produced. First, one thinks of collisions of heavy nuclei, e.g. lead on lead, at high energies (energy per nucleon $\geqslant$200 GeV). Calculations with the URQMD-model of the Frankfurt school show that through *nuclear shock waves* [28–30] nuclear matter gets compressed to 5–10 times of its usual value, $\rho_0 \approx 0.17\ \mathrm{fm}^{-3}$, and heated up to temperatures of $kT \approx 200$ MeV. As a consequence about 10,000 pions, 100 $\Lambda$'s, 40 $\Sigma$'s and $\Xi$'s and about as many antiprotons and many other particles are created in a single collision. It seems conceivable that it is possible in such a scenario for some $\Lambda$'s to get captured by a nuclear cluster. This happens indeed rather frequently for one or two $\Lambda$-particles; however, more of them get built into nuclei with rapidly decreasing probability only. This is due to the low probability for finding the right conditions for such a capture in the phase space of the particles: the numerous particles travel with every possible momenta (velocities) in all directions. The chances for hyperons and antibaryons to meet gets rapidly worse with increasing number. In order to produce multi-$\Lambda$-nuclei and antimatter nuclei, one has to look for a different source.

In the framework of meson field theory the energy spectrum of baryons has a peculiar structure, depicted in Figure 8.21. It consists of an upper and a lower con-

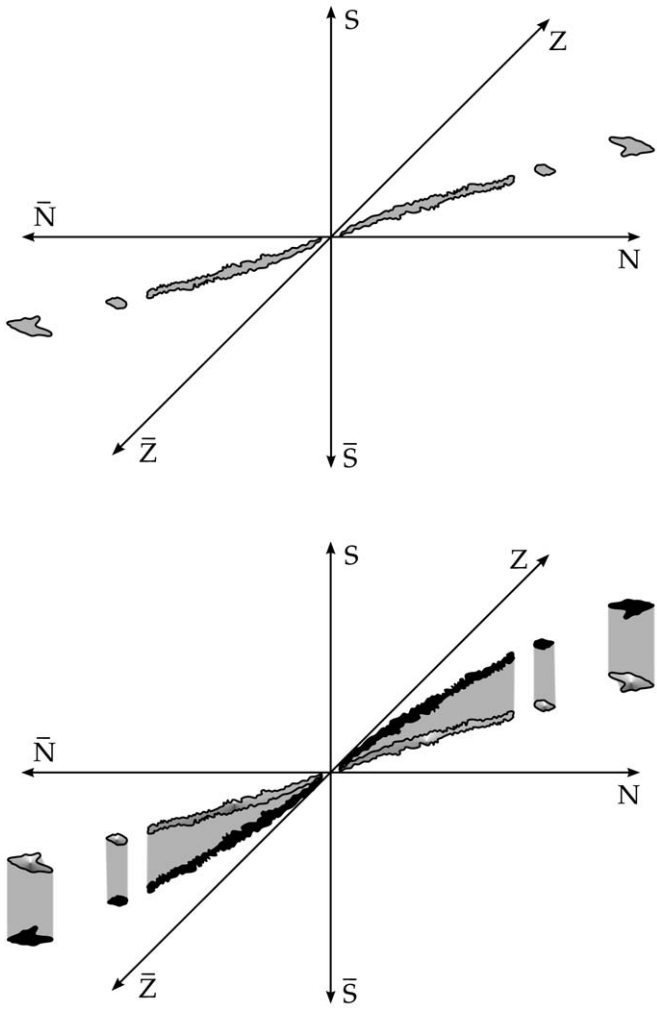


**FIGURE 8.20** The extension of the periodic system into the sectors of strangeness ($S$, $\bar{S}$) and antimatter ($\bar{Z}$, $\bar{N}$). The stable valley winds out of the known proton ($Z$) and neutron ($N$) plane into the $S$ and $\bar{S}$ sector, respectively. The same can be observed for the antimatter sector. In the upper part of the figure only the stable valley in the usual proton ($Z$) and neutron ($N$) plane is plotted, however, extended into the sector of antiprotons and antineutrons. In the second part of the figure it has been indicated, how the stable valley winds out of the $Z$–$N$ plane into the strangeness sector.

tinuum, as it is known from the electrons (see, e.g. [25]). Of special interest in the case of the baryon spectrum is the potential well, built of the scalar and the vector potential, which rises from the lower continuum. It is known since P.A.M. Dirac (1930) that the negative energy states of the lower continuum have to be occupied by particles (electrons or, in our case, baryons). Otherwise our world would

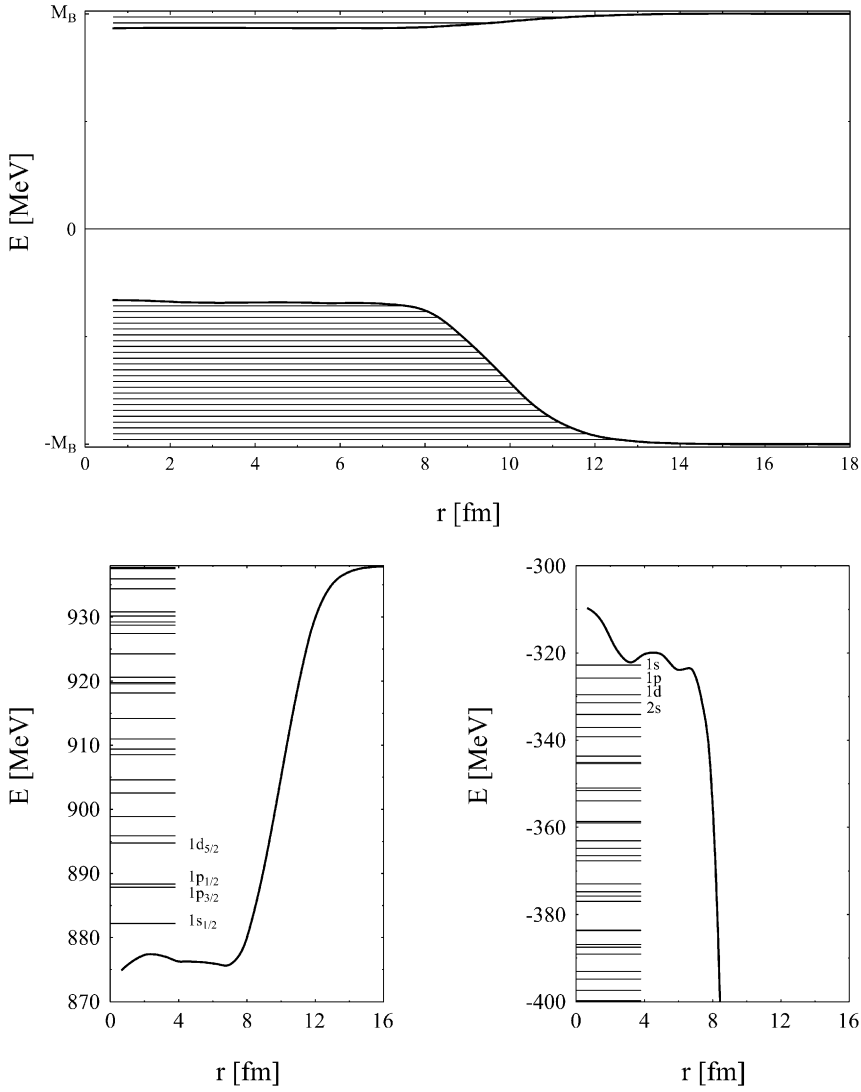


**FIGURE 8.21** Baryon spectrum in a nucleus. Below the positive energy continuum exists the potential well of real nucleons. It has a depth of 50–60 MeV and shows the correct shell structure. The shell model of nuclei is realized here. However, from the negative continuum another potential well arises, in which about 40,000 bound particles are found, belonging to the vacuum. A part of the shell structure of the upper well and the lower (vacuum) well is depicted in the lower figures.

be unstable, because the "ordinary" particles are found in the upper states which can decay through the emission of photons into lower lying states. However, if the "underworld" is occupied, the Pauli-principle will prevent this decay. Holes in the occupied "underworld" (Dirac sea) are antiparticles.

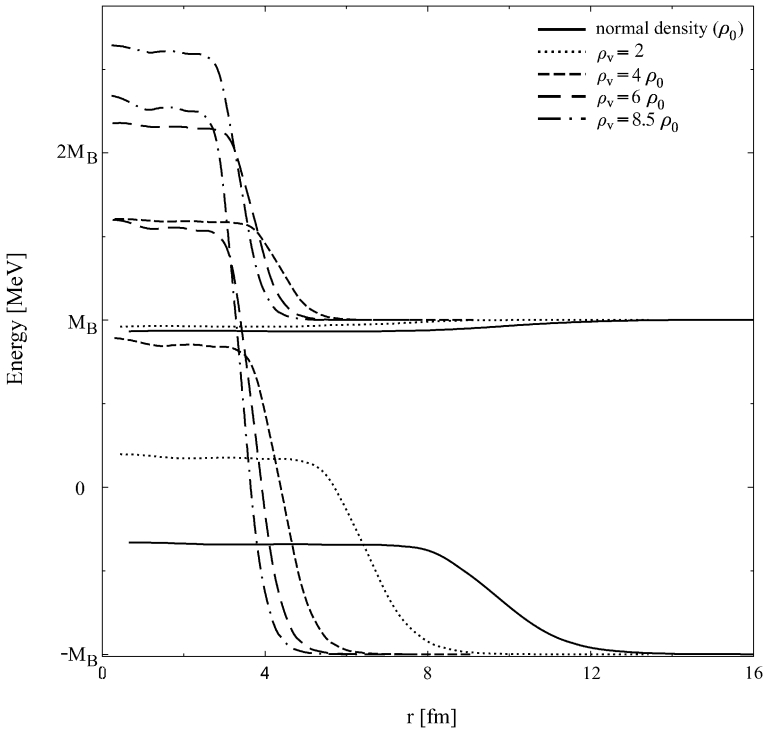


**FIGURE 8.22** The lower well rises strongly with increasing primary nucleon density, and even gets supercritical (spontaneous nucleon emission and creation of bound antinucleons). Supercriticality denotes the situation, when the lower well enters the upper continuum.

The occupied states of this underworld including up to 40,000 occupied bound states of the lower potential well represent the *vacuum*. The peculiarity of this strongly correlated vacuum structure in the region of atomic nuclei is that—depending on the size of the nucleus—more than 20,000 up to 40,000 (occupied) bound nucleon states contribute to this polarization effect. Obviously, we are dealing here with a *highly correlated vacuum*. A pronounced shell structure can be recognized [31–33]. Holes in these states have to be interpreted as bound antinucleons (antiprotons, antineutrons). If the primary nuclear density rises due to compression, the lower well increases while the upper decreases and soon is converted into a repulsive barrier (Figure 8.22). This compression of nuclear matter can only be carried out in relativistic nucleus–nucleus collision with the help of shock waves, which have been proposed by the Frankfurt school [28,29] and which have since then been confirmed extensively (for references see, e.g. [34]). These *nuclear shock waves* are accompanied by heating of the nuclear matter. Indeed, density and temperature are intimately coupled in terms of the hydrodynamic Rankine–Hugoniot equations. Heating as well as the violent dynamics cause the creation of many holes in the very deep (measured from $-M_Bc^2$) vacuum well. These numerous bound holes resemble antimatter clusters which are bound in the medium; their

wave functions have large overlap with antimatter clusters. When the primary matter density decreases during the expansion stage of the heavy ion collision, the potential wells, in particular the lower one, disappear.

The bound antinucleons are then pulled down into the (lower) continuum. In this way antimatter clusters may be set free. Of course, a large part of the antimatter will annihilate on ordinary matter present in the course of the expansion. However, it is important that this mechanism for the production of antimatter clusters out of the highly correlated vacuum does not proceed via the phase space. The required coalescence of many particles in phase space suppresses the production of clusters, while it is favored by the direct production out of the highly correlated vacuum. In a certain sense, the highly correlated vacuum is a kind of cluster vacuum (vacuum with cluster structure). The shell structure of the vacuum levels (see Figure 8.21) supports this latter suggestion. Figure 8.23 illustrates this idea.

The mechanism is similar for the production of multi-hyper nuclei ($\Lambda$, $\Sigma$, $\Xi$, $\Omega$). Meson field theory predicts also for the $\Lambda$ energy spectrum at finite primary nucleon density the existence of upper and lower wells. The lower well belongs to the vacuum and is fully occupied by $\Lambda$'s.

Dynamics and temperature then induce transitions ($\Lambda\bar{\Lambda}$ creation) and deposit many $\Lambda$'s in the upper well. These numerous bound $\Lambda$'s are sitting close to the primary baryons: in a certain sense a giant multi-$\Lambda$ hypernucleus has been created. When the system disintegrates (expansion stage) the $\Lambda$'s distribute over the nucleon clusters (which are most abundant in peripheral collisions). In this way multi-$\Lambda$ hypernuclei can be formed.

Of course this vision has to be worked out and probably refined in many respects. This means much more and thorough investigation in the future. It is particularly important to gain more experimental information on the properties of the lower well by (e, e′p) or (e, e′pp′) and also ($\bar{p}_c p_b$, $p_c \bar{p}_b$) reactions at high energy ($\bar{p}_c$ denotes an incident antiproton from the continuum, $p_b$ is a proton in a bound state; for the reaction products the situation is just the opposite) [35]. Also the reaction (p, p′d), (p, p′$^3$He), (p, p′$^4$He) and others of similar type need to be investigated in this context. The systematic scattering of antiprotons on nuclei can contribute to clarify these questions. Problems of the meson field theory (e.g., Landau poles) can then be reconsidered. An effective meson field theory has to be constructed. Various effective theories, e.g., of Walecka-type on the one side and theories with chiral invariance on the other side, seem to give different strengths of the potential wells and also different dependence on the baryon density [36]. The Lagrangians of the Dürr–Teller–Walecka-type and of the chirally symmetric mean field theories look quite differently. We exhibit them—without further discussion—in the following equations:

$$\mathcal{L} = \mathcal{L}_{\text{kin}} + \mathcal{L}_{\text{BM}} + \mathcal{L}_{\text{vec}} + \mathcal{L}_0 + \mathcal{L}_{\text{SB}};$$

Non-chiral Lagrangian:

$$\mathcal{L}_{\text{kin}} = \frac{1}{2}\partial_\mu s \partial^\mu s + \frac{1}{2}\partial_\mu z \partial^\mu z - \frac{1}{4}B_{\mu\nu}B^{\mu\nu} - \frac{1}{4}G_{\mu\nu}G^{\mu\nu} - \frac{1}{4}F_{\mu\nu}F^{\mu\nu},$$

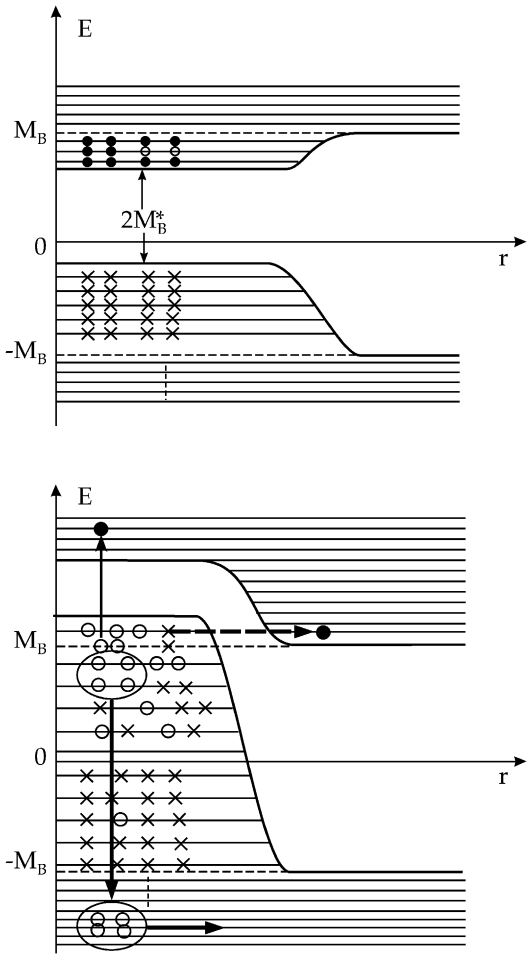


**FIGURE 8.23** Due to the high temperature and the violent dynamics, many bound holes (antinucleon clusters) are created in the highly correlated vacuum, which can be set free during the expansion stage into the lower continuum. In this way, antimatter clusters can be produced directly from the vacuum. The horizontal arrow in the lower part of the figure denotes the spontaneous creation of baryon–antibaryon pairs, while the antibaryons occupy bound states in the lower potential well. Such a situation, where the lower potential well reaches into the upper continuum, is called supercritical.

$$\mathcal{L}_{\mathrm{BM}} = \sum_B \bar{\psi}_B \Big[ i\gamma_\mu \partial^\mu - g_{\omega B}\gamma_\mu \omega^\mu - g_{\phi B}\gamma_\mu \phi^\mu - g_{\rho B}\gamma_\mu \tau_B \rho^\mu - e\gamma_\mu \frac{1}{2}(1+\tau_B)A^\mu - m_B^* \Big] \psi_B,$$

$$\mathcal{L}_{\mathrm{vec}} = \frac{1}{2} m_\omega^2 \omega_\mu \omega^\mu + \frac{1}{2} m_\rho^2 \rho_\mu \rho^\mu + \frac{1}{2} m_\phi^2 \phi_\mu \phi^\mu,$$

$$\mathcal{L}_0 = -\frac{1}{2}m_s^2 s^2 - \frac{1}{2}m_z^2 z^2 - \frac{1}{3}bs^3 - \frac{1}{4}cs^4;$$

Chiral Lagrangian:

$$\mathcal{L}_{\text{kin}} = \frac{1}{2}\partial_\mu\sigma\,\partial^\mu\sigma + \frac{1}{2}\partial_\mu\zeta\,\partial^\mu\zeta + \frac{1}{2}\partial_\mu\chi\,\partial^\mu\chi - \frac{1}{4}B_{\mu\nu}B^{\mu\nu} - \frac{1}{4}G_{\mu\nu}G^{\mu\nu} - \frac{1}{4}F_{\mu\nu}F^{\mu\nu},$$

$$\mathcal{L}_{\text{BM}} = \sum_B \bar{\psi}_B\Big[i\gamma_\mu\partial^\mu - g_{\omega B}\gamma_\mu\omega^\mu - g_{\phi B}\gamma_\mu\phi^\mu - g_{\rho B}\gamma_\mu\tau_B\rho^\mu - e\gamma_\mu\frac{1}{2}(1+\tau_B)A^\mu - m_B^*\Big]\psi_B,$$

$$\mathcal{L}_{\text{vec}} = \frac{1}{2}m_\omega^2\frac{\chi^2}{\chi_0^2}\omega_\mu\omega^\mu + \frac{1}{2}m_\rho^2\frac{\chi^2}{\chi_0^2}\rho_\mu\rho^\mu + \frac{1}{2}m_\phi^2\frac{\chi^2}{\chi_0^2}\phi_\mu\phi^\mu + g_4^4\big(\omega^4 + 6\omega^2\rho^2 + \rho^4\big),$$

$$\mathcal{L}_0 = -\frac{1}{2}k_0\chi^2\big(\sigma^2+\zeta^2\big) + k_1\big(\sigma^2+\zeta^2\big)^2 + k_2\left(\frac{\sigma^4}{2} + \zeta^4\right) + k_3\chi\sigma^2\zeta - k_4\chi^4 + \frac{1}{4}\chi^4\ln\frac{\chi^4}{\chi_0^4} + \frac{\delta}{3}\ln\frac{\sigma^2\zeta}{\sigma_0^2\zeta_0^2},$$

$$\mathcal{L}_{\text{SB}} = -\left(\frac{\chi}{\chi_0}\right)^2\left[m_\pi^2 f_\pi\sigma + \left(\sqrt{2}m_K^2 f_K - \frac{1}{\sqrt{2}}m_\pi^2 f_\pi\right)\zeta\right].$$

The non-chiral model contains the scalar–isoscalar field $s$ and its strange counterpart $z$, the vector–isoscalar fields $\omega_\mu$ and $\phi_\mu$, and the $\rho$-meson $\rho_\mu$ as well as the photon $A_\mu$ fields. For more details see [36]. In contrast to the non-chiral model, the $SU(3)_L \times SU(3)_R$ Lagrangian contains the dilaton field $\chi$ introduced to mimic the trace anomaly of QCD in an effective Lagrangian at tree level (for an explanation of the chiral model see [36,13]).

The connection of the chiral Lagrangian with the Walecka-type can be established by the substitution $\sigma = \sigma_0 - s$ (and similarly for the strange condensate $\zeta$). Then, e.g., the difference in the definition of the effective nucleon mass in both models (non-chiral: $m_N^* = m_N - g_s s$, chiral: $m_N^* = g_s\sigma$) can be removed, yielding:

$$m_N^* = g_s\sigma_0 - g_s s \equiv m_N - g_s s. \tag{2}$$

Nevertheless, if the parameters in both cases are adjusted such that ordinary nuclei (binding energies, radii, shell structure, ...) and properties of infinite nuclear matter (equilibrium density, compression constant $K$, binding energy) are well reproduced, the prediction of both effective Lagrangians for the dependence of the properties of the correlated vacuum on density and temperature is remarkably different. This is illustrated to some extend in Figure 8.24. Accordingly, the chirally symmetric meson field theory predicts much higher primary densities (and temperatures) until the effects of the correlated vacuum are strong enough

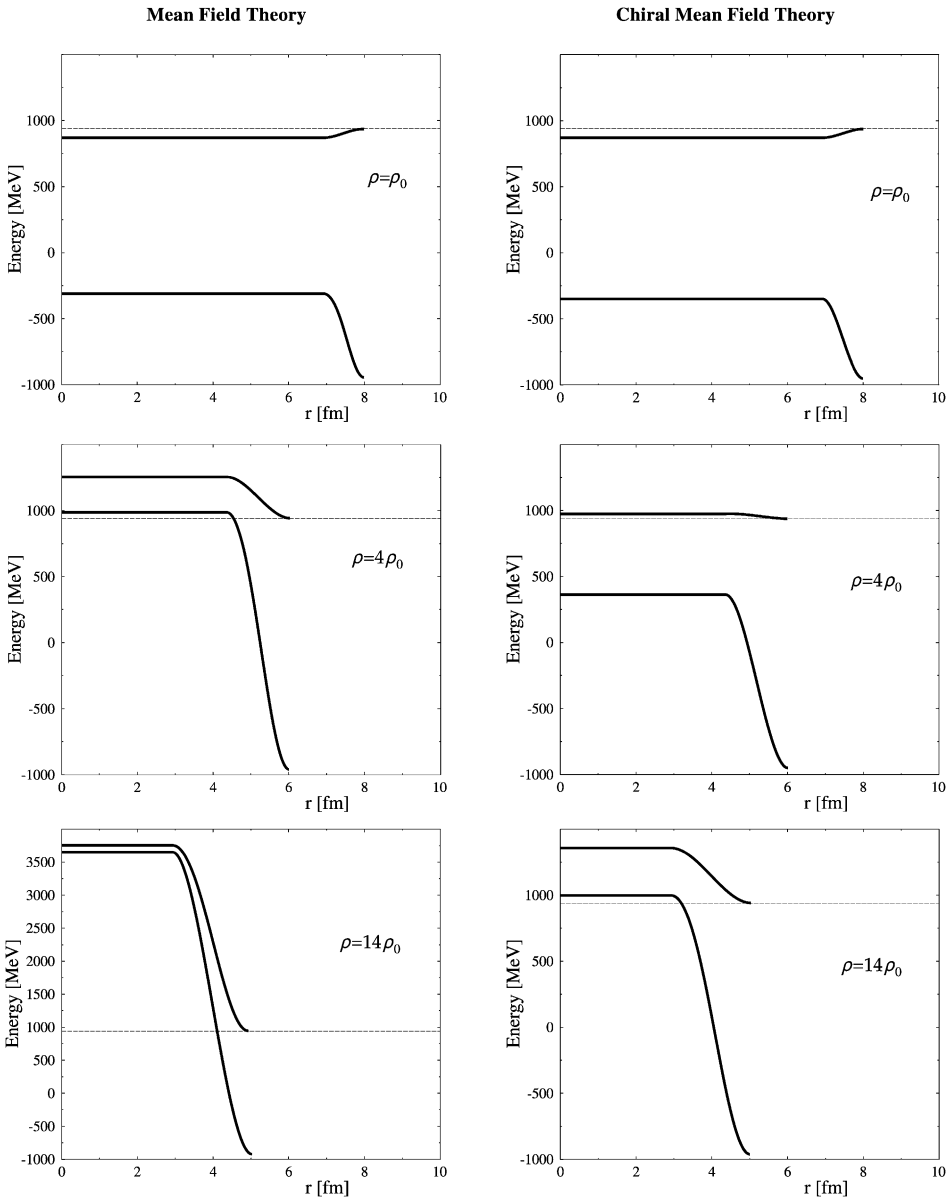


**FIGURE 8.24** The potential structure of the shell model and the vacuum for various primary densities $\rho = \rho_0, 4\rho_0, 14\rho_0$. At left the predictions of ordinary Dürr–Teller–Walecka-type theories are shown; at right those for a chirally symmetric meson field theory as developed by P. Papazoglu, S. Schramm *et al.* [36,13]. Note however, that this particular chiral mean-field theory does contain $\omega^4$ terms. If introduced in both effective models, they seem to predict quantitatively similar results.

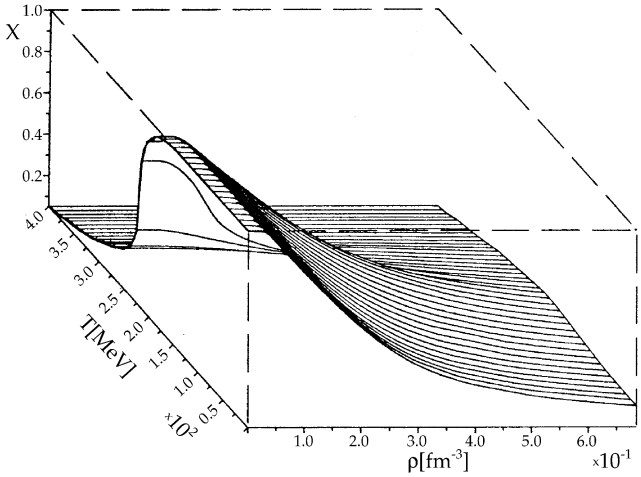


**FIGURE 8.25** The strong phase transition inherent in Dürr–Teller–Walecka-type meson field theories, as predicted by J. Theis *et al.* [37]. Note that there is a first-order transition along the $\rho$-axis (i.e. with density), but a simple transition along the temperature $T$-axis. Note also that this is very similar to the phase transition obtained recently from the Nambu–Jona–Lasinio-approximation of QCD [38].

so that the mechanisms described here become effective. In other words, according to chirally symmetric meson field theories the antimatter-cluster production and multi-hypermatter-cluster production out of the highly correlated vacuum takes place at considerably higher heavy ion energies as compared to the predictions of the Dürr–Teller–Walecka-type meson field theories. This in itself is a most interesting, quasi-fundamental question to be clarified. Moreover, the question of the nucleonic substructure (form factors, quarks, gluons) and its influence on the highly correlated vacuum structure has to be studied. The nucleons are possibly strongly polarized in the correlated vacuum: the $\Delta$ resonance correlations in the vacuum are probably important. Is this highly correlated vacuum state, especially during the compression, a preliminary stage to the quark-gluon cluster plasma? To which extent is it similar or perhaps even identical with it? It is well known for more than 10 years that meson field theories predict a phase transition qualitatively and quantitatively similar to that of the quark-gluon plasma [37]—see Figure 8.25.

## 6. CLUSTERS OF MATTER AND ANTIMATTER

Presently it is widely accepted that the relativistic mean-field (RMF) model [40] gives a good description of nuclear matter and finite nuclei [41]. Within this approach the nucleons are supposed to obey the Dirac equation coupled to mean meson fields. Large scalar and vector potentials, of the order of 300 MeV, are necessary to explain the strong spin–orbit splitting in nuclei. The most debated

aspect of this model is related to the negative-energy states of the Dirac equation. In most applications these states are simply ignored (no-sea approximation) or "taken into account" via the non-linear and derivative terms of the scalar potential. On the other hand, explicit consideration of the Dirac sea combined with the G-parity arguments leads to such interesting conjectures as the existence of deeply-bound antinucleon states in nuclei [42] or even spontaneous production of nucleon–antinucleon pairs [43,44]. Unfortunately, the experimental information on the antinucleon effective potential in nuclei is obscured by the strong absorption caused by annihilation. The real part of the antiproton effective potential might be as large as 200–300 MeV, with the uncertainty reaching 100% in the deep interior of the nucleus.

Keeping in mind all possible limitations of the RMF approach, below we consider yet another interesting application of this model. Namely, we study properties of light nuclear systems containing a few real antibaryons [39]. At first sight this may appear ridiculous because of the fast annihilation of antibaryons in the dense baryonic environment. But as our estimates show, due to a significant reduction of the available phase space for annihilation, the life time of such states might be long enough for their observation. In a certain sense, these states are analogous to the famous baryonium states in the $N\bar{N}$ system [45], although their existence has never been unambiguously confirmed. To our knowledge, up till now a self-consistent calculation of antinucleon states in nuclei has not been performed. Our calculations can be regarded as the first attempt to fill this gap. We consider first two nuclear systems, namely $^{16}$O and $^{8}$Be, and study the changes in their structure due to the presence of an antiproton. Then we discuss the influence of small antimatter clusters on heavy systems like $^{208}$Pb.

## 7. THEORETICAL FRAMEWORK

Below we use the RMF model which previously has been successfully applied for describing ground states of nuclei at and away from the $\beta$-stability line. For nucleons, the scalar and vector potentials contribute with opposite signs in the central potential, while their sum enters in the spin–orbit potential. Due to G-parity, for antiprotons the vector potential changes sign and therefore both the scalar and the vector mesons generate attractive potentials.

To estimate uncertainties of this approach we use three different parameterizations of the model, namely NL3 [46], NL–Z2 [47] and TM1 [48]. In this paper we assume that the antiproton interactions are fully determined by the G-parity transformation.

We solve the effective Schrödinger equations for both the nucleons and the antiprotons. Although we neglect the Dirac sea polarization, we take into account explicitly the contribution of the antibaryon into the scalar and vector densities. For protons and neutrons we include pairing correlations within the BCS model with a $\delta$-force (volume pairing) [49]. Calculations are done within the blocking approximation [50] for the antiproton, and assuming the time-reversal invariance of the nuclear ground state. The coupled set of equations for nucleons, antinucleons

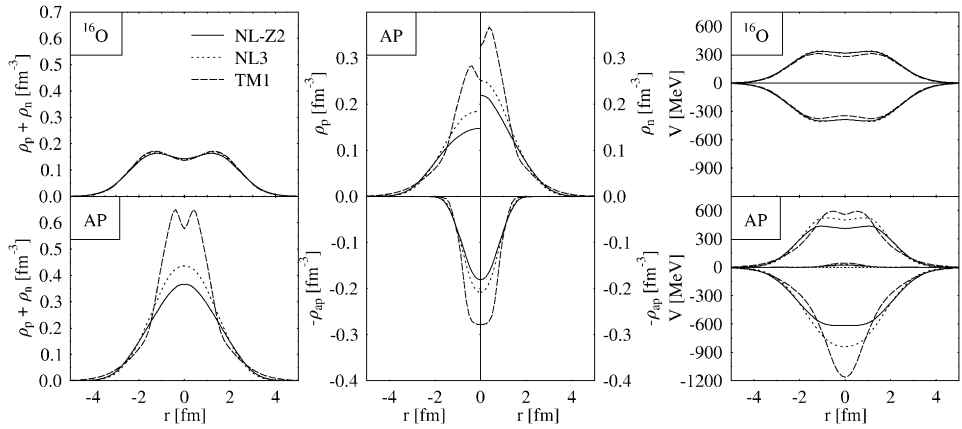


**FIGURE 8.26** The left panel represents the sum of proton and neutron densities as function of nuclear radius for $^{16}$O without (top) and with an antiproton (denoted by AP). The left and right parts of the upper middle panel show separately the proton and neutron densities, the lower part of this panel displays the antiproton density (with minus sign). The right panel shows the scalar (negative) and vector (positive) parts of the nucleon potential. Small contributions shown in the lower row correspond to the isovector ($\rho$-meson) part.

and meson mean fields is solved iteratively and self-consistently. The numerical code employs axial and reflection symmetry, allowing for axially symmetric deformations of the system.

## 8. STRUCTURE OF LIGHT NUCLEI CONTAINING ANTIPROTONS

As an example, we consider the nucleus $^{16}$O with one antiproton in the lowest bound state. This nucleus is the lightest nucleus for which the mean-field approximation is acceptable, and it is included into the fit of the effective forces NL3 and NL–Z2. The antiproton state is assumed to be in the $s1/2^+$ state. The antiproton contributes with the same sign as nucleons to the scalar density, but with opposite sign to the vector density. This leads to an overall increase of attraction and decrease of repulsion for all nucleons. The antiproton becomes very deeply bound in the $s1/2^+$ state. To maximize attraction, protons and neutrons move to the center of the nucleus, where the antiproton has its largest occupation probability. This leads to a cold compression of the nucleus to a high density. Figure 8.26 shows the densities and potentials for $^{16}$O with and without the antiproton. For normal $^{16}$O all RMF parameterizations considered produce very similar results. The presence of an antiproton dramatically changes the structure of the nucleus. The sum of proton and neutron densities reaches a maximum value of (2–4)$\rho_0$, where $\rho_0 \simeq 0.15\ \text{fm}^{-3}$ is the normal nuclear density, depending on the parametrization. The largest compression is predicted by the TM1 model. This follows from the fact that this parametrization gives the softest equation of state as compared to other forces considered here.

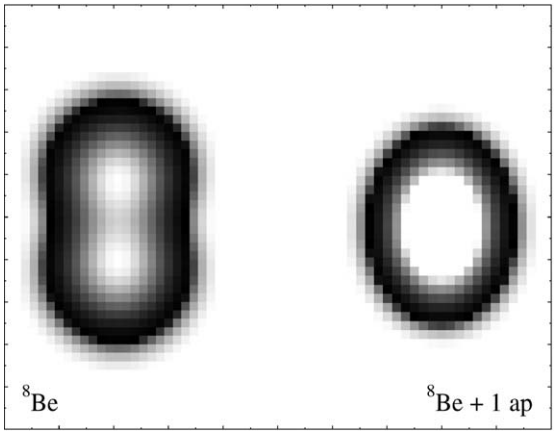


**FIGURE 8.27** Contour plot of nucleon densities for $^8$Be without (left) and with (right) antiproton calculated with the parametrization NL3. The maximum density of normal $^8$Be is 0.20 fm$^{-3}$, while for the nucleus with the antiproton it is 0.61 fm$^{-3}$.

Since nucleons feel a deeper potential as compared to the nucleus without the antiproton, their binding energy increases too. The nucleon binding is largest within the NL3 parametrization. In the TM1 case, the s$1/2^+$ state is also deep, but higher levels are less bound as compared to the NL3 and NL–Z2 calculations. This is a consequence of the smaller spatial extension of the potential in this case. The highest s$1/2^-$ level is even less bound than for the system without an antiproton. The total binding energy of the system is predicted to be 828 MeV for NL–Z2, 1051 MeV for NL3, and 1159 MeV for TM1. For comparison, the binding energy of a normal $^{16}$O nucleus is 127.8, 128.7 and 130.3 MeV in the case of NL–Z2, NL3, and TM1, respectively. Due to this anomalous binding we call these systems Super Bound Nuclei (SBN).

As a second example, we investigate the effect of a single antiproton inserted into the $^8$Be nucleus, see Figure 8.27. In this calculation only the NL3 parametrization was used (the effect is similar for all three forces). The normal $^8$Be nucleus is not spherical, exhibiting a clearly visible $2\alpha$ structure with the deformation $\beta_2 \simeq 1.20$ in the ground state. Inserting the antiproton gives rise to compression and change of nuclear shape. Its maximum density increases by a factor of three from 0.20 to 0.61 fm$^{-3}$. The cluster structure of the ground state completely vanishes. A similar effect has been predicted in Ref. [51] for the case of the $K^-$ bound state in the $^8$Be nucleus. In our case the binding energy increases from 52.9 MeV (the experimental value is 56.5 MeV) to about 700 MeV!

## 9. DOUBLY-MAGIC LEAD WITH ANTIPROTON AND ANTI-ALPHA

We would like to discuss here the structural effect of an antiproton or an anti-alpha nucleus in the doubly magic lead nucleus. Contour plots of the sum of proton and neutron densities are shown in Figure 8.28: lead with an antiproton

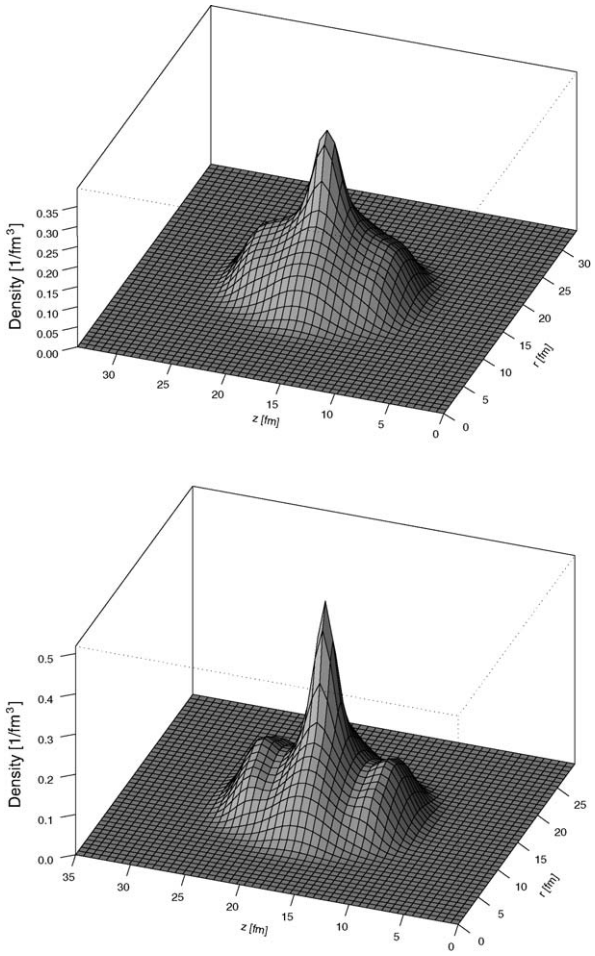


**FIGURE 8.28** Surface plots of the sum of proton and neutron densities for the systems: $^{208}$Pb with $\bar{p}$ (top) and $^{208}$Pb with $\bar{\alpha}$ (bottom).

(and lead with an anti-alpha nucleus). In these cases we encounter a quite different scenario: again, the complete system is affected, but not in the sense that the whole nucleus shrinks and becomes very dense. Here, a small and localized region of high density develops within the heavy system. Additionally, the lead nucleus deforms itself. This effect is largest for the case of lead with $\bar{\alpha}$. The single-particle levels (Figure 8.29) reflect this behavior and indicate the cause for the deformation of lead: In a small region with a deep potential, only states with small angular momenta can be bound deeply. States with higher angular momenta do not have much overlap with the potential. This is exactly what can be concluded from Figure 8.29. We see that basically only the lowest s- and p-states can be bound deeper than for lead without any antiparticles present. Higher lying states do not gain significantly binding or are even lesser bound.

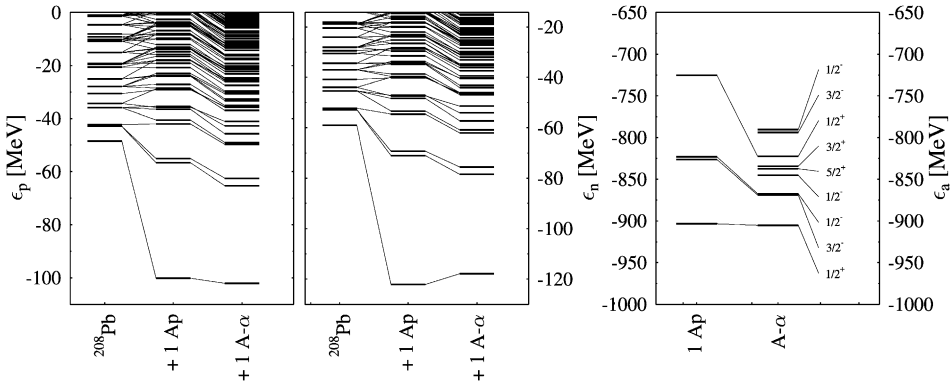


**FIGURE 8.29** Single particle levels of protons (left), neutrons (middle) and antiproton levels (right) for the systems $^{208}$Pb, $^{208}$Pb $+ \bar{p}$ and $^{208}$Pb $+ \bar{\alpha}$.

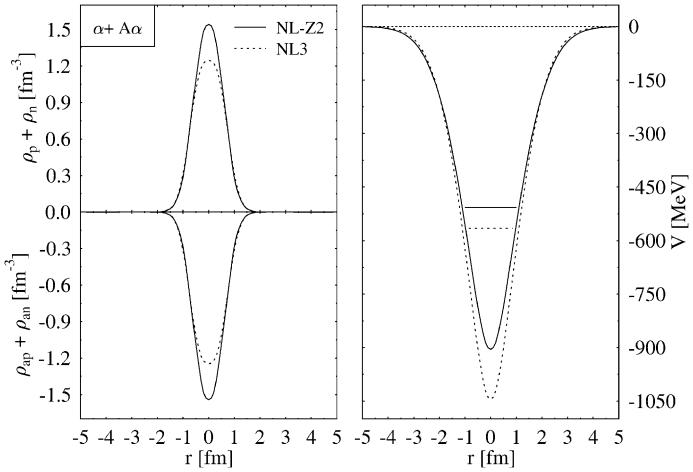


**FIGURE 8.30** The left panel shows the sum of proton and neutron densities (top) as well as the corresponding sum for antibaryons for the $\alpha$–$\bar{\alpha}$ system. The right panels shows the scalar potentials and the single particles levels of the nucleons and antinucleons.

The deformation effect probably has two reasons: firstly, a deformation might be energetically favorable to gain some binding for the higher lying states. Secondly, the distortion of the system due to the presence of antiparticles destroys the magicity of the system.

## 10. SYSTEMS WITH TOTAL BARYON NUMBER ZERO

It is interesting to consider finite systems having total baryon number zero, i.e. systems with the same amount of baryons and antibaryons. In the following we will present the cases of an $\alpha$–anti-$\alpha$ and an $^{16}$O–anti-$^{16}$O system. Figure 8.30 shows the

results for a system consisting of an $\alpha$–$\bar{\alpha}$ system. The total system possesses a quite small radius and large baryon and antibaryon densities. The total baryon density is exactly zero. Due to the inverse coupling of antibaryons to the vector field and the negative charge of the antibaryons, all sources and potentials except for the scalar one vanish completely! All particles occupy a single particle state with exactly the same energy, and they all feel the same potential, namely the scalar potential, to which all particles present in the system couple alike. The binding energy of this nuclear system is huge: 2649 MeV with the force NL3 and 2235 MeV with NL–Z2. This is about 100 times larger than the binding energy of one $\alpha$, and about 20 times larger than the binding energy of 8 nucleons, namely, doubly magic oxygen.

A similar structural effect occurs for the system of $^{16}$O–anti-$^{16}$O. Again, all potentials except the scalar one vanish exactly. The binding energy of this system is 13227 MeV with NL3. All nucleons and antinucleons reside in the lowest s- and p-levels. They are quite deeply bound (the lowest s1/2$^+$ levels is bound by about 750 MeV).

## 11. LIFE TIME, FORMATION PROBABILITY AND SIGNATURES OF SBNS

The crucial question concerning a possible observation of the SBNs is their life time. The only decay channel for such states is the annihilation on surrounding nucleons. The mean life time of an antiproton in nucleonic matter of density $\rho_B$ can be estimated as $\tau = \langle \sigma_A v_{\rm rel} \rho_B \rangle^{-1}$, where angular brackets denote averaging over the wave function of the antiproton and $v_{\rm rel}$ is its relative velocity with respect to nucleons. In vacuum the $N\bar{N}$ annihilation cross section at low $v_{\rm rel}$ can be parametrized as [52] $\sigma_A = C + D/v_{\rm rel}$ with $C = 38$ mb and $D = 35$ mb. For $\langle \rho_B \rangle \simeq 2\rho_0$ this would lead to a very short life time, $\tau \simeq 0.7$ fm/c (for $v_{\rm rel} \simeq 0.2c$). However, one should bear in mind that the annihilation process is very sensitive to the phase space available for decay products. For a bound nucleon and antinucleon the available energy is $Q = 2m_N - B_N - B_{\bar{N}}$, where $B_N$ and $B_{\bar{N}}$ are the corresponding binding energies. As follows from our calculations, this energy is strongly reduced compared to $2m_N$, namely, $Q \simeq$ 600–680 MeV (TM1), 810–880 MeV (NL3) and 990–1050 MeV (NL–Z2) for the lowest antiproton states.

For such low values of $Q$ many important annihilation channels involving two heavy mesons ($\rho$, $\omega$, $\eta$, $\eta'$, ...) are simply closed. Other two-body channels such as $\pi\rho$, $\pi\omega$ are considerably suppressed due to the closeness to the threshold. As is well known, the two-pion final states contribute only about 0.4% of the annihilation cross section. Even in vacuum all above mentioned channels contribute to $\sigma_A$ not more than 15% [53]. Therefore, we expect that only multi-pion final states contribute significantly to antiproton annihilation in the SBN. But these channels are strongly suppressed due to the reduction of the available phase space. Our calculations show that changing $Q$ from 2 to 1 GeV results in suppression factors 5, 40 and 1000 for the annihilation channels with 3, 4 and 5 pions in the final state, respectively. Applying these suppression factors to the experimental branching ratios [54] we come to the conclusion that in the SBNs the annihilation rates can be

easily suppressed by factor of 20–30. There could be additional suppression factors of a structural origin which are difficult to estimate at present. This brings the SBN life time to the level of 15–20 fm/c which makes their experimental observation feasible. The corresponding width, $\Gamma \sim 10$ MeV, is comparable to that of the $\omega$-meson.

Let us discuss now how these exotic nuclear states can be produced in the laboratory. We believe that the most direct way is to use antiproton beams of multi-GeV energy. This high energy is needed to suppress annihilation on the nuclear surface which dominates at low energies. To form a deeply bound state, the fast antiproton must transfer its energy and momentum to one of the surrounding nucleons. This can be achieved through reactions of the type $\bar{p}N \to B\bar{B}$ in the nucleus,

$$\bar{p} + (A, Z) \to B + {}_{\bar{B}}(A-1, Z'), \tag{3}$$

where $B = n, p, \Lambda, \Sigma$. The fast baryon $B$ can be used as a trigger of events where the antibaryon $\bar{B}$ is trapped in the nucleus. Obviously, this is only possible in inelastic $\bar{p}N$ collisions accompanied by the production of pions or particle–hole excitations. One can think even about producing an additional baryon–antibaryon pair and forming a nucleus with two antibaryons in the deeply bound states. In this case two fast nucleons will be knocked out from the nucleus.

Without detailed transport calculations it is difficult to find the formation probability, $W$, of final nuclei with trapped antinucleons in these reactions. A rough estimate can be obtained by assuming that antiproton stopping is achieved in a single inelastic collision somewhere in the nuclear interior, i.e., taking the penetration length of the order of the nuclear radius $R$. From the Poisson distribution in the number of collisions the probability of such an event is

$$w_1 = \frac{R}{\lambda_{\rm in}} \exp\left(-\frac{R}{\lambda}\right), \tag{4}$$

where $\lambda_{\rm in}^{-1} = \sigma_{\rm in}\rho_0$ and $\lambda^{-1} = (\sigma_{\rm in} + \sigma_A)\rho_0$ (here $\sigma_{\rm in}$ and $\sigma_A$ are the inelastic and annihilation parts of the $\bar{p}N$ cross section). The exponential factor in Eq. (4) includes the probability to avoid annihilation. For initial antiproton momenta $p_{\rm lab} \simeq 10$ GeV we use $\sigma_{\rm in} \simeq 25$ mb, $\sigma_A \simeq 15$ mb [54] and get $\lambda \simeq 1.6$ fm which is comparable with the radii of light nuclei. For an oxygen target, using $R \simeq 3$ fm leads to $w_1 \simeq 0.17$.

In fact we need relatively small final antiproton momenta to overlap significantly with the momentum distribution of a bound state, namely, $\Delta p \sim \pi/R_{\bar{p}}$, where $R_{\bar{p}} \simeq 1.5$ fm is the characteristic size of the antiproton spatial distribution (see Figure 8.26). The probability of such a momentum loss can be estimated by the method of Refs. [55,56] which was previously used for calculating proton spectra in high-energy pA collisions. At relativistic bombarding energies the differential cross sections of the $\bar{p}p \to \bar{p}X$ and $pp \to pX$ reactions are similar. The inelastic parts of these cross sections drop rapidly with transverse momentum, but they are practically flat as a function of longitudinal momentum of secondary particles. Thus, the probability of the final antiproton momentum to fall in the interval

$\Delta p$ is simply $\Delta p/p_{\rm lab}$. For $p_{\rm lab} = 10\,{\rm GeV}$ and $\Delta p = 0.4\,{\rm GeV}$ this gives 0.04. Assuming the geometrical fraction of central events ∼20% we get the final estimate $W \simeq 0.17\times 0.04\times 0.2 \simeq 1.4\cdot 10^{-3}$. One should bear in mind that additional reduction factors may come from the matrix element between the bare massive antibaryon and the dressed almost massless antibaryon in a deeply bound state. But even with extra factors $\sim 10^{-1}$–$10^{-2}$ which may come from the detailed calculations the detection of SBNs is well within the modern experimental possibilities.

Finally, we mention a few possible signatures of SBNs which can be used for their experimental detection. First of all, we remind the reader that according to the Dirac picture, any real antibaryon should be interpreted as a hole in the otherwise filled Dirac sea. Therefore, the nucleons from the positive-energy states of the Fermi sea can make direct transitions to the vacant negative-energy states of the Dirac sea. These super-transitions will be accompanied by the emission of a single pion or kaon depending on the nature of the trapped antibaryon. The energy of such a super-transition is fixed by the discrete levels of the initial and final baryons and according to our calculations should be of about 1 GeV. Obviously, this emission should be isotropic in the rest frame of the nucleus. The 1-pion or 1-kaon annihilation is a unique feature of finite nuclear systems. In vacuum such transitions are forbidden by the energy-momentum conservation. Therefore, the observation of a line in the pion or kaon spectrum at energies between 1 and 2 GeV would be a clear signal of the deep antibaryon states in nuclei. One can also look for narrow photon lines with energies in the range from 40 to 200 MeV corresponding to the transitions of nucleons and antibaryons between their respective levels. It is interesting to note that these signals will survive even if due to the lack of time the nucleus does not fully rearrange to a new structure.

Another strong signal may come from the collective response of the target nucleus to the presence of an antibaryon. Initially the nucleons will acquire radial acceleration due to the attractive interaction with the trapped antibaryon. This will lead to a collective motion similar to monopole oscillations around the compressed SBN state. Moreover, annihilation of the antibaryon will leave the nuclear remnant in a nonequilibrium state of high density. The nuclear system will expand and eventually break up into fragments. Therefore, the decay of the SBN state will result in nuclear multifragmentation with large collective flow of fragments. Both proposed signatures require rather ordinary measurements, which should be easy to perform with standard detectors.

## 12. COLD COMPRESSION: NUCLEAR AND QUARK MATTER

It is interesting to look at the antibaryon–nucleus system from somewhat different point of view. An antibaryon implanted into a nucleus acts as an attractor for surrounding nucleons. Due to the uncompensated attractive force these nucleons acquire acceleration towards the center. As the result of this inward collective motion the nucleons pile up producing local compression. If this process would be completely elastic it would generate monopole-like oscillations around the compressed SBN state. The maximum compression is reached when the attractive

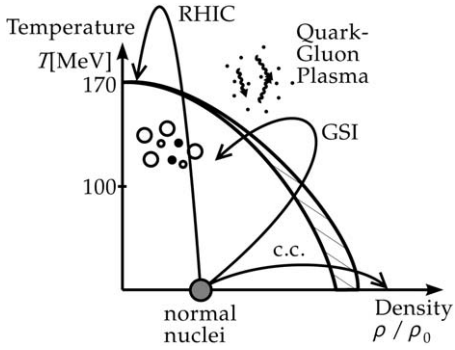


**FIGURE 8.31** The phase diagram of strongly interacting matter. The antiproton-induced cold compression (c.c.) takes place at low temperatures and high densities, a regime that cannot be accessed in heavy-ion collisions. The curves with arrows denote dynamic trajectories of matter in heavy-ion collisions as expected at the future GSI facility and the relativistic heavy-ion collider (RHIC) at Brookhaven National Laboratory.

potential energy becomes equal to the compression energy. Simple estimates show that local baryon densities up to 5 times the normal nuclear density may be obtained in this way. It is most likely that the deconfinement transition will occur at this stage and a high-density cloud containing an antibaryon and a few nucleons will appear in the form of a multi-quark–antiquark cluster. One may speculate that the whole $^4$He or even $^{16}$O nucleus can be transformed into the quark phase by this mechanism. As shown in Ref. [57], an admixture of antiquarks to cold quark matter is energetically favorable. The problem of annihilation is now transferred to the quark level. But the argument concerning the reduction of available phase space due to the entrance-channel nuclear effects should work in this case too. Thus one may hope to produce relatively cold droplets of the quark phase by the inertial compression of nuclear matter initiated by an antibaryon.

The admixture of antibaryons to finite nuclei provides an almost unique doorway to the study of cold compressed nuclear and/or quark matter in the laboratory. This region of the phase diagram of strongly interacting matter, see Figure 8.31, is not accessible by collisions of heavy ions, which produce matter which is simultaneously hot and dense.

## 13. THE VACUUM IN QUANTUM ELECTRODYNAMICS

It is generally accepted that the physical vacuum has a nontrivial structure. This conclusion was first made by Dirac on the basis of his famous equation for a fermion field which describes simultaneously particles and antiparticles. The Dirac equation in the vacuum has a simple form

$$\left(i\gamma^\mu \partial_\mu - m\right)\Psi(x) = 0, \tag{5}$$

where $\gamma^\mu = (\gamma^0, \boldsymbol{\gamma})$ are Dirac matrices, $m$ is the fermion mass and $\Psi(x)$ is a 4-component spinor field. For a plane wave solution $\Psi(x) = e^{-ipx}u_p$ this equation is

written as

$$(\hat{p} - m)u_p = 0, \tag{6}$$

where $\hat{p} = \gamma^0 E - \boldsymbol{\gamma}\mathbf{p}$. Multiplying by $(\hat{p} + m)$ and requiring that $u_p \neq 0$ one obtains the equation $E^2 - \mathbf{p}^2 - m^2 = 0$ which has two solutions

$$E^{\pm}(\mathbf{p}) = \pm\sqrt{\mathbf{p}^2 + m^2}. \tag{7}$$

Here the + sign corresponds to particles with positive energy $E_N(\mathbf{p}) = E^+(\mathbf{p})$, while the − sign corresponds to solutions with negative energy. To ensure stability of the physical vacuum Dirac has assumed that these negative-energy states are occupied forming what is called now the Dirac sea. Then the second solution of Eq. (7) receives natural interpretation: it describes holes in the Dirac sea. These holes are identified with antiparticles. Their energies are obviously given by $E_{\bar{N}}(\mathbf{p}) = -E^-(-\mathbf{p}) = \sqrt{\mathbf{p}^2 + m^2}$. Unfortunately, the Dirac sea brings divergent contributions to physical quantities such as energy density, and one should introduce a proper regularization scheme to get rid off these divergences. This picture has received numerous confirmations in quantum electrodynamics and other fields.

One of the most fascinating aspects is the structure of the vacuum in QED and its change into charged vacuum states under the influence of strong (supercritical) electric fields [58]. We shortly remind of this phenomenon.

Figure 8.32 shows the diving of the deeply bound states into the lower energy continuum of the Dirac equation.

In the supercritical case the dived state is degenerate with the (occupied) negative electron states. Hence spontaneous $e^+e^-$ *pair creation* becomes possible, where an electron from the Dirac sea occupies the additional state, leaving a hole in the sea which escapes as a positron while the electron's charge remains near the source. This is a fundamentally new process, whereby the neutral vacuum of QED becomes unstable in supercritical electrical fields. It decays within about $10^{-19}$ s into a charged vacuum. The charged vacuum is now stable due to the Pauli principle, that is the number of emitted particles remains finite. The vacuum is first charged twice because two electrons with opposite spins can occupy the 1s shell. After the $2p_{1/2}$ shell has dived beyond $Z_{\mathrm{cr}} = 185$, the vacuum is charged four times, etc. This change of the vacuum structure is not a perturbative effect, as are the radiative QED effects (vacuum polarization, self-energy, etc.).

The time-dependence of the energy levels in a supercritical heavy-ion collision is depicted in Figure 8.33. An electron (or hole) which was in a certain molecular eigenstate at the beginning of the collision can be transfered with a certain probability into different states by the dynamics of the collision. This can lead to the hole production in an inner shell by excitation of an electron to a higher state and/or hole production by ionization of an electron to the continuum. Further possibilities are induced positron production by excitation of an electron from the lower continuum to an empty bound level and direct pair production [59].

A comparison of the theoretical predictions and expectations and experimental data is shown in Figure 8.34. Sharp positron peeks can be expected if there were a mechanism in the heavy ion collision leading to a time delay. This may be caused

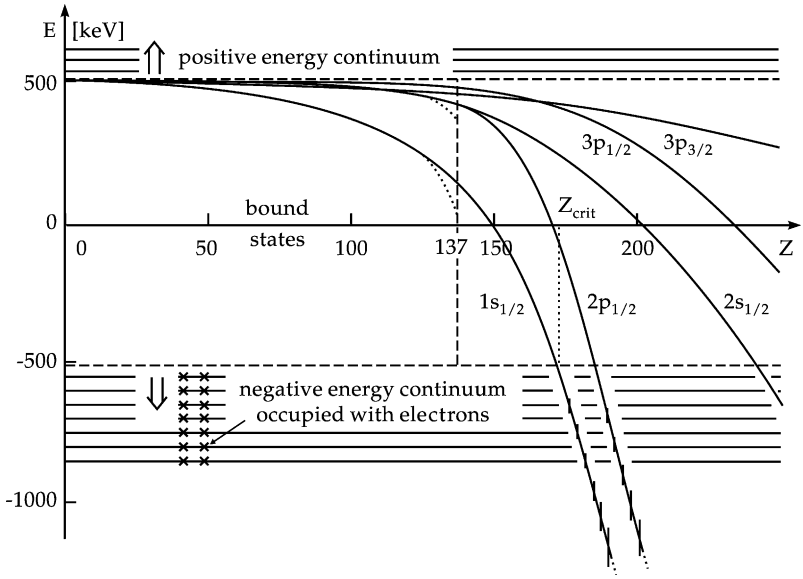


**FIGURE 8.32** Lowest bound states of the Dirac equation for nuclei with charge $Z$. While the Sommerfeld fine-structure energies (dashed line) for $\xi = 1$ (s states) end at $Z = 137$, the solutions for extended Coulomb potentials (full line) can be traced down to the negative-energy continuum reached at the critical charge $Z_{cr}$ for the 1s state. The bound states entering the continuum obtain a spreading width as indicated.

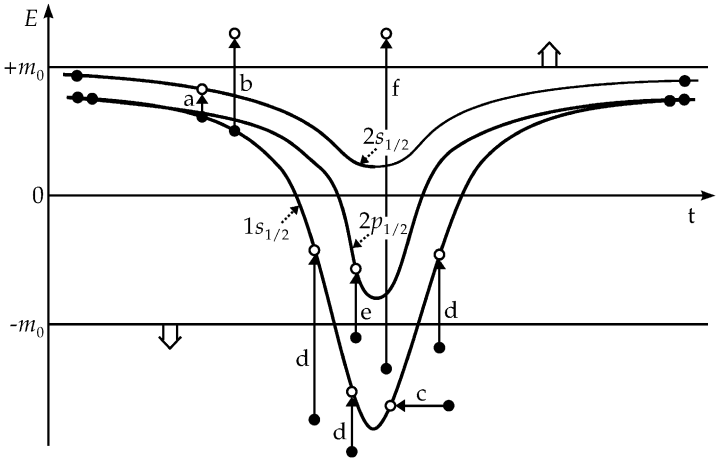


**FIGURE 8.33** Time dependence of the quasi-molecular energy levels in a supercritical heavy-ion collision. The arrows denote various excitation processes which lead to the production of holes and positrons.

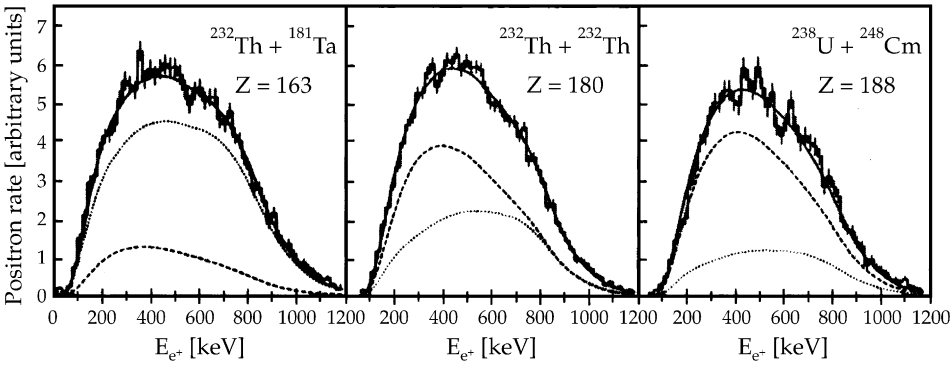


**FIGURE 8.34** Positron energy spectra measured in collisions of Th + Ta, Th + Th, and U + Cm at energies of about 6 MeV per nucleon. The QED predictions (dashed lines) and the experimentally determined background from nuclear pair conversion (dotted lines) add up to the full lines which are in close agreement with experiment.

by a pocket in the potential between the two ions. Spontaneous pair production should then be enhanced in supercritical systems. Until now, however, the situation remains inconclusive [59].

## 14. ON SUPERHEAVY ELEMENT FORMATION AND BEYOND

Superheavy (SH) nuclei obtained in "cold" fusion reactions with Pb or Bi target [60] are along the proton drip line and very neutron-deficient with a short half-life. In fusion of actinides with $^{48}$Ca more neutron-rich SH nuclei are produced [61] with much longer half-life. But they are still far from the center of the predicted "island of stability" formed by the neutron shell around $N = 184$ (see the nuclear map in Figure 8.35). In the "cold" fusion, the cross sections of SH nuclei formation decrease very fast with increasing charge of the projectile and become less than 1 pb for $Z > 112$. Heaviest transactinide, Cf, which can be used as a target in the second method, leads to the SH nucleus with $Z = 118$ being fused with $^{48}$Ca. Using the next nearest elements instead of $^{48}$Ca (e.g., $^{50}$Ti, $^{54}$Cr, etc.) in fusion reactions with actinides is expected less encouraging, though experiments of such kind are planned to be performed. In this connection other ways to the production of SH elements in the region of the "island of stability" should be searched for.

About twenty years ago transfer reactions of heavy ions with $^{248}$Cm target have been evaluated for their usefulness in producing unknown neutron-rich actinide nuclides [62,63]. The cross sections were found to decrease very rapidly with increasing atomic number of surviving target-like fragments. However, Fm and Md neutron-rich isotopes have been produced at the level of 0.1 μb. Theoretical estimations for production of primary superheavy fragments in the damped U + U collision have been also performed at this time within the semiphenomenological diffusion model [64]. In spite of obtained high probabilities for the yields of

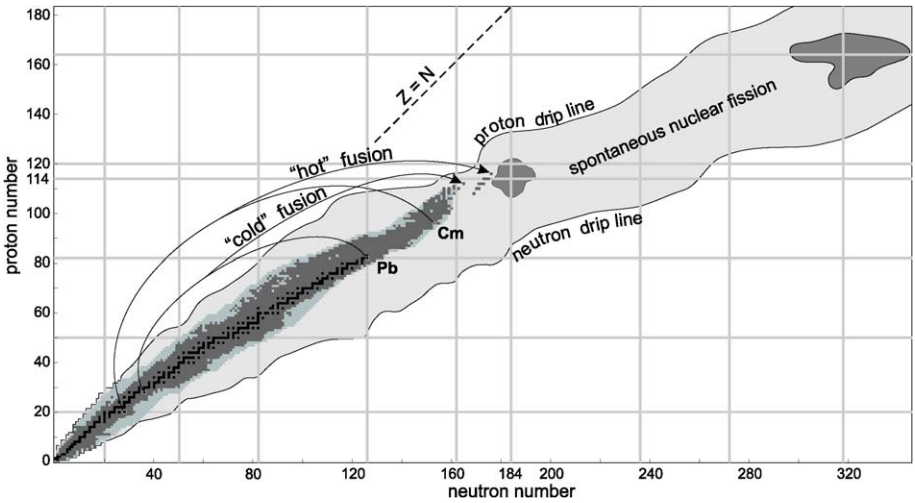


**FIGURE 8.35** Nuclear map. Predicted islands of stability are shown around $Z = 114$, $N = 184$ and $Z = 164$, $N = 318$.

superheavy primary fragments (more than $10^{-2}$ mb for $Z = 120$), the cross sections for production of heavy nuclei with low excitation energies were estimated to be rather small: $\sigma_{CN}(Z = 114, E^* = 30\,\text{MeV}) \sim 10^{-6}$ mb for U + Cm collision at 7.5 MeV/nucleon beam energy. The authors concluded, however, that "fluctuations and shell effects not taken into account may considerably increase the formation probabilities."

Here we study the processes of low energy collisions of very heavy nuclei (such as U + Cm) within the recently proposed model of fusion–fission dynamics [65]. The purpose is to find an influence of the nearest closed shells $Z = 82$ and $N = 126$ (formation of $^{208}$Pb as one of the primary fragments) on nucleon rearrangement between primary fragments. We try to estimate how large the charge and mass transfer can be in these reactions and what the cross sections for production of surviving neutron-rich SH nuclei are. Direct time analysis of the collision process allows us to estimate also the lifetime of the composite system consisting of two touching heavy nuclei with total charge $Z > 180$. Such "long-lived" configurations may lead to spontaneous positron emission from super-strong electric fields of quasi-atoms by a fundamental QED process (transition from neutral to charged QED vacuum) [66,67], see schematic Figure 8.36.

## 14.1 Adiabatic dynamics of heavy nuclear system

Besides the distance between the nuclear centers, $R$, the mass transfer, $\alpha = (A_1 - A_2)/(A_1 + A_2)$ and dynamic deformations of nuclear surfaces, $\beta$, play a most important role in fusion–fission and deep inelastic processes of low energy heavy-ion collisions. The corresponding multi-dimensional adiabatic potential energy surface was calculated here within the semi-empirical two-core approach [68] based

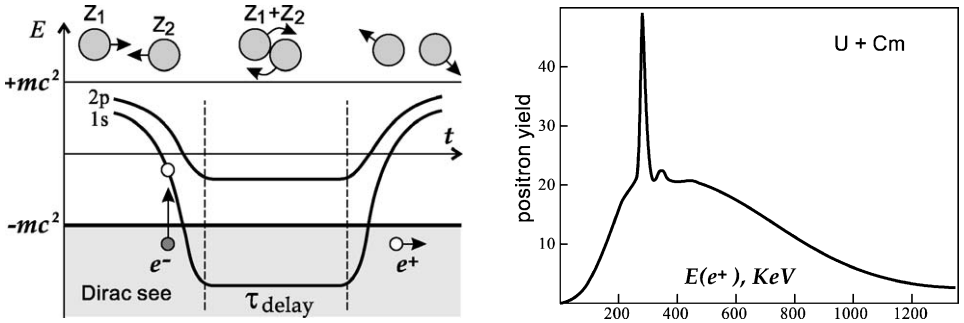


**FIGURE 8.36** Schematic figure of spontaneous decay of the vacuum and spectrum of the positrons formed in supercritical electric field ($Z_1 + Z_2 > 173$).

on the two-center shell model idea [69]. Projections onto the $R$–$\alpha$ and $R$–$\beta$ planes of the three-dimensional potential energy are shown in Figure 8.37 for the nuclear system formed in collision of $^{232}$Th + $^{250}$Cf. There is no potential pocket typical for lighter systems, the potential is repulsive everywhere. However, the potential energy is not so much steep in the region of contact point and two nuclei may keep in contact for a long time increasing their deformations and transferring nucleons to each other (see below).

We studied the whole dynamics of such a nuclear system by numerical solution of the coupled Langevin-type equations of motion, inertialess motion along the mass-asymmetry coordinate was derived just from the corresponding master equation for nucleon transfer [65]. The inertia parameters $\mu_R$ and $\mu_\beta$ were calculated within the Werner–Wheeler approach [70]. Parameters of the friction forces and nucleon transfer rate were taken from Ref. [65], where they have been estimated from successful description of experimental regularities of heavy ion deep inelastic scattering and fusion–fission reactions. Damping of the shell effects due to the excitation energy has been taken into account in the level density parameter both on the dynamic stage of the reaction and in statistical treatment of decay of the primary fragments.

The cross sections are calculated in a natural way. A large number of events (trajectories) are tested for a given impact parameter. Each event in studied reactions ends in the exit channel with two excited primary fragments. The corresponding double differential cross-section is calculated as follows

$$\frac{d^2\sigma_\alpha}{d\Omega\, dE}(E,\theta) = \int_0^\infty b\, db \frac{\Delta N_\alpha(b,E,\theta)}{N_{\rm tot}(b)} \frac{1}{\sin(\theta)\Delta\theta\,\Delta E}. \tag{8}$$

Here $\Delta N_\alpha(b,E,\theta)$ is the number of events at a given impact parameter $b$ in which the system enters into the channel $\alpha$ with kinetic energy in the region $(E, E+\Delta E)$ and center-of-mass outgoing angle in the region $(\theta, \theta+\Delta\theta)$, $N_{\rm tot}(b)$ is the total number of simulated events for a given value of impact parameter.

The expression (8) describes the energy, angular, charge and mass distributions of the *primary* fragments formed in the reaction. Subsequent de-excitation of these fragments via fission or emission of light particles and gamma-rays was taken into

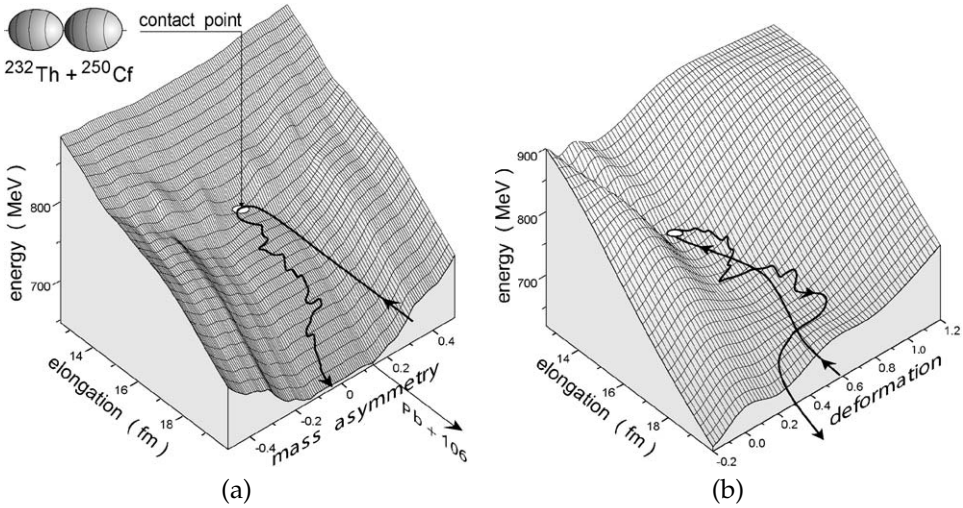


**FIGURE 8.37** Potential energy surface for the nuclear system formed by $^{232}$Th + $^{250}$Cf as a function of $R$ and $\alpha$ ($\beta = 0.22$) (a), and $R$ and $\beta$ ($\alpha = 0.037$) (b). Typical trajectory is shown by the thick curves with arrows.

account within the statistical model leading to the *final* fragment distributions. The sharing of the excitation energy between the primary fragments was assumed to be proportional to their masses. These fragments possess also some definite deformations at scission configuration. We assumed that the dynamic deformation relaxes rather fast to the ground state deformation (faster than neutron evaporation) and simply added the deformation energy to the total excitation energy of a given nucleus. Neutron emission during an evolution of the system was also taken into account. However, it was found that the pre-separation neutron evaporation does not influence significantly the final distributions.

## 14.2 Damped collisions of transuranium nuclei

Found in such a way mass and charge distributions of the primary and survived fragments formed in the $^{232}$Th + $^{250}$Cf collision at 800 MeV center-of mass energy are shown in Figure 8.38. The pronounced shoulder can be seen in the mass distribution of the primary fragments near the mass number $A = 208$. It could be explained by existence of noticeable valley on the potential energy surface (see Figure 8.37a), which corresponds to formation of doubly magic nucleus $^{208}$Pb ($\alpha = 0.137$). The emerging of the nuclear system into this valley resembles the well-known quasi-fission process and may be called "inverse (or anti-symmetrizing) quasi-fission" (the final mass asymmetry is larger than initial one). For $\alpha > 0.137$ (one fragment becomes lighter than lead) the potential energy sharply increases and the mass distribution of the primary fragments falls down rapidly at $A < 208$ ($A > 274$). The same is for the charge distribution at $Z < 82$ ($Z > 106$). As a result, in the charge distribution of survived heavy fragments, Figure 8.38b, there is also a

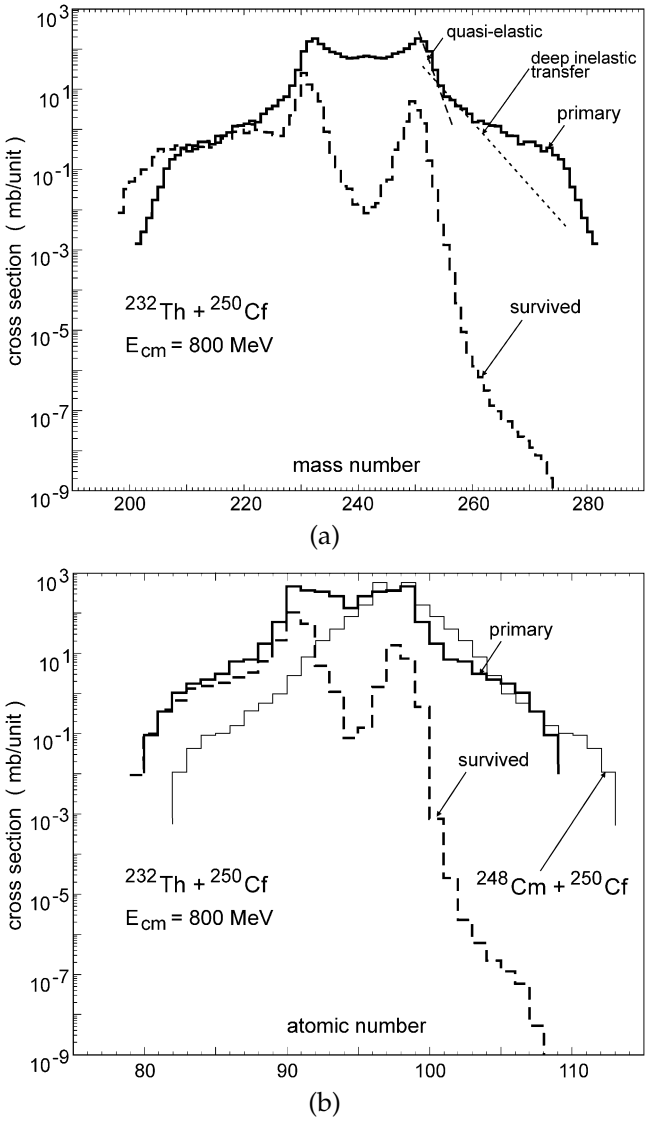


**FIGURE 8.38** Mass (a) and charge (b) distributions of primary (solid histograms) and survived (dashed histograms) fragments in the $^{232}$Th + $^{250}$Cf collision at 800 MeV center-of-mass energy. Thin solid histogram in (b) shows the primary fragment distribution in the hypothetical reaction $^{248}$Cm + $^{250}$Cf.

shoulder at $Z = 106$ and the yield of nuclei with $Z > 107$ was found in this reaction at the level of less than 1 pb. This result differs sharply from those obtained within the diffusion model [64], where the yield of heavy primary fragments decreases slowly and monotonically with increasing charge number.

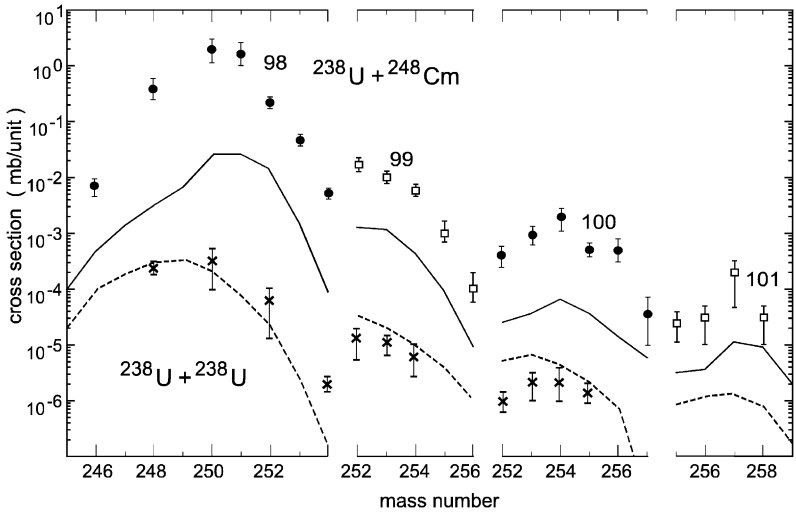


**FIGURE 8.39** Isotopic yield of the elements 98–101 in the reactions $^{238}U + ^{238}U$ (crosses) [71] and $^{238}U + ^{248}Cm$ (circles and squares) [62]. The curves show the result of our calculations.

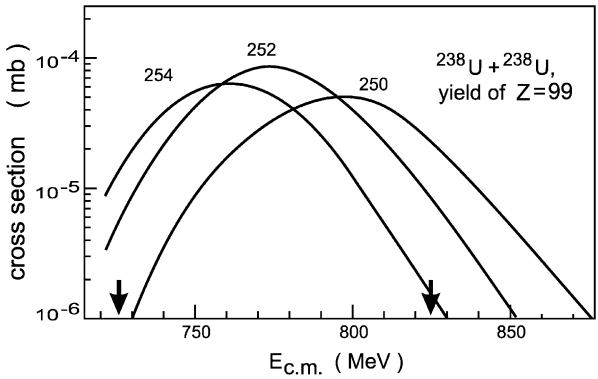


**FIGURE 8.40** Excitation functions for the yields of Es isotopes (numbers near the curves) for the $^{238}U + ^{238}U$ reactions. The arrows indicate potential energy of two nuclei in contact ($r_0 = 1.16$ fm) for tip or nose-to-nose (left) and side or belly-to-belly (right) configurations.

In Figure 8.39 the available experimental data on the yield of SH nuclei in collisions of $^{238}U + ^{238}U$ [71] and $^{238}U + ^{248}Cm$ [62] are compared with our calculations. In these experiments thick targets have been used, which means that the experimental data were, in fact, integrated over the energy in the region of about 750–850 MeV [71,62]. The estimated excitation functions for the yield of heavy surviving nuclei, shown in Figure 8.40, demonstrate not so sharp as in fusion reactions but still rather strong dependence on beam energy. In spite of that, the agreement of our calculations with experimental data is quite acceptable (worse for few-nucleon transfer and better for massive transfer processes).

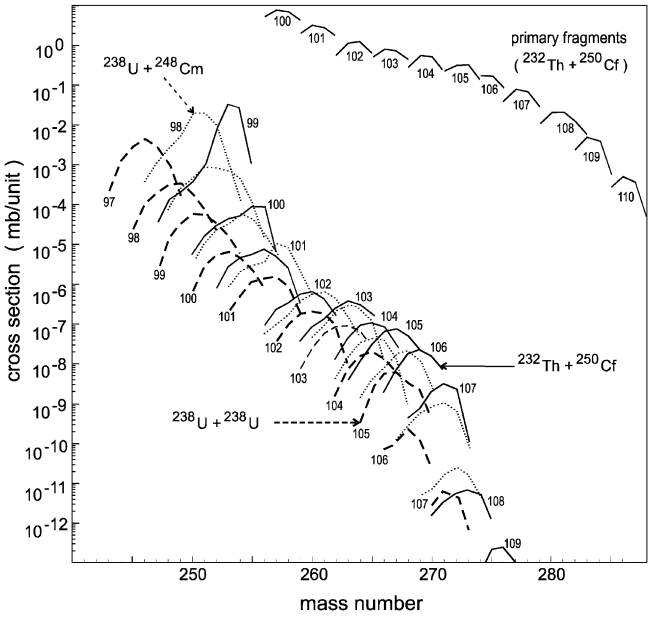


**FIGURE 8.41** Yield of superheavy nuclei in collisions of $^{238}U + ^{238}U$ (dashed), $^{238}U + ^{248}Cm$ (dotted) and $^{232}Th + ^{250}Cf$ (solid lines) at 800 MeV center-of-mass energy. Solid curves in upper part show isotopic distribution of primary fragments in the Th + Cf reaction. In the case of U + Cm the upper curve only is marked by $Z$-number ($Z = 98$), the others are one by one up to $Z = 107$.

The estimated isotopic yields of SH nuclei in the $^{232}Th + ^{250}Cf$, $^{238}U + ^{238}U$ and $^{238}U + ^{248}Cm$ collisions at 800 MeV center-of-mass energy are shown in Figure 8.41. Thus there is a real chance for production and chemical study of the long-lived neutron-rich SH nuclei up to $^{274}_{107}Bh$ produced in the reaction $^{232}Th + ^{250}Cf$. As can be seen from Figures 8.40 and 8.41 the yield of SH elements in damped reactions depends strongly on beam energy and on nuclear combination which should be chosen carefully. In particular, in Figure 8.38 the estimated yield of the primary fragments obtained in the hypothetical reaction $^{248}Cm + ^{250}Cf$ (both constituents are radioactive) is shown, demonstrating a possibility for production of SH neutron-rich nuclei up to the element 112 (complementary to lead fragments in this reaction).

## 14.3 Giant quasi-atoms and spontaneous positron formation

The time analysis of the reactions studied shows that in spite of non-existing attractive potential pocket the system consisting of two very heavy nuclei may hold in contact rather long in some cases. During this time it moves over multidimensional potential energy surface with almost zero kinetic energy (result of large nuclear viscosity), a typical trajectory is shown in Figure 8.37. The total reaction time distribution, $\frac{d\sigma}{d\log(\tau)}$ ($\tau$ denotes the time after the contact of two nuclei), is

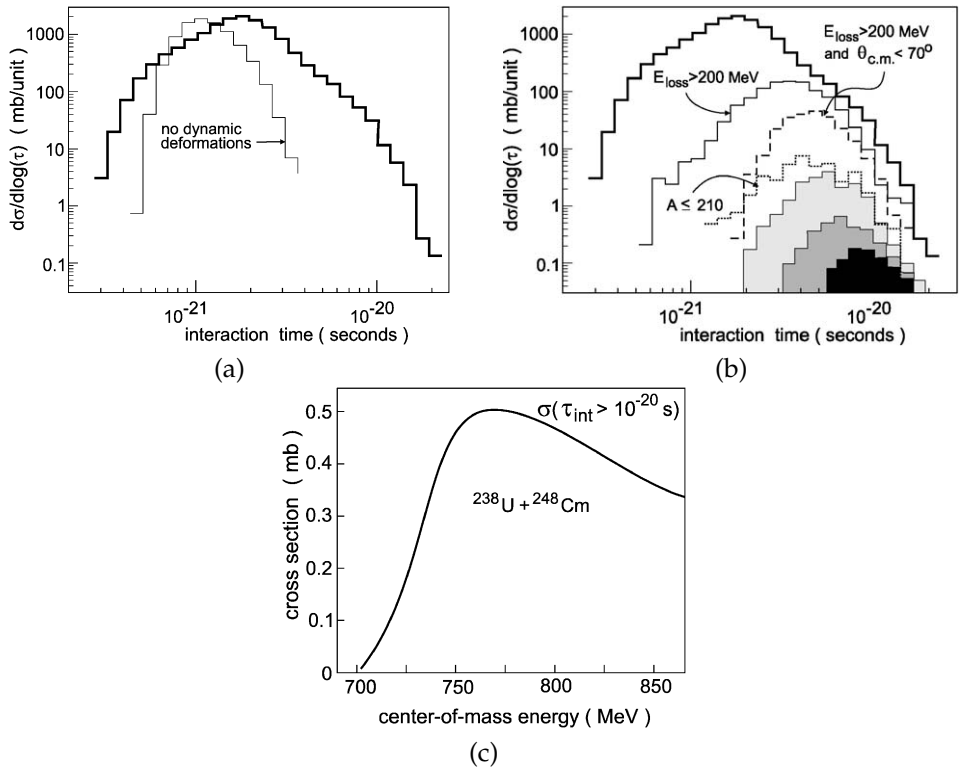


**FIGURE 8.42** Reaction time distributions for the $^{238}$U + $^{248}$Cm collision at 800 MeV center-of-mass energy. Thick solid histograms correspond to all events with energy loss more than 30 MeV. (a) Thin solid histogram shows the effect of switching-off dynamic deformations. (b) Thin solid, dashed and dotted histograms show reaction time distributions in the channels with formation of primary fragments with $E_{\text{loss}} > 200$ MeV, $E_{\text{loss}} > 200$ MeV and $\theta_{\text{c.m.}} < 70°$ and $A \leqslant 210$, correspondingly. Hatched areas show time distributions of events with formation of the primary fragments with $A \leqslant 220$ (light gray), $A \leqslant 210$ (gray), $A \leqslant 204$ (dark) having $E_{\text{loss}} > 200$ MeV and $\theta_{\text{c.m.}} < 70°$. (c) Cross section for events with interaction time longer than $10^{-20}$ s depending on beam energy.

shown in Figures 8.42 and 8.43 for the $^{238}$U + $^{248}$Cm collision. We found that the dynamic deformations are mainly responsible here for the time delay of the nucleus–nucleus collision. Ignoring the dynamic deformations in the equations of motion significantly decreases the reaction time, whereas the nucleon transfer influences the time distribution not so strong, see Figure 8.42a.

As mentioned above, the lifetime of a giant composite system more than $10^{-20}$ s is quite enough to expect for spontaneous $e^+e^-$ production from the strong electric field as a fundamental QED process ("decay of the vacuum") [66,67]. The absolute cross section for long events ($\tau > 10^{-20}$ s) was found to be maximal just at the beam energy ensuring two nuclei to be in contact, see Figure 8.42c. Note that the same energy is also optimal for production of the most neutron-rich SH nu-

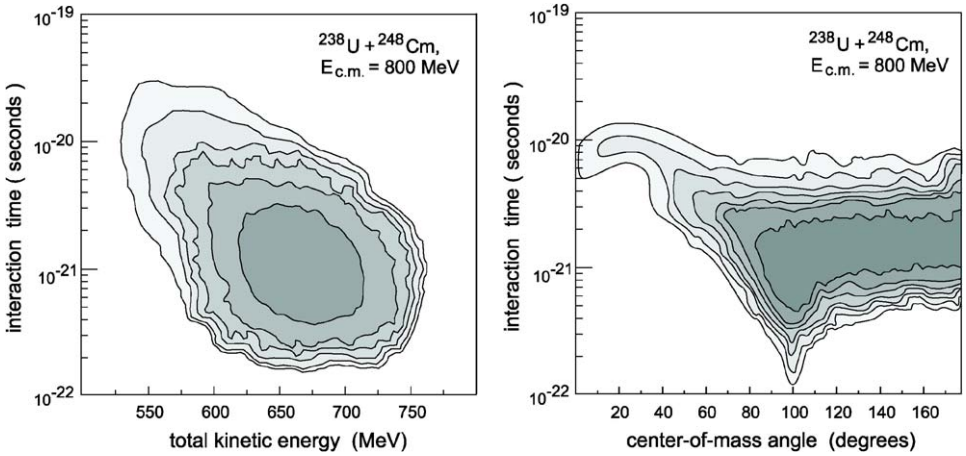


**FIGURE 8.43** Energy–time (a) and angular–time (b) distributions of primary fragments in the $^{238}U + ^{248}Cm$ collision at 800 MeV ($E_{loss} > 15$ MeV). The landscape is shown in logarithmic scale—lines are drawn over one order of magnitude. The quasi-elastic peak is removed.

clei (Figure 8.40). Of course, there are some uncertainties in the used parameters, mostly in the value of nuclear viscosity. However we found only a linear dependence of the reaction time on the strength of nuclear viscosity, which means that the obtained reaction time distribution is rather reliable, see logarithmic scale on both axes in Figure 8.42a.

Formation of the background positrons in these reactions forces one to find some additional trigger for the longest events. Such long events correspond to the most damped collisions with formation of mostly excited primary fragments decaying by fission. However there is also a chance for production of the primary fragments in the region of doubly magic nucleus $^{208}Pb$, which could survive against fission due to nucleon evaporation, see Figures 8.44a and 8.38. The number of the longest events depends weakly on impact parameter up to some critical value. On the other hand, in the angular distribution of all the excited primary fragments (strongly peaked at the center-of-mass angle slightly larger than 90°) there is the rapidly decreasing tail at small angles, see Figure 8.44b. Thus the detection of the surviving nuclei in the lead region at the center-of-mass angles less than 60° could be a definite witness for a long reaction time.

The production of long-lived neutron-rich SH nuclei in collisions of transuranium ions seems to be quite possible due to a large mass and charge rearrangement in the "inverse quasi-fission" process caused by the $Z = 82$ and $N = 126$ nuclear shells. Radiochemical identification of $^{267,268}Db$ isotopes, produced in the U + Cm or Th + Cf reactions, could be performed, for example, to test this conclusion. If the found cross section will be higher than 10 pb, then the subsequent experiments with such reactions could be planned aimed to the production of SH nuclei just in the region of the "island of stability." Parallel search for spontaneous positron

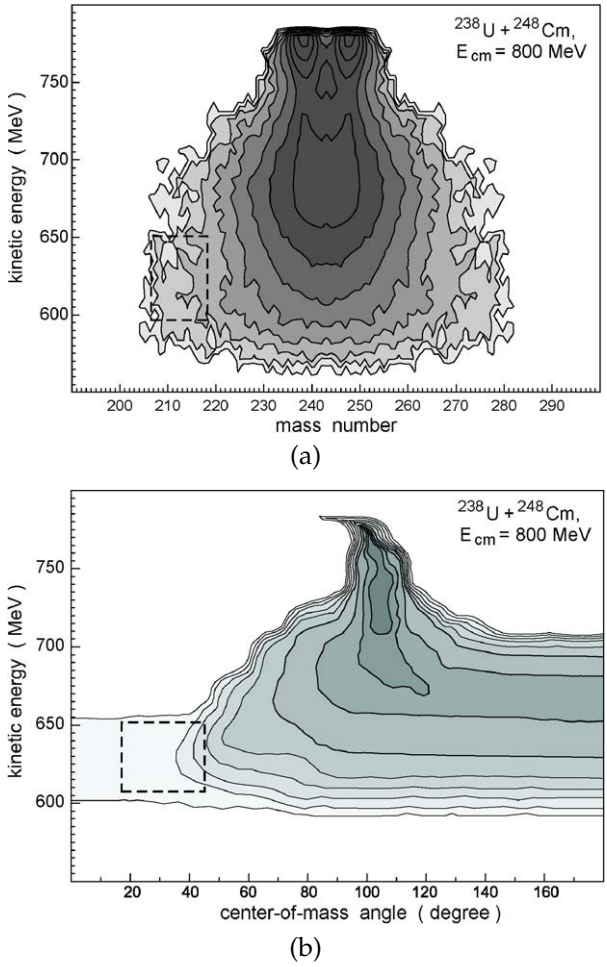


**FIGURE 8.44** Energy–mass (a) and energy–angular (b) distributions of primary fragments in the $^{238}U + ^{248}Cm$ collision at 800 MeV ($E_{loss} > 15$ MeV). Logarithmic landscape of the corresponding double differential cross sections. Lines are drawn over each half order of magnitude. The dashed rectangles show the regions of the longest events.

emission from a supercritical electric field of long-lived quasi-atoms formed in these reactions is also quite promising.

## 15. SHORT REFLECTION ON THE CHEMISTRY OF SUPERHEAVY ELEMENTS

The chemistry of superheavy elements has been theoretically investigated already during the years 1970–1971 by B. Fricke and W. Greiner [15]. Utilizing Dirac–Hartree–Fock calculations the Periodic System obtained is shown in Figure 8.45.

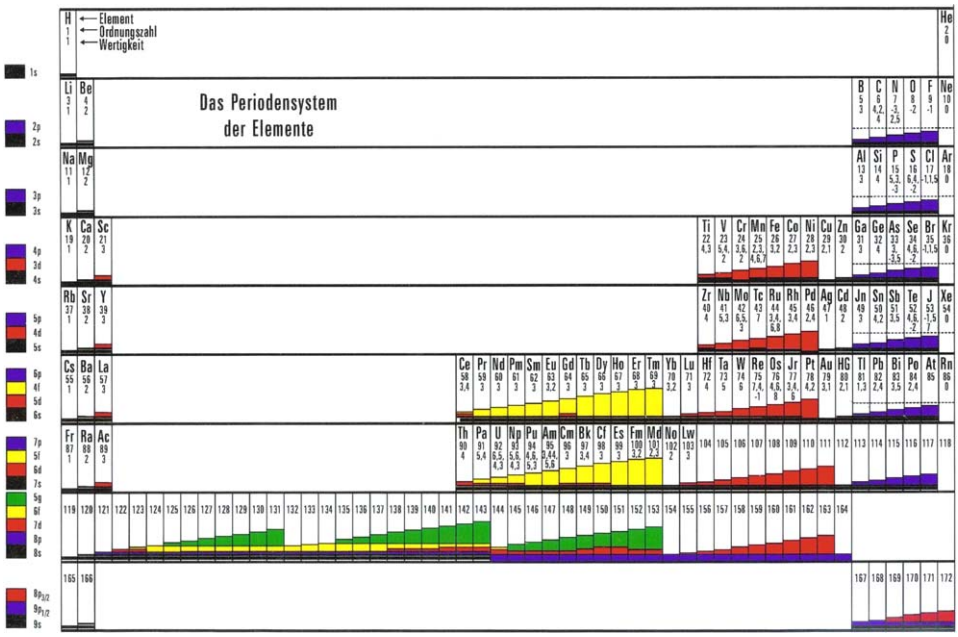


**FIGURE 8.45** The "chemical" periodic system according tho the Dirac–Hartree–Fock calculations by Fricke and Greiner (1970). The different orbitals and their occupation are depicted by shading. Thus, element 112 is eka-mercury and element 114 is eka-lead.

Many of these early predictions have been confirmed. Most recently the chemistry of elements 112 and 114 as eka-mercury and eka-lead have been established by Robert Eichler and his colleagues at Dubna [73,74], confirming exactly early theoretical predictions.

## 16. CONCLUDING REMARKS—OUTLOOK

The extension of the periodic system into the sectors hypermatter (strangeness) and antimatter is of general and astrophysical importance. Indeed, microseconds after the big bang the new dimensions of the periodic system, we have touched upon, certainly have been populated in the course of the baryo- and nucleogenesis. Of course, for the creation of the universe, even higher dimensional extensions (charm, bottom, top) come into play, which we did not pursue here. It is an open question, how the depopulation (the decay) of these sectors influences the distribution of elements of our world today. Our conception of the world will certainly gain a lot through the clarification of these questions.

The experimental verification of the decay of the vacuum is most important. A fundamental process like this must be experimentally clarified and soundly based. I hope that the proposed triggers for long time delay in the formation of

giant nuclear systems may help to bring this important fundamental physics forward.

One of our goals has also been to demonstrate that energetic antiproton beams can be used to study new interesting phenomena in nuclear physics. We discuss the possible existence of a completely new kind of strongly interacting systems where both the nucleons and the antinucleons coexist within the same volume and where annihilation is suppressed due to the reduction of the available phase space. Such systems are characterized by large binding energy and high nucleon density. Certainly, antinucleons can be replaced by antihyperons or even by antiquarks. We have presented the first self-consistent calculation of a finite nuclear system containing one antiproton in a deeply bound state. For this study we have used several versions of the RMF model which give excellent description of ordinary nuclei. The presence of an antiproton in a light nucleus like $^{8}$Be or $^{16}$O changes drastically the whole structure of the nucleus leading to a much more dense and bound state. In heavy systems the presence of a few antinucleons distorts and deforms the nuclear system leading to a localized central region of highly increased density. This is a mechanism for cold compression. We also found that nuclear systems with total baryon number zero show extremely deep and symmetric states.

It is clear however that these structural changes can occur only if the life time of the antibaryons in the nuclear interior is long enough.

One should bear in mind that originally the RMF model was formulated within the Hartree and no-sea approximations. Implementing the Dirac sea may require serious revision of the model and inclusion of additional terms. Hartree calculations including the Dirac sea and Hartree–Fock calculations including exchange terms lead to smaller nucleon potentials in normal nuclei. Shallower potentials will produce smaller attraction for antinucleons, but the qualitative effect that the presence of antiprotons reduces repulsion and enhances attraction for nucleons will remain valid. We expect that the additional binding and compression of the nucleus will appear even for an antinucleon potential as low as 200 MeV.

In summary, on the basis of the RMF model we have studied the structure of nuclear systems containing a few real antibaryons. We have demonstrated that the antibaryons act as strong attractors for the nucleons leading to enhanced binding and compression of the recipient nucleus. As our estimates show the life times of antibaryons in the nuclear environment could be significantly enhanced due to the reduction of the phase space available for annihilation. Narrow peaks in the pion or kaon spectra at the energy around 1 GeV are proposed as the most clear signature of deeply-bound antibaryon states in nuclei.

For the Gesellschaft für Schwerionenforschung (GSI), which I helped initiating in the sixties, the questions raised here could point to the way ahead. The FAIR project, meanwhile approved by the funding agencies, can—at least to some extent—follow this path.

Indeed, what is needed is a *vision on a long term basis*. The ideas proposed here, the verification of which will need the *commitment for 2–4 decades of research*, could be such a vision with considerable attraction for the best young physicists. The new dimensions of the periodic system made of hyper- and antimatter cannot be examined in the "stand-by" mode at CERN (Geneva); a dedicated facility is nec-

essary also for this field of research, which can in future serve as a home for the universities. The GSI—which has unfortunately become much too self-sufficient—could be such a home for new generations of physicists, who are interested in the *structure of elementary matter*. GSI would then not develop just into a detector laboratory for CERN, and as such become obsolete. I can already see the enthusiasm in the eyes of young scientists, when I unfold these ideas to them—similarly as it was more than 35 years ago, when the nuclear physicists in the state of Hessen initiated the construction of GSI.

## REFERENCES


[1] S.G. Nilsson, *et al.*, *Phys. Lett. B* **28** (1969) 458;
S.G. Nilsson, *et al.*, *Nucl. Phys. A* **131** (1969) 1;
S.G. Nilsson, *et al.*, *Nucl. Phys. A* **115** (1968) 545.

[2] U. Mosel, B. Fink, W. Greiner, Contribution to "Memorandum Hessischer Kernphysiker", Darmstadt, Frankfurt, Marburg, 1966.

[3] U. Mosel, W. Greiner, *Z. Phys.* **217** (1968) 256;
U. Mosel, W. Greiner, *Z. Phys.* **222** (1968) 261.

[4] J. Grumann, U. Mosel, B. Fink, W. Greiner, *Z. Phys.* **228** (1969) 371;
J. Grumann, Th. Morovic, W. Greiner, *Z. Naturforsch. A* **26** (1971) 643.

[5] A. Sandulescu, R.K. Gupta, W. Scheid, W. Greiner, *Phys. Lett. B* **60** (1976) 225;
R.K. Gupta, A. Sandulescu, W. Greiner, *Z. Naturforsch. A* **32** (1977) 704;
R.K. Gupta, A. Sandulescu, W. Greiner, *Phys. Lett. B* **64** (1977) 257;
R.K. Gupta, C. Parrulescu, A. Sandulescu, W. Greiner, *Z. Phys. A* **283** (1977) 217.

[6] G.M. Ter-Akopian, *et al.*, *Nucl. Phys. A* **255** (1975) 509;
Yu.Ts. Oganessian, *et al.*, *Nucl. Phys. A* **239** (1975) 353 and 157.

[7] D. Scharnweber, U. Mosel, W. Greiner, *Phys. Rev. Lett.* **24** (1970) 601;
U. Mosel, J. Maruhn, W. Greiner, *Phys. Lett. B* **34** (1971) 587.

[8] G. Münzenberg, *et al.*, *Z. Phys. A* **309** (1992) 89;
S. Hofmann, *et al.*, *Z. Phys. A* **350** (1995) 277 and 288.

[9] R.K. Gupta, A. Sandulescu, W. Greiner, *Z. Naturforsch. A* **32** (1977) 704.

[10] A. Sandulescu, W. Greiner, *Rep. Prog. Phys.* **55** (1992) 1423;
A. Sandulescu, R.K. Gupta, W. Greiner, F. Carstoin, H. Horoi, *Int. J. Mod. Phys. E* **1** (1992) 379.

[11] A. Sobiczewski, *Phys. Part. Nucl.* **25** (1994) 295.

[12] K. Rutz, M. Bender, T. Bürvenich, T. Schilling, P.-G. Reinhard, J.A. Maruhn, W. Greiner, *Phys. Rev. C* **56** (1997) 238.

[13] P. Papazoglou, D. Zschiesche, S. Schramm, J. Schaffner–Bielich, H. Stöcker, W. Greiner, nucl-th/9806087, *Phys. Rev. C* **59** (1999) 411.

[14] P. Papazoglou, PhD thesis, University of Frankfurt, 1998;
Ch. Beckmann, P. Papazoglou, D. Zschiosche, S. Schramm, H. Stoecker, W. Greiner, *Phys. Rev. C* **65** (2002) 024301.

[15] B. Fricke, W. Greiner, *Phys. Lett. B* **30** (1969) 317;
B. Fricke, W. Greiner, J.T. Waber, *Theor. Chim. Acta (Berlin)* **21** (1971) 235.

[16] A. Sandulescu, D.N. Poenaru, W. Greiner, *Sov. J. Part. Nucl.* **11** (6) (1980) 528.

[17] H. Klein, thesis, Inst. für Theoret. Physik, J.W. Goethe-Univ. Frankfurt a.M., 1992;
D. Schnabel, thesis, Inst. für Theoret. Physik, J.W. Goethe-Univ. Frankfurt a.M., 1992.

[18] D. Poenaru, J.A. Maruhn, W. Greiner, M. Ivascu, D. Mazilu, R. Gherghescu, *Z. Phys. A* **328** (1987) 309;
D. Poenaru, J.A. Maruhn, W. Greiner, M. Ivascu, D. Mazilu, R. Gherghescu, *Z. Phys. A* **332** (1989) 291.

[19] E.K. Hulet, J.F. Wild, R.J. Dougan, R.W. Longheed, J.H. Landrum, A.D. Dougan, M. Schädel, R.L. Hahn, P.A. Baisden, C.M. Henderson, R.J. Dupzyk, K. Sümmerer, G.R. Bethune, *Phys. Rev. Lett.* **56** (1986) 313.

[20] K. Depta, W. Greiner, J. Maruhn, H.J. Wang, A. Sandulescu, R. Hermann, *Int. J. Modern Phys. A* **5** (20) (1990) 3901;
K. Depta, R. Hermann, J.A. Maruhn, W. Greiner, in: P. David (Ed.), *Dynamics of Collective Phenomena*, World Scientific, Singapore, 1987, p. 29;
S. Cwiok, P. Rozmej, A. Sobiczewski, Z. Patyk, *Nucl. Phys. A* **491** (1989) 281.
[21] A. Sandulescu, W. Greiner in discussions at Frankfurt with J. Hamilton (1992/1993).
[22] J.H. Hamilton, A.V. Ramaya, *et al.*, *J. Phys. G* **20** (1994) L85–L89.
[23] B. Burggraf, K. Farzin, J. Grabis, Th. Last, E. Manthey, H.P. Trautvetter, C. Rolfs, Energy shift of first excited state in $^{10}$Be?, *J. Phys. G: Nucl. Part. Phys.* **25** (9) (1999) L71–L73.
[24] P. Hess, *et al.*, Butterfly and Belly Dancer Modes in $^{96}$Sr + $^{10}$Be + $^{146}$Ba, in preparation.
[25] W. Greiner, B. Müller, J. Rafelski, *QED of Strong Fields*, Springer Verlag, Heidelberg, 1985. For a more recent review see W. Greiner, J. Reinhardt, *Supercritical Fields in Heavy-Ion Physics*, Proceedings of the 15th Advanced ICFA Beam Dynamics Workshop on Quantum Aspects of Beam Physics, World Scientific, 1998.
[26] B. Povh, *Rep. Prog. Phys.* **39** (1976) 823;
B. Povh, *Annu. Rev. Nucl. Part. Sci.* **28** (1978) 1;
B. Povh, *Nucl. Phys. A* **335** (1980) 233;
B. Povh, *Prog. Part. Nucl. Phys.* **5** (1981) 245;
B. Povh, *Phys. Blätter* **40** (1984) 315.
[27] J. Schaffner, C. Greiner, H. Stöcker, *Phys. Rev. C* **45** (1992) 322;
J. Schaffner, C. Greiner, H. Stöcker, *Nucl. Phys. B* **24** (1991) 246;
J. Schaffner, C.B. Dover, A. Gal, D.J. Millener, C. Greiner, H. Stöcker, *Ann. Phys.* **235** (1994) 35.
[28] W. Scheid, W. Greiner, *Ann. Phys.* **48** (1968) 493;
W. Scheid, W. Greiner, *Z. Phys.* **226** (1969) 364.
[29] W. Scheid, H. Müller, W. Greiner, *Phys. Rev. Lett.* **13** (1974) 741.
[30] H. Stöcker, W. Greiner, W. Scheid, *Z. Phys. A* **286** (1978) 121.
[31] I. Mishustin, L.M. Satarov, J. Schaffner, H. Stöcker, W. Greiner, *J. Phys. G (Nucl. Part. Phys.)* **19** (1993) 1303.
[32] P.K. Panda, S.K. Patra, J. Reinhardt, J. Maruhn, H. Stöcker, W. Greiner, *Int. J. Mod. Phys. E* **6** (1997) 307.
[33] N. Auerbach, A.S. Goldhaber, M.B. Johnson, L.D. Miller, A. Picklesimer, *Phys. Lett. B* **182** (1986) 221.
[34] H. Stöcker, W. Greiner, *Phys. Rep.* **137** (1986) 279.
[35] J. Reinhardt, W. Greiner, in press.
[36] P. Papazoglou, D. Zschiesche, S. Schramm, H. Stöcker, W. Greiner, *J. Phys. G* **23** (1997) 2081;
P. Papazoglou, S. Schramm, J. Schaffner-Bielich, H. Stöcker, W. Greiner, *Phys. Rev. C* **57** (1998) 2576.
[37] J. Theis, G. Graebner, G. Buchwald, J. Maruhn, W. Greiner, H. Stöcker, J. Polonyi, *Phys. Rev. D* **28** (1983) 2286.
[38] S. Klimt, M. Lutz, W. Weise, *Phys. Lett. B* **249** (1990) 386.
[39] T. Bürvenich, I.N. Mishustin, L.M. Satarov, J.A. Maruhn, H. Stöcker, W. Greiner, *Phys. Lett. B* **542** (3–4) (2002) 261.
[40] B.D. Serot, J.D. Walecka, *Adv. Nucl. Phys.* **16** (1985) 1.
[41] P.G. Reinhard, *Rep. Prog. Phys.* **52** (1989) 439.
[42] N. Auerbach, A.S. Goldhaber, M.B. Johnson, L.D. Miller, A. Picklesimer, *Phys. Lett. B* **182** (1986) 221.
[43] I.N. Mishustin, *Sov. J. Nucl. Phys.* **52** (1990) 722.
[44] I.N. Mishustin, L.M. Satarov, J. Schaffner, H. Stöcker, W. Greiner, *J. Phys. G* **19** (1993) 1303.
[45] O.D. Dalkarov, V.B. Mandelzweig, I.S. Shapiro, *Nucl. Phys. B* **21** (1970) 66.
[46] G. Lalazissis, J. König, P. Ring, *Phys. Rev. C* **55** (1997) 540.
[47] M. Bender, K. Rutz, P.-G. Reinhard, J.A. Maruhn, W. Greiner, *Phys. Rev. C* **60** (1999) 34304.
[48] Y. Sugahara, H. Toki, *Nucl. Phys. A* **579** (1994) 557.
[49] M. Bender, K. Rutz, P.-G. Reinhard, J.A. Maruhn, *Eur. Phys. J. A* **8** (2000) 59.
[50] K. Rutz, M. Bender, P.-G. Reinhard, J.A. Maruhn, W. Greiner, *Nucl. Phys. A* **634** (1998) 67.
[51] Y. Akaishi, T. Yamazaki, *Phys. Rev. C* **65** (2002) 044005.
[52] C.B. Dover, T. Gutsche, M. Maruyama, A. Faessler, *Prog. Part. Nucl. Phys.* **29** (1992) 87.

[53] C. Amsler, *Rev. Mod. Phys.* **70** (1998) 1293.
[54] J. Sedlák, V. Ŝimák, *Sov. J. Part. Nucl.* **19** (1988) 191.
[55] R.C. Hwa, *Phys. Rev. Lett.* **52** (1984) 492.
[56] L.P. Csernai, J.I. Kapusta, *Phys. Rev. D* **29** (1984) 2664.
[57] I.N. Mishustin, L.M. Satarov, H. Stöcker, W. Greiner, *Phys. Rev. C* **59** (1999) 3343.
[58] W. Greiner, B. Müller, J. Rafelski, *Quantum Electrodynamics of Strong Fields*, second ed., Springer Verlag, December 1985.
[59] J. Reinhardt, W. Greiner, *Quantum Electrodynamics*, third ed., Springer Verlag, February 2003.
[60] S. Hofmann, G. Münzenberg, *Rev. Mod. Phys.* **72** (2000) 733.
[61] Yu.Ts. Oganessian, V.K. Utyonkov, Yu.V. Lobanov, F.Sh. Abdullin, A.N. Polyakov, I.V. Shirokovsky, Yu.S. Tsyganov, G.G. Gulbekian, S.L. Bogomolov, B.N. Gikal, A.N. Mezentsev, S. Iliev, V.G. Subbotin, A.M. Sukhov, A.A. Voinov, G.V. Buklanov, K. Subotic, V.I. Zagrebaev, M.G. Itkis, J.B. Patin, K.J. Moody, J.F. Wild, M.A. Stoyer, N.J. Stoyer, D.A. Shaughnessy, J.M. Kenneally, P.A. Wilk, R.W. Lougheed, R.I. Il'kaev, S.P. Vesnovskii, *Phys. Rev. C* **70** (2004) 064609.
[62] M. Schädel, W. Brüchle, H. Gäggeler, J.V. Kratz, K. Sümmerer, G. Wirth, G. Herrmann, R. Stakemann, G. Tittel, N. Trautmann, J.M. Nitschke, E.K. Hulet, R.W. Lougheed, R.L. Hahn, R.L. Ferguson, *Phys. Rev. Lett.* **48** (1982) 852.
[63] K.J. Moody, D. Lee, R.B. Welch, K.E. Gregorich, G.T. Seaborg, R.W. Lougheed, E.K. Hulet, *Phys. Rev. C* **33** (1986) 1315.
[64] C. Riedel, W. Nörenberg, *Z. Phys. A* **290** (1979) 385.
[65] V. Zagrebaev, W. Greiner, *J. Phys. G* **31** (2005) 825.
[66] J. Reinhard, U. Müller, W. Greiner, *Z. Phys. A* **303** (1981) 173.
[67] W. Greiner (Ed.), *Quantum Electrodynamics of Strong Fields*, Plenum Press, New York and London, 1983;
W. Greiner, B. Müller, J. Rafelski, *QED of Strong Fields*, second ed., Springer, Berlin and New York, 1985.
[68] V.I. Zagrebaev, *Phys. Rev. C* **64** (2001) 034606;
V.I. Zagrebaev, in: *Tours Symposium on Nucl. Phys.* V, AIP Conf. Proc., vol. 704, 2004, p. 31, see also invited talk at the IX International Conference on Nucleus Collisions, Rio de Janeiro, Brazil, August 28–September 1, 2006.
[69] U. Mosel, J. Maruhn, W. Greiner, *Phys. Lett. B* **34** (1971) 587;
J. Maruhn, W. Greiner, *Z. Phys.* **251** (1972) 431.
[70] F.G. Werner, J.A. Wheeler, unpublished;
K.T.R. Davies, A.J. Sierk, J.R. Nix, *Phys. Rev. C* **13** (1976) 2385.
[71] M. Schädel, J.V. Kratz, H. Ahrens, W. Brüchle, G. Franz, H. Gäggeler, I. Warnecke, G. Wirth, G. Herrmann, N. Trautmann, M. Weis, *Phys. Rev. Lett.* **41** (1978) 469.
[72] S. Hofmann, *et al.*, *Eur. Phys. J. A* **32** (2007) 251.
[73] R. Eichler, *et al.*, *Nucl. Phys. A* **787** (2007) 373c.
[74] R. Eichler, *et al.*, *Nature* **72** (2007) 447.

CHAPTER 9

# Asymptotic Behavior of MP2 Correlation Energies for Closed-Shell Atoms☆

**Karol Jankowski**[*], **Romuald Słupski**[*,**] and **Jesus R. Flores**[***]

Contents



Abstract

The asymptotic behavior of the second-order energy of the Møller–Plesset perturbation theory, especially adapted to take advantage of the closed-shell atomic structure (MP2/CA), is studied. Special attention is paid to problems related to the derivation of formulae for the asymptotic expansion coefficients (AECs) for two-particle partial-wave expansions in powers

[*] Institute of Physics, Nicholas Copernicus University, 87-100 Toruń, Poland
[**] Computing Centre, Nicholas Copernicus University, 87-100 Toruń, Poland
[***] Departamento de Química Física Universidad de Vigo, 36-200 Vigo, Spain

☆ This work is dedicated to Professor Ingvar Lindgren on the occasion of his 75th birthday, with our best wishes for many more years of splendid activity

Advances in Quantum Chemistry, Vol. 53
ISSN 0065-3276, DOI:10.1016/S0065-3276(07)53009-1

of $(l+1/2)^{-1}$. These formulae providing a direct relationship between the Hartree–Fock orbitals defining the zero-order problem and the asymptotic structure of various constituents of the second-order energy are of interest for complete-basis-set limit studies of the correlation energies in general many-electron systems. Two ways of employing the easily available theoretical AECs in studies of correlation energies are indicated. The results obtained for the $Zn^{2+}$ ion are encouraging.

## 1. INTRODUCTION

The slow convergence of the many-electron wave functions in the basis of configuration state functions defined as Slater determinants constructed from one electron wave functions (we shall refer to such methods as configuration interaction (CI) ones) causes essential methodological problems that greatly restrict the reliable description of electron correlation effects by *ab initio* methods even in medium size many-electron systems. In the last decade we witness an intensive development of various strategies to overcome these problems. Two of them seem to be especially attractive: (1) The strategie consisting in designing methods based on the use of explicitly correlated, i.e., dependent on interelectronic variables, basis functions (for reviews and references, see, e.g. [1–6]); (2) The approaches aiming at reaching extremely accurate energies by various methods of using results obtained in calculations based on hierarchies of correlation consistent (cc) basis sets [7] in extrapolations to the complete-basis-set (CBS) limit (for reviews and references see, e.g. [8–12]. It seems, however, that even in the future CI type approaches will keep to be preferred in various applications. Moreover, CI type wave functions and energies provide convenient references in methodological discussion of the multitude of methods being developed within the many-electron theory. Therefore, the understanding of the convergence characteristics of the energies in CI type approaches with respect to extensions of the orbital basis sets is really important.

A distinguished role in electron correlation studies is played by the second-order Møller–Plesset [13] perturbation theory (MP2), which provides the simplest way of proceeding beyond the Hartree–Fock (HF) picture. Numerous versions of this theory give rise to most of the computational post-HF results obtained so far. Moreover, since despite of its simplicity, MP2 accounts for most of the difficulties faced in the description of electron correlation effects, this method is broadly used as the first testing ground of the efficiency of new quantum-chemical approaches and in the research aiming at collecting information on the nature of electron correlation helpful for designing more efficient approaches. In line with the latter application, we would like to study the asymptotic behavior of MP2 correlation energies for closed-shell atoms. The choice of these systems is caused by the fact that in their case the MP2 method, if especially adapted to take advantage of the closed-shell structure [14], has proven its capacity of providing highly accurate correlation energies for larger systems. The attractiveness of this approach is to a large extent due to the formulation in terms of symmetry-adapted pair (SAP) functions and partial waves (PW) expansions, which cause that the corresponding pair

energies and partial-wave energy increment disclose regularities unavailable for other many electron systems. To underline the closed-shell-specific simplifications available in this MP2 approach we refer to it by the acronym MP2/CA. Information provided by the MP2/CA results are a valuable, but rather underestimated, source of inspiration in studies of electron correlation effects both in atomic and molecular systems.

For atomic systems let us just mention that, in the case of Ne-like systems, with $10 \leqslant Z \leqslant 28$, the MP2 energies represent between 99.18% and 99.91% of the values obtained by Chakravorty and Davidson [15]; in turn, for the Ar-like systems the former energies represent between 98.24% and 100.56% of the latter ones. This high accuracy is mainly due to the fact that for closed-shell atoms one has to deal with predominantly *dynamical correlation effects* [16] which are expected to be well represented by the lowest order of MP perturbation theory. At present MP2/CA energies are available for closed-shell atoms up to 86 electrons, which is due to the application of the very efficient p-version finite element method (FEM) by Flores [17]. An extensive critical review of the MP2/CA energies and their constituents obtained so far by means of the MP2/CA approach can be found in our review article [18]. The availability of MP2/CA energy information is especially important for larger than 18 electron atoms for which we do not have access either to more accurate *ab initio* results or to dependable estimates from experimental data. Therefore, the second-order picture of correlation effects in larger closed-shell atoms is gaining increasing interest as a realistic model of a many electron system for which in the innermost and outermost regions the electrons move in different, close-to-extremal conditions.

The inspiring role of MP2/CA results in studies of molecular systems may be illustrated by the following example, relevant to the topic of this paper: When in 1984 one of us (KJ), jointly with Prof. Ahlrichs and his Group [19], have demonstrated that the structure of orbital basis sets effective in the description of electron correlation has to be essentially different from those commonly used at that time, we were strongly employing the guidance provided by the results on the l-dependence of the MP2 correlation energy for closed-shell atoms previously obtained in the Toruń Group. In turn, our Karlsruhe findings led Dunning [7] to the idea of developing his famous hierarchies of correlation consistent (cc) basis sets—cc-pVxZ, which are ubiquitous in quantum chemistry these days. Since Dunnings bases have the important attribute of providing results well suited for extrapolations to the complete basis set (CBS) limit, during the last decade there have been developed several extrapolation techniques which are either purely semiempirical or based on theoretical results for He-like atoms obtained at the second-order level of the $1/Z$ perturbation theory by Schwartz [20] and Kutzelnigg and Morgan III [21].

Returning to the role of the MP2/CA approach, it seems to us that results of this method can provide additional information useful for better formulating extrapolation procedures for molecules. Our viewpoint might be supported by the following arguments: (1) MP2/CA results are obtained for larger atoms whose diverse electronic-shell structure gives also rise to correlation effects resembling those present in molecules; (2) Unlike the second-order energies in $1/Z$ perturba-

tion theory which is rather specific to small atomic systems, the MP2/CA energies directly represent correlation energies defined in a way similar to that for molecules. Very recently [22] we have obtained benchmark MP2 results for the $Zn^{2+}$, which plays for 3d-electron systems a similar role as Ne for smaller atoms and molecules. The accuracy of these results made it possible [23] to determine the first (leading) asymptotic expansion coefficients (AECs) for each SAP energy to a very high accuracy. Since these AECs did not agree with the results obtained when using a "brute force" generalization of the formulas obtained by Kutzelnigg and Morgan [21], we have derived formulae for the first AECs in the asymptotic expansion of SAP pair energies [24]. Comparison of the theoretical AECs, based on our formulae, with their counterparts determined from computational results reveals a very close agreement.

In this chapter we would like to present a somewhat modified derivation of our AEC formulae for the PW expansions of SAP energies in the MP2/CA approach. This derivation is complemented with a discussion of the relationship of the energy increments in CI related PW expansions, which are indexed with a dyad of indices, with the energy contributions of extrapolation procedures based on powers of $(l + 1/2)^{-1}$ identified by the single index $l$. Next we would like to present two applications of the theoretical AECs. The first one consists in using them to construct theoretical estimates for the PW increments of the SAP energies as well of larger portions of the MP2/CA energy. The second application involves setting up a reliable method of calculating SAP energies in which energies obtained for angularly restricted basis sets are corrected by values of the basis set truncation errors evaluated when using theoretical AECs.

## 2. THEORY

### 2.1 Main partial wave (PW/m) structure of the MP2/CA theory

In this chapter we employ a special version of the second-order Møller–Plesset [13] perturbation theory (MP2/CA) which is especially useful in applications to closed-shell atoms. In this approach the first-order wave function consists of spinorbitals and symmetry-adapted pair functions (SAPF). A detailed presentation of the MP2/CA method can be found in Ref. [14]. For sake of describing the nomenclature used, we repeat here the basic equations.

The Møller–Plesset (MP) perturbation theory [13] is based on the zero-order Hamiltonian of the form:

$$H_0 \equiv H_{\mathrm{HF}} = \sum_{i=1}^{N} f(i). \tag{1}$$

The Fock operator, $f(i)$, can be written in spin-orbital form as (see, e.g., Ref. [25]):

$$f(i) = h(i) + \sum_{n=1}^{N} \big[J_n(i) - K_n(i)\big], \tag{2}$$

where $h(i)$ denotes the bare nuclear one-electron Hamiltonian and $J_n(i)$ $K_n(i)$ stand for the standard Coulomb and exchange potentials, respectively.

The zero-order wave function, i.e., the single determinant HF function, consists of canonical HF spinorbitals satisfying the equations:

$$f(1)\varphi_k(1) = \epsilon_k\varphi_k(1), \quad (k = 1, \ldots, N). \tag{3}$$

The MP perturbation operator, $V$, takes the form

$$V = \sum_{i<j} r_{ij}^{-1} - \sum_{n=1}^{N}\sum_{i=1}^{N}\big[J_n(i) - K_n(i)\big], \tag{4}$$

and the first-order wave function at the $N$-electron level satisfies the equation

$$\big(H_{\mathrm{HF}} - E^0\big)\Psi^{(1)} + \big(V - E^{(1)}\big)\Psi_{\mathrm{HF}} = 0. \tag{5}$$

Owing to the Brillouin theorem, the first-order wave function in the MP perturbation theory consists entirely of double excitations on the zero-order HF function. Hence, $\Psi^{(1)}$ can be represented as (see, e.g., Refs. [25,26])

$$\Psi^{(1)}(1, 2, \ldots, N) = 2^{-1/2}\sum_{i<j}\hat{\mathcal{A}}\Big[u_{ij}(i, j)\prod_{k\neq i,j}\varphi_k(k)\Big], \tag{6}$$

where $\hat{\mathcal{A}}$ denotes the $N$-electron antisymmetrizer and the pair functions $u_{ij}$ are strongly orthogonal to the spinorbitals $\varphi_i(1)$, defining the HF function, i.e.,

$$\Omega(1, 2)u_{ij}(1, 2) = u_{ij}(1, 2), \tag{7}$$

with the strong-orthogonality projection operator $\Omega(1, 2)$ defined as

$$\Omega(1, 2) = \Omega(1)\Omega(2) \quad \text{with} \quad \Omega(1) = 1 - \sum_{k=1}^{N}\big|\varphi_k(1)\big\rangle\big\langle\varphi_k(1)\big|. \tag{8}$$

It is convenient to transform the set of pair functions $u_{ij}$ corresponding to spinorbitals defined by the same pair of shell quantum numbers $(n_i l_i, n_j l_j)$, and different magnetic quantum numbers, into a set of symmetry-adapted pair functions (SAPF), $u(T^*|1, 2)$, which satisfy the equations [14]

$$\big[f(1) + f(2) - \epsilon_{n_i l_i} - \epsilon_{n_j l_j}\big]u(T^*|1, 2) + \Omega(1, 2)r_{12}^{-1}u_0(T^*|1, 2) = 0. \tag{9}$$

Here, the label $T^*$ denotes the set of quantum numbers required for the specification of the pair function:

$$T^* \leftrightarrow (T, M, M_S) \quad \text{with} \quad T \leftrightarrow (n_i l_i, n_j l_j, L, S), \tag{10}$$

where the zero-order SAPF is defined as

$$u_0(T^*|1, 2) = \hat{\mathcal{B}}\big[R_0^T(r_1, r_2)Z_{LM}^{l_i l_j}(\delta_1, \delta_2)\widetilde{S}(SM_S|\sigma_1, \sigma_2)\big], \tag{11}$$

$$\text{with} \quad R_0^T(r_1, r_2) = R_{n_i l_i}(r_1)R_{n_j l_j}(r_2). \tag{12}$$

$\widetilde{S}(SM_S|\sigma_1,\sigma_2)$ stands for the spin part of the SAPF, and $R_{n_i l_i}(r)$ and $R_{n_j l_j}(r)$ denote the radial parts of the HF orbitals of the pair. The angular part of the pair function is defined as an eigenfunctions of the angular momentum operator of the pair corresponding to the quantum numbers $(L,M)$

$$Z_{LM}^{j_1 j_2}(\delta_1,\delta_2) \equiv \left[Y_{j_1}(\delta_1)Y_{j_2}(\delta_2)\right]_L^M = \sum_{m_1,m_2} (-1)^{j_1-j_2+M}[L]^{1/2} \begin{pmatrix} j_1 & j_2 & L \\ m_1 & m_2 & -M \end{pmatrix} Y_{j_1}^{m_1}(\delta_1)Y_{j_2}^{m_2}(\delta_2), \quad (13)$$

where $\delta$ stands for the pair of spherical polar angles $\theta$ and $\phi$ and $(\cdots)$ is the Wigner $3j$ symbol. The symbol $[l_1,l_2,\ldots,l_k]$ denotes the product $(2l_1+1)(2l_2+1)\cdots(2l_k+1)$.

The first-order SAPFs are defined in the following partial wave (PW) expansion form

$$u(T^*|1,2) = \sum_{j_1 j_2} u_{j_1 j_2}(T^*|1,2) \quad (14)$$

$$\text{with} \quad u_{j_1 j_2}(T^*|1,2) = \hat{\mathcal{B}}\left[R_{j_1 j_2}^T(r_1,r_2)Z_{LM}^{j_1 j_2}(\delta_1,\delta_2)\widetilde{S}(SM_S|\sigma_1,\sigma_2)\right], \quad (15)$$

where $R_{j_1 j_2}^T(r_1,r_2)$ denote the radial pair functions corresponding to each term of the PW expansion (for closed-shell states these functions do not depend on $M_L$ and $M_S$). These functions, belonging to the subspace spanned by pairs of virtual radial HF functions, can be efficiently approximated by various methods, e.g., by means of the variational-perturbation approach.

We observe that, if the radial basis sets used in the calculations consist of pairs of one-electron functions, we have to deal just with a CI representation of the individual pair functions, and, as a consequence, at the $N$-electron level, with a CI-doubles representation of the total first-order wave function. Having established the relationship of the PW expansion defined by Eq. (14) with the standard CI method, in what follows, we shall refer to this expansion as *the main PW expansion* and use the acronym PW/m.

Within the MP2/CA approach the correlation energy of an $N$-electron atom can be decomposed in a way which is very advantageous from the points of view of physical intuitions as well as computational methodology. At the first important step, the total second-order energy is decomposed into *symmetry-adapted pair (SAP) energies* $E^{(2)}(T^*)$ defined by the individual SAPFs $u(T^*|1,2)$

$$E^{(2)} = \sum_{T^*} E^{(2)}(T^*), \quad \text{with } E^{(2)}(T^*) = \left\langle u(T^*)\middle|\Omega r_{12}^{-1}\middle|u_0(T^*)\right\rangle. \quad (16)$$

Each SAP energy can be further decomposed into PW/m increments, $E_{j_1 j_2}^{(2)}(T^*)$, defined in terms of the PW/m components $u_{j_1 j_2}(T^*|1,2)$ of the SAPF,

$$E^{(2)}(T^*) = \sum_{j_1 j_2} E_{j_1 j_2}^{(2)}(T^*), \quad (17)$$

where

$$E^{(2)}_{j_1 j_2}(T^*) = \langle u_{j_1 j_2}(T^*) | \Omega r_{12}^{-1} | u_0(T^*) \rangle. \tag{18}$$

We shall refer to the energy increment $E^{(2)}_{j_1 j_2}(T^*)$, which is the most elementary portion of the MP2/CA energies, as the $(j_1 j_2)$ PW/m energy increment. One can easily check that the values of $E^{(2)}(T^*)$ and $E^{(2)}_{j_1 j_2}(T^*)$ are independent on $M_L$ and $M_S$ (see Ref. [14]). Hence, the pair energy is identified by the set $T$ given in Eq. (10). Note from Eq. (18) that, for PWs defined by $j_1$ and $j_2$ greater than the maximum angular momentum quantum number of the occupied orbitals, $l_{\mathrm{occ}}$, the strong orthogonality conditions are automatically satisfied, and we have

$$E^{(2)}_{j_1 j_2}(T^*) = \langle u_{j_1 j_2}(T^*) | r_{12}^{-1} | u_0(T^*) \rangle, \quad \text{for } \min(j_1, j_2) > l_{\mathrm{occ}}. \tag{19}$$

We refer to these PWs as *free PWs* (FPW/m) and to the remaining PWs as *orthogonalized PWs* (OPW/m) (see Ref. [27]). The FPW/m functions are effective in representing the pair functions in the neighborhood of the electron coalescence point, whereas the OPW/m ones are efficient in the region of the whole correlation hole. The SAP energies and the PW/m energy increments disclose many interesting regularities, which is especially true for the FPW/m energies. These regularities turned out to be helpful in the discussions of dynamical correlation effects not only in closed-shell but also in open-shell atoms. For a detailed presentation and discussion of these regularities see Ref. [18].

So far we have specified the structure of the SAPF and SAP pair energies by means of the sets of standard quantum numbers $T^*$ and $T$, respectively. However, in studies of the asymptotic behavior of the SAP energies it turns out to be useful to supplement this specification in an identical way as Kutzelnigg and Morgan have done in the case of two-electron states of He-like systems [21]. To characterize the behavior of the first-order wave function at the singular point, these authors have ingeniously employed the idea of *natural* and *unnatural parity* of two-electron states, which has been used in atomic spectroscopy studies for the first time by Banerjee [28]. The parity of a two-electron state corresponding to the quantum number $L$ is defined as

- *natural* if its parity is equal to $(-1)^L$, e.g., for 1s2s $^3$S, 2p3p $^1$D states,
- *unnatural* if its parity equal to $(-1)^{L+1}$, e.g., for $(2p)^2$ $^3$P, 3p3d $^1$D states.

The usefulness of this complementary characteristics will be shown later in this chapter.

## 2.2 Alternative partial wave (PW/a) expansion of MP2/CA pair energies

It has been shown by Schwartz [29] and Kutzelnigg and Morgan [21] that for two-electron atoms the PW structure of the second-order energy defined within the perturbation theory based on the bare nuclei zero-order Hamiltonian, also known as the 1/Z perturbation theory (with the acronym 1/Z-PT), is determined by the

singularities present in the equation determining the first-order wave function

$$\left[h(1)+h(2)-E_{n_i}-E_{n_j}\right]\Psi^{(1)}(LSM_LM_S|1,2)+\left(r_{12}^{-1}-E^{(1)}\right)\Psi^{(0)}(LSM_LM_S|1,2)=0, \tag{20}$$

where $E_{n_i}$ and $E_{n_j}$ are eigenvalues corresponding to the hydrogen wave functions employed for the construction of the zero-order function $\Psi^{(0)}(LSM_LM_S|1,2)$.

It has been shown [29,21] that, as a consequence of the correlation cusp condition [30] in the coalescence region ($\vec{r}_1 = \vec{r}_2$), $\Psi^{(1)}$ is approximately known and takes the form

$$\Psi^{(1)}(1,2) \simeq \alpha r_{12}\Psi^{(0)}(1,2) = \alpha \sum_{l=0}^{\infty}(r_{12})_l P_l(\cos\vartheta_{12})\Psi^{(0)}(1,2), \tag{21}$$

where $(r_{12})_l$ stands for the radial part in the partial-wave expansion of $r_{12}$

$$(r_{12})_l = \frac{1}{2l+3}\frac{r_<^{l+2}}{r_>^{l+1}} - \frac{1}{2l-1}\frac{r_<^{l}}{r_>^{l-1}}, \tag{22}$$

and $\vartheta_{12}$ is the angle between the two radius vectors. The coefficient $\alpha$ takes the following values:

- $\alpha = 1/2$ for natural-parity singlet states [30],
- $\alpha = 1/4$ for natural and unnatural triplet states [31],
- $\alpha = 1/6$ for unnatural-parity singlet states [21].

In their seminal paper Kutzelnigg and Morgan (KM) [21,32] have made a significant progress towards the understanding of the structure of the PW expansion of the second-order energies within 1/Z-PT for two-electron states. When using their original approach supplemented by an efficient technique for the evaluation of radial integrals inspired by the work of Hill [33], these authors derived formulas for the leading asymptotic expansion coefficients (AEC) for all four possible types of two-electron atomic states in terms of just two integrals involving the radial parts of hydrogen-like wave functions.

To learn about the nature of the singularities present in Eq. (9) for the first-order SAPs, $u(T^*|1,2)$, we compare this equation with its counterpart, Eq. (20), for the first-order wave function $\Psi^{(1)}(LSM_LM_S|1,2)$ of the 1/Z-PT for states of two-electron atoms. One can see that former equation can be obtained from the latter one in the following way:

1. The one-electron Hamiltonians, $h(i)$ are replaced by the Fock operators (2) introducing the Coulomb and exchange potentials.
2. The hydrogen energies $E_{n_i}$ are replaced by the HF orbital energies $\epsilon_{n_j l_j}$.
3. The $r_{12}^{-1}$ operator is replaced by the $\Omega(1,2)r_{12}^{-1}$ one.

Let us note that the Coulomb and exchange potentials do not introduce any new singular terms and that the strong-orthogonality projection operator, $\Omega(1,2)$ does not modify the high-$l$ terms. Hence, we arrive at the conclusion that in the electron coalescence region Eqs. (9) and (20) disclose the same singular structure.

An important consequences of our finding is that the first-order SAPs, $u(T^*|1,2)$, of the MP2/CA method take at $\vec{r}_1 = \vec{r}_2$ the form [29]

$$u(T^*|1,2) \simeq \alpha r_{12} u_0(T^*|1,2) = \sum_{l=0}^{\infty} \tilde{u}_l(T^*|1,2), \tag{23}$$

where

$$\tilde{u}_l(T^*|1,2) \equiv \alpha (r_{12})_l P_l(\cos\vartheta_{12}) u_0(T^*|1,2), \tag{24}$$

and that the Kutzelnigg–Morgan [21] formulae for the AECs derived for the second-order 1/Z-PT energies of two-electron atoms should apply for the SAP energies in MP2/CA with just one minor modification consisting in replacing the hydrogen-like orbitals by HF ones in radial integrals.

It should be emphasized that Eqs. (20) and (9) define the first-order wave functions not only for different perturbation approaches but, first of all, for different physical situations. The former wave functions correspond to real ground- or excited states of two-electron atoms, whereas all of the latter pair functions correspond to the ground state of an $N$-electron atom, providing corrections to the Hartree–Fock description of its electron pairs. However, from the mathematical point of view, in both cases we have to deal with equations defining pair functions of identical symmetry characteristic.

Let us make the observation that Eqs. (23) and (24) represent an alternative partial wave expansion of the SAPF in which the individual terms are defined by the degrees $l$ of the Legendre polynomials. To distinguish this expansion from the PW/m expansion (15), where the individual terms are defined by pairs of orbital momentum quantum numbers of one-electron wave functions employed in the CI representation of the pair function, we shall refer to it as *auxiliary PW expansion* and denote it by the acronym PW/a. This expansion turned out to be well suited for representing the first-order pair functions at the interelectronic cusp. Unlike the PW/m expansion is it not directly related to the CI approach. Let us stress the important fact that for pairs defined by other than s-electrons the PW/m and PW/a expansions of the second-order energies need not be the same.

To obtain the PW/a expansion of the MP2/CA correlation energy for a pair corresponding to the quantum numbers $T^*$ we insert

$$u(T^*|1,2) = \alpha r_{12} u_0(T^*|1,2) + \chi(T^*|1,2), \quad \text{where } \chi(T^*|1,2) = O(r_{12}^2), \tag{25}$$

into Eq. (16) and obtain for $l > 3$

$$E^{(2)}(T^*) = \langle u(T^*)|\Omega r_{12}^{-1}|u_0(T^*)\rangle = \langle u(T^*)|r_{12}^{-1}|u_0(T^*)\rangle \tag{26}$$

$$= \langle \alpha r_{12} u_0(T^*|1,2)|r_{12}^{-1}|u_0(T^*)\rangle + \langle \chi(T^*)|r_{12}^{-1}|u_0(T^*)\rangle, \tag{27}$$

where the term involving $\chi(T^*)$ is in the large-$l$ regime proportional to $(l+1/2)^{-8}$ (see Ref. [21]).

Hence, for $l \gg 3$ we can write

$$E_l^{(2)}(T^*) \simeq \widetilde{E}_l^{(2)}(T^*) = \sum_{l=0}^{\infty} \widetilde{E}_l^{(2)}(T^*) \tag{28}$$

with the PW/a SAP energy increments

$$\widetilde{E}_l^{(2)}(T^*) = \langle \tilde{u}_l(T^*)|r_{12}^{-1}|u_0(T^*)\rangle. \tag{29}$$

## 2.3 Correspondence of the PW/a and PW/m SAP pair-energy increments

To find the relationship between the increments $\widetilde{E}_l^{(2)}(T^*)$ (29) and $E_{j_1j_2}^{(2)}(T^*)$ (18) defined within the PW/a and PW/m expansions, respectively, let us start with establishing the relation between the different angular parts of the $\tilde{u}_l(T^*|1,2)$ and $u(T^*|1,2)$ PW components. To this aim we shall use the following expression

$$P_k(\cos\vartheta_{12})Z_{\mathrm{LM}}^{t_1t_2}(\delta_1,\delta_2) = \sum_{v_1v_2} c_{t_1t_2;v_1v_2}^{L,k} Z_{\mathrm{LM}}^{v_1v_2}(\delta_1,\delta_2), \tag{30}$$

where

$$c_{t_1t_2;v_1v_2}^{L,k} = (-1)^{k+L}[t_1,t_2,v_1,v_2]^{1/2} \begin{Bmatrix} v_1 & v_2 & L \\ t_2 & t_1 & k \end{Bmatrix} \begin{pmatrix} t_1 & v_1 & k \\ 0 & 0 & 0 \end{pmatrix} \begin{pmatrix} t_2 & v_2 & k \\ 0 & 0 & 0 \end{pmatrix} \tag{31}$$

and $\{\cdots\}$ denotes the Wigner 6-$j$ symbol, which can be easily obtained when using standard techniques of the quantum theory of angular momentum (see, e.g., Varshalovich et al. [34]).

Now taking into account Eqs. (29), (23) and (30) as well as the invariance of $(r_{12})_l\, P_l(\cos\vartheta_{12})$ under coordinate exchange, we can write for the energy increment in the PW/a expansion:

$$\widetilde{E}_l^{(2)}(T^*) = \alpha\langle u_0(T^*)(r_{12})_l P_l(\cos\vartheta_{12})|r_{12}^{-1}|u_0(T^*)\rangle = \sum_{j_1j_2} c_{l_il_j;j_1j_2}^{L,l}\varepsilon_{j_1j_2}^{l}(T^*), \tag{32}$$

where

$$\varepsilon_{j_1j_2}^{l}(T^*) \equiv \langle v_{j_1j_2}^{l}(T^*)|\Omega r_{12}^{-1}|u_0(T^*)\rangle = \langle v_{j_1j_2}^{l}(T^*)|r_{12}^{-1}|u_0(T^*)\rangle \quad \text{for } (j_1,j_2) > 3 \tag{33}$$

with

$$v_{j_1j_2}^{l}(T^*|1,2) = \alpha\hat{\mathcal{B}}\big[(r_{12})_l R_{n_il_i}(r_1)R_{n_jl_j}(r_2)Z_{LM}^{j_1j_2}(\delta_1,\delta_2)\widetilde{S}(SM_S|\sigma_1,\sigma_2)\big]. \tag{34}$$

Note that the function $v_{j_1j_2}^{l}(T^*|1,2)$ has the structure compatible with partial waves in the PW/m expansion (15). Therefore, it may be considered as a constituent of the $(j_1j_2)$-component of the first-order SAPF $u(T^*|1,2)$. By this token the term $c_{l_il_j;j_1j_2}^{L,l}\varepsilon_{j_1j_2}^{l}(T^*)$ in Eq. (32) constitutes a contribution to the $(j_1j_2)$-PW increment to the MP2 energy of the same pair.

Hence, from (32) one can see that the $l$th PW/a increment to the pair energy can be represented as a sum consisting of PW/m increments defined by various $(j_1j_2)$-indices. One can also notice that the number of nonzero $c_{l_il_j;j_1j_2}^{L,l}$ coefficients is

rather small due to the following conditions imposed on the $(j_1, j_2)$ indices:

$$|l_i - l| \leqslant j_1 \leqslant l_i + l, \qquad |l_j - l| \leqslant j_2 \leqslant l_j + l,$$
$$l_i + l + j_1 = \text{even}, \qquad l_j + l + j_2 = \text{even}. \tag{35}$$

For example (see Ref. [24]), for the $(np)^2\ ^3P$ pairs there are only two non-zero coefficients. Now, since in the large-$l$ regime, the residual energies defined as sums involving PW/a or PW/m increments starting with some $l_{\min} \gg 1$ are almost identical, i.e.,

$$\sum_{(j_1 \leqslant j_2) \geqslant l_{\min}}^{\infty} E^{(2)}_{j_1 j_2}(T^*) \simeq \sum_{l=l_{\min}}^{\infty} \widetilde{E}^{(2)}_{l}(T^*), \tag{36}$$

then inserting into the right-hand side of this Eq. (32), and reordering the terms, we find that for $(j_1, j_2) \gg 1$

$$E^{(2)}_{j_1 j_2}(T^*) \simeq \sum_{l=\max(|j_1 - l_i|, |j_2 - l_j|)}^{\min(j_1 + l_i, j_2 + l_j)} c^{L,l}_{l_i l_j; j_1 j_2} \varepsilon^{l}_{j_1 j_2}(T^*). \tag{37}$$

In this way, we have obtained an expression for the dominating contribution to the high-$(j_1 j_2)$ PW/m increments to the MP2 energy for the SAP defined by $T^*$ in terms of integrals involving known functions only. Hence, we are now in a position to find for the PW/m expansion the leading AECs, i.e., the coefficient of the $(l + 1/2)^{-k}$ term with minimum $k$.

## 2.4 Single index labels ($l$-labels) for PW/m increments

Taking into account that, unlike the PW/a increments, the PW/m ones, $E^{(2)}_{j_1 j_2}(T^*)$, are labeled by a dyads of indices, the question arises how to associate these increments with the single-index-labeling ($l$-labeling) of the energy contributions that are required for defining the $l$-dependence of the SAP energy in asymptotic expansion studies based on powers of $(l + 1/2)^{-1}$. This problem arises for electron pairs not consisting of two s-electrons. The $l$-labeling is simple if the pair energy consists just of one sequence of "diagonal" PW/m increments, i.e., defined by the dyad $j_1 = j_2 = j$, because then we just take $l = j$. However, the situation is not unique for pairs defined by one sequence of "nondiagonal" PW/m increments for which $j_1 \neq j_2$ and in the case when we have to deal with a "complex" pair energy that consists of several sequences of PW/m increments defined by different index dyads like, e.g., the $(nd)^2\ ^1D$ pair energy consists of three series of increments defined by the dyads: $(j, j)$, $(j, j + 2)$, and $(j, j + 4)$.

There are three straightforward ways of establishing the index-dyad correspondence: (a) $l = \max(j_1, j_2)$, (b) $l = \min(j_1, j_2)$, and (c) $l = (j_1 + j_2)/2$. For diagonal PW/m increments all these links are identical. However, in the remaining cases each link results in different $l$ values, e.g., in case (c), $l$ may even take half-integer values. Each of the three links leads, of course, to another value of the $l$th energy increment. In the case of a complex pair energy, the $l$th energy increment is defined

as a sum of all PW/m increments whose dyads are linked with the same $l$ by one of the three ways indicated. Let us define the $l$th contributions to the SAP energy corresponding to cases (a)–(c) as

$$\Delta E_l^{\text{top}}(T^*) \equiv \sum_{(j_1,j_2)\in \max(j_1,j_2)=l} E_{j_1 j_2}^{(2)}(T^*), \tag{38}$$

$$\Delta E_l^{\min}(T^*) \equiv \sum_{(j_1,j_2)\in \min(j_1,j_2)=l} E_{j_1 j_2}^{(2)}(T^*), \tag{39}$$

$$\Delta E_l^{\text{av}}(T^*) \equiv \sum_{(j_1,j_2)\in (j_1+j_2)/2=l} E_{j_1 j_2}^{(2)}(T^*). \tag{40}$$

These definitions are applicable to all possible PW/m structures of SAP energies. The singly-indexed SAP pair-energy increments satisfy the inequalities

$$\left|\Delta E_l^{\min}\right| \leqslant \left|\Delta E_l^{\text{av}}\right| \leqslant \left|\Delta E_l^{\text{top}}\right|. \tag{41}$$

These contributions are equal for SAP energies consisting of a single sequence of diagonal PW/m increments.

Let us illustrate the results of applying the definitions (38)–(40) in the case of the $(\text{nd})^2\ {}^1\text{D}$ pair for $l = 10$:

$$\begin{aligned}
\Delta E_{10}^{\text{top}} &= E_{10\,10}^{(2)} + 2E_{10\,8}^{(2)} + 2E_{10\,6}^{(2)},\\
\Delta E_{10}^{\min} &= E_{10\,10}^{(2)} + 2E_{10\,12}^{(2)} + 2E_{10\,14}^{(2)},\\
\Delta E_{10}^{\text{av}} &= E_{10\,10}^{(2)} + 2E_{11\,9}^{(2)} + 2E_{12\,8}^{(2)}.
\end{aligned} \tag{42}$$

Since configurational-pair- and shell-energies as well as the total MP2/CA energy are defined as sums over SAP energies, we define for these larger energy portions the $l$-contributions of any type considered as appropriate sums of pair energies of the relevant type

The nonuniqueness of the definition of the $l$-label of various portions of the MP2 energy, which may arise for electron pairs of non-s electrons, might cause some doubts concerning the structure of the asymptotic series of MP2 energies. For example, Gribakin and Ludlow [35] have suggested that as a result of the existence of complex pairs, in the asymptotic expansion of the MP2 energy, the term next the $(l_{\text{top}}+1/2)^{-4}$ one may be of the order $(l_{\text{top}}+1/2)^{-5}$, rather than $(l_{\text{top}}+1/2)^{-6}$. We have studied this problem, and found that, the AECs are the same for all the $l$-contributions ((38)–(40)). This finding is a result of the fact that the differences of the labels involved in these definitions are negligible for $l \to \infty$. Consequently, no terms of the order $(l_{\text{top}}+1/2)^{-5}$ are required in the asymptotic expansion.

Note should be made of the fact that the choice of the definition of the $l$-contributions may be relevant in computations of accurate MP2/CA energies. This is especially true if one would like to take advantage of the knowledge of the theoretical AECs in extrapolations to the complete-basis-set (CBS) limit. We have found that, in this case, using the $\Delta E_l^{\text{av}}(T^*)$ definition leads to the most accurate results. Therefore, we have used this definition in all computations below.

Summarizing this subsection, we would like to emphasize that getting insight in the structure of the PW/m expansion of the SAP energies would be impossible without the information about the shape of the first-order wave function in the electron coalescence region attainable for the PW/a expansion.

## 2.5 Formulae for the PW/m asymptotic expansion coefficients of MP2/CA pair energies

To obtain the formulae for the leading AECs for the PW/a and PW/m expansions, we have to extract from the expressions $\tilde{E}_l^{(2)}(T^*)$, Eq. (29) and $\varepsilon_{j_1 j_2}^l(T^*)$, Eq. (37), respectively, which represent the portions of the PW increments that dominate in the large-$l$ regime, the coefficient of the lowest-$k$ terms in the $(l+1/2)^{-k}$ expansion.

The formulae for the two leading AECs in the case of the PW/a expansion for He-like atoms in the 1/Z-PT have been derived by in a very original way by Kutzelnigg and Morgan (KM) [21]. However, unlike the present rather straightforward approach which is based on the analysis of singularities in Eq. (9) and on the expression for the second-order pair energy (18), these authors have started from the Hylleraas functional which requires dealing with kinetic energy terms (the $D_l$ terms in Ref. [21]). These terms are rather cumbersome when proceeding to the MP2 approach and might have masked the simple structure of the leading AE coefficients. In the light of our conclusions concerning the similarity of the singularity structure of Eqs. (9) and (20) the expressions for $\widetilde{E}_l^{(2)}(T^*)$ differ only in the radial integrals, where the hydrogen-like orbitals have to be replaced by the HF ones. Hence, since $\widetilde{E}_l^{(2)}(T^*)$ is proportional to the $B_l$ term studied in Ref. [21], we can use, in the PW/a case the results of the extrapolation procedure evaluated in an elegant way by Kutzelnigg and Morgan just for the $B_l$ term. In this way we avoid going through a rather lengthy, tiresome and errorprone procedure. The formulae of the leading AECs for the PW/a expansion of the MP2/CA SAP energies are for all but the natural singlet pairs identical to those presented by KM in Table I of Ref. [21], provided that the radial integrals are modified. In the natural singlet case, we have not been able to obtain the same formula for the second in importance AEC associated with the $(l+1/2)^{-6}$ term, i.e., the formulae obtained by multiplying the coefficient of $(l+1/2)^{-4}$ by the "universal" factor $-5/4$.

Unfortunately, it is not possible to use the results of Ref. [21] when extrapolating the increments $E_{j_1 j_2}^{(2)}(T^*)$ in the case of the PW/m expansion. Our extrapolation procedure is based on Eq. (37). The first step consists the evaluation of all integrals involving functions of angular variables and extracting from the radial integrals the explicit dependence on the indices defining the partial waves. The expressions obtained are considerably more complex than in the PW/a case. As one can see from Eq. (37) the $\varepsilon_{j_1 j_2}^l(T^*)$, representing components of the PW/a increments, have not only to be multiplied by the coefficient $c_{j_1 j_2}^l(T^*)$ (Eq. (31)) but also be summed over the index $l$. As a result the extrapolation procedure is much more complex than in the PW/a case considered by Kutzelnigg and Morgan. We have not managed yet to set up a concise general extrapolation procedure for the

PW/m SAP energies. Instead we follow a less elegant, pedestrian way to perform the extrapolation. Therefore, below we report just the final results. More details and discussion are given in Ref. [24].

Let us present, in the notation of KM [21], our formulae for the leading AECs in the PW/m expansion of the SAP energies:

1. Natural-parity singlet pairs:

$$a_1^{\mathrm{HF}} = -\frac{3}{8} N R_+^{(5)} F_0 \quad \text{(identical with the PW/a coefficient)}. \tag{43}$$

2. Natural-parity triplet pairs:

$$a_1^{\mathrm{HF}} = -N\left[\frac{5}{64} F_0 R_-^{(7)} + \frac{-35}{256}(F_1 - G_1) R_+^{(5)}\right]. \tag{44}$$

3. Unnatural-parity triplet pairs:

$$a_1^{\mathrm{HF}} = \frac{35}{128} N F_1 R_+^{(5)}. \tag{45}$$

4. Unnatural-parity singlet pairs:

$$a_1^{\mathrm{HF}} = -N\left[\frac{-21}{128} F_1 R_-^{(7)} + \frac{231}{2048}(F_2 - G_2) R_+^{(5)}\right]. \tag{46}$$

The following notation is used:

$$N = \frac{1}{1 + \delta_{n_i n_j} \delta_{l_i l_j}},$$

$$F_0 = G_0 = (2l_1 + 1)(2l_2 + 2) \begin{pmatrix} l_1 & l_2 & L \\ 0 & 0 & 0 \end{pmatrix}^2,$$

$$F_p = (-1)^L (2l_1 + 1)(2l_2 + 1) \times \sum_{n=0}^{2\min(l_1, l_2)} (2n + 1)\big[n(n+1)\big]^p \begin{Bmatrix} l_1 & l_1 & n \\ l_2 & l_2 & L \end{Bmatrix} \begin{pmatrix} l_1 & l_1 & n \\ 0 & 0 & 0 \end{pmatrix} \begin{pmatrix} l_2 & l_2 & n \\ 0 & 0 & 0 \end{pmatrix},$$

$$G_p = (2l_1 + 1)(2l_2 + 1) \times \sum_{n=|l_1 - l_2|}^{l_1 + l_2} (2n + 1)\big[n(n+1)\big]^p (-1)^{L+n} \begin{Bmatrix} l_1 & l_2 & n \\ l_1 & l_2 & L \end{Bmatrix} \begin{pmatrix} l_1 & l_2 & n \\ 0 & 0 & 0 \end{pmatrix}^2,$$

$$R_+^{(5)} = \int_0^\infty \rho_+(r, r) r^5 dr, \quad R_-^{(7)} = \int_0^\infty \rho'_-(r, r) r^7 dr,$$

where

$$\rho_{\pm}(r,r') = \frac{1}{2}\left|R_{n_1 l_1}(r)R_{n_2 l_2}(r') \pm R_{n_1 l_1}(r')R_{n_2 l_2}(r)\right|^2,$$

$$\rho'_{-}(r,r') = \frac{\partial^2 \rho_{-}(r,r')}{\partial r'^2}.$$

For a discussion of the differences between formulae (43)–(46)) and their KM counterparts see Refs. [23,24].

## 3. APPLICATIONS

In this section we would like to discuss some problems related to the energy extrapolation methodology and to present some pilot of applications of the formulae for the AECs. All numerical results are related to the $Zn^{2+}$ ion. This choice is due to the fact that for this ion we have recently [22,23] performed very extensive numerical studies resulting in MP2/CA energy increments of unprecedented accuracy. For the ion considered we have obtained results for 56 SAPs including 28 natural parity singlet pairs (NS pairs), 18 natural parity triplet pairs (NT pairs), 7 unnatural parity triplet pairs (UT pairs), and 3 unnatural parity singlet pairs (US pairs). By a method especially designed to eliminate the impact of numerical inaccuracies present in the computed PW/m energy increments in the PW/m expansion including up to $l = 45$, we have determined the two most important AECs for each pair [23]. Hence, we have been in a position to make comparison of the computed and theoretical AECs reported by KM. We found no agreement for all but the NS pairs, which, from the present point of view, was caused by the fact that these authors derived their formulae for a different (PW/a) partial wave expansion.

As we have mentioned in the Introduction, the PW/m structure of the SAP energies and their sums disclose several useful general properties. In Figure 9.1 we visualize one of them relevant to designing extrapolation procedures. We present the PW/m increments, $E^{(2)}_{j_1 j_2}(T^*)$, for three $(ns)^2$ pairs ($n = 1, 2, 3$), and three configurational pairs: $2p^2$, 2p3p, and $3p^2$. Notice that in all cases, for $l \leqslant 2$, i.e., for the orthogonalized PWs, the values of the PW increments vary for the individual pairs in a rather random way. A threshold for regular decrease of their values can be observed for each pair for $l \geqslant 3$, i.e., when we have to deal with free PWs (FPWs). It is obvious from Figure 9.1 that any PW extrapolation procedure is meaningful only for the FPWs. The OPW contributions can only be obtained in the computational way. Let us remind that the classification into OPWs and FPWs depends on the maximum orbital momentum quantum number of the electrons defining the HF determinant. Therefore, the threshold $l$-value for extrapolation procedures depends on the atom considered. Taking into account the fact of existence of two categories of PW increments, one can easily explain the nonmonotonic approach to the $l$-limit value observed for low-$l$ contributions to the MP2 energy mentioned by Gribakin and Ludlow [35].

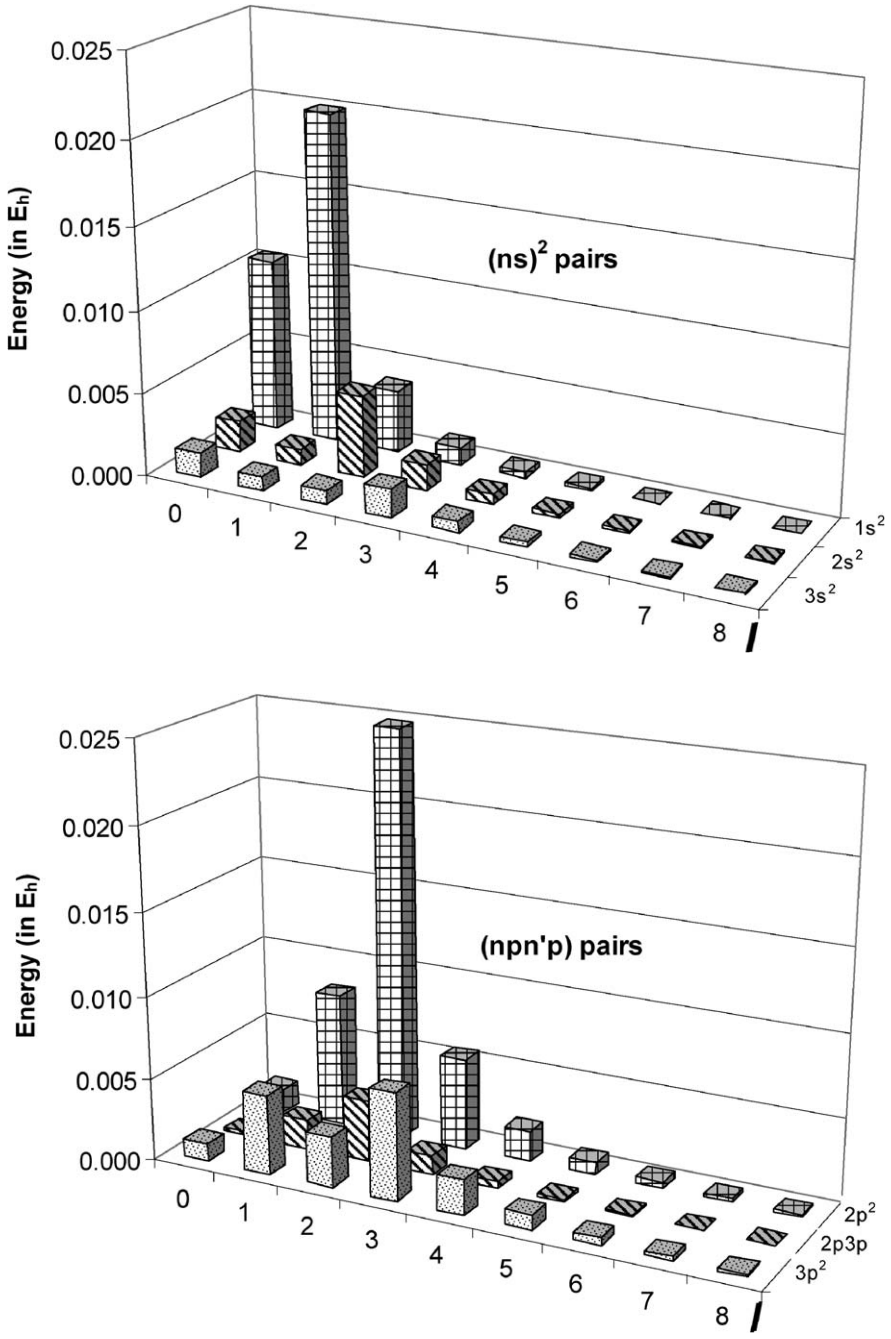


**FIGURE 9.1** PW/m contributions to the SAP energies for the $(ns)^2\ ^1S$ ($n = 1, 2, 3$) pairs and to npn'p configuration pair energies (signs reversed). For numerical values see Ref. [22].

### 3.1 Theoretical estimates of PW/m energy contributions

The knowledge of the theoretical values of the leading AECs, $a_k^{\mathrm{HF}}(T^*)$, can be used for construction of the following estimates to the SAP pair energies:

$$E_{ll}^{\mathrm{est}}(T^*) = \frac{a_k^{\mathrm{HF}}(T^*)}{(l+1/2)^k}, \tag{47}$$

where $k = 4$ for NS, $k = 6$ for NT, UT, and $k = 8$ for US pairs.

To get an idea about the efficiency of the simple theoretical estimates $E_{ll}^{\mathrm{est}}(T^*)$ in reproducing the values of the PW/m energy increments, we compare in Table 9.1 their values for selected pairs of $Zn^{2+}$ (one from each of the four symmetry types) with the corresponding accurate values. We can see from the table that the estimated PW/m increments differ most significantly from their accurate counterparts for $l = 3$, i.e., for the first FPW, which may be an indication that this partial wave should be omitted in extrapolation procedures. For larger values of $l$ the difference drops reasonably fast to the value of less than 5% percent. These example indicate that in many cases one can replace extensive computations of higher-PW increments by employing the simple theoretical formula (47). The remaining error is certainly caused by reducing the PW/m expansion to just one term. To see what would be the improvement if the next important term is taken into account, we include in the last two columns of Table 9.1 the modified estimates based on the following two-term formula

$$\widetilde{E}_{ll}^{\mathrm{est}}(T^*) = \frac{a_4^{\mathrm{HF}}(T^*)}{(l+1/2)^4} + \frac{b_6^{\mathrm{compt}}(T^*)}{(l+1/2)^6}, \tag{48}$$

in which the unknown theoretical coefficient in the second term is replaced by the coefficient $b_6^{\mathrm{compt}}(T^*)$ determined in Ref. [23] from very accurate extrapolations of computed PW/m energy increments. We note from the results that the inclusion of the $(l+1/2)^{-6}$ term in (48) leads for every $l$ to a significant reduction of the differences with the accurate PW/m increments. The inclusion of the second term in the estimation expression for NS is also desirable from the methodological point of view, because it is of the same order in the asymptotic expansion as the leading term for the NT and UT pairs. Hence, the knowledge of the second AECs for NS pairs would together with the already known leading AECs for NS and NT secure the knowledge of the total MP2/CA energy up to the $(l+1/2)^{-6}$ terms.

The present results also imply that one can obtain moderately accurate values of, at least, the first AEC by means of very accurate values of $E_{ll}^{\mathrm{est}}(T^*)$ even for low $l$; this conclusion could be important because for methods other than MP2 or in the case of molecules it may not be possible to obtain AECs theoretically

The simple method of obtaining estimates of the SAP PW/m energy increments can easily be extended to the case of larger portions of the MP2/CA energy such as, for example, configurational pair energies. To obtain an estimate of these energies corresponding to the $l$th term of the PW/m expansion, one has to take a sum over the $l$th estimates in all SAPs setting up the configurational pair. In Figure 9.2 we compare the estimates of the PW/m contributions to configurational

**TABLE 9.1** Comparison of accurate calculated PW/m energy increments, $E_{ll}^{(2)}(T^*)$ for $Zn^{2+}$ with theoretical estimates based on the first term of the asymptotic expansion $E_{ll}^{\mathrm{est}}(T^*)$. $\widetilde{E}_{ll}^{\mathrm{est}}(T^*)$ is based on the first two terms of the asymptotic expansion (in $\mu E_h$, all signs reversed)

| Pair | $l$ | $E_{ll}^{(2)}(T^*)$[a] | $E_{ll}^{\mathrm{est}}(T^*)$ | $\delta$ (%)[b] | $\widetilde{E}_{ll}^{\mathrm{est}}(T^*)$ | $\delta$ (%) |
|---|---|---|---|---|---|---|
| $2s^2\ {}^1S$[c] | 3 | 1596.845 | 1748.74 | 9.51 | 1488.16 | 6.81 |
| | 4 | 598.639 | 639.95 | 6.90 | 582.26 | 2.73 |
| | 5 | 273.009 | 286.77 | 5.04 | 269.47 | 1.29 |
| | 6 | 141.631 | 147.00 | 3.80 | 140.65 | 0.69 |
| | 7 | 80.566 | 82.93 | 2.94 | 80.24 | 0.40 |
| $2p3p\ {}^1P$[d] | 3 | 44.739 | 45.87 | 2.53 | | |
| | 4 | 5.889 | 6.14 | 4.31 | | |
| | 5 | 1.186 | 1.23 | 4.02 | | |
| | 6 | 0.314 | 0.32 | 3.41 | | |
| | 7 | 0.100 | 0.10 | 2.83 | | |
| $2p3p\ {}^3S$[e] | 3 | 172.096 | 133.80 | 22.25 | | |
| | 4 | 34.153 | 29.62 | 13.28 | | |
| | 5 | 9.736 | 8.89 | 8.74 | | |
| | 6 | 3.475 | 3.26 | 6.16 | | |
| | 7 | 1.448 | 1.38 | 4.57 | | |
| $3p^2\ {}^3P$[f] | 3 | 695.972 | 637.08 | 8.46 | | |
| | 4 | 142.562 | 141.03 | 1.07 | | |
| | 5 | 41.994 | 42.30 | 0.75 | | |
| | 6 | 15.347 | 15.52 | 1.18 | | |
| | 7 | 6.502 | 6.58 | 1.20 | | |

*a* Natural parity singlet.

*b* Unnatural parity singlet.

*c* Natural parity triplet.

*d* Unnatural parity triplet.

*e* Values are taken from Ref. [22].

*f* $\delta = 100 \times \left| \dfrac{E_{ll}^{\mathrm{est}}(T^*) - E_{ll}^{(2)}(T^*)}{E_{ll}^{(2)}(T^*)} \right|$.

pair energies for three pairs with accurate computed values. We present the estimates obtained when using only the AECs defining the $(l + 1/2)^{-4}$ terms, i.e., providing estimates of the contribution from the NS pairs. We also display the estimates that are obtained when triplet pairs are taken into account, i.e., our estimates take also into account contributions from the $(l + 1/2)^{-6}$ terms. One can easily notice that for small $l$-values the former set of estimates is far off of the accurate values, which is especially true for the $3d^2$ pair. Let us note that taking into account the estimates from the triplet pairs improves the agreement in all cases.

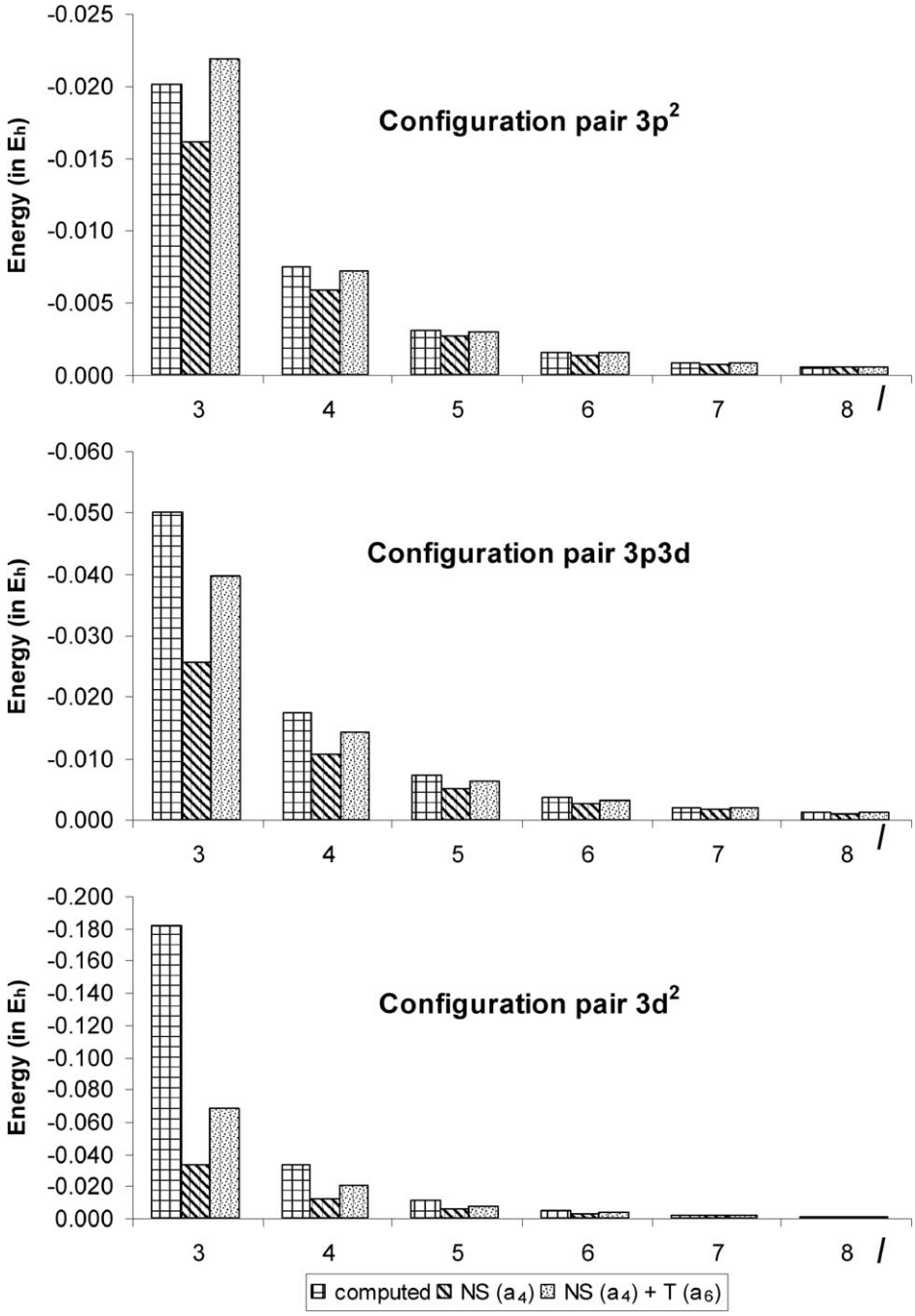


**FIGURE 9.2** Comparison of theoretical estimates of the PW/m contributions to configurational pair energies including only NS pairs [NS($a_4$)] and including all pairs [NS($a_4$) + T($a_6$)] with accurate [computed] results from Ref. [22].

Taking into account our findings at the individual SAP level we might expect that the remaining discrepancies would be significantly reduced if we had access to the theoretical values of AECs defining the $(l+1/2)^{-6}$ terms for the NS pairs. However, one can see in Figure 9.2 that even taking into account the $(l+1/2)^{-6}$ terms in a limited scale accounting for the triplet pairs is necessary to get a more realistic estimate of the individual PW/m contributions to the configurational pair energies. The same is, of course, true also for larger portions of the MP2/CA energies including the total one. Therefore, any attempts of approximating the latter energy just in terms of a global theoretical AEC multiplied by $(l+1/2)^{-4}$ like, e.g., in Ref. [35], are of rather limited accuracy due to the complete neglect of the triplet pairs. Moreover, this accuracy will deteriorate when proceeding to larger atoms where the ratio of the triplet to singlet contributions to the MP2/CA energy increases. Let us just mention that for the Ne atom this ratio is 0.50 whereas for $Zn^{2+}$ it increases to 0.83.

## 3.2 Extrapolation procedure for MP2/CA energies

Let us now have a look at the usefulness of our theoretical AEC-formulae in calculations of accurate SAP energies in radially saturated basis sets including orbitals defined by quantum numbers $l \leqslant l_{\max}$, which are followed by extrapolations to the CBS limit. This extrapolation is accomplished by taking into account the basis set truncation error, $\delta E_{l_{\max}}$, due to omission of functions of $l > l_{\max}$. For $l$-contributions to the pair energy, $\Delta E_l^{(2)}$, having asymptotic expansions of the form

$$\Delta E_l^{(2)} = a_4\left(l+\frac{1}{2}\right)^{-4} + a_6\left(l+\frac{1}{2}\right)^{-6} + a_8\left(l+\frac{1}{2}\right)^{-8} + \cdots \tag{49}$$

this truncation error is defined as [8,12]

$$\begin{aligned}\delta E_{l_{\max}} &= \sum_{l=l_{\max}+1}^{\infty} \Delta E_l^{(2)} \\ &\approx \frac{a_4}{3}(l_{\max}+1)^{-3} + \frac{a_6}{5}(l_{\max}+1)^{-5} + \frac{a_8}{7}(l_{\max}+1)^{-7} + \cdots .\end{aligned} \tag{50}$$

Now we define the extrapolated SAP energies as

$$\mathcal{E}_{l_{\max}}^{(2)}(T^*) = \sum_{l=0}^{l_{\max}} E_{ll}^{(2)}(T^*) + \delta E_{l_{\max}}. \tag{51}$$

The approximate SAP energies, $\mathcal{E}_{l_{\max}}^{(2)}(T^*)$ for $Zn^{2+}$ calculated for all four types of pair functions when using Eq. (51) are compared in Table 9.2 with the accurate values $E_{\mathrm{FEM}}^{(2)}(T^*)$. For each type the correction (50) consists of just one term defined by the relevant leading AEC obtained from our theoretical formulas (43)–(46).

It is apparent from the table that the approximate pair energies are close to their accurate counterpart. Only for $l_{\max} = 2$, which is the lowest value for which any extrapolation is meaningful, the errors are relatively large. The accuracy increases

**TABLE 9.2** Comparison of approximate pair energies $\mathcal{E}^{(2)}_{l_{max}}$ for $Zn^{2+}$ consisting of calculated PW increments up to $l_{max}$ and the theoretical value of the basis set truncated error $\delta E_{l_{max}}$ (in $\mu E_h$, all sign reversed)

| Pair | $l_{max}$ | $\mathcal{E}^{(2)}_{l_{max}}(T^*)$ | $\delta$ (%)[a] | $\widetilde{\mathcal{E}}^{(2)}_{l_{max}}(T^*)$[e] | $\delta$ (%)[b] | $E^{(2)}_{FEM}(T^*)$ [22] |
|---|---|---|---|---|---|---|
| $2s^2\ ^1S$[c] | 2 | 11077 | 3.57 | 10687 | −0.11 | 10699 |
| | 3 | 10800 | 0.99 | 10711 | 0.11 | |
| | 4 | 10731 | 0.35 | 10706 | 0.06 | |
| | 5 | 10709 | 0.15 | 10702 | 0.03 | |
| | 6 | 10700 | 0.07 | 10701 | 0.02 | |
| $2p3p\ ^1P$[d] | 2 | 1089 | 4.38 | | | 1043 |
| | 3 | 1047 | 0.43 | | | |
| | 4 | 1044 | 0.08 | | | |
| | 5 | 1043 | 0.02 | | | |
| | 6 | 1043 | 0.01 | | | |
| $2p3p\ ^3S$[e] | 2 | 990 | 15.12 | | | 1164 |
| | 3 | 1130 | 3.00 | | | |
| | 4 | 1154 | 0.94 | | | |
| | 5 | 1161 | 0.34 | | | |
| | 6 | 1163 | 0.17 | | | |
| $3p^2\ ^3P$[f] | 2 | 22531 | 0.62 | | | 22393 |
| | 3 | 22430 | 0.17 | | | |
| | 4 | 22405 | 0.05 | | | |
| | 5 | 22397 | 0.02 | | | |
| | 6 | 22394 | 0.01 | | | |

*a* Natural parity singlet.

*b* Unnatural parity singlet.

*c* Natural parity triplet.

*d* Unnatural parity triplet.

*e* $\delta = 100 \times \left| \dfrac{\mathcal{E}^{(2)}_{l_{max}}(T^*) - E^{(2)}_{FEM}(T^*)}{E^{(2)}_{FEM}(T^*)} \right|$.

*f* Includes the $\tilde{a}_2$-contribution in $\delta_{l_{max}}$.

very rapidly with increasing $l_{max}$ proving the usefulness of the theoretical AECs. To get an idea about the effect of including the second term in the asymptotic expansion (49) for NS pairs, we have again replaced the unknown theoretical value of $a_6$ by the coefficient $b_6^{compt}$ determined in Ref. [23]. The approximate energies $\widetilde{\mathcal{E}}^{(2)}_{l_{max}}(T^*)$ are also displayed in Table 9.2. In this case we obtain a substantially better agreement for all $l_{max}$ values. The high accuracy attained already for the lowest $l_{max}$ values, is a strong argument for searching the formula for the $a_6$.

**TABLE 9.3** Comparison of the approximate M-shell, $\mathcal{E}^{(2)}_{l_{\max}}(M)$[a] , and total, $\mathcal{E}^{(2)}_{l_{\max}}(\mathrm{Zn}^{2+})$[a] , second-order energies with accurate results (in $mE_h$, all signs reversed)

| $l_{\max}$ | M-shell | | | Total | | |
|---|---|---|---|---|---|---|
| | $\mathcal{E}^{(2)}_{l_{\max}}(M)$ | $\delta$ (%) | $E^{(2)}_{\mathrm{FEM}}(M)$ | $\mathcal{E}^{(2)}_{l_{\max}}$(total) | $\delta$ (%) | $E^{(2)}_{\mathrm{FEM}}$ [22] |
| 2 | 1085.49 | −3.73 | 1046.499 | 1615.15 | −0.96 | 1600.186 |
| 3 | 1022.17 | 2.32 | | 1571.91 | 1.77 | |
| 4 | 1039.88 | 0.63 | | 1592.46 | 0.48 | |
| 5 | 1044.73 | 0.17 | | 1597.82 | 0.15 | |
| 6 | 1046.04 | 0.04 | | 1599.26 | 0.06 | |

*a* See text.

The high accuracy of the results achieved at the SAP level is reflected in calculations for larger portions of the MP2/CA energies. In Table 9.3 we compare the approximate intrashell second-order energies for the M-shell electrons, $\mathcal{E}^{(2)}_{l_{\max}}(M)$, and the approximate total second energies, $\mathcal{E}^{(2)}_{l_{\max}}(\mathrm{Zn}^{2+})$ with the accurate computed FEM values [22]. For both energies, the approximate results are very close to their FEM counterparts resulting from very extensive numerical computations. It is interesting to note that already for $l_{\max} = 4$ the relative error of the approximated values is less than 1%.

## 4. CONCLUSIONS

In this chapter we have been concerned with the derivation and applications and of formulae for the leading asymptotic expansion coefficients (AECs) of the partial-wave (PW) expansion in powers of $(l + 1/2)^{-1}$ for the symmetry-adapted pair (SAP) energies which are building blocks of the second-order Møller–Plesset correlation energies for closed-shell $N$-electron atoms (MP2/CA). An essential step in our derivation consists in removing some nonuniqueness in the broadly used PW-expansion terminology. We have distinguished two PW expansions. First, the main PW expansion (PW/m), which is of importance in all orbital based (CI) approaches because the PW/m components of SAPF are directly defined by the angular momenta of the orbitals used in their computation. Second, the auxiliary PW expansion (PW/a), for which the PW increments (PW/a) are defined by the order, $l$, of the Legendre polynomial $P_l(\cos\vartheta_{12})$ in the expansion of the pair function. These two expansions are identical only if pairs of s-electrons are considered. This fact has caused that the formulae for the AECs for pair energies based on the PW/a expansion, which were derived by Kutzelnigg and Morgan [21] for states of He-like ions within the framework of the $1/Z$ expansion perturbation theory, could not be adapted to yield agreement with our computed AECs for the SAP energies defined for the PW/a expansion. To obtain the AEC-formulae for

the SAP energies of the MP2/CA approach, we have derived an equation relating the PW/m and PW/a energy increments. The theoretical formulae obtained are in close agreement with the computationally determined ones for Ne and $Zn^{2+}$ (see Refs. [23,24]).

We have also been concerned with discussion of the relationship of the PW/m energy increments, which are indexed with a dyad if quantum numbers, with the energy contributions used in the extrapolation defined in terms of powers of $(l + 1/2)^{-1}$ that are labeled by the single quantum number $l$. One may consider several ways of linking these energy contributions. Although they correspond to identical asymptotic expansions, the way of establishing the link may be significant in various applications of the theoretical AECs. Some attention has been paid to the existence of an "extrapolation threshold" defined in a way that excludes from the extrapolation procedure the orthogonalized PW/m increments.

Establishing an explicit relationship between the HF orbitals defining the zero-order problem and the asymptotic behavior of the MP2/CA SAP energies is certainly of interest from the methodological point of view. However, the easy access to theoretical AECs opens the way to their application in studies related to bases-set-extrapolation problems in systems other than closed-shell atoms. We have demonstrated two encouraging ways of application of the theoretical AECs. The first one consists in using them to construct theoretical estimates for the PW/m energy increments of the SAP energies as well as for larger portions of the MP2/CA energy. It has been found that these estimates are close to the accurate values even in the neighborhood of the extrapolation threshold. The second application consists in setting up a reliable method of calculating approximate SAP energies in which energies calculated for angularly restricted basis sets are corrected by values of the basis set truncation errors evaluated when using theoretical AECs. The energies obtained disclosed a very good agreement with the accurate results even for truncations starting close to the extrapolation threshold. Mention should be made that in both examples the close agreement is found for energy contributions defined by the $l_{av}$ indices defined above. Our results indicate that to reach reliable estimates of the MP2/CA energy or its shell- or intershell contributions, one has to take into account the AECs corresponding both to the fourth and sixth power in the $(l + 1/2)^{-1}$ expansion, which is not always the case in CBS limit extrapolation methods.

The present results provide an exact relationship between the Hartree–Fock wave function and the leading AECs in the PW/m expansion of the MP2/CA SAP energies and, consequently, of larger portions of the correlation energy including the total second-order energy. As we have demonstrated in this chapter, they are very useful in reducing the computational effort in MP2/CA computations. There is still one problem to be solved in order to further increase the accuracy attainable when using the theoretical AECs. This problem consists in deriving the formula for the coefficient of the $(l + 1/2)^{-6}$ term in the PW/m expansion of the natural parity singlet states. Knowing this formula and taking into account that we already know the formulae for the leading AECs for both types of triplet pairs which are also associated with the $(l+1/2)^{-6}$ term, we would have complete information on

the asymptotic convergence of the MP2/CA energies including all terms of sixth order. We continue working on this problem.

Given that the behavior of PW/m increments can be described by short asymptotic formulae for relatively low $l$, it is also possible to obtain with a degree of accuracy sufficient for the purposes of efficient extrapolation, the AECs through those PW/m increments if they are computed very accurately, for instance by numerical methods. This conclusion is also of importance because it may be very difficult to obtain theoretically the AECs for methods other than MP2 or molecules.

We believe that our findings will open the way to new applications of theoretical MP2/CA results, in investigations aiming at providing theoretical foundations for reliable methods of attaining complete-basis-set limits in molecular calculations.

## ACKNOWLEDGEMENTS

K.J. would like to acknowledge financial support by the Polish Ministry of Higher Education (grant N204 126 31/2930). JRF acknowledges the financial support of the Xunta de Galicia through the project PGIDT05PXIB31402PR.

## REFERENCES

[1] W. Kutzelnigg, W. Klopper, *J. Chem. Phys.* **94** (1991) 1985.
[2] J. Komasa, *J. Chem. Phys.* **110** (1999) 7909.
[3] O. Hino, Y. Tanimura, S. Ten-no, *Chem. Phys. Lett.* **353** (2002) 317.
[4] S. Ten-no, F.R. Manby, *J. Chem. Phys.* **119** (2003) 5358.
[5] D.P. Tew, W. Klopper, *J. Chem. Phys.* **123** (2005) 074101.
[6] H.-J. Werner, F.R. Manby, *J. Chem. Phys.* **121** (2006) 054114.
[7] T.H. Dunning Jr., *J. Chem. Phys.* **90** (1989) 1007.
[8] W. Klopper, K.L. Bak, P. Jørgensen, J. Olsen, T. Helgaker, *J. Phys. B: At. Mol. Opt. Phys.* **32** (1999) R103.
[9] D. Feller, K.A. Peterson, *J. Chem. Phys.* **110** (1999) 8384.
[10] T.H. Dunning Jr., *J. Phys. Chem. A* **104** (2000) 9062.
[11] K.L. Bak, A. Halkier, P. Jørgensen, J. Olsen, T. Helgaker, W. Klopper, *J. Mol. Struct.* **567–568** (2001) 375.
[12] W. Klopper, *Mol. Phys.* **99** (2001) 481.
[13] C. Møller, M.S. Plesset, *Phys. Rev.* **36** (1934) 618.
[14] K. Jankowski, P. Malinowski, *Phys. Rev. A* **21** (1980) 45.
[15] S.J. Chakravorty, E.R. Davidson, *J. Phys. Chem.* **100** (1996) 6167.
[16] O. Sinanoğlu, *Adv. Chem. Phys.* **6** (1964) 315.
[17] J.R. Flores, *Chem. Phys. Lett.* **195** (1992) 377.
[18] J.R. Flores, K. Jankowski, R. Słupski, *Mol. Phys.* **98** (2000) 1125.
[19] K. Jankowski, R. Becherer, P. Scharf, H. Schiffer, R. Ahlrichs, *J. Chem. Phys.* **83** (1985) 1413.
[20] C. Schwartz, *Meth. Comput. Phys.* **2** (1963) 241.
[21] W. Kutzelnigg, J.D. Morgan III, *J. Chem. Phys.* **96** (1992) 4484.
[22] J.R. Flores, R. Słupski, K. Jankowski, P. Malinowski, *J. Chem. Phys.* **121** (2004) 12334.
[23] J.R. Flores, R. Słupski, K. Jankowski, *J. Chem. Phys.* **124** (2006) 104107.
[24] K. Jankowski, R. Słupski, J.R. Flores, *Mol. Phys.* **104** (2006) 2213.

[25] O. Sinanoğlu, *Proc. Roy. Soc. (London) A* **260** (1961) 379.
[26] K.C. Pan, H.F. King, *J. Chem. Phys.* **56** (1972) 4667.
[27] K. Jankowski, P. Malinowski, M. Polasik, *J. Phys. B: At. Mol. Phys.* **13** (1980) 3909.
[28] S.N. Banerjee, *J. Phys. B: At. Mol. Phys.* **9** (1976) 21.
[29] C. Schwartz, *Phys. Rev.* **126** (1962) 1015.
[30] T. Kato, *Comm. Pure Appl. Math.* **10** (1957) 151.
[31] R.T. Pack, W. Byers-Brown, *J. Chem. Phys.* **45** (1966) 556.
[32] J.D. Morgan III, in: C.A. Tsipis, V.S. Popov, D.R. Herschbach, J.S. Avery (Eds.), *New Methods in Quantum Theory*, Kluver, Dordrecht, 1996, pp. 311–338.
[33] R.N. Hill, *J. Chem. Phys.* **83** (1985) 1173.
[34] D.A. Varshalovich, A.N. Moskalev, V.K. Khersonskii, *Quantum Theory of Angular Momentum*, World Scientific, Singapore, 1988.
[35] G.F. Gribakin, J. Ludlow, *J. Phys. B: At. Mol. Opt. Phys.* **35** (2002) 339.

CHAPTER 10

# A Computer-Algebraic Approach to the Derivation of Feynman–Goldstone Perturbation Expansions for Open-Shell Atoms and Molecules

**Stephan Fritzsche**[*], **Brajesh K. Mani**[**] and **Dilip Angom**[**]

Contents



[*] Institut für Physik, Universität Kassel, D-34132 Kassel, Germany
[**] Physical Research Laboratory, Navarangpura-380 009, Gujarat, India

Advances in Quantum Chemistry, Vol. 53
ISSN 0065-3276, DOI:10.1016/S0065-3276(07)53010-8

**Abstract** Many-body perturbation theory has a long tradition in studying the electronic structure of atoms and molecules. Over the years, this theory helped provide accurate predictions on a large number of properties, such as correlation energies, hyperfine structures, isotope shifts, polarizabilities, decay rates, and several others. For many open-shell atoms and molecules, however, its application has been hampered by the size and complexity of all perturbation expansions if two or more electrons and/or holes appear in open shells. To overcome these difficulties in dealing with open-shell systems, a computer-algebraic approach is suggested which facilitates the treatment of second-quantized operators and extended model spaces and, hence, the derivation of perturbation expansions. This approach is based on Wick's theorem and an algebraic representation of the model space functions in order to 'formalize' the derivation. Below, we explain the basic steps and how computer algebra can be utilized interactively in deriving perturbation expansions of various kinds. Apart from predicting the electronic structure and properties of atoms and molecules with complex shell structures, such a formal approach might be useful and applicable also for studying the dynamics of quantum systems.

## DEDICATION

Over the last decades, Ingvar Lindgren has contributed extensively to the advancement of atomic many-body perturbation theory (MBPT). His well-known textbook on this topic [1], together with John Morrison, has helped a whole generation of young physicists to understand the electronic structure and interactions of atoms and ions. In particular, the use and foundation of multidimensional model spaces in MBPT [2], as appropriate and necessary for open-shell atoms and molecules, facilitated the investigation of a large number of properties. Beside establishing new insights into the demands of extended model spaces, Ingvar's recent contributions to the relativistic many-body theory and its merge with quantum electro-dynamics (QED) [3,4] deserves, among many others, to be accentuated. On the occasion of Ingvar Lindgren's 75th birthday, therefore, we wish to dedicate to his work our recent search for computer-algebraic routes in deriving perturbation expansions for open-shell atoms and molecules.

## 1. INTRODUCTION

Many-body perturbation theory (MBPT) was developed originally in the 1950s by Brueckner [5,6], Bethe [7], Goldstone [8], and several others for investigating nuclear structures and the many-body problem of strongly interacting particles (see the textbook of DeShalit and Talmi [9] for a brief historical account). In the early 1960s, Kelly [10,11] pioneered the application of MBPT for studying correlation effects on the structure and properties of atoms. Since then, the methods of MBPT have been used very successfully to predict a large number of atomic and molecular properties, often in excellent agreement with experimental data.

Usually, an accurate description of the inter-electronic interaction in (many-electron) atoms and molecules poses serious challenges. An appropriate scheme is to separate out a *mean-field* part from the atomic or molecular Hamiltonian, which approximates the electron–electron interaction in terms of a central field potential. This part is referred to as the zeroth-order Hamiltonian. It has a complete set of one-electron functions (spectrum) and the many-electron states constructed from this set is often taken as the basis of MBPT. The choice of a 'reference state', which is a good approximation to the atomic or molecular states of interest, is the starting point of the MBPT computations [1]. The aim of almost all many-body perturbation techniques is then to incorporate the effects of the remaining inter-electronic (Coulomb) interaction perturbatively. This allows for—order-by-order—to determine corrections to the reference state or for some desired property. In practice, of course, the particular choice of the mean-field Hamiltonian depends on the size and shell-structure of the system and may raise questions by its own. The use of a Hartree–Fock potential, for instance, is typically appropriate for those systems, for which relativistic effects are not important, while, otherwise, a Dirac–Fock potential (based on Dirac's relativistic wave equation of the electron) might be more advisable [12,13]. The use of the traditional MBPT is suitable when it converges within a few orders. Broadly speaking, the *convergence* of the perturbation expansions is expected to be reasonable fast, when the mean-field potential incorporates already a 'major part' of the inter-electronic interactions.

A systematic application of MBPT often leads to a proliferation of terms and contributions due to higher-order excitations which may complicate the computations considerably. To facilitate the handling of these terms, the 'diagrammatic evaluation' of the expression from perturbation theory has been found helpful to elevate the complexity of perturbation expansions arising from the number or increasing order of the perturbations [14]. Still, the difficulty with the increasing number of terms remain. As shown recently for single-valence atoms [15], for example, there are 1648 diagrams at fourth-order MBPT to calculate the properties of one-electron operators. In the past, therefore, most applications of MBPT techniques were restricted to (i) rather low orders of perturbation theory and (ii) to atomic and molecular states with simple shell structures. Up to the present, there are (almost) no systematic studies available for atoms with more than two electrons *and/or* holes outside of closed shells otherwise, or if—apart from the dominant Coulomb correlations—one or several additional perturbations $V = V_1 + V_2 + \cdots$ need to be taken into account. The latter restriction hereby oc-

curs frequently if the relativistic corrections to the Coulomb repulsion among the electrons should be treated independently (usually, in first- or second-order only) in the perturbation expansions. A possible solution to avoid this rapid proliferation of terms is the Coupled-Cluster Approach (CCA). This approach is equivalent for taking into account the one-, two-, ... $n$-particle interactions in all orders [16]. Currently, the Coupled-Cluster Singe–Double (CCSD) approximation is applied most frequently, including sometime important triple and quadruple excitations. This approximation is based on the fact, that single and double excitations often describe more than 99% of all correlation effects.

A further restriction on the use of many-body perturbation techniques arises from the (quasi-) degenerate energy structure, which occurs for most open-shell atoms and molecules. In these systems, a single reference state fails to provide a good approximation for the physical states of interest. A better choice, instead, is the use of a multi-configurational reference state or model space, respectively. Such a choice, when combined with configuration interactions calculations, enables one to incorporate important correlation effects (within the model space) to all orders. The extension and application of perturbation expansions towards open-shell systems is of interest for both, the traditional order-by-order MBPT [1] as well as in the case of the CCA [17].

The rapid increase in computing power, nowadays available, has made large-scale MBPT computations a reality. However, the size and complexity of the perturbation expansions involved make such computations rather cumbersome—if real open-shell systems or second- and higher-order effects need to be considered. An new alternative for rendering these calculations tractable is using the algorithms and techniques of 'computer algebra' [18]. In particular, the development of general-purpose computer algebra systems (CAS) provides a very promising route to overcome the challenges above and to carry further the calculations through a maze of MBPT diagrams or algebraic terms. When compared with the (purely) algebraic or graphical approaches, the use of computer algebra is much more efficient and reliable. In this contribution, therefore, we shall describe how computer algebra can be utilized to attack the problem. To this end, we also developed the GOLDSTONE program which we shall introduce and briefly describe below.

## 2. RAYLEIGH–SCHRÖDINGER PERTURBATION THEORY

### 2.1 Overview

In perturbation theory, one often starts with an *a priori* partitioning of the many-body atomic or molecular Hamiltonian,

$$H = H_o + V, \tag{1}$$

into an (unperturbed) model operator ($H_o$) and the perturbation $V$, which describes the *rest interaction* of the system. Here, $H_o$ is supposed to provide a 'good' approximation to the full Hamiltonian $H$ and should have eigenfunctions and eigenvalues which are simple to determine. In practice, moreover, the partitioning of the Hamiltonian should ensure already that the perturbation expansions

to be derived converge reasonably fast and that the computations remain overall tractable. Usually, the model operator ($H_o$) is taken as a sum of one-particle operators in which the (mean) interaction among the electrons is approximated by a central field $V(r)$. In the non-relativistic theory, these one-particle operators can be chosen simply as the Hartree–Fock operators, $h_{\mathrm{HF}}$, but could be replaced also by the corresponding Dirac–Fock operators, $h_{\mathrm{DF}}$, if the system is to be treated relativistically.

Starting from the partitioning (1) of the Hamiltonian, two *kinds* of perturbation expansions are frequently distinguished: the Brillouin–Wigner (BW) and Rayleigh–Schrödinger (RS) perturbation expansions. Since the BW expansions depend on the exact energy, which remains unknown until the problem has been solved, they have to be determined iteratively. For the computation of atomic or molecular properties, therefore, the BW theory is found of little practical value. In addition, this theory is not so suitable for degenerate states. On the other hand, the RS expansions depend on the eigenvalues of $H_o$. This offers the great advantage of solving a perturbation expansion with all the (algebraic) terms well defined, and including the case of a degenerate model space. For these reasons, we shall restrict ourselves in the following to the RS perturbation theory which forms the basis for (almost) all applications of the theory to more complex systems. Historically, Kato [19] and Bloch [20] pioneered the RS perturbation expansion, but based always on a single (unperturbed) eigenfunction even for those systems where there are other, nearly-degenerate solutions of $H_o$.

For the model operator $H_o$, the Schrödinger equation has a *complete* (and orthonormal) set of eigenfunctions

$$H_o|\phi_\alpha\rangle = E_\alpha^o|\phi_\alpha\rangle \tag{2}$$

with

$$\langle\phi_\alpha|\phi_\beta\rangle = \delta_{\alpha\beta}. \tag{3}$$

These eigenfunctions define a basis in the $N$-electron Hilbert space. To account for the effects of the rest interaction $V$ perturbatively, the full Hilbert space $\mathcal{H}$ of $H_o$ is separated into two parts: the *model space* $\mathcal{M}$ and its 'complement', $\mathcal{H} \ominus \mathcal{M}$, which includes all the remaining dimensions. To these subspaces, we assign the projection operators

$$P = \sum_{|\phi_\alpha\rangle \in \mathcal{M}} |\phi_\alpha\rangle\langle\phi_\alpha|, \tag{4}$$

$$Q = 1 - P = \sum_{|\phi_\beta\rangle \notin \mathcal{M}} |\phi_\beta\rangle\langle\phi_\beta|, \tag{5}$$

which satisfy the relations

$$P = P^\dagger = PP, \quad PQ = QP = 0 \tag{6}$$

and

$$[P, H_o] = [Q, H_o] = 0. \tag{7}$$

In general, a proper choice of $\mathcal{M}$ is very crucial to apply many-body perturbation techniques. Typically, a faster convergence of the perturbation expansions is found, if a large part of the required solution lies within the model space $\mathcal{M}$. In other words, a good deal of the 'correlation effects' should be found already within $\mathcal{M}$; this part of the overall correlation contributions is treated exactly by diagonalizing an effective Hamiltonian. In comparison, the correlation effects arising from the complementary space $\mathcal{H} \ominus \mathcal{M}$, should be reasonably 'weak' so that they can be treated perturbatively. Here, we shall not discuss what the term 'weak' means and how it could be quantified (if this is practical at all). For simple systems, such as closed-shell or alkali-like atoms and ions, a single eigenstate of $H_o$ is often a good approximation to the exact state, giving rise to a 1-dimensional model space $\mathcal{M}$. Computations based on such a model space are called *single reference* calculations. For open-shell systems, in contrast, multidimensional model spaces are very crucial; this 'extension' of the model spaces for several (nearly degenerate) eigenvalues has been discussed by Lindgren [2,21], and at several places elsewhere.

For several decades, the methods of MBPT have been developed and applied mainly within the framework of the nonrelativistic (quantum) theory. A relativistic formulation of the theory was developed only in the 1980s and 1990s [12,22,23], based more often than not on the *no-pair* Hamiltonian. In this approximation, the 'translation' of the standard methods from the non-relativistic into the relativistic framework is quite simple, but this neglects also all the effects of the negative continuum as well as the (so-called) 'radiative corrections' (from QED) right from the beginning [24]. A more consistent treatment of the many-body correlation and QED effects has been worked out only recently by Lindgren and coworkers [3,4] by providing a formalism for energy-dependent MBPT.

## 2.2 Generalized Bloch equation

For open-shell atoms and molecules, its often desirable to obtain a representation for several (nearly degenerate) states owing to the large number of close lying states, and for calculating most properties apart from energies. In the following, therefore, let us consider $d$ different solutions of the (many-electron) Schrödinger equation

$$H|\psi_\alpha\rangle = E_\alpha|\psi_\alpha\rangle \quad \alpha = 1, \ldots, d, \tag{8}$$

which span a $d$-dimensional subspace of the $N$-electron Hilbert space. As discussed earlier, it is difficult to solve this eigenvalue equation due to the interelectronic interaction. If, however, we partition the Hamiltonian (as outlined above), we will be able to derive an operator equation which can be solved by means of perturbation techniques.

In the following, we suppose that each of the desired solution of Eq. (8) has a significant part *inside* of this model space. We shall denote the 'projections' of these physical states $|\psi_\alpha\rangle$ onto $\mathcal{M}$ as the model functions $|\psi_\alpha^o\rangle$ and assume, that they are linearly independent. Below, however, we shall find that these model functions

are only the (pure) projections, $|\psi_\alpha^o\rangle = P|\psi_\alpha\rangle$, if an *intermediate* normalization is applied for the physical states in the derivation of the perturbation expansions [cf. Subsection 2.3]. For other normalizations, in general, this simple relation is no longer fulfilled. For an adiabatic 'switch off' of the rest interaction $V$, obviously, the $d$ eigenfunctions of $H$ are just equivalent with the (orthogonal) basis functions $\{|\phi_\alpha\rangle\}$ of the model space. Here, we shall not further discuss this *one-to-one* correspondence between the physical states $|\psi_\alpha\rangle$ and the model functions $|\psi_\alpha^o\rangle$ [25], but simply assume that such a correspondence always exist in all our applications of the theory.

The distinction of the model functions $\{|\psi_\alpha^o\rangle;\ \alpha = 1,\ldots,d\}$ enables us to (formally) define the wave operator $\Omega$ for the 'reversed' projection. This wave operator maps the model functions 'back' onto the exact states [26,27],

$$|\psi_\alpha\rangle = \Omega\big|\psi_\alpha^o\big\rangle. \tag{9}$$

Note that the wave operator used here has a very similar meaning as the time evolution operator $U(0,+\infty)$ in the time-dependent perturbation theory. Having the wave operator, we can then define an effective operator $H_{\text{eff}} \equiv H_o + V_{\text{eff}}$ which, if applied onto the model functions

$$H_{\text{eff}}\big|\psi_\alpha^o\big\rangle = (H_o + V_{\text{eff}})\big|\psi_\alpha^o\big\rangle = E_\alpha\big|\psi_\alpha^o\big\rangle, \tag{10}$$

gives rise to the exact eigen energies. In this definition, the operator $V_{\text{eff}}$ is known also as the effective interaction. In the derivation of perturbation expansions, one central aim is a simple representation of these operators. Owing to the definition of these effective operators, they are defined only *within* the model space $\mathcal{M}$.

If we multiply the eigenvalue equation (10) from the left by $\Omega$, we obtain

$$\Omega H_{\text{eff}}\big|\psi_\alpha^o\big\rangle = E_\alpha|\psi_\alpha\rangle = H|\psi_\alpha\rangle = H\Omega\big|\psi_\alpha^o\big\rangle,$$

or simply

$$\Omega H_{\text{eff}} P = H\Omega P. \tag{11}$$

Using the partitioning (1) of the Hamiltonian $H$, therefore, we arrive at

$$[\Omega, H_o]P = (V\Omega - \Omega V_{\text{eff}})P, \tag{12}$$

the 'equation of motion' for deriving the wave operator $\Omega$, known also as the *generalized* Bloch equation in the literature [1]. This equation can be solved either iteratively or by casting it into a *recursive* form. Using the latter form, in particular, the perturbation expansions can be derived *order-by-order*, until the physical entities of interest have been converged sufficiently. For the $d$ physical states, whose projections are *in* the model space $\mathcal{M}$ to a significant part, the generalized Bloch equation is fully *equivalent* to the Schrödinger equation (8). Moreover, this form (12) of the Bloch equation is independent of the particular choice of the normalization of the states. Apart from the intermediate normalization of the physical states, a hermitian normalization can be applied in which the effective Hamiltonian $H_{\text{eff}}$ remains to be hermitian.

Often, the Bloch equation is represented and manipulated graphically by means of (so-called) Feynman–Goldstone diagrams. In this contribution, however, we shall not explain this graphical representation of the operators and matrix elements in detail. Instead, we are concerned below with the use of computer algebra in deriving perturbation expansions for the (matrix elements of the) effective Hamiltonian or for any other property of free atoms or molecules. Today, the application of CAS offers a valuable alternative to the algebraic or graphical derivation (representation) of perturbation expansions.

## 2.3 Intermediate normalization

Most applications of many-body perturbation techniques make use of the model functions

$$\left|\psi_\alpha^o\right\rangle = P|\psi_\alpha\rangle, \tag{13}$$

i.e. the projection of the exact states onto the model space $\mathcal{M}$. Together with Eq. (9), this gives rise to

$$P = P\Omega P, \tag{14}$$

which is equivalent to the condition $\langle\psi_\alpha|\psi_\alpha^o\rangle = 1$ and which is known as *intermediate* normalization condition. From Eq. (11), the effective operators then become

$$H_{\text{eff}}P = PH\Omega P, \quad V_{\text{eff}}P = PV\Omega P, \tag{15}$$

while the generalized Bloch equation assumes the form

$$[\Omega, H_o]P = (V\Omega - \Omega PV\Omega)P. \tag{16}$$

This is the *standard* form of the generalized Bloch equation and the starting point of most derivations in the framework of the RS perturbation theory. As indicated by the projection operator $P$ on the rhs, Eq. (16) is defined only (for the states) within the model space. However, this standard form is less general than Eq. (12) and has the drawback that the effective Hamiltonian and effective interaction (15) are *not* hermitian. Similarly, the model functions $|\psi_\alpha^o\rangle$, i.e. the eigenvectors of $H_{\text{eff}}$, are in general *not* orthogonal to each other as they are projections from some orthonormal space upon a smaller (sub-)space. This 'non-orthogonality' of the model functions may lead to difficulties especially for the computation of transition amplitudes since, then, the atomic or molecular states on the lhs and rhs of the amplitudes are not described equivalently with respect to the perturbation operator $V$.

In intermediate normalization, the projector $P$ and the wave operator $\Omega$ can be understood (and illustrated) in a very simple way: While $P$ projects an arbitrary state $|\psi_\alpha\rangle \in \mathcal{H}$ onto the model space, the wave operator $\Omega$ transforms each function with the projection $|\psi_\alpha^o\rangle \in \mathcal{M}$ *back* onto the exact state $|\psi_\alpha\rangle$. In intermediate normalization, this property is independent of the (size of the) component which lies within the complementary space ($\mathcal{H} \ominus \mathcal{M}$), owing to the two properties $\Omega P = \Omega$ and $\Omega Q = 0$, respectively.

Hermitian normalization:
The effective operators in equation (15) are hermitian, if we replace the normalization condition (14) by

$$P = P\Omega^{\dagger}\Omega P; \tag{17}$$

this form is known also as *isometric* normalization or Jørgensen condition [28]. With this condition, the effective Hamiltonian reads as

$$H_{\text{eff}}P = P\Omega^{\dagger}H\Omega P. \tag{18}$$

Since the operators are hermitian, the eigenfunctions are always orthogonal as well. Using the condition (17), an analogue form to the effective Hamiltonian (18) applies also for any additional perturbation, $h_{\text{eff}}P = P\Omega^{\dagger}h\Omega P$, as they arise for instance in the computation of transition amplitudes, hyperfine constants, oscillator strength, etc.

Apart from rather formal considerations, (almost) all techniques and implementations of the RS perturbation theory are based until now on the generalized Bloch equation with intermediate normalization. This operator equation is equivalent not only to the Schrödinger equation (for the states of interest), but enables one also to derive perturbation expansions for atomic and molecular properties other than correlation energies, e.g. transition probabilities. The terms in the corresponding expansions can be represented (and manipulated) either graphically by means of Feynman–Goldstone diagrams or algebraically. In general, a *perturbation expansion* hereby refers to an algebraic (or graphical) representation of any observable by means of one- and two-particle integrals, which can be calculated from a given *(complete)* one-particle spectrum. Below, we shall focus on the algebraic derivation of such expansions and show how computer algebra can be applied very efficiently and in a concise manner.

## 2.4 Order-by-order perturbation expansions

The generalized Bloch equation (12) is the basis of the RS perturbation theory. This equation determines the wave operator and, together with Eq. (11), the energy corrections for all states of interest; especially, it leads to perturbation expansions which are independent of the energy of the individual states, just referring the 'unperturbed' basis states. Another form, better suitable for computations, is to cast this equation into a *recursive* form which connects the wave operators of two consecutive orders in the perturbation $V$. To obtain this form, let us start from the standard representation of the Bloch equation (16) in *intermediate* normalization and define

$$\Omega = \Omega^{(0)} + \Omega^{(1)} + \Omega^{(2)} + \cdots, \tag{19}$$

where $\Omega^{(n)}$ denotes that part of the wave operator, which comprises all terms of order $n$ in the perturbation $V$. Then, by equating terms of equal powers in $V$ on

the rhs and lhs, we obtain the equations [2]

$$\left[\Omega^{(1)}, H_o\right]P = QVP, \tag{20}$$

$$\left[\Omega^{(2)}, H_o\right]P = \left(QV\Omega^{(1)} - \Omega^{(1)}PV\right)P, \tag{21}$$

$$\left[\Omega^{(3)}, H_o\right]P = \left(QV\Omega^{(2)} - \Omega^{(1)}PV\Omega^{(1)} - \Omega^{(2)}PV\right)P, \tag{22}$$

$$\vdots$$

or, the general form,

$$\left[\Omega^{(n)}, H_o\right]P = \left(QV\Omega^{(n-1)} - \sum_{m=1}^{n-1} \Omega^{(n-m)}PV\Omega^{(m-1)}\right)P. \tag{23}$$

This is the *recursive* form of the generalized Bloch equation. In a similar way, we can separate the effective Hamiltonian and effective interaction (15) due to the powers of $V$. Despite the fact, that the effective Hamiltonian (15) is not hermitian in intermediate normalization, we can diagonalize the corresponding (Hamiltonian) matrix and shall obtain (always) real energies, as they represent the exact energies of the system. This property is satisfied for each order independently.

To treat the order-by-order calculations in a generic way, we can consider Eq. (23) in the form

$$\left[\Omega^{(n)}, H_o\right] = A,$$

where $A$ is an operator with a representation similar to $\Omega^{(n)}$, except for an energy denominator. We can simplify the commutator on the lhs, if we evaluate its matrix elements with respect to the eigenfunctions of the model operator $H_o$,

$$\left\langle\phi_\rho\middle|\left[\Omega^{(n)}, H_o\right]\middle|\phi_\alpha\right\rangle = \left(E_\rho^o - E_\alpha^o\right)\left\langle\phi_\rho\middle|\Omega^{(n)}\middle|\phi_\alpha\right\rangle = \langle\phi_\rho|A|\phi_\alpha\rangle. \tag{24}$$

Owing to the definition of the wave operator in intermediate normalization, i.e. $\Omega P = \Omega$ and $\Omega Q = 0$, then only those matrix elements will be *non-zero* for which we have $|\phi_\alpha\rangle \in \mathcal{M}$ and $|\phi_\rho\rangle \notin \mathcal{M}$. For this reason, the energy difference is always $(E_\rho^o - E_\alpha^o) \neq 0$ and the matrix elements of the wave operator become

$$\left\langle\phi_\rho\middle|\Omega^{(n)}\middle|\phi_\alpha\right\rangle = \frac{\langle\phi_\rho|A|\phi_\alpha\rangle}{(E_\rho^o - E_\alpha^o)}. \tag{25}$$

We shall analyze these matrix elements later in more detail. Here, let us note only that the 'characteristic energy denominators' in the RS perturbation theory arises always from the energy difference of two unperturbed eigenvalues, from which one of the corresponding eigenfunctions is *inside* and one *outside* of the model space.

## 2.5 Coupled-cluster and all-order expansions

The first-order terms in the perturbation expansion of the wave operator have contributions due to zero-, one- and two-particle (interaction) terms. In second-order,

then, we find contributions due to zero- to four-body effective interactions. For atoms and molecules with $N$ active electrons, generally, the $n$th-order expansion of the wave operator has contributions from zero up to $2^n$-particle interaction terms (and maximal, of course, $N$-body terms). Among these effective interactions, the two-body terms are usually the largest, and almost the entire correlation effects are contained in the zero- to four-body terms. Owing to these considerations, we would incorporate correlation effects to a very large extent—if we calculate the contributions from the single and double excitations to all orders in the perturbation expansion.

Such a partitioning of the correlation contributions (into classes of virtual excitations) is indeed possible, if the wave operator $\Omega$ is separated into one-, two-, ..., and up to $n$-body terms

$$\Omega = \Omega_0 + \Omega_1 + \Omega_2 + \cdots, \tag{26}$$

where $\Omega_n$ denotes the effective $n$-body wave operator. In practice, moreover, it is often useful to *factorize* these operators in terms of (so-called) cluster operators $S_i$,

$$\Omega_1 = S_1, \quad \Omega_2 = S_2 + \frac{1}{2}\{S_1^2\}, \quad \Omega_3 = S_3 + \{S_2 S_1\} \frac{1}{3}\{S_1^3\}, \quad \ldots. \tag{27}$$

Diagrammatically, these cluster operators $S_i$ represent the *connected* $i$-body terms, i.e. those 'diagrams' which cannot be separated into topologically unconnected parts. Typically, the wave and cluster operators are related to each other due to the exponential ansatz

$$\Omega = \exp(S) \tag{28}$$

with $S = S_1 + S_2 + \cdots$, which is known as the Coupled-Cluster Approximation (CCA) in the literature [16,29,30]. In the formalism of the second quantization [cf. Subsection 3.1], the cluster operators $S_i$ consist out of the cluster amplitudes and the particle creation and annihilation operators. Quite similar to the Bloch equation (12) for the wave operator, the cluster amplitudes are solutions to a set of nonlinear algebraic equations

$$[S_n, H_o]P = \left(QV\Omega^{(n-1)} - \Omega PV\Omega\right)_{\text{conn}} P, \tag{29}$$

where the subscript *conn* denotes the connected terms. Although the partitioning of the cluster operator into $n$-particle terms $S_n$ is inspired by perturbation theory, this approach to the many-body problem is a *non-perturbative* one.

From the expansion (27) it can be shown that the CCA includes also those three-, ..., $n$-body excitations which factorize into one- and two-particle cluster amplitudes. However, despite of the benefit of CCA to incorporate selected $n$-body contributions to all order into the computations, setting up the equations for open-shell systems is a highly *nontrivial* task, in particular when compared with the usual MBPT computations. For simple shell structures, there are a number of coupled-cluster codes available today, both in the nonrelativistic as well as the relativistic framework [31–34].

### 2.6 Open-shell atoms and molecules

Open-shell atoms or molecules are characterized by having partially occupied (outer) shells, usually referred to as the valence shells of the system. Since the number of possible shell states is then larger as the number of electrons in these shells, there are several distributions of the electrons among these shell states possible, giving rise often to a large number of degenerate ($N$-electron) states. For atoms, for example, there are $\binom{l}{m}$ degenerate many-electron states, if $l$ denotes the number of valence electrons and $m$ the number of available vacancies, respectively. Apparently, this number of degenerate states increases even further if applied to molecules.

For open-shell systems, therefore, the model space is no longer simple and sometimes not even known *before* the computations really start. For closed-shell systems, in contrast, the model space can be formed by a single many-electron state, which is taken as the *reference* state and which is sufficient in order to classify the single-electron states into particle (unoccupied) and hole (occupied or core) states, respectively. In open-shell systems, instead, the valence shells are neither empty nor completely filled. To facilitate the handling of such open shells, we shall provide (and discuss) a orbital notation in Subsection 3.4 which is appropriate for the derivation of perturbation expansions.

One important property of Eq. (23), which manifests itself very easily in the diagrammatic evaluation of the perturbation expansions, is the linked-diagram theorem (LDT). According to this theorem, only a selected class of terms survives in the perturbation expansion of the wave operator, while all *unlinked* diagrams cancel in each order of perturbation theory; in addition, this theorem ensures the size consistency of MBPT and coupled-cluster theory. Based on LDT, Eq. (23) simplify to

$$\left[\Omega^{(n)}, H_o\right] P = \left(QV\Omega^{(n-1)}P\right)_{\text{linked}} \tag{30}$$

for all closed-shell systems. In Eq. (30), the subscript *linked* indicates that only the 'linked diagrams', i.e. the open and connected ones, need to be considered on the rhs. This follows from the observation that, if the diagrams of $PV\Omega^{(n-1)}P$ are closed, the second term on the rhs of Eq. (23) is unlinked entirely and just cancels the unlinked contributions from the first term $V\Omega^{(n-1)}P$. When compared with the closed-shell systems, the presence of additional valence electrons makes the nature of the $PV\Omega^{(n-1)}P$ diagrams different for all open-shell atoms and molecules. Since the (one-electron) states of the valence shells can be either occupied or virtual, there are now a certain number of *free* lines which emanate from this term. In the diagrammatic language, this gives rise to the *(back-)folded* diagrams, a topic to which we shall return in Subsection 3.3.

## 3. OPERATOR REPRESENTATIONS

### 3.1 Second quantization and particle–hole formalism

The Hamiltonian and most other operators in atomic and molecular structure theory can be represented usually also in the 'language' of *second quantization*. For

many-particle systems, this language enables one to take into account Pauli's exclusion principle in a very simple and concise way. In the formalism of second quantization, the creation operator $a_i^\dagger$ 'creates' an electron in the (one-electron) state $i$, while the annihilation operator $a_i$ 'deletes' the electron from this state. Conventionally, these operators are defined with respect to the *vacuum* in which no electron (nor positrons within a relativistic framework) are present. For this definition of the vacuum, the unperturbed Hamiltonian simply read as

$$H_o = \sum_i a_i^\dagger a_i \epsilon_i \tag{31}$$

while, for instance, the instantaneous Coulomb interaction is given by

$$V = \frac{1}{2} \sum_{ijkl} a_i^\dagger a_j^\dagger a_k a_l \langle ij | r_{12}^{-1} | lk \rangle, \tag{32}$$

with $r_{12}^{-1} \equiv 1/|\mathbf{r}_1 - \mathbf{r}_2|$. Using the formalism of second quantization often helps simplifying the evaluation of the higher-order terms in perturbation expansions and has been found essential also for developing those many-body methods techniques, which are based on different classes of excitations, see Subsection 2.5.

For many-electron atoms (and molecules), however, it is often much more convenient to start from a 'many-particle' vacuum $|o\rangle$, the so-called *reference state*, instead of using the (pure) vacuum above. Owing to this re-definition of the vacuum, we have to distinguish then between *occupied* and *unoccupied* electron orbitals in order to specify some particular $N$-electron state (of either the model space or from its complement). In the language of the particle–hole formalism, moreover, we refer to the occupied orbitals as 'hole states' and the unoccupied orbitals as 'particle states' of the system. In the literature, one often assigns the indices $a, b, c, \ldots$ to the hole states and $r, s, t, \ldots$ to the particle states, whereas the indices $i, j, k, \ldots$ are utilized for those summations in which we need not distinguish between particles and holes explicitly. In our computer-algebraic approach, however, we shall not make much use of these orbital indices as it appears more appropriate in this case to distinguish a number of orbital classes and to count through each class by means of an integer index, cf. Section 4.3.

In practice, there is quite a difference between atoms and molecules as far as the representation of the one-particle spectrum is concerned. In atomic physics, one often utilizes a 'radial-angular' representation of the one-electron orbitals in order to allow for the analytic integration over all spin-angular coordinates of the system [35,36]. This so-called 'angular reduction' will be briefly discussed below in Subsection 4.4. However, in order to exploit the symmetry of free atoms the reference state must 'coincide' with a closed-shell determinant $|o\rangle \equiv |\Phi\rangle$, i.e. a reference state which should not depend on the magnetic quantum numbers of the one-electron functions. Unfortunately, the complexity of the perturbation expansions increases very rapidly if the number of electrons in the physical states of interest differ from (the number of electrons in) the reference state.

## 3.2 Normal-order. Wick's theorem

In the second-quantized operators (31) and (32), the summation over the particle indices $i, j, \ldots$ runs over all the electron states of the (complete one-electron) spectrum. If these operators act to the right upon the *reference* state, i.e. the many-electron vacuum of the particle–hole formalism, some of these (strings of) creation and annihilation operators 'create' excitations while other gives simply zero, i.e. no contribution. For the pure vacuum, in particular, the behavior of the second-quantized operators can be read off quite easily because the creation operators appear *left* of the annihilation operators in expressions (31) and (32), respectively.

In general, a given sequence of creation and annihilation operators is said to be *normal ordered*, if all the creation operators appear *left* of all annihilation operators. Such an ordering of the operator strings simplifies the manipulation of operator products as well as the evaluation of their matrix elements, as the action of these operators can be *read off* immediately. In the particle–hole formalism, its hereby obvious that we can 'annihilate' only those particles or holes which exist initially; in fact, an existing hole is nothing else than that there is no electron in this hole state. In this formalism, therefore, an operator in second quantization is normal ordered with regard to the reference state $|\Phi\rangle$, iff

$$\left.\begin{array}{c}\text{all creation operators of the particle states}\\ \text{and}\\ \text{all annihilation operators of the hole states}\end{array}\right\}\ \text{all particle–hole creation operators}$$

appears *left* of

$$\left.\begin{array}{c}\text{all annihilation operators of the particle states}\\ \text{and}\\ \text{all creation operators of the hole states}\end{array}\right\}\ \text{all particle–hole annihilation operators.}$$

Hereby, the exact sequence of the creation and annihilation operators can be chosen rather arbitrary within each of these blocks (up to some phase factor), since all the operators anticommute for each block independently,

$$\left\{a_r^\dagger, a_c\right\} = \left\{a_r, a_c^\dagger\right\} = 0.$$

Of course, the number of permutations, which are required to bring a given operator string into a certain sequence, determines the sign of the expression: Each interchange of two (particle–hole) creation or annihilation operators leads to an additional phase factor $(-1)$ and, possibly, to a contraction of terms. For applications, therefore, it is reasonable to define a (so-called) *normal-order sequence* which specifies the relative position of the (particle–hole) creation or annihilation operators more precisely; we write this sequence symbolically as

$$\left(a_r^\dagger\right) - (a_c) - \left(a_c^\dagger\right) - (a_r) \tag{33}$$

and say: The creation and annihilation operators of a given operator string obey a normal-order sequence iff all the creation operators of particle states $(a_r^\dagger)$ appear *left* of all annihilation operators of hole states $(a_c)$ and, in turn, *left* of all creation

operators of hole states ($a_c^\dagger$) and, finally, *left* of all annihilation operators of particle states ($a_r$). Again, this does not determine the exact sequence within each of these 'blocks' of operators but ensures that no additional (contracted) term arise as long one stays within this normal-order sequence.

To represent the normal-order form of some given operator product, *curly* brackets are used around the string of creation and annihilation operators. These brackets indicate that all operators simply anticommute, i.e. that no contraction need to be taken into account. Using the well-known anticommutation relations for electrons (fermions), we can always transform any product of operators into its normal form by performings successively all the necessary permutations. Apart from a change of sign, an additional term is obtained in this rearrangement procedure every time when we 'interchange' the creation and annihilation operator of one and the same orbital ($a_k a_k^\dagger = -a_k^\dagger a_k + 1$).

With these definitions, we can re-write the operators $H_o$ and $V$ from above into normal order with respect to the (many-electron) reference state $|\Phi\rangle$ as

$$H_o = E_o + \sum_i \{a_i^\dagger a_i\}\epsilon_i, \quad E_o = \sum_a \epsilon_a, \tag{34}$$

$$V = V_o + V_1 + V_2 \tag{35}$$

with

$$V_o = \sum_a \langle a| - u(r)|a\rangle + \frac{1}{2}\sum_{ab}\langle ab||ab\rangle, \tag{36}$$

$$\begin{aligned} V_1 &= \sum_{ij}\{a_i^\dagger a_j\}\langle i|v|j\rangle \\ &= \sum_{ij}\{a_i^\dagger a_j\}\Big[\langle i| - u(r)|j\rangle + \sum_a \langle ia||ja\rangle\Big], \end{aligned} \tag{37}$$

$$V_2 = \frac{1}{2}\sum_{ijkl}\{a_i^\dagger a_j^\dagger a_l a_k\}\langle ij|r_{12}^{-1}|kl\rangle. \tag{38}$$

In these formulas, we made use of the usual abbreviation

$$\langle ij||kl\rangle = \langle ij|r_{12}^{-1}|kl\rangle - \langle ij|r_{12}^{-1}|lk\rangle, \tag{39}$$

in order to combine the *direct* and *exchange* matrix elements of the electron–electron interaction (32) within a single symbol. The second term of $V_1$ in (37) is nothing else than the Hartree–(Dirac–)Fock potential of the reference state $|\Phi\rangle$, that is the effective one-particle potential is just equal to the *difference* between the Hartree–Fock and those potential which was uses for generating the one-particle spectrum (in addition to the nuclear potential $V_{\mathrm{nuc}}$). In other words: We find that all one-particle excitations must vanish identically, $V_1 \equiv 0$, if the Hartree–(Dirac–)Fock orbitals are used in the computations. In quantum chemistry, the perturbation expansions which starts from this choice of the one-particle potential are often called Møller–Plesset perturbation expansions. In the relativistic theory, moreover, one should better start from the Dirac–Fock–Breit 'mean field' in order to avoid all

terms in perturbation expansion due to effective one-particle interactions $V_1$ in Eq. (37).

Similar to the interaction operators (34) and (35) from above, the wave operator $\Omega$ can be cast into normal form as

$$\Omega = 1 + \sum_{ij} \{a_i^\dagger a_j\} x_j^i + \frac{1}{2} \sum_{ijkl} \{a_i^\dagger a_j^\dagger a_l a_k\} x_{kl}^{ij} + \cdots . \tag{40}$$

In this form, the wave operator can 'operate' upon the entire space, i.e. the model space $\mathcal{M}$ and its complement $\mathcal{H} \ominus \mathcal{M}$. Since, namely, the operator strings represent genuine excitations, the wave operator gives nonvanishing results only when it acts onto states which belong to $\mathcal{M}$.

To determine the wave operator $\Omega$ from the Bloch equation (16), one of the major tasks in the derivation of all perturbation expansions is to evaluate the operator products $V\Omega$ and $\Omega PV\Omega$, i.e. to bring them into normal order. Owing to the possible contractions, a large number of terms typically arise and may render this evaluation very cumbersome. A remarkable simplification in this 're-ordering' of the creation and annihilation operators is achieved by means of Wick's theorem, including of all the necessary contractions. Apart from the normal product $\{\ldots\}$ of the given operator string, according to this theorem, one has to include also the normal products of all possible contractions of the corresponding creation and annihilation operators. For two normal ordered operators $\{A\}$ and $\{B\}$, Wick's theorem is often written in the (symbolic) form:

$$\{A\} \cdot \{B\} = \{AB\} + \{\widehat{AB}\}, \tag{41}$$

where the 'hat' in the second term stands for *all* contractions, i.e. the contraction over all pairs of operators for which a particle–hole annihilation operator from $\{A\}$ appears to the left of a particle–hole creation operator from $\{B\}$. Besides the single contractions, all the double, triple, ..., $n$-fold contractions have also to be taken into account. A proof of Wick's theorem is given by Lindgren and Morrison [1] and in many textbooks on quantum field theory. Wick's theorem can also be represented graphically and it is this form, which has often been utilized in the *diagrammatic* derivation of perturbation expansions.

In the GOLDSTONE program below [cf. Section 4], Wick's theorem is fulfilled implicitly by performing a pairwise permutation of the operators until all operators are in normal order. This ensures that all contractions are taken into account easily. Of course, this step-wise procedure gives the same results as a more sophisticated implementation of Wick's theorem which, in particular, is helpful for large operator strings.

### 3.3 Diagrammatic representations

The operators above in second quantization can be represented and manipulated also 'diagrammatically', that is by means of Feynman–Goldstone diagrams. Usually, these representations provide a simple and transparent approach to evaluate the various contributions from the perturbation expansions. There are different graphical representations known, which were developed by Goldstone [8],

Hugenholtz [37], Brandow [38], Sandars [39] and several others. These graphical representations are closely related to the Feynman diagrams as applied in quantum field theory. In atomic and molecular physics, the graphs due to Goldstone are used most frequently and are referred to as Feynman–Goldstone diagrams below. In contrast, the representations of Hugenholtz and Brandow are more compact, but also more difficult to apply in practice, especially if the theory is to be addressed to 'new problems'. The Feynman–Goldstone diagrams have been applied in a very large number of studies and have been discussed in detail in the text by Lindgren and Morrison [1].

To each diagram or fragment of a diagram, an algebraic expression can be assigned uniquely. For the computation of atomic and molecular properties, therefore, one can first derive the graphical expansions and later 'translate' them (back) into algebraic terms as appropriate for numerical studies. For this translation of the diagrams, the Goldstone rules [1,8,40] are of great help. Similar rules apply also for the angular integration if the symmetry of free atoms is to be utilized [41,42]. But drawing and combining the diagrams requires a high proficiency and is prone for making errors concerning, especially, the signs and labeling of the terms. Here, we shall not discuss these graphical techniques since our emphasis is placed below onto the use of computer algebra for the derivation and manipulation of open-shell perturbation expansions.

## 3.4 Orbital notation for open-shell atoms

Open shells arise in atomic and molecular systems if some but not all orbitals from a given set of degenerate orbital functions are occupied by electrons. In order to describe such systems by means of some approximate state vectors, different possibilities exist of how the electrons from the open shells can be 'distributed' among the different orbital functions. For open-shell systems, therefore, one requires model spaces which are usually more complex (and demanding with regard to the necessary derivations) than those for a corresponding closed-shell structure, if the latter one exist at all. For example, in order to represent the excited states of noble gases, the complexity of the model space increases very rapidly with each additional 'one-electron' excitation (with regard to the ground state), although the number of electrons is the same in all these cases and equivalent to the closed-shell $^1S_0$ ground state of these atoms. For open-shell structures, obviously, the model functions *do not* coincide with the reference state $|\Phi\rangle$ which, instead, is taken usually as the 'nearest' closed-shell configuration. Apart from the (a) unoccupied particle states and (b) occupied core states of the model space, we shall find then (c) valence states which are occupied in some but not all the functions of the model space, $|\phi_\alpha\rangle \in \mathcal{M}$.

Instead of having just one sort (c) of valence states, it is often more convenient to distinguish two classes of such orbitals owing to their relative position (in energy) with regard to the Fermi level of the reference state $|\Phi\rangle$. This leads us to the following distinction of orbitals on which the GOLDSTONE program [cf. Subsection 4.7] is based below:

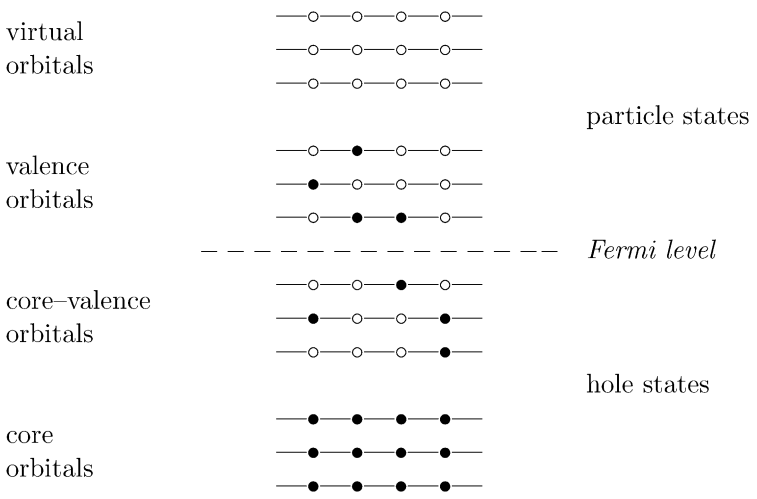


**FIGURE 10.1** Classification of the electron orbitals. Each 'column' in this figure can be interpreted as (the occupation of) a determinant $|\phi_\alpha\rangle \in \mathcal{M}$ from the model space. While it is convenient to distinguish between four classes of orbitals for open-shell atoms and molecules (left side), the definition of the Fermi level itself just separates the particle from the hole states (right side).

(i) *core orbitals* designate the hole states (with regard to the many-electron vacuum $|\Phi\rangle$), which are occupied in all determinants of the model space $|\phi_\alpha\rangle \in \mathcal{M}$;
(ii) *core–valence orbitals* are all those hole states which are unoccupied in at least one determinant $|\phi_\alpha\rangle \in \mathcal{M}$;
(iii) *valence orbitals* are particle states which are occupied in some or all determinants of the model space $|\phi_\alpha\rangle \in \mathcal{M}$;
(iv) *virtual orbitals* denote all those particle states which remain unoccupied within the whole model space $\mathcal{M}$.

This classification of the one-electron orbitals is displayed in Figure 10.1. While, due to this definition, it is possible to have completely unoccupied core–valence orbitals or (completely) occupied valence orbitals in the model space, they could be eliminated always by a proper re-definition of the many-electron vacuum state $|\Phi\rangle$. The distinction of the valence states into core–valence and valence orbitals has the great advantage that we need not to deal explicitly with the particular choice of the vacuum in the derivation of perturbation expansions. As we shall see below, namely, the 'projection upon the vacuum' appears rather frequently in the derivations for open-shell structures and can be carried out formally, if all the core and core–valence orbitals (i.e. all the orbitals up to the Fermi level) are taken into account separately from the rest of the orbital functions.

The re-definition of the vacuum determines also the (so-called) *effective particle character* of a given quantum system or model space. In the following, we shall often denote the desired many-particle states of the system (and the determinants

of the model space) by their number of *occupied* valence orbitals $m$ as well as the number of *unoccupied* core–valence orbitals $n$; we shall briefly refer to these states as $(m, n)$ states (model spaces). The $1s^2\ 2s^2\ {}^1S_0$ ground state of beryllium-like ions, for instance, can be described either within a $(0, 0)$ model space, with 1s and 2s being both core orbitals, or by means of a $(2, 0)$ model space. In the latter case, the 2s and 2p orbitals are treated as valence orbitals, while only the 1s remains in the core. Owing to the small energy separation of the 2s and 2p energies, the latter choice of the model space would allows to treat the $2s^2 + 2p^2$ configuration mixing *within* the model space and, hence, help improve the convergence properties of the corresponding perturbation expansions. Moreover, a neon atom with an $2p \rightarrow 3s$ electronic excitation would be called an *effective one-particle–one-hole* $(1, 1)$ system in this language.

## 3.5 Extended model spaces

For open-shell systems, multidimensional model spaces are necessary in general in order to account for that the 'unperturbed' solutions $\{|\phi_\alpha\rangle\}$ of the model operator $H_o$ are degenerate. If we act with the wave operator $\Omega$ in second quantization (40) to the right upon some determinant $|\phi_\alpha\rangle \in \mathcal{M}$, we see of course that each term of this operator leads to an excitation of occupied electron orbitals. These excitations can be classified due to:

- *internal excitations* which lead simply to another determinant $|\phi_\beta\rangle \in \mathcal{M}$ of the model space, or
- *external excitation*, carrying this function out of the model space.

Obviously, any excitation *of* a core orbitals or excitation *into* a virtual orbital always leads 'out of the model space' owing to our definitions above. The other terms of the wave operator, in contrast, which include only creation and annihilation operators of the (core–)valence orbitals, may result in either internal or external excitations, in dependence also of the particular basis function $|\phi_\alpha\rangle \in \mathcal{M}$ under consideration.

For a simple treatment of the (RS) perturbation expansions, it is often desirable to have just *one* wave operator $\Omega$, which is defined on the whole model space. This desire requests however that the distinction of internal and external excitations must apply for all determinants $|\phi_\alpha\rangle \in \mathcal{M}$ in the same way [43]. This can be seen, for instance, from the second term (on the rhs) of the Bloch Eq. (16) which contains the operator product $PV\Omega P$. The projector $P$, standing left of this product, eliminates all contributions of the operator $V\Omega$ which leads out of the model space. For a single wave operator, acting on the whole model space, this projection must be the same for all determinants $|\phi_\alpha\rangle \in \mathcal{M}$. We therefore find that an unique dispartment of the excitations into internal and external ones is a necessary and sufficient condition. The importance of the proper choice of the model space and their classification has been discussed in detail by Lindgren [43].

## 3.6 Projection operators. Representation of the model space

For open-shell systems, a simple treatment of the model space is as important as the handling (and evaluation) of the operators in second quantization. On the rhs of the Bloch Eq. (16), hereby the projection operator $P$ appears in two different ways: While the projector at the right side simply indicates that the wave operator is defined only within the model space $\mathcal{M}$, the second projector, which appears 'between' the operators $\Omega$ and $V$, requires further care. In a graphical representation of the wave operator, namely, this 'sandwiched' projector leads to the so-called *folded* or *backward* diagrams for all open-shell systems, which seem to violate the LDT (at least at the first glance). When considered in more detail, however, this 'backfolding' indicates that all excitations of this operator have first to *come back to the model space* in order to account for correlations within the open shells. The folding of the particle paths (within a diagrammatic representation) is made usually to indicate that special care has to be taken about this sandwiched projector operators wherever they appear in course of the derivation.

From a practical viewpoint, it has been found useful to assign formally a representation in second quantization also to the projection operator

$$P = \sum_{\alpha\in\mathcal{M}} |\phi_\alpha\rangle\langle\phi_\alpha| = \sum_{\alpha\in\mathcal{M}} \big(\hat{\boldsymbol{a}}^\dagger\big)_\alpha |o\rangle\langle o| \big(\hat{\boldsymbol{a}}\big)_\alpha . \tag{42}$$

In this notation, $(\hat{\boldsymbol{a}}^\dagger)_\alpha$ means an operator string of creation and annihilation operators which just 'creates' the model state $|\phi_\alpha\rangle$ out of the (many-electron) vacuum:

$$|\phi_\alpha\rangle = \big(\hat{\boldsymbol{a}}^\dagger\big)_\alpha |o\rangle, \tag{43}$$

with $|o\rangle \equiv |\Phi\rangle$. Similarly, $(\hat{\boldsymbol{a}})_\alpha$ designates the adjoint operator to this operator string. From our classification of the electron orbitals in Subsection 3.4, it then follows immediately that the operators $\{(\hat{\boldsymbol{a}}^\dagger)_\alpha\}$, which span the model space $\mathcal{M}$ due to Eq. (43), may contain only annihilation operators of the core–valence orbitals *and/or* creation operators of the valence orbitals. In Section 4.3 we shall define an extended normal-order (sequence) of all operators in second quantization which takes the classification of the electron orbitals in Figure 10.1 into account. From the (second-quantized) representation (42) of the projection operator, however, we see already that any 'sandwiched' $P$ refers to an (intermediate) projection onto the vacuum and, hence, to a restriction in the summation over the hole and particle states as it is characteristic for most open-shell diagrams.

The intermediate projection of operators or states upon the vacuum can be used also in order to classify the wave operator (and other perturbation expansions) in a different way. In the Bloch Eq. (16) and the effective Hamiltonian $H_{\text{eff}}$ in Eq. (10), namely, the 'order' of the individual terms in the perturbation expansion is determined just by the number of interactions $V$, which occur in each term. A different classification of the diagrams is obtained in the (so-called) 'Q-box' formalism as applied, for instance, in nuclear physics. In this formalism, the 'order' of a perturbation expansion results from the number of 'foldings', i.e. the number of projections $|o\rangle\langle o|$ upon the vacuum. In each of these *new* orders, the number of interaction lines is no longer fixed but may vary from application to application.

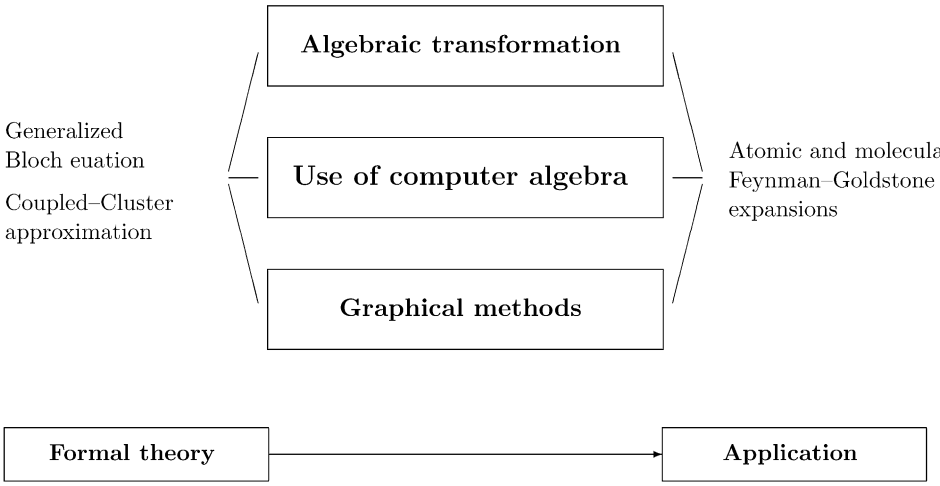


**FIGURE 10.2** Different lanes for the derivation of atomic and molecular perturbation expansions. They all aim for the derivation of formulas which can immediately be used for numerical computations on the respective properties. The emphasis of the present work in placed on the computer-algebraic line.

This approach, which has been investigated in nuclear structure theory [44], has however not been applied so far for atoms or molecules.

In summary, there are three different lanes available for evaluating the operator products on the rhs of the generalized Bloch Eq. (23) and for all *effective* operators, such as the Hamiltonian (15) or any other interaction operator. These alternatives are displayed in Figure 10.2; beside of the (i) purely algebraic transformation, i.e. the use of the fermion anticommutation rules for the creation and annihilation operators, $\{a_k^\dagger, a_{k'}\} = \delta_{k,k'}$, (ii) a variety of graphical methods and rules have been developed during the last decades [8,37,38]. For atoms with simple shell structures, for instance, these rules are explained and applied in rather detail in the textbook by Lindgren and Morrison [1]. Today, a promising *new* alternative is provided by (iii) computer algebra on which we shall place our emphasis below. All of these three lanes aim for an transformation of the operator products into a form which efficiently allows to *read off* the action of these operators (if applied upon some function) and, eventually, to evaluate all requested matrix elements with regard to the model functions. In particular, all these methods help translate the formal theory into a representation, from which the properties of atoms and molecules can be obtained immediately. Even if Wick's theorem (41) is applied, however, the *direct* use of the anticommutation relations (upper lane in Figure 10.2) is usually not feasible for most open-shell system—if not supported by further computational tools. In the next section, therefore, we shall discuss how computer-algebraic systems can be utilized nowadays to *define* the operators and to perform all the transformations as described above. To this end, we shall briefly introduce the GOLDSTONE program in Subsection 4.7, an computer-algebraic en-

vironment which facilitates the interactive derivation of perturbation expansions for open-shell atoms and molecules.

## 4. DERIVATION OF PERTURBATION EXPANSIONS

### 4.1 Feynman–Goldstone perturbation expansions

In the previous sections, we already saw how (perturbation) *expansions* arise due to the evaluation of operator products in second quantization, such as $V\Omega$ and others, i.e. due to the re-arrangement all the operator strings in these products into a *normal-order sequence*. In this transformation process, frankly speaking, the electron anticommutation rule is applied successively to some particular pair of particle–hole creation and annihilation operators (which are not yet in the proper order), leading to an additional term every time when the creation and annihilation operator of the same orbital functions in interchanged. Hereby, the term *perturbation expansion* generally refers to either an algebraic or graphical representation of some operator or observable in terms of one-, two-, ... $n$-particle integrals which can be calculated later by means of any 'complete' one-particle spectrum. Typically, every atomic or molecular property, which is associated with one or several states of the overall system, can be written in terms of such a (more or less elaborate) expansion.

In the derivation of perturbation expansions, there are usually three tasks necessary which have to be solved:

(a) the evaluation of the wave operator in normal order;
(b) the evaluation of the effective Hamiltonian $H_{\text{eff}}$ or effective perturbation $V_{\text{eff}}$ as well as
(c) the use of the wave operator from above in order to derive the perturbation expansion of any further property of interest.

These three tasks mark the path which we have to follow in order to proceed from the Bloch Eq. (16), an operator equation, down to the computation of atomic and molecular properties. Although these tasks can be solved also graphically, below we describe how they can be handled by means of the GOLDSTONE program, our computer-algebraic approach. Usually, each task above refers to the evaluation of one (or several) Feynman–Goldstone perturbation expansions. These expansions either concern an operator, such as the wave operator $\Omega$, or the simplification of matrix elements, often calculated with regard to functions $|\phi_\alpha\rangle \in \mathcal{M}$ from the model space. After a *full* contraction of these Feynman–Goldstone expansions has been achieved [see below], these expansions can be calculated quite easily using the one-particle spectrum as supposed above.

In particular, having the model operator (34) and the wave operator (40) in second quantization, we can evaluate the commutator on the lhs of the Bloch Eq. (16) and bring it into its normal-order form by analyzing term by term,

$$[\Omega, H_o] = \sum_{ij} \{a_i^\dagger a_j\} (\epsilon_i - \epsilon_j) x_j^i + \frac{1}{2} \sum_{ijkl} \{a_i^\dagger a_j^\dagger a_l a_k\} (\epsilon_i + \epsilon_j - \epsilon_k - \epsilon_l) x_{kl}^{ij} + \cdots . \quad (44)$$

An analogue representation applies independently also for the wave operator $\Omega^{(n)}$ in every order $n$ of the order-by-order expansion. That is, if we are able to bring the operator products on the rhs of the corresponding Bloch equations (20)–(23) into normal form, we can identify the terms on the left- and right-hand side in order to express the amplitudes of the wave operator. For each order $n$, this finally results in an equation for the coefficients $x^{(n)i}_{\ j}, x^{(n)ij}_{\ \ kl}, \ldots$ which can be derived either algebraically or by using graphical rules.

In fact, the wave operator $\Omega$ can be used to evaluate both, the effective Hamiltonian $H_{\mathrm{eff}}$ as well as any other atomic or molecular property of interest. Since $H_{\mathrm{eff}}$ is defined only *within* the model space $\mathcal{M}$, however, it is often more convenient for open-shell systems to evaluate the matrix elements of $H^{(n)}_{\mathrm{eff}} = PH\Omega^{(n)}P$ (or of any other interaction operators) with regard to the functions $|\phi_\alpha\rangle \in \mathcal{M}$, instead of deriving an explicit representation of the effective Hamiltonian. From the diagonalization of the Hamiltonian matrix, calculated up to the order $n$ in the wave operator, we then immediately obtain the energies up to the order $n+1$, $E^{(n+1)}_\alpha$, as well as the model functions $|\psi^o_\alpha\rangle$ (up to the $n$th order). These model functions are obtained

$$\left|\psi^o_\alpha\right\rangle = \sum_{\beta\in\mathcal{M}} c^{(n)}_{\alpha\beta}|\phi_\beta\rangle \tag{45}$$

as linear combination of those determinants $\{|\phi_\beta\rangle\}$ which span an orthonormal basis in the model space; as usual, here the complex coefficients $\{c^{(n)}_{\alpha\beta}\}$ are called a representation of the atomic or molecular states in intermediate normalization. Moreover, having the wave operator $\Omega$ and the model functions $|\psi^o_\alpha\rangle$, we see that all other properties can be traced back always to matrix elements between the unperturbed functions (determinants) $|\phi_\alpha\rangle \in \mathcal{M}$, rather independent on the particular form of the corresponding (transition) operator.

## 4.2 Vacuum amplitudes

Unlike the wave operator, the two other tasks above, (b) and (c), require he evaluation and simplification of matrix elements of *effective* operators

$$\langle\phi_\alpha|A_{\mathrm{eff}}|\phi_\beta\rangle = \left\langle o\right|(\hat{\boldsymbol{a}})_\alpha A_{\mathrm{eff}}\left(\hat{\boldsymbol{a}}^\dagger\right)_\beta\left|o\right\rangle \tag{46}$$

with regard to the functions $\{|\phi_\alpha\rangle\}$ of the model space. Apparently, if we 'combine' all the creation and annihilation operators of $(\hat{\boldsymbol{a}})_\alpha$ and $(\hat{\boldsymbol{a}}^\dagger)_\beta$ with those from the effective operators, this evaluation is equivalent to the computation of (so-called) *vacuum amplitudes*. If, for instance, we bring the (newly constructed) effective operator $(\hat{\boldsymbol{a}})_\alpha A_{\mathrm{eff}}(\hat{\boldsymbol{a}}^\dagger)_\beta$ into normal form, we find that all terms *vanish identically*,

$$\left\langle o\right|a^\dagger_i a_j \ldots a_k\left|o\right\rangle \equiv 0,$$

for which not *all* the creation and annihilation have been contracted completely, i.e. for which some of these operators remain (and where the vacuum state has been supposed to be normalized, $\langle o|o\rangle = 1$). The analysis of these vacuum amplitudes

in the manipulation of operator (strings), in particular, facilitates the treatment of open shells; they are very useful also for any computer-algebraic manipulation, since all shell structures can now be treated analogously and on equal footing with the atomic or molecular interactions (operators). This evaluation of the vacuum amplitudes makes it clear again why it is essential to bring first all the creation and annihilation in the operator products into their normal order—before we should begin with any numerical computation of the perturbation expansions.

For the calculation of the total (or correlation) energies, the effective Hamiltonian or effective perturbation are the operators we need to consider,

$$A_{\rm eff} = H_{\rm eff} \quad \text{or} \quad A_{\rm eff} = V_{\rm eff},$$

respectively. In studying other atomic and molecular properties, however, we often have to calculate the matrix elements of various one-particle $F = \sum_p^N f(\mathbf{r}_p)$ or two-particle operators $G = \sum_{p<q}^N \mathrm{g}(\mathbf{r}_p, \mathbf{r}_q)$, symmetric in all pairs of particle indices $[\mathbf{r}_p, \mathbf{r}_q]$. In these operators, the summation index $p(q)$ runs over the coordinates of the $N$ electrons of the system. For these operators, a second-quantized form can be obtained usually analogue to the representation of the (one- and two-particle contributions of the) perturbations $V_1$ and $V_2$ in (37)–(38)

$$F = \sum_{ij} a_i^\dagger a_j \langle i|f|j\rangle = \sum_{ij} \left\{a_i^\dagger a_j\right\} \langle i|f|j\rangle + \sum_a \langle a|f|a\rangle, \tag{47}$$

$$\begin{aligned} G &= \frac{1}{2} \sum_{ijkl} a_i^\dagger a_j^\dagger a_l a_k \langle ij|\mathrm{g}|kl\rangle \\ &= \frac{1}{2} \sum_{ijkl} \left\{a_i^\dagger a_j^\dagger a_l a_k\right\} \langle ij|\mathrm{g}|kl\rangle + \sum_{ij} \left\{a_i^\dagger a_j\right\} \sum_a (\langle ia|\mathrm{g}|ja\rangle - \langle ia|\mathrm{g}|aj\rangle) \\ &\quad + \frac{1}{2} \sum_{ab} (\langle ab|\mathrm{g}|ab\rangle - \langle ab|\mathrm{g}|ba\rangle). \end{aligned} \tag{48}$$

As for the effective Hamiltonian, in general, we need the matrix elements of these operators with regard to the model functions $|\phi_\alpha\rangle$ but not for those functions from *outside* of the model space, i.e. the complementary space $\mathcal{H} \ominus \mathcal{M}$ (which is described not even by the Bloch equation). Therefore, the corresponding effective operators are

$$A_{\rm eff} = \Omega^\dagger F \Omega \quad \text{and} \quad A_{\rm eff} = \Omega^\dagger G \Omega. \tag{49}$$

With this notation and the vacuum amplitudes (46), we can summarize the result of this section by saying that the wave operator $\Omega^{(n)}$ as well as any effective operator and matrix element can be written always as *perturbation expansion*, independent of the particular shell structure of the system. More often than not, moreover, we shall be interested only in the vacuum amplitudes on the rhs of Eq. (46), i.e. only in the completely contracted terms of the operator product $[(\hat{\boldsymbol{a}})_\alpha A_{\rm eff} (\hat{\boldsymbol{a}}^\dagger)_\beta]$, once it has been brought into its normal-order sequence. In fact, these are the

only terms which eventually 'survive' through all the manipulation of the operator terms or diagrams.

With this brief discussion of the three basic steps (a)–(c) from Subsection 4.1, we have arrived at our original destination to represent all physical quantities of interest as sum (of products) of one- and two-particle amplitudes. In practice, each of these expansions are often lengthy and the complexity of these expansions increases rapidly if the number of particle and holes is increased in the valence shells. The latter can be seen easily from the fact that each (valence-shell) particle of hole introduces an *additional* creation or annihilation operator into the operator strings $(\hat{\boldsymbol{a}})_\alpha$ and $(\hat{\boldsymbol{a}}^\dagger)_\beta$, respectively. In contrast to other, e.g. multiconfigurational, expansions of the wave functions, however, the explicit form of the approximate states $|\psi_\alpha\rangle$ cannot be derived so easily in MBPT or the CCA. For this reason also, a straightforward and simply handling of the perturbation expansions decides how successfully the theory can be applied to open-shell atoms and molecules in the future.

## 4.3 Extended normal-order sequence of operator strings

If applied to the reference state $|\Phi\rangle$, an operator $\{A\}$ in normal order enables us immediately to recognize those terms which 'survive' in the computation of the vacuum amplitudes. The same applies for any model function and, hence, for real multidimensional model spaces, if a proper normal-order sequence is defined for all the particle–hole creation and annihilation operators from the four classes of orbitals (i)–(iv) in Subsection 3.4. In addition to the specification of a proper set of indices for the physical operators, such as the effective Hamiltonian or any other one- or two-particle operator, however, the definition and classification of the model-space functions now plays a crucial role. In order to deal properly with the model-spaces of open-shell systems, an unique set of indices is required, in particular, for identifying the operator strings of the model-space functions $(\hat{\boldsymbol{a}})_\alpha$ and $(\hat{\boldsymbol{a}}^\dagger)_\beta$, respectively. Apart from the particle and hole states (with regard to the many-electron vacuum), we therefore need a clear and simple distinction between different classes of creation and annihilation operators. For this reason, it is convenient for the derivation of open-shell expansions to specify a (so-called) *extended normal-order sequence*. Six different types of orbitals have to be distinguished hereby in order to reflect not only the classification of the core, core–valence, ... orbitals, following our discussion in Subsection 3.4, but also the range of summation which is associated with these orbitals. While some of the indices refer a class of orbitals as a whole, others are just used to indicate a particular core–valence or valence orbital, respectively.

In the GOLDSTONE program below, we distinguish the following six types of orbitals with the following indices:

| | |
|---|---|
| $r_1, r_2, \ldots$ | index to represent a summation over all virtual and valence orbitals; |
| $m_1, m_2, \ldots$ | summation index only over all valence orbitals; |
| $n_1, n_2, \ldots$ | any (fixed) index of some valence orbital which need to be specified explicitly at some proper stage of the computations; |
| $c_1, c_2, \ldots$ | summation index over all core and core–valence orbitals; |
| $b_1, b_2, \ldots$ | summation index only over all core–valence orbitals; |
| $a_1, a_2, \ldots$ | any (fixed) index of some core–valence orbital which, again, need to be specified at some proper stage of the computations. |

While the (small) letters indicate the index type, different indices of the same type are distinguished by an additional integer. Although this notation is in slight contrast to what is usually applied in most textbooks about many-body perturbation theory, it has great advantages for the computational implementation. As indicated above, any summation index now carries all information about the class(es) of orbitals and the summation associated with it. For instance, in order to define the Fock space function (43), we can simply use one or several *fixed* valence or core–valence orbitals by taking the orbital indices $n_1, n_2, \ldots$ or $a_1, a_2 \ldots$, respectively, and without that these functions would have to be specified already right from the beginning of the derivation.

With this definition of the orbital indices, we now say that any (given) string of creation and annihilation operators obeys an *extended normal-order sequence*,

$$\left(a_r^\dagger\right) - \left(a_m^\dagger\right) - \left(a_n^\dagger\right) - (a_a) - (a_b) - (a_c) - \left(a_c^\dagger\right) - \left(a_b^\dagger\right) - \left(a_b^\dagger\right) - (a_n) - (a_m) - (a_r), \tag{50}$$

if these operators are arranged in a way, so that all creation operators of virtual orbitals appear *left* of all creation operators of valence orbitals (and including each an implicit summation) and, in turn, *left* of all creation operators of fixed valence orbitals—and so on—up to *left* of all annihilation operators of virtual orbitals. Such an ordering of the creation and annihilation operators enables one easily to 'read off', for example, the action of a projector operator $P$ which occurs on the left- or right-hand side of such an operator string. Moreover, each individual term (diagram) of the perturbation expansion now *contains* all the information about the necessary summations over the various orbitals which have to be carry out in further computations.

In fact, the definition of the extended normal-order sequence (50) is very crucial to our implementation of the GOLDSTONE program. Therefore, in order to make this convention more transparent for the reader, let us consider the effective one-particle part of the operator (47), $F_1 = \sum_{ij} \{a_i^\dagger a_j\} \langle i|f|j\rangle$. Using the definitions of the orbital indices from above, this operator can be explicitly written as

$$F_1 = a_{r_1}^+ a_{r_2} \langle r_1|f|r_2\rangle + a_{r_1}^+ a_{c_2} \langle r_1|f|c_2\rangle + a_{c_1}^+ a_{r_2} \langle c_1|f|r_2\rangle + a_{c_2} a_{c_1}^+ \langle c_1|f|c_2\rangle, \tag{51}$$

where an implicit summation (over the corresponding part of the one-electron spectrum) is associated with the indices $r_1, r_2, c_1$ and $c_2$. Moreover, if we project this operator to the right upon the model space of an alkaline-earth metal (i.e. for

an effective two-particle system), the operator products $F_1 P$ then simply reads

$$F_1 P = a_{r_1}^+ a_{m_2} \langle r_1 | f | m_2 \rangle + a_{r_1}^+ a_{c_2} \langle r_1 | f | c_2 \rangle \tag{52}$$

due to the representation (42) of the projection operator. Finally, for example, the Fock space representation of an (excited) alkaline-earth type model function is

$$(ns\ n'p) \rightarrow a_{n_1}^+ a_{n_2}^+ |o\rangle, \tag{53}$$

including the two *fixed* but yet unspecified indices $n_1$ and $n_2$ in order to represent two valence orbitals.

## 4.4 Angular reduction

Often, a remarkable simplification in the evaluation of individual Feynman–Goldstone diagrams (terms in an perturbation expansion) can be achieved, if the symmetry of the system and the corresponding one-electron orbitals is utilized. Clearly, this simplification depends on the particular system under consideration and is quite different for atoms, molecules, quantum dots, etc.; it also depends, for instance, of whether a nonrelativistic or relativistic framework is applied for calculating the individual contributions [45]. For open-shell atoms and molecules, unfortunately, a 'symmetry-adapted' MBPT has never been worked out in full detail, although this request has been known for many years now and it would still be highly desirable to have it done [46,47]. However, since we shall focus in this contribution on the derivation of the perturbation expansions in the language of 'one-electron orbitals', not much need to be said here in general about the symmetry reduction of the Feynman–Goldstone diagrams.

For free atoms especially, the integration over all the spin and angular variables (in the standard notion of spin-orbital functions) can be carried out analytically in most expansions due to the symmetry of the one-electron functions with respect to a rotation and inversion of the coordinates. In this case, each orbital index $a \equiv (a_n, a_l, a_{m_l}, a_{m_s})$ is equivalent to four quantum numbers, the principal quantum number $a_n$, the orbital number $a_l$ as well as the two magnetic quantum numbers $a_{m_l}$ and $a_{m_s}$ within the nonrelativistic theory and quite similar also within a relativistic framework, respectively. Using the techniques of Racah's algebra [48], its then often possible to replace the summation over all the magnetic quantum numbers by a proper product of Wigner $6-j$ and/or $9-j$ symbols (and some characteristic factors), at least, if a closed-shell determinant is assumed for the reference state $|\Phi\rangle$. For atoms, this analytical evaluation of the one- and two-particle amplitudes is known also as *angular reduction* of the Feynman–Goldstone diagrams in the literature [13,49,50].

To support such a symmetry reduction of diagrams (as well as of other expressions from Racah's algebra), we developed the RACAH program during the last decade [51,52]. Figure 10.3 displays a typical (Racah) expression as it occurs frequently in the spin-angular integration of quantum systems and at many places elsewhere. Most generally, these expressions may contain any number of Wigner $3n-j$ symbols, spherical harmonics, rotation matrices, etc. Since a first version of

$$\text{Racahexpr} := \sum_{j_1,j_2,l_1,\cdots} (-1)^{2j_1-j_2+\cdots}\, j_1^{3/2}\,[j_2]\ldots \begin{pmatrix} \cdot & \cdot & j_1 \\ \cdot & \cdot & \cdot \end{pmatrix} \begin{pmatrix} j_1 & j_2 & \cdot \\ \cdot & \cdot & \cdot \end{pmatrix} \begin{Bmatrix} \cdot & j_3 & \cdot \\ j_1 & \cdot & \cdot \\ J & \cdot & j_2 \end{Bmatrix} \ldots$$

$$\times \int d\Omega_1 Y_{l_1 m_1}(\Omega_1) Y_{l_2 m_2}(\Omega_2) \int d\beta d^{j_3}_{p_3 q_3}(\beta) d^{j_4}_{p_4 q_4}(\beta') \ldots$$

**FIGURE 10.3** Structure of Racah expressions as simplified by the RACAH program [51,52].

the code in 1997, the RACAH program has grown considerably and has been updated in a number of steps [53–55]. Today, this program provides an interactive and user-friendly tool which is organized in some hierarchical order. In addition to the algebraic manipulations, we now support also numerical computations for a wide class of symbols and functions as discussed in Ref. [56].

## 4.5 Basic steps in deriving perturbation expansions

In Subsections 4.1 and 4.2, we saw how the wave operator $\Omega$ and the matrix elements of all effective operators, if calculated with regard to the eigenfunctions of the model operator $H_o$, can be traced back always to a *sum* of Feynman–Goldstone terms (or diagrams if derived graphically). It is *this* form which we call an atomic or molecular perturbation expansion. To explain the procedure of deriving such expansions for open-shell atoms and molecules, let us now explain the four basic steps in the derivation by using a notation, which is closely related to the computer-algebraic manipulation of the operators and matrix elements. Further details on the implementation of these steps within the framework of MAPLE will be outlined later in Subsection 4.7.

Although the size and complexity of the perturbation expansions increases rapidly with any further particle in either the valence or core–valence orbitals, the steps below are rather general and independent of the shell structure of the particular atom or molecule. In the following, therefore, we assume only that all the operators of interest have a representation in second quantization and that the matrix elements are calculated with regard to the basis function $|\phi_\alpha\rangle \in \mathcal{M}$ from the model space. Then, the four steps below apply for both, the computation of correlation energies as well as for many other atomic and molecular (transition) properties:

1. *Evaluation of the operator products* as they occur either on the rhs of the Bloch Eq. (23) or in the definition of the effective operators (15) and (49). The aim of this step is to bring all the creation and annihilation operators (in each term of the expansions) into the extended normal-order form (50). The result is a sequence of normal-ordered operator terms (briefly referred to as Feynman-Goldstone diagrams).
2. *Definition and representation of the model space*. To characterize (the basis functions of) the model space, we make use of the number of *occupied* valence orbitals and the number of *unoccupied* core–valence orbitals. Within the orbital language of

the perturbation expansions, these 'occupation numbers' determine entirely the form of the projection operators (42), i.e. the number of creation and annihilation operators with fixed orbital indices $n_1, n_2, \ldots$ and $a_1, a_2, \ldots$, respectively. The basis functions $|\phi_\alpha\rangle \in \mathcal{M}$ are described as Fock space functions (43) with regard to the reference state $|\Phi\rangle$, while the dual functions $\langle\phi_\beta|$ can be generated easily by applying the (adjoint) creation and annihilation operators in *reversed* order. This representation is particularly simple as long as the shell structure obeys a $(1,0)$ and $(0,1)$ model space with either a single valence electron or a single (valence) hole, respectively. In the case of two or more valence electrons *and/or* holes in free atoms, in contrast, it might be more appropriate to couple the basis functions of the model space right from the beginning in a way in order to have a well-defined *total* angular momentum $J$, but details about such a coupling procedure is beyond of the scope of the present work.

3. *Evaluation of the vacuum amplitudes (46)* as they arise by combining the operator strings from step (1) and the Fock space representation $(\hat{\boldsymbol{a}})_\alpha$ and $(\hat{\boldsymbol{a}}^\dagger)_\beta$ of the model space functions from step (2). As described above, there is no summation associated with the indices $n_i$ and $a_j$ in the definition of the model-space functions (43).

   In course of the evaluation of the vacuum amplitudes, only those terms 'survive' eventually in this step which are completely contracted, i.e. those with no creation or annihilation operators at all in the final expression. In other words, each (non-zero) vacuum amplitude is written as a superposition of just one- and two-particle matrix elements of various kinds (due to the one- and two-particle character of all atomic and molecular interactions), and including summations over the core, core–valence, valence *and/or* virtual orbitals. In certain cases, it has been found useful to *combine* the steps (1) and (3) and to evaluate the vacuum amplitudes directly from the rhs of the 'full' matrix elements in second quantization.
4. *Symmetry reduction* of all completely contracted Feynman–Goldstone 'diagrams'. This step depends on the particular representation of the one-particle spectrum as outlined in Subsection 4.4 and is the angular reduction in the case of free atoms.

Once these steps have been performed successfully for a given property and shell structure of the system, there remains only the (summation of the) one- and two-electron amplitudes which have to be calculated numerically. Often, the computation of these (radial) amplitudes takes the most (CPU) time and need to be implemented by a traditional, algorithmic language rather than in the framework of computer-algebraic systems [57,58]. For complex quantum systems, however, similar amplitudes usually appear at different places in the perturbation expansions and, hence, terms of different sorts might be 'combined' algebraically before the numerical computations start. In a graphical representation, such 'common' pieces of otherwise topological different diagrams are called 'fragments' which can be manipulated also by means of computer-algebraic tools.

## 4.6 Advantages of using computer algebra

Today, computer algebra is known for providing an efficient route in many fields of advanced scientific computing. New generations of general-purpose computer-algebra systems (CAS), such as MATHEMATICA, MAPLE and several others, have been developed and enable their user to solve complex tasked within a uniform framework and, usually, at one and the same platform. The term 'technical computing' has been coined to denote the ability of modern-day CAS for combining symbolic algorithms, fast numerical computations, programming, visualization, and up to the presentation of scientific documents. Despite its great merits, however, symbolic techniques are not yet so widely used in atomic physics or quantum chemistry, neither in research nor in education. Therefore, before we shall describe the implementation of the GOLDSTONE program, let us briefly summarize the advantages of computer algebra for deriving and evaluating perturbation expansions.

Several features make general-purpose CAS very useful for research in applied mathematics. Apart from (i) the fast and reliable manipulation of standard mathematical expressions, these features concern in particular (ii) the *sound* mathematical foundation of most CAS, i.e. their broad knowledge about the rules in making transformations of different types. Often, moreover, (iii) the treatment of large expression is an important pre-condition for dealing with complex chemical or physical systems and are of utmost practical significance for the description of quantum many-particle systems. For these few reasons alone, the importance of symbolic methods can hardly be overrated. By developing a proper (hierarchy of) algorithms and symbolic tools, a great potential is seen especially for all those formalisms which are well established mathematically but which become cumbersome (or even prohibitive in practice), if applied to complex systems [59–61]. For the derivation of atomic and molecular perturbation expansions, in particular, CAS facilitate:

- the creation of a problem-adapted language which is closely related to the mathematical formulation of the MBPT and the coupled-cluster ansatz;
- to make the derivation of the perturbation expansions more transparent for the user;
- the derivation of expansions independent of the shell structure of the systems;
- to follow new ideas in many-body perturbation theory;
- the reliability of the derivations;
- a user-friendly and interactive work.

In the derivation of perturbation expansions, the request for 'reliability' concerns especially the handling of the phases and weights for which the traditional routes [cf. Figure 10.2] are prone for making errors. For a large number of terms (in a given perturbation expansion), moreover, one may get confused quite easily about the expansion *as a whole* and about the various possibilities for defining proper 'approximations' to these expansions; overall, computer-algebraic tools allow here a reliable *book keeping* of all the operators and amplitudes which appear in course of the derivation.

At the first glance, the 'transparency' in deriving atomic and molecular perturbation expansions, mentioned above, might be less obvious since many of the details remain hidden of course to the user by applying computer-algebraic tools. Here, the main advantage in utilizing these tools arises from the fact that one can focus on (and check for alternatives of) a certain part of the derivation, without that all the transformations *before* and *after* this particular step need to be performed by hand explicitly. Moreover, these tools usually enables one to keep the full expansion together without the need to split it into several pieces. In general, such a 'black-box' approach is likely to be even necessary in order to manage a certain complexity as given often by open-shell atoms and molecules.

## 4.7 The GOLDSTONE program

The four basic steps in the derivation of perturbation expansions, outlined in Subsection 4.5, can be implemented most easily by means of a general-purpose CAS with a wide-spread use in the community of atomic and molecular structure theory. Making use of MAPLE's symbolic environment, therefore, the GOLDSTONE program has been developed as an interactive tool for deriving perturbation expansions for different shell structures and properties of atoms and molecules. Apart from the 'evaluation' of general operator products in second quantization, i.e. from transforming them into a sequence of normal-ordered operator terms, this program facilitates the definition of interaction operators, model spaces as well as classifications of various sorts. It also supports the successive solution of the Bloch Eq. (23) order-by-order, at least, as far as CPU time and memory is available. Owing to its interactive design, we expect the GOLDSTONE program of common interest, both in teaching atomic and molecular perturbation theory as well as for carrying out advanced research studies.

From the very beginning, hereby, emphasis was placed on developing a self-contained and user-friendly tool, which neither requires detailed knowledge about the theoretical background of MBPT nor about the special names and abbreviations as used in the literature. Instead, attention has been paid for designing a 'language' as close as possible to standard applications in atomic and molecular structure. A first example in using the program will be shown below in Section 5 in deriving the expressions for the second- and third-order correlation energies of closed-shell atoms and ions.

Following MAPLE's philosophy, the GOLDSTONE program has been organized in a hierarchical order. It presently includes about 120 individual procedures which can be invoked either interactively or simply as language elements in order to built up commands at some higher level of the hierarchy. In practice, however, only about 20 (main) procedures need to be known by the user; they are briefly summarized and explained in Table 10.1 for providing the reader with a first impression about the GOLDSTONE program. One of the basic procedures is, for example, `Goldstone_OperatorProduct()` for evaluating the operator product of two or more terms, $\mathrm{oplist}_1 \times \mathrm{oplist}_2 \times \cdots \times \mathrm{oplist}_n$, including all the possible contractions. In this routine, each argument, $\mathrm{oplist}_i$, can be either an individual operator term (diagram) or perturbation expansion by its own. Figure 10.4 shows a

**TABLE 10.1** Main commands of the GOLDSTONE program for deriving atomic and molecular perturbation expansions within an (one-electron) 'orbital picture'

| | |
|---|---|
| `Goldstone_ApplyWickTheorem()` | Applies Wick's theorem to either a single diagram or a whole expansion of diagrams. |
| `Goldstone_convert()` | Converts certain expressions between different representations. |
| `Goldstone_DefineModelFunction()` | Defines either a ⟨bra| or |ket⟩ model function (43) with regard to the references state $\|\Phi\rangle$. |
| `Goldstone_IsNormalOrdered()` | Returns a boolean value *true* if an expression is normal-ordered and *false* otherwise. |
| `Goldstone_LinearizeOperator()` | Linearizes an expansion with regard to a given operator. |
| `Goldstone_NormalProduct()` | Evaluates the normal-order form $\{A{\cdot}B{\cdot}\cdots\}$ of a product of two or more operators in second quantization. |
| `Goldstone_OperatorProduct()` | Evaluates the operator product $A \cdot B \cdot \cdots$ of two or more operators in second quantization, including all contractions. |
| `Goldstone_print()` | Prints an operator expression in a fast and convenient way. |
| `Goldstone_ProjectOperator()` | Projects a given operator expansion to the lhs or rhs onto the P or Q space. |
| `Goldstone_select()` | Selects different kinds of diagrams from a given expansion. |
| `Goldstone_SetAdjoint()` | Returns the adjoint operator for a given expansion. |
| `Goldstone_SetModelSpaceOccupation()` | Define the occupation of the model space in terms of the number of valence-particles and the number of valence-holes. |
| `Goldstone_SetNormalOrder()` | Brings an operator expression into normal-order; i.e. into an extended *normal-order-sequence* as defined in Eq. (50). |
| `Goldstone_SetOperator()` | Defines the internal representation of various operators. |
| `Goldstone_simplify()` | Attempts to simplify an expansion. |
| `Goldstone_SolveNextOrderEnergy()` | Solves the energy diagrams $E^{(n+1)}$ of the order-by-order Bloch Eq. (23) by starting from the $n$th order solution of the wave operator $\Omega^{(n)}$. |
| `Goldstone_SolveNextOrderOmega()` | Solves the wave operator diagrams $\Omega^{(n+1)}$ of the order-by-order Bloch Eq. (23) by starting from the $n$th order solution of the wave operator $\Omega^{(n)}$. |
| `Goldstone_type()` | Returns a boolean value *true* if an expression has a given type or *false* otherwise. |
| `Goldstone_VacuumExpectationValue()` | Evaluates the vacuum expectation value (46). |

**Goldstone_ApplyWicksTheorem(oplist)**

Applies Wick's theorem to the first creation or annihilation operator which is not in *normal-order* with respect to all other operators on its left-hand side. oplist can be either of type `diagram` or `expansion`.

**Output:** An `expansion` is returned.

**Additional information:** Wick's theorem is independently applied to the first *non-ordered* operator in each `diagram`. ♣ All contracted terms are included in the output. Because Wick's theorem is applied just to the first *non-ordered* operator (by going from the left side to the right) only *single-contractions* can occur. ♣ oplist may contain also some projection operator $|o\rangle\langle o|$ onto the vacuum in the operator string. ♣ Some string of creation and/or annihilation operators is said to be non-ordered if this string does not form a normal-order sequence.

**Goldstone_OperatorProduct(oplist$_1$,oplist$_2$,...,oplist$_n$)**

Evaluates the operator product of oplist$_1 \times$ oplist$_2 \times \cdots \times$ oplist$_n$ including all contractions where oplist$_i$ can be either of type `diagram` or `expansion`.

**Output:** An `expansion` is returned.

**Additional information:** The output contains usually more than $(n_1 \times n_2 \times \cdots \times n_n)$ `diagram` where $n_i$ is the number of diagrams in oplist$_i$. ♣ Besides the normal-order part of the product, all terms which result from the contraction of the $n$ operators are also included.

**FIGURE 10.4** Part of the user manual as provided for the GOLDSTONE program.

short description of this command as it will be found also in a user manual which is currently prepared together with the code. To distinguish the commands of the GOLDSTONE program from MAPLE's internal functions, they all start with the prefix `Goldstone_`. Beside of the main procedures, there are many other functions which are not visible for the user but applied at some *hidden* level in the hierarchy.

Internally, the GOLDSTONE program is based on a number of data structures, such as `diagram` to represent a single operator term or `expansion` to represent a perturbation expansion as a whole, i.e. a sequence of different terms with possibly different topology. In Figure 10.4, we have used this notation to characterize the type of the arguments and the (expected) output of procedures. Moreover, we often use the term `oplist` if either of these data structure may occur as an argument. Apart from the computational requests concerning the memory and CPU time of the code, there are no further restrictions of the GOLDSTONE program with regard to the number and complexity of the individual diagrams.

## 5. APPLICATION OF THE GOLDSTONE PROGRAM

### 5.1 Wave operator and energy corrections

To illustrate the use of the GOLDSTONE program, let us consider the wave operator and correlation energies of some atom or molecule. For close-shell systems, of course, we can choose always a 1-dimensional model space, $|o_c\rangle$, which coincides with the reference state $|\Phi\rangle$. In this case, the total energy of the system up to first order is equal to the vacuum expectation value of the normal-ordered Hamiltonian

$H = H_o + V$,

$$E^{(0)} + E^{(1)} = \langle o_c|H|o_c\rangle = \sum_a \epsilon_a + \sum_a \left[\frac{1}{2}(V_{\rm HF})_{aa} + \langle a| - V(r)|a\rangle\right], \quad (54)$$

which can be written by means of the Hartree–Fock potential $V_{\rm HF}$. In this expression, $V(r)$ denotes an (arbitrary) potential as applied in the generation of the one-particle spectrum, for instance, by diagonalizing the one-particle Hamiltonian, $h = -\frac{\nabla}{2} + V_{\rm nuc}(r) + V(r)$, within a proper basis set. Since the total energy of the atom cannot depend on such an arbitrary choice of the potential $V(r)$, it is not surprising that it is subtracted again in expression (54). In particular, if we apply the Hartree–Fock potential, $V(r) = V_{\rm HF}$, for generating the one-electron spectrum, we just obtain the standard Hartree–Fock expression for the total energy (in first order)

$$E_{\rm HF} = \sum_a \epsilon_a - \frac{1}{2}\sum_a (V_{\rm HF})_{aa}.$$

For all higher-order correlation energies (of closed-shell systems), moreover, we can follow similar lines and evaluate the vacuum expectation values $E^{(n)} = \langle o_c|V\Omega^{(n-1)}|o_c\rangle$. This results in the standard Moeller–Plesset expressions for the energy corrections.

For open-shell atoms and molecules, in contrast, the computation of the total energies requires to evaluate first the individual terms of the wave operator $\Omega^{(k)}$ and the energy $E^{(k)}$ successively order-by-order up to an given order $n$. Having the wave operator, $\Omega^{[n]} = \Omega^{(0)} + \Omega^{(1)} + \cdots + \Omega^{(n)}$, we need to evaluate the matrix elements of the effective Hamiltonian (15) or (18) with regard to the model space. For this, we can follow immediately the steps in Subsection 4.5, once the occupation of the model space, i.e. the shell structure of the atoms or molecules, has been specified in terms of the number of *valence particles* and the number of *valence holes* of the system [cf. `Goldstone_SetModelSpaceOccupation()`].

## 5.2 Evaluation of the second- and third-order correlation energies for closed-shell atoms

With these few remarks above, we are prepared to demonstrate the *interactive* use of the GOLDSTONE program. For the sake of simplicity (and in order to keep the output of the program feasible for this contribution), we shall restrict ourselves to the low-order correlation energies of closed-shell atoms. The treatment of open-shell systems will be shown elsewhere, together with a more detailed description of the code. For a first encounter with the GOLDSTONE module, however, we shall display here the steps as needed to obtain the second- and third-order correlation energies. This includes the evaluation of the wave operator (up to second order) which could be utilized-later-also for calculating other properties, such as correlation energies [62,63], $g$-factors [64], hyperfine structures and isotope shifts

[65,66], quadrupole moments [67], decay rates [68], parity non-conserving transitions [69,70], photoionization cross sections [71], and several others.

Not much need to be said here to understand the MAPLE dialog below; once, the GOLDSTONE program has been loaded by executing the command

```
> with(Goldstone);
```

all the procedures of this code can be utilized as any internal command of MAPLE. As usual, every command has to be terminated by either a colon or semicolon, where the former is used in order to *suppress* the output to screen. The orbital indices, which are shown below, correspond directly to the distinction of the core, core–valence, valence and virtual orbitals as explained above in Subsection 4.3, and including the implicit (Einstein) summation over all those indices which appear twice within a single *diagram* (operator term).

We first define the rest interaction $V$ for the case that the one-particle spectrum has obtained by means of an arbitrary potential $V$. In the GOLDSTONE program, this operator can be assigned to the variable `Vrest` by entering

```
> v0 := Goldstone_SetOperator("V0"):
> v1 := Goldstone_SetOperator("V1"):
> v2 := Goldstone_SetOperator("V2"):
> Vrest := Goldstone_AddOperators(v0,v1,v2):
```

In addition, we need to specify the occupation of the model space in terms of the number of *valence particles* and the number of *valence holes*,

```
Goldstone_SetModelSpaceOccupation(0,0);
Occupation numbers nvp = 0 and nvc = 0
```

which are both zero for closed-shell atoms. From these occupation numbers, usually, the program derives the internal representation of the model functions (43) in second quantization, i.e. the number of *fixed* orbitals $n$ and $a$ of these functions.

With these definitions of the perturbation and the model space, we can now solve successively the Bloch equation (16) for the energy corrections ($\in_n$) and wave operator ($w_n$). As discussed above, we shall need the wave operator up to order $(n-1)$ if we wish to determine the energy correction to order $n$:

```
> e1 := Goldstone_SolveNextOrderEnergy(Vrest):
> w1 := Goldstone_SolveNextOrderOmega(Vrest):
> e2 := Goldstone_SolveNextOrderEnergy(Vrest):

> Goldstone_print(e2):

===> (-1)^0 1 v1(c1|r2) v1(r2|c1) X0 1 / ( ( + Er2 - Ec1 ) )
------------------------------------------------------------------------------- 1
===> (-1)^2 1/2 v2(c1;c2|r3;r4) v2(r4;r3|c2;c1) X0 1 / ( ( + Er4 + Er3 - Ec1 - Ec2 ) )
------------------------------------------------------------------------------- 2
===> (-1)^1 1/2 v2(c1;c2|r3;r4) v2(r4;r3|c1;c2) X0 1 / ( ( + Er4 + Er3 - Ec2 - Ec1 ) )
------------------------------------------------------------------------------- 3
```

Every term in this expansion (as indicated by the integer at the end of the line) represents a Feyman–Goldstone diagram and could be drawn also graphically. These are the (three) well-known 'diagrams' of the second-order correlation energy for closed-shell systems as found at different places in the literature. If we assume a Hartree–Fock (one-particle) spectrum, instead,

```
> VHF := Goldstone_AddOperators(v0,v2):
```

$$-\frac{1}{2}\frac{\langle c_1c_2|v_{12}|r_3r_4\rangle\langle r_4r_3|v_{12}|c_2c_1\rangle\Omega_0\Omega_0}{(\epsilon_{r_4}+\epsilon_{r_3}-\epsilon_{c_1}-\epsilon_{c_2})}$$

$$\frac{1}{2}\frac{\langle c_1c_2|v_{12}|r_3r_4\rangle\langle r_4r_3|v_{12}|c_1c_2\rangle\Omega_0\Omega_0}{(\epsilon_{r_4}+\epsilon_{r_3}-\epsilon_{c_2}-\epsilon_{c_1})}$$

$$\frac{1}{2}\frac{\langle c_1c_2|v_{12}|r_3r_4\rangle V_0V_0\langle r_4r_3|v_{12}|c_2c_1\rangle\Omega_0\Omega_0}{(\epsilon_{r_4}+\epsilon_{r_3}-\epsilon_{c_1}-\epsilon_{c_2})(\epsilon_{r_4}+\epsilon_{r_3}-\epsilon_{c_1}-\epsilon_{c_2})}$$

$$-\frac{1}{2}\frac{\langle c_1c_2|v_{12}|r_3r_4\rangle V_0V_0\langle r_4r_3|v_{12}|c_1c_2\rangle\Omega_0\Omega_0}{(\epsilon_{r_4}+\epsilon_{r_3}-\epsilon_{c_2}-\epsilon_{c_1})(\epsilon_{r_4}+\epsilon_{r_3}-\epsilon_{c_2}-\epsilon_{c_1})}$$

$$-\frac{1}{2}\frac{\langle c_1c_2|v_{12}|r_3r_4\rangle\langle r_4r_3|v_{12}|r_5r_6\rangle\langle r_6r_5|v_{12}|c_2c_1\rangle\Omega_0\Omega_0}{(\epsilon_{r_6}+\epsilon_{r_5}-\epsilon_{c_1}-\epsilon_{c_2})(\epsilon_{r_4}+\epsilon_{r_3}-\epsilon_{c_1}-\epsilon_{c_2})}$$

$$\frac{1}{2}\frac{\langle c_1c_2|v_{12}|r_3r_4\rangle\langle r_4r_3|v_{12}|r_5r_6\rangle\langle r_6r_5|v_{12}|c_1c_2\rangle\Omega_0\Omega_0}{(\epsilon_{r_6}+\epsilon_{r_5}-\epsilon_{c_2}-\epsilon_{c_1})(\epsilon_{r_4}+\epsilon_{r_3}-\epsilon_{c_2}-\epsilon_{c_1})}$$

$$-\frac{\langle c_1c_2|v_{12}|r_3r_4\rangle\langle r_4c_5|v_{12}|r_6c_1\rangle\langle r_3r_6|v_{12}|c_5c_2\rangle\Omega_0\Omega_0}{(\epsilon_{r_3}+\epsilon_{r_6}-\epsilon_{c_2}-\epsilon_{c_5})(\epsilon_{r_4}+\epsilon_{r_3}-\epsilon_{c_1}-\epsilon_{c_2})}$$

$$\frac{\langle c_1c_2|v_{12}|r_3r_4\rangle\langle r_4c_5|v_{12}|r_6c_2\rangle\langle r_3r_6|v_{12}|c_5c_1\rangle\Omega_0\Omega_0}{(\epsilon_{r_3}+\epsilon_{r_6}-\epsilon_{c_1}-\epsilon_{c_5})(\epsilon_{r_4}+\epsilon_{r_3}-\epsilon_{c_2}-\epsilon_{c_1})}$$

**FIGURE 10.5** LaTeX output of the GOLDSTONE program for the third-order energy correction for closed-shell atoms and molecules. Only the first eight (out of (14)) terms are show in this figure. See text for further explanation.

the first term must vanish due to Brillouin's theorem and only the last two terms would 'survive' in the expansion, known sometimes as the *direct* and *exchange* diagram.

Suppose we have started from a Hartree–Fock spectrum, that is we have used the variable VHF in all the steps above. Then, the third-order correlation energy for closed-shell atoms is obtained with the GOLDSTONE program by typing

```
> w2 := Goldstone_SolveNextOrderOmega(VHF):
> e3 := Goldstone_SolveNextOrderEnergy(VHF):
```

Here, we shall not 'print' the expansion immediately to screen by using the `Goldstone_print()` command but write the corresponding LaTeX output to the file `out.tex`

```
> Goldstone_print_latex("header",`out.tex`):
> Goldstone_print_latex("expansion",e3):
> Goldstone_print_latex("end"):
```

The result is seen in Figure 10.5 where, however, we have restrict the output to the first few terms. For closed-shell systems, there are in total 14 diagrams in the expansion of the third-order correlation energies which can be compared directly with the expression by Blundell *et al.* [72], if we replace $\Omega_0 \equiv 1$ in order to adopt

this output for a wave operator in *intermediate normalization*. In the interactive treatment of the perturbation expansions, moreover, one can often *combine* topologically equivalent diagrams by using the command `Goldstone_simplify()`, which has a number of optional arguments.

## 6. FINAL REMARKS

Although many-body perturbation techniques have proven to be very accurate and efficient in predicting a large variety of atomic and molecular properties, not too many studies exist (so far) for open-shell systems, in particular if two or more electrons (and/or holes) reside outside of closed shells. For such shell structures, the main challenge in applying the Rayleigh–Schrödinger theory arises today from the complexity of the perturbation expansion which increases rapidly with the 'order' of the perturbation and the number of open shells. To make such perturbation expansion manageable, computer-algebraic algorithms offer a very promising route whose full 'strength' can hardly be foreshadowed

In this contribution, we have described the basic steps in obtaining atomic and molecular perturbation expansions from the view point of computer-algebra. In particular, it is shown how the derivation of Rayleigh–Schrödinger expansions can be traced back always to a few basic steps as outlined in Subsection 4.5. With the design of the GOLDSTONE program, moreover, we provide a flexible and powerful tool for interactive work whose syntax resembles the (mathematical) 'language' as used formally for deriving such perturbation expansions. This program is based on Wick's theorem and an algebraic representation of the model space, i.e. of its basis functions and projectors; it can therefore be applied to most open-shell atoms and molecules rather independent of the particular shell structure and the number of perturbations (operators) involved.

Today, the main emphasis in applying the Rayleigh–Schrödinger theory and coupled-cluster approach is placed certainly on the computation of correlation energies and bound-state transition properties. In contrast, less attention has been paid to 'bound-free' transitions concerning the emission or capture of electrons by atomic and molecular systems. These processes are typically associated with inner-shell 'holes' and, hence, additional open shells. For medium and heavy elements (and ions), moreover, a relativistic theory is required right from the beginning in order to describe them properly [73,74]. The same arguments held if many-body perturbation techniques ought to be applied to the properties of super-heavy elements [75–77]. Therefore, beside of the *no-pair* approximation which neglects the negative continuum and radiative (QED) corrections, the merging of many-body perturbation and QED techniques has been discussed recently by Lindgren and coworkers [4,78]. Although the full power of these new developments is not yet foreseeable, this brings us back to a current 'highlight' of atomic physics to which Ingvar Lindgren has contributed significantly. Computer-algebraic techniques may help apply and extent these ideas to a large number of atomic and molecular systems.

## REFERENCES


[1] I. Lindgren, J. Morrison, *Atomic Many-Body Theory*, second ed., Springer, Berlin, 1986.
[2] I. Lindgren, *J. Phys. B* **7** (1974) 2441.
[3] I. Lindgren, H. Persson, S. Salomonson, L. Labzowsky, *Phys. Rev. A* **51** (1995) 1167.
[4] I. Lindgren, S. Salomonson, D. Hedendahl, *Phys. Rev. A* **73** (2006) 062502.
[5] K.A. Brueckner, *Phys. Rev.* **97** (1955) 1353.
[6] K.A. Brueckner, *Phys. Rev.* **100** (1955) 36.
[7] H. Bethe, *Phys. Rev.* **103** (1956) 1353.
[8] J. Goldstone, *Proc. Roy. Soc. A* **239** (1957) 267.
[9] A. De-Shalit, I. Talmi, *Nuclear Shell Theory*, Academic Press, New York, 1963.
[10] H.P. Kelly, *Phys. Rev.* **131** (1963) 684.
[11] H.P. Kelly, *Phys. Rev.* **136** (1964) 896.
[12] I. Lindgren, *Phys. Scr. T* **34** (1991) 36.
[13] W.R. Johnson, *Atomic Physics: A Numerical Approach*, Lecture notes, 1994, unpublished.
[14] E. Avgoustoglou, W.R. Johnson, D.R. Plante, J. Sapirstein, S. Sheinerman, S.A. Blundell, *Phys. Rev. A* **46** (1992) 5478.
[15] A. Derevianko, E.D. Emmons, *Phys. Rev. A* **66** (2002) 012503.
[16] F. Coester, H. Kümmel, *Nucl. Phys.* **17** (1960) 477.
[17] I. Lindgren, *Phys. Scr.* **32** (1985) 291.
[18] W.F. Perger, M. Xia, K. Flurchick, M.I. Bhatti, *Comput. Sci. Eng.* **3** (2001) 38.
[19] T. Kato, *Prog. Theor. Phys.* **4** (1949) 514;
T. Kato, *Prog. Theor. Phys.* **5** (1950) 95.
[20] C. Bloch, *Nucl. Phys.* **6** (1958) 329.
[21] I. Lindgren, D. Mukherjee, *Phys. Rep.* **151** (1987) 93.
[22] S.A. Blundell, W.R. Johnson, J. Sapirstein, *Phys. Rev. A* **40** (1989) 2233.
[23] S.A. Blundell, W.R. Johnson, Z.W. Liu, J. Sapirstein, *Phys. Rev. A* **39** (1989) 3768.
[24] J. Sapirstein, *Rev. Mod. Phys.* **70** (1998) 55.
[25] T.T.S. Kuo, S.Y. Lee, K.F. Ratcliff, *Nucl. Phys. A* **176** (1971) 65.
[26] C. Møller, *K. Dan. Vid. Selsk.* **22** (1945) 1.
[27] C. Møller, *K. Dan. Vid. Selsk.* **23** (1946) 19.
[28] P. Jørgensen, *Am. Rev. Phys. Chem.* **26** (1975) 359.
[29] J. Hubbard, *Proc. R. Soc. A* **240** (1957) 539.
[30] I. Lindgren, *Int. J. Quant. Chem. S* **12** (1978) 33.
[31] A. Banerjee, J. Simons, *J. Chem. Phys.* **76** (1982) 4548.
[32] S. Salomonson, P. Öster, *Phys. Rev. A* **40** (1989) 5548;
S. Salomonson, P. Öster, *Phys. Rev. A* **40** (1989) 5559.
[33] S. Salomonson, P. Öster, *Phys. Rev. A* **41** (1990) 4670.
[34] E. Eliav, U. Kaldor, Y. Ishikawa, *Phys. Rev. A* **49** (1994) 1724.
[35] G. Gaigalas, S. Fritzsche, *Comput. Phys. Commun.* **149** (2002) 39;
G. Gaigalas, O. Scharf, S. Fritzsche, *Comput. Phys. Commun.* **166** (2005) 141.
[36] A. Surzhykov, P. Koval, S. Fritzsche, *Comput. Phys. Commun.* **165** (2005) 139.
[37] N.M. Hugenholtz, *Physica* **23** (1957) 481.
[38] B.H. Brandow, *Rev. Mod. Phys.* **39** (1967) 771.
[39] P.G.H. Sandars, *Adv. Chem. Phys.* **14** (1969) 365.
[40] F.E. Harris, H.J. Monkhorst, D.L. Freeman, *Algebraic and Diagrammatic Methods in Many-Fermion Theory*, Oxford Univ. Press, New York, 1992.
[41] D.A. Varshalovich, A.N. Moskalev, V.K. Khersonskii, *Quantum Theory of Angular Momentum*, World Scientific, Singapore, 1988.
[42] E. El-Baz, B. Castel, *Graphical Methods of Spin Algebras in Atomic, Nuclear, and Particle Physics*, Marcel Dekker, New York, 1972.
[43] I. Lindgren, *Phys. Scr.* **36** (1987) 591.
[44] T.T.S. Kuo, E. Osnes, Folded-Diagram Theory of the Effective Interaction in Nuclei, Atoms and Molecules, *Lecture Notes in Physics*, vol. 364, Springer, Heidelberg, 1990.

[45] E.P. Wigner, *Group Theory and its Application to the Quantum Mechanics of Atomic Spectra*, Academic Press, New York, 1959.
[46] S. Fritzsche, *Phys. Scr. T* **100** (2002) 37.
[47] G. Gaigalas, S. Fritzsche, E. Gaidamauskas, G. Kirsanskas, T. Zalandauskas, *Comput. Phys. Commun.* **175** (2006) 52.
[48] G. Racah, *Phys. Rev.* **61** (1941) 186;
G. Racah, *Phys. Rev.* **62** (1942) 438;
G. Racah, *Phys. Rev.* **76** (1949) 1352.
[49] D.M. Brink, G.R. Satchler, *Angular Momentum*, second ed., Oxford Univ. Press, Oxford, 1968.
[50] W.R. Johnson, in: D. Liesen (Ed.), *Physics with Multiply Charged Ions*, in: *NATO ASI Ser.*, vol. 348, Plenum Press, New York, 1995, p. 1.
[51] S. Fritzsche, *Comput. Phys. Commun.* **103** (1997) 51.
[52] S. Fritzsche, S. Varga, D. Geschke, B. Fricke, *Comput. Phys. Commun.* **111** (1998) 167.
[53] S. Fritzsche, T. Inghoff, T. Bastug, M. Tomaselli, *Comput. Phys. Commun.* **139** (2001) 314.
[54] O. Scharf, G. Gaigalas, S. Fritzsche, M. Gedvilas, E. Gaidamauskas, G. Kiršanskas, *Nucl. Instrum. Meth. B* **235** (2005) 135.
[55] J. Pagaran, S. Fritzsche, G. Gaigalas, *Comput. Phys. Commun.* **174** (2006) 616.
[56] S. Fritzsche, T. Inghoff, M. Tomaselli, *Comput. Phys. Commun.* **153** (2003) 422.
[57] S. Fritzsche, *J. Electron Spectrosc. Relat. Phenom.* **114–116** (2001) 1155.
[58] S. Fritzsche, A. Surzhykov, T. Stöhlker, *Phys. Rev. A* **72** (2005) 012704.
[59] S. Fritzsche, *Int. J. Quant. Chem.* **106** (2006) 98.
[60] K. Rykhlinskaya, S. Fritzsche, *Comput. Phys. Commun.* **171** (2005) 119;
K. Rykhlinskaya, S. Fritzsche, *Comput. Phys. Commun.* **174** (2006) 903.
[61] T. Radtke, S. Fritzsche, *Comput. Phys. Commun.* **173** (2005) 91;
T. Radtke, S. Fritzsche, *Comput. Phys. Commun.* **175** (2006) 145.
[62] W.R. Johnson, S.A. Blundell, J. Sapirstein, *Phys. Rev. A* **37** (1988) 2764;
W.R. Johnson, S.A. Blundell, J. Sapirstein, *Phys. Rev. A* **38** (1988) 2699.
[63] C.C. Cannon, A. Derevianko, *Phys. Rev. A* **69** (2004) 030502.
[64] E. Lindroth, A. Ynnerman, *Phys. Rev. A* **47** (1993) 961.
[65] A.M. Mårtensson-Pendrill, L. Pendrill, S. Salomonson, A. Ynnerman, H. Warston, *J. Phys. B* **23** (1990) 1749.
[66] A.C. Hartley, A.M. Mårtensson-Pendrill, *J. Phys. B* **24** (1991) 1193.
[67] C. Sur, K.V.P. Latha, B.K. Sahoo, R.K. Chaudhuri, B.P. Das, D. Mukherjee, *Phys. Rev. Lett.* **96** (2006) 193001.
[68] H.S. Chou, W.R. Johnson, *Phys. Rev. A* **56** (1997) 2424.
[69] S.A. Blundell, W.R. Johnson, J. Sapirstein, *Phys. Rev. A* **43** (1991) 3407.
[70] V.A. Dzuba, V.V. Flaumbaum, P.G. Silvestrov, O.P. Shuskov, *Phys. Lett. A* **141** (1989) 147.
[71] S. Salomonson, S.L. Carter, H.P. Kelly, *J. Phys. B* **18** (1985) L149;
S. Salomonson, S.L. Carter, H.P. Kelly, *Phys. Rev. A* **39** (1989) 5111.
[72] S.A. Blundell, D.S. Guo, W.R. Johnson, J. Sapirstein, *At. Data Nucl. Data Tables* **37** (1987) 103.
[73] A. Surzhykov, S. Fritzsche, A. Gumberidze, T. Stöhlker, *Phys. Rev. Lett.* **88** (2002) 153001.
[74] S. Fritzsche, P. Indelicato, T. Stöhlker, *J. Phys. B* **38** (2005) S707.
[75] E. Eliav, U. Kaldor, Y. Ishikawa, *Phys. Rev. Lett.* **74** (1995) 1079.
[76] M. Sewtz, H. Backe, A. Dretzke, G. Kube, W. Lauth, P. Schwamb, K. Eberhardt, C. Grüning, P. Thörle, N. Trautmann, P. Kunz, J. Lassen, G. Passler, C.Z. Dong, S. Fritzsche, R.G. Haire, *Phys. Rev. Lett.* **90** (2003) 163002.
[77] S. Fritzsche, *Eur. Phys. J. D* **33** (2005) 15.
[78] I. Lindgren, S. Salomonson, D. Hedendahl, *Can. J. Phys.* **83** (2005) 183.

CHAPTER 11

# Experiments on Highly Charged Heavy Ions in Conjunction with Exotic Atoms

**P. Indelicato[1a], M. Trassinelli[a,h], D.F. Anagnostopoulos[c], S. Boucard[a], D.S. Covita[b], G. Borchert[d], A. Dax[g], J.P. Egger[e], D. Gotta[d], A. Gruber[f], A. Hirtl[f], M. Hennebach[d], H. Fuhrmann[f], E.-O. Le Bigot[a], Y.-W. Liu[g], B. Manil[a,i], N. Nelms[j], S. Schlesser[a], J.M.F. dos Santos[b], L.M. Simons[g], L. Stingelin[g], J. Veloso[b], A. Wasser[g], A. Wells[j]** and **J. Zmeskal[f]**

Contents



[a] Laboratoire Kastler Brossel, École Normale Supérieure, CNRS, Université Pierre et Marie Curie-Paris 6, Case 74, 4 place Jussieu, F-75252 Paris, Cedex 05, France
[b] Department of Physics, Coimbra University, P-3000 Coimbra, Portugal
[c] Department of Material Science and Engineering, University of Ioannina, Ioannina, GR-45110, Greece
[d] Institut für Kernphysik, Forschungszentrum Jülich, D-52425 Jülich, Germany
[e] Institut de Physique de l' Université de Neuchâtel, CH-2000 Neuchâtel, Switzerland
[f] Stefan Meyer Institut für subatomare Physik, Austrian Acad. of Sci., A-1090 Vienna, Austria
[g] Paul Scherrer Institut, Villigen PSI, CH5232 Villigen, Switzerland
[h] GSI, Plankstr. 1, D-64291, Darmstadt, Germany
[i] CIRIL, GANIL, BP 5133, 14070 Caen Cedex 5, France
[j] Department of Physics and Astronomy, University of Leicester, Leicester LEI7RH, England, UK
[1] Corresponding author. E-mail: paul.indelicato@lkb.ens.fr

Advances in Quantum Chemistry, Vol. 53
ISSN 0065-3276, DOI:10.1016/S0065-3276(07)53011-X

Abstract We demonstrate how combining highly-charged ions and exotic atoms measurements can provide high-accuracy information on particle properties, like the pion mass, on interactions, like the pion-proton strong interaction at low energy, and bound-state QED in strong fields. The use of highly-charged ion X-rays emitted by the plasma inside a super-conducting ion source provides a very detailed characterization of the response function of the X-ray spectrometer used to study exotic atoms, allowing for very accurate measurements. Conversely the use of the same high-resolution and high transmission spectrometer provides very accurate measurements of X-ray lines of few-electron ions.

## 1. INTRODUCTION

Exotic atoms are atoms in which electrons are replaced by negatively-charged "stable" particles (i.e., particles that live long enough to form a bound state with a nucleus). These systems have been used for a long time to derive the mass of the particle with greater accuracy that what is possible with conventional magnetic mass spectrometers. Because the particles have necessarily a mass much larger than the electron mass, the transition energies are very often in the X-ray domain. The Bohr radius of the orbitals is also much smaller than in normal atoms, leading to a higher probability of presence of the particle inside the atomic nucleus. This fact can be used either to measure the nuclear charge distribution properties if the particle is a lepton (the muon, see, e.g. [1]), or properties of the strong interaction at very low energy if the particle is sensitive to it. A few years ago, a new experimental program was started to measure X-rays from light exotic atoms, in the energy range from 1.6 to 10 keV. This program aimed at doing accurate measurement of transition energies for exotic atoms as free as possible from environmental perturbations. A specific device, the cyclotron trap I, was developed to decelerate the particles and allow to stop them in a low pressure gas [2]. This device uses a pair of super-conducting coils to guide exotic particles to a gaseous target, while they interact with energy degraders.

Because of the limited intensity of available particle beams, a high-efficiency X-ray spectrometer was needed to observe the X-rays emitted by the exotic atoms. A new instrument based on large area spherically-bent crystals and specialized X-ray Charge Coupled Devices (CCD) [3], was build. When studying exotic atoms composed of mesons or baryons, the interest is not only in the line energy shifts, caused by the strong interaction, but also in the line broadening. The particle can be captured by the nucleus, leading to a finite lifetime of the lower atomic state. In order to measure accurately this broadening, that can be related to low-energy capture cross sections, it was also necessary to have a high-resolution instrument. This lead to the development of specific techniques to obtain spherically-bent crystals with resolution close to the theoretical limit. This is also useful to resolve lines that could correspond to an atom containing both the particle and electrons, either by recapture from the target gas, or from the cascade preceding the formation of the initial state of the observed transition. The presence of such an electron can

cause an apparent energy shift, or an extra broadening that could cause errors in the interpretation of the results.

A first version of the experimental set-up was successfully used at CERN on LEAR (Low Energy Antiproton Ring), to study 3d $\rightarrow$ 2p transitions in antiprotonic hydrogen and deuterium [4], to obtain information on the antiproton–nucleon interaction. It was also used to measure the mass of the charged pion for the first time in a low density gas, using transitions between circular levels of pionic nitrogen [5], using copper K$\alpha$ transitions as X-ray standards.

An instrument as the one described above has a complex response function, very narrow but slightly asymmetric. To obtain high-accuracy measurements of the energy and intrinsic linewidth of a transition, it is necessary to characterize in detail this response function with narrow reference lines. The resolution of the instrument is typically between 0.28 and 0.4 eV, while X-rays from inner-shell transitions of atom in solid targets (as produced by X-ray tubes or fluorescence targets) provides lines with natural widths larger than 1.5 eV.

In order to measure the pion mass with improved accuracy and to improve our knowledge of the pionic hydrogen strong interaction shift and broadening, an improved experimental set-up was designed. The aim was to obtain a precision below 2 ppm for the charged pion mass, and to improve by an order of magnitude the strong interaction shift and broadening, compared to previous experiments [6]. A new CCD detector, with a larger active area and improved resolution was build [7]. A new cyclotron trap, the cyclotron trap II was designed to enable efficient capture of muons from the pion decays. This allowed to use lines of muonic oxygen as X-ray standards, effectively measuring the pion to muon mass ratio. More examples on the use of exotic atom as X-ray standards can be found in [8]. However such standards, because of the low X-ray intensity provided, cannot be used conveniently to perform the full characterization of the response function. It was then noticed that the magnetic configuration of the cyclotron trap II, with adaptation of the polar pieces, could provided a magnetic bottle with a high mirror ratio, that could be used to build an electron cyclotron resonance ion trap (ECRIT), whose plasma could provide intense X-ray beams from highly ionized ions, as observed in Ref. [9]. The transformation of the cyclotron trap into an ECRIT was realized [10] and X-ray from few-electron ions were produced. It was found that intense spectra of the 1s2s $^3S_1 \rightarrow 1s^2\ ^1S_0$ relativistic M1 transition in helium-like sulfur, chlorine and argon could be produced [11,12], with energy close to the one of the $n$p $\rightarrow$ 1s, $n = 2, 3, 4$, transitions in pionic hydrogen, that were to be studied to obtain the strong shift and broadening of the $n = 1$ state. These lines have been used to fully characterize the instrument [13].

A detailed account of the series of experiments performed with the initial version of the setup presented here, and of previous work can be found in [14].

The paper is organized as follows. In Section 2, we describe in more detail the spectrometer and its characterization. In Section 3, we describe the present status of the pion mass measurement and the test of the Klein–Gordon equation. In Section 4, we describe the present status of the pionic hydrogen experiment. In Section 5 we present preliminary results on transition energies in highly-charged ions, and Section 6 is our conclusion.

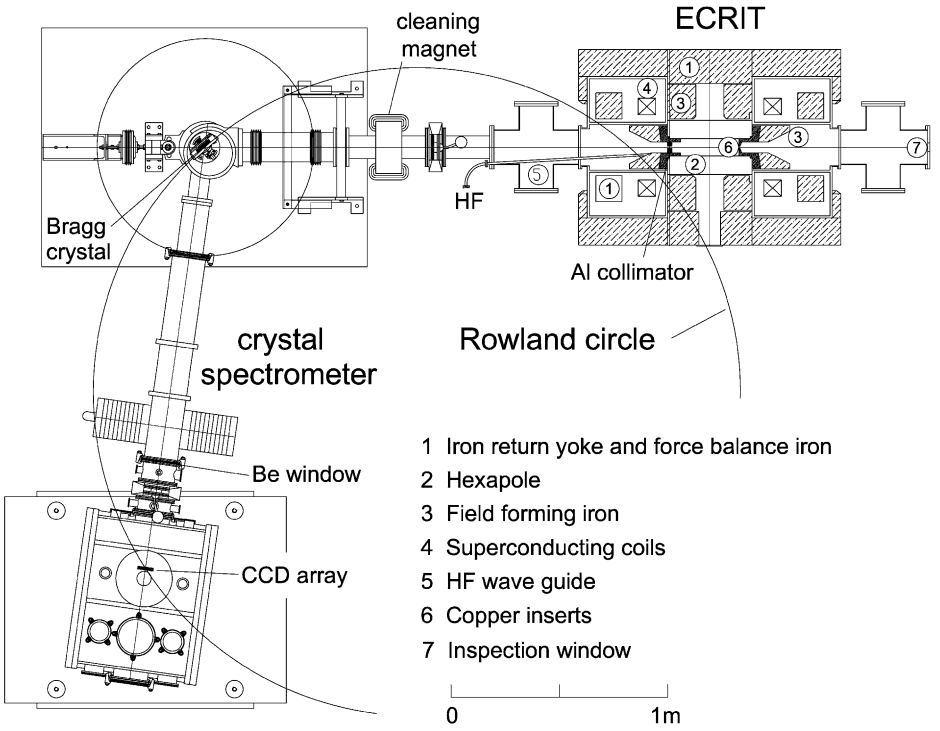


**FIGURE 11.1** Set up of the PSI ECRIT together with the Bragg crystal spectrometer.

## 2. EXPERIMENTAL METHOD

### 2.1 Experimental setup

The experimental setup is presented in Figure 11.1, in the case of the study of highly charged ions produced by the ECRIT [10,13]. The experimental setup is very similar in the case of exotic atoms. In that case the ECRIT hexapole is removed and replaced by a target composed of a metallic frame covered with a thin glued kapton foil. The target is gas-tight and tested to support up to 1.5 bars. The target is connected to a dry vacuum pump and to a gas distribution system. In the case of the pionic hydrogen experiment, they are equipped with a cold finger, connected to a two-stage cryo-cooling device that can cool the gas down to liquid hydrogen temperatures. Plastic degrader foils are positioned to decelerate the particle beam. One of the degrader is a plastic scintillator, connected to a photomultiplier tube, to monitor the incoming particle beam intensity. Fluorescence targets can be introduced in front of the gas target to provide beam-time calibration and stability checks. The inside of the cyclotron trap II, with its kapton entrance window, the degraders and the target in position is shown on Figure 11.2.

The spectrometer is composed of a crystal chamber, a CCD detector, and connecting vacuum pipes. The crystal can be rotated with high-precision, using a sine

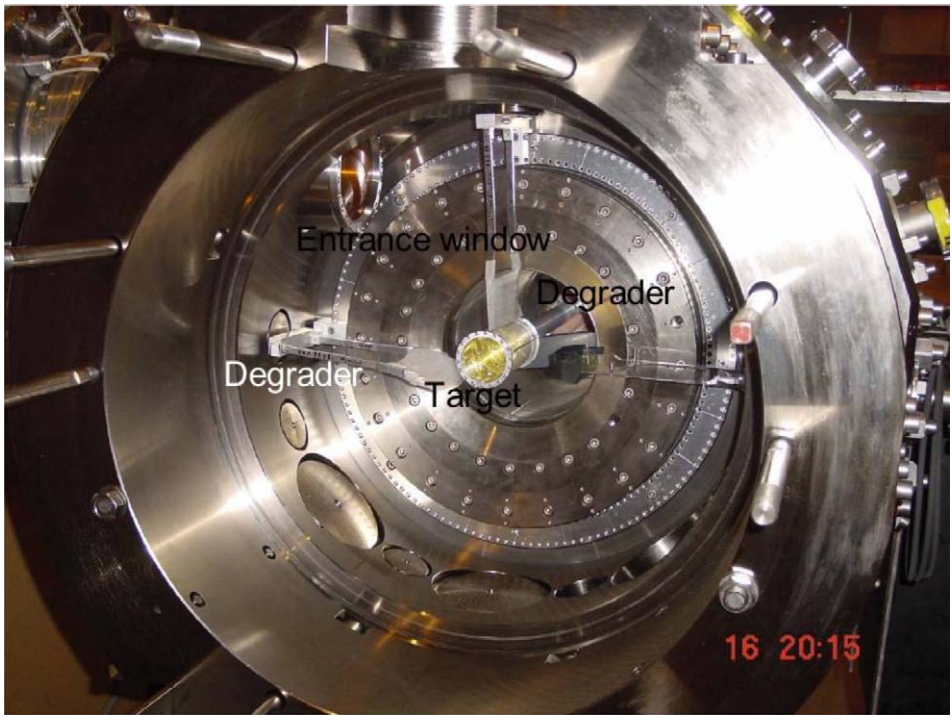


**FIGURE 11.2** Inside view of the anticyclotron trap II, with the degraders and target in position. One of the degrader (horizontal, right) is a plastic scintillator used to monitor particle beam intensity.

arm and a piezoelectric actuator. The angles can be measured with 0.5″ accuracy with an Heidenhain encoder. The spectrometer operates under vacuum (typically $10^{-6}$ mbar) to minimize X-ray absorption and enable to connect the CCD detector to the spectrometer with a very thin window. The CCD detector has been designed so that both the pionic nitrogen and muonic oxygen $5g \rightarrow 4f$ transitions can be observed simultaneously, when performing the pionic mass measurement [15]. The height of the detector has been chosen to optimize counting rate by covering most of the X-rays line as reflected by the spherical crystal. The detector is described in detail in Ref. [7]. In order to achieve the desired accuracy, it was necessary to measure accurately both the relative position of each CCD chip in the detector and the pixel to pixel distance, at the operating CCD temperature (−100 °C). An optical cross grating has been designed and manufactured by the Laboratory of Micro- and Nanotechnology of the Paul Scherrer Institut (PSI), which could project a well defined image on the CCD, when lighted by a far-away white light source. This image was recorded and used to obtain both the relative positions and the interpixel distance from the detector. This distance has been measured to be $39.9775 \pm 0.0006$ µm (a 15 ppm accuracy) [16].

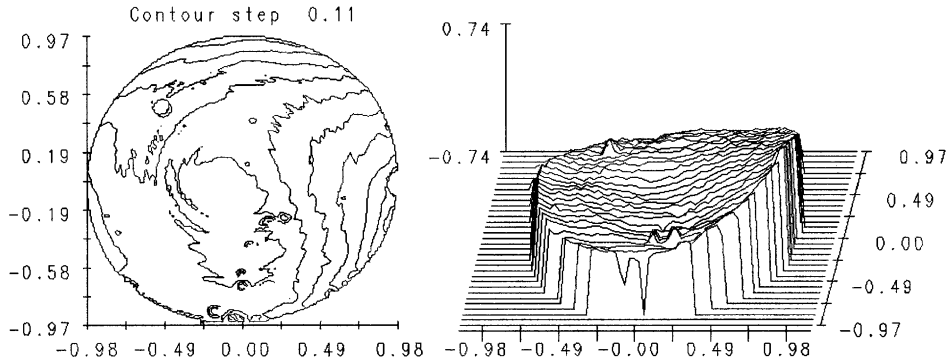


**FIGURE 11.3** Surface mapping of a 2.9 m spherically bent (100) quartz crystal with a two-wave interferometer, with respect to a 2 m reference lens. Deviation from a perfect sphere are smaller than 1.5 laser wavelength (640 nm).

## 2.2 Manufacturing and checking of the crystals

To achieve the characteristics required by the planned experiments, it was necessary to develop completely new techniques to manufacture the crystals. The work started in the early 90's. In order to achieve high-efficiency, it was chosen to use spherically-bent crystals of large area (10 cm in diameter), in the Johann geometry [17], in order to have a good refocusing of the X-rays in the direction perpendicular to the dispersion plane. The most difficult in manufacturing such crystals, is to preserve the quality of the diffracting planes. Obtaining a good, uniform bending requires using thin (≈200–300 μm) crystals. In such a case cutting and polishing the crystal is very delicate, and usually causes severe damages. In order to avoid such problems, a method was developed in which a thick slab of crystal (Si or quartz) was optically polished in one side and attached to a reference flat by optical contacting (i.e, using molecular adhesion forces between two very smooth surfaces). The slab was then cut, etched and polished to the desired thickness. It was then removed from the flat and attached to a spherical quartz lens of high quality (polished to $\lambda/50$) in a clean room. The lenses have a radius of curvature of ≈3 m. Using a relatively large radius is necessary to minimize crystal mosaicity. Since the lenses are transparent, the back of the crystals can be inspected, bad contact to the lens being revealed by Newton interference rings. The crystals where then checked optically by the mean of a two-wave interferometer manufactured by Zygo® and compared to a 2 m reference lens. The interference pattern for a quartz crystal is displayed on Figure 11.3, showing that the total amplitude of the deviation from a perfect sphere are below 1.5 He–Ne laser wavelength (604 nm) peak-to-valley. Silicon crystals displayed a more pronounced deviation, in a "Mexican hat" shape, as can be seen in Figure 11.4 for the crystal used for measuring the pion mass, and the peak-to-valley amplitude is around $3.5 \times \lambda_{\text{He–Ne}}$, with a RMS value of $0.55 \times \lambda_{\text{He–Ne}}$. The penetration length in the crystal, along the X-ray path, is around 9.3 μm at 4 keV for the $\pi$ polarization (peak reflectivity 60%) and 2.5 μm for the $\sigma$ polarisation (99% peak reflectivity) [18]. Such deviations, assum-

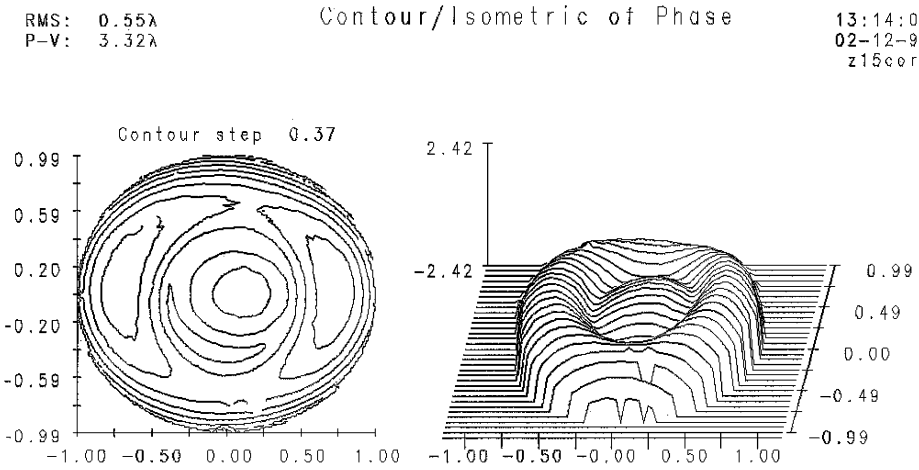


**FIGURE 11.4** Surface mapping of the 2.9 m spherically bent (220) Si crystal that was used for the measurement of the pion mass, with a two-wave interferometer, with respect to a 2 m reference lens. Deviation from a perfect sphere are smaller than 3.5 laser wavelength (640 nm).

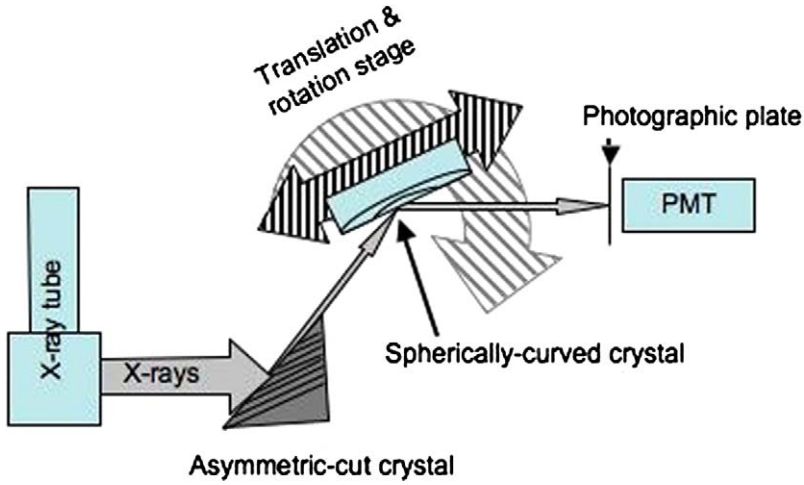


**FIGURE 11.5** Setup to measure the bending uniformity of the spherically-curved crystal with X-rays. The reflecting planes inside the asymmetric-cut crystal are represented.

ing they represent real deformations of the X-ray planes, should play a small role in average, since the X-ray line is reflected by a sizable portion of the crystal.

The crystals were also analyzed using a parallel beam provided by a X-ray tube with a copper anode, and diffracted by an asymmetric-cut triangular-shaped crystal (Figure 11.5). The crystal was cut so that the reflecting planes form an angle slightly below the Bragg angle for the K lines of Cu with the surface. The X-ray tube was used with a wide (1 cm) focus. X-rays impinging on the crystal at roughly

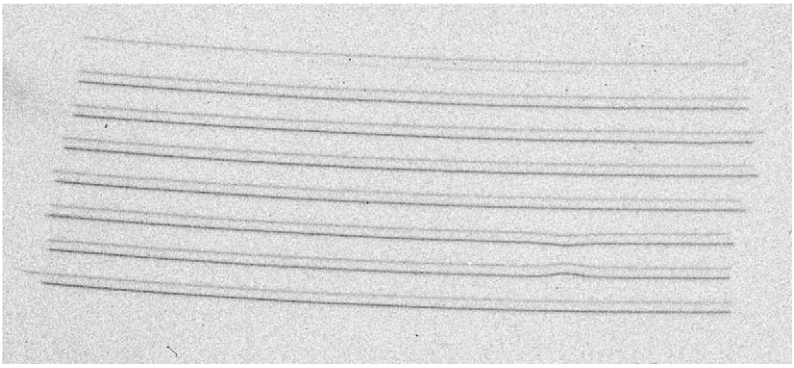

**FIGURE 11.6** Typical X-ray map of the spherically-bent Si (220) crystal obtained with the K$\alpha$ doublet of Cu and an asymmetric cut crystal to provide a highly parallel X-ray beam.

twice the Bragg angle, thus exit at a quasi grazing incidence, forming a narrow beam of very low divergence. The crystal to be tested is then placed on precision rotation and translation stages, parallel to the reticular planes in the crystal to form a two-crystal spectrometer in non-dispersive mode. The crystal is then translated in a succession of steps of equal length to scan its surface. The stage is rotated until a maximum of intensity is found with an X-ray detector, insuring that the Bragg condition is met for the area of the crystal under investigation. A photographic plate is positioned in front of the X-ray detector to record the reflected X-rays. A perfect bend crystal would lead to a series of parallel lines (actually pairs of lines, since both K$\alpha_1$ and K$\alpha_2$ are observed). An example of recorded pattern is shown on Figure 11.6.

One can observe in the lower right corner the effect of a local defect, appearing as a distortion of one of the lines. Most of the recorded pictures did not show any deviation, showing the high quality and uniformity of the X-ray diffracting planes. Only pictures recorded close to the edge of the crystals were found to have sizeable defects. The edges were thus masked during all data taking.

## 2.3 Data analysis

To achieve the desired accuracy in X-ray energies, from the spectra collected in the different experiments, one needs to know precisely the line shape produced by the spectrometer. This line shape can be used to fit the experimental spectra. An extra difficulty comes from the two-dimensional nature of the spectra. Theoretical line shapes are produced by the following procedure: crystal diffraction profiles at the studied line energy are obtained from the XOP code [18]; a complete Monte-Carlo simulation is then made, using this diffraction profile and all geometrical informations from the instrument. The CCD detector is positioned perpendicular to the optical axis of the spectrometer. There is thus only one place on the detector (the intersection of the optical axis and of the detector) located at the focal distance. Away from this point, lines are slightly defocused. Once obtained, the

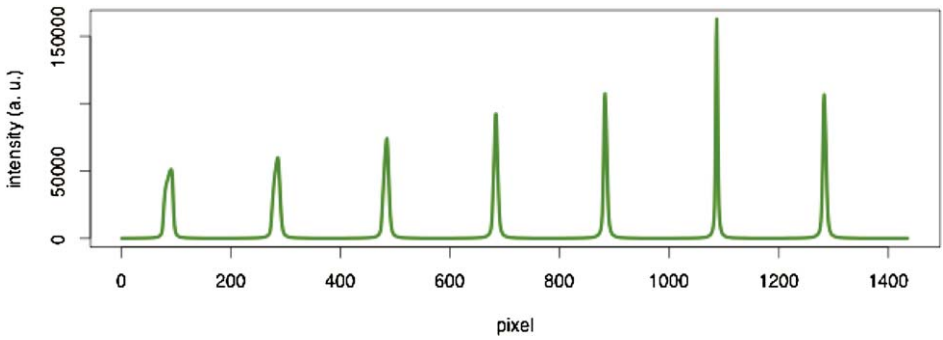


**FIGURE 11.7** Simulated line profiles along the horizontal axis; The change in shape of the line is due to the line going away from the focal position, which is here around pixel number 1100.

simulated two-dimensional profile is projected onto the horizontal axis, using exactly the same algorithm as for the experimental spectra. The line shape provided by the simulation changes along the horizontal axis of the detector as shown on Figure 11.7, due to the fact that it gets more and more out of focus. Each line in an experimental spectra is then fitted using the line shape corresponding to its actual position on the detector. To perform the fit to the experimental data, the line profiles resulting from the simulation are fitted with splines, convolved with a Gaussian, that represents extra broadening due to crystal imperfections and other unknown physical phenomena contributing to the final line shape. The line position and intensity, and the Gaussian width are the three parameters adjusted in the fitting procedure, using a Levenberg–Marquardt algorithm [19,20].

An example of fitted profile, for the relativistic M1 transition in heliumlike chlorine is presented on Figure 11.8. The line width is 0.4 eV for a transition energy of 2756.9 eV. The width of the Gaussian profile that is convolved with the simulated profile, to account for crystal imperfections, is found to be 0.09 eV.

## 3. MEASUREMENT OF THE PION MASS

The mass of the charged pion has a great importance for medium-energy particle physics and nuclear physics. In the last two decades, exotic atoms have provided the most precise measurements. A previous experiment performed in 1986 [21,22] has however led to difficulties. It was performed using pionic magnesium in a solid target and a crystal spectrometer, with near ppm precision. In such an experiment, the pion after capture, because of its large mass, will eject most of the electrons of the target atom, by Auger effect. However the recapture probability of the electron in the solid is large. A few years later, this mass was used for a measurement of the mass of the muonic neutrino, using the reaction $\pi^+ \rightarrow \mu^+ + \nu_\mu$, where $\pi^+$ represents a charged pion at rest, trapped on a surface, $\mu$ is a muon, and $\nu_\mu$ a muonic neutrino [23]. It was then found that the value obtained in 1986 lead to a negative value for the square of the neutrino mass. There was then a

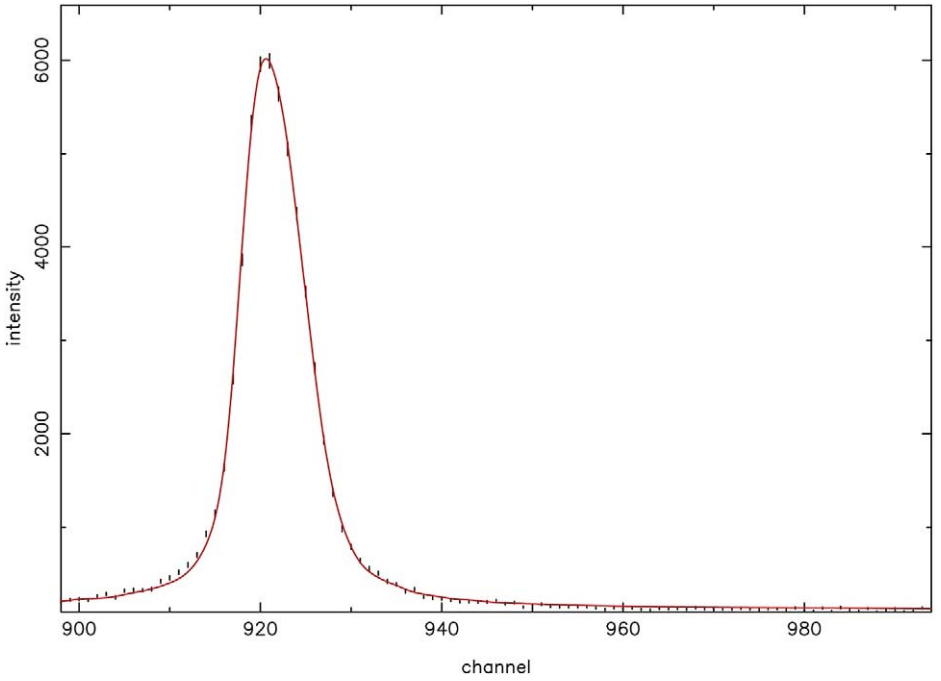


**FIGURE 11.8** Experimental spectrum of the relativistic M1 transition in He-like chlorine fitted with the profile described in the text. The line width (FWHM) is equal to 0.4 eV.

reanalysis of the 1986 experiment. It was found, using new cascade calculations, that the electron recapture in the solid was leading to a larger electron numbers in the (electronic) K-shell of pionic magnesium. Depending on the hypothesis in the cascade calculation, one would get one or two K-shell electrons, leading to two different values of the mass. Only the largest one was leading to a positive muonic neutrino squared mass [24]. A new, more accurate measurement of the muon recoil from pion disintegration, confirmed the result [25]. This first experiment using the cyclotron trap and a dilute gas target was performed at the Paul Scherrer Institut, which has the world most intense pion beam, generated by a 570 MeV, 1.3 mA proton beam, that has since been upgraded to 1.8 mA. The measurement was performed using Cu K X-rays as a reference. The 4 keV pionic transition was reflected using the (220) plane of a Si crystal, while the Cu 8 keV X-rays were reflected by the (440) plane. This led to a value with an accuracy roughly twice as large as in the Mg experiment but without any ambiguity from electron screening and in agreement with the high value of Ref. [24]. Knowing accurately the value of the pion mass is essential for other important experiment, like the measurement of strong interaction shift in pionic atoms, as will be described in Section 4, or for setting limits to the muonic neutrino mass (even though the interest of such limits has since diminished due to the observation of neutrino oscillations [26] and of the cosmological radiation background, which sets much tighter bounds on the muonic neutrino mass). Besides, the use of a Cu X-ray standard, was limiting the

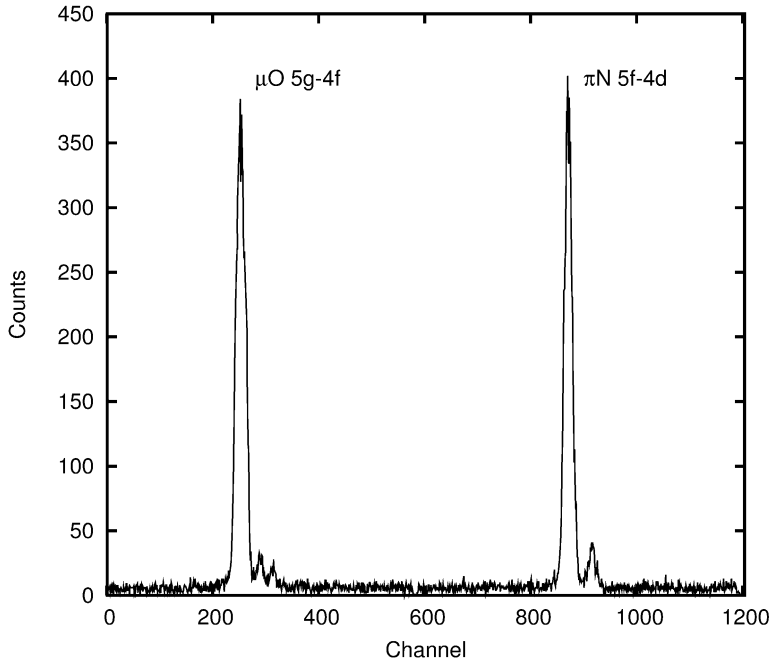


**FIGURE 11.9** Spectrum of the 5 → 4 transitions in pionic nitrogen and muonic oxygen.

precision by leading to irreducible systematic effects. It was then proposed to use a muonic line from oxygen as a reference, effectively measuring the pion mass in term of the muon mass, which is known from muonium spectroscopy (see, e.g. [27] and references therein) to an accuracy of $8.9 \times 10^{-8}$. This standard energy can be evaluated with a uncertainty of ≈0.3 ppm.

A new experiment was thus done, using the improvement described in Sections 1 and 2 which lead to a statistical accuracy in the comparison between the pionic and muonic line, compatible with a final uncertainty below 2 ppm [7]. To reach such an accuracy, the CCD detector characterization described in [16] was required.

The characteristics of the 5 → 4 transitions for pionic nitrogen and muonic oxygen are quite different as shown in Figure 11.9. These differences are principally due to the spin of the orbiting particle, which determines the fine structures of the transition. The muonic oxygen 5g → 4f transition is split into three different lines due to the spin of the muon: $5g_{9/2} \rightarrow 4f_{7/2}$, $5g_{7/2} \rightarrow 4f_{7/2}$ and $5g_{7/2} \rightarrow 4f_{5/2}$, which have theoretical intensity ratios of 35:1:27 [28]. The presence of the naturally occurring oxygen isotope $^{18}$O (0.205%) makes a noticeable contribution from $\mu^{18}$O $5g_{9/2} \rightarrow 4f_{7/2}$ and $5g_{7/2} \rightarrow 4f_{5/2}$ transitions. No fine structure splitting due to the spin occurs in the case of pionic nitrogen. As for the muonic oxygen, the parallel transition 5f → 4d has to be taken into account as well as the contribution from the naturally occurring $^{15}$N (0.36%) 5g → 4f transition.

The fit of the pionic nitrogen transition has been performed while fixing the distance of the parallel transition using QED predictions. On the other hand, if we keep this distance free, we can measure the energy difference between the 5g $\rightarrow$ 4f and 5f $\rightarrow$ 4d pionic nitrogen transitions and we can compare it to the theoretical prediction to test Klein–Gordon equation validity. We obtain $E(5f \rightarrow 4d) - E(5g \rightarrow 4f) = (2.3002 \pm 0.0069^{+0.0119}_{-0.0000})$ eV. The first error comes from the fit results. The second error is systematic and it is due to the contribution from pionic nitrogen 5f $\rightarrow$ 4d with a spectator electron in the K-shell. Using the high statistics pionic nitrogen spectrum, we estimate this contribution to be lower than 0.16% for the 5g $\rightarrow$ 4f transition. However, the cascade model for non-circular transitions is completely different from the circular ones because in this case radiative transitions can be more probable than Auger transitions. We estimate that less than 2% of the pionic atoms emitting a 5f $\rightarrow$ 4d photon have a remaining electron in the K-shell.

Previous tests of the Klein–Gordon equation has been obtained from the observation of pionic titanium transitions [29] with an accuracy of 2%, and from the observation of pionic nitrogen transitions [5].

## 4. PIONIC HYDROGEN AND THE STRONG-INTERACTION AT LOW ENERGY

Quantum Chromodynamics is the theory of quarks and gluons, that describe the strong interaction at a fundamental level, in the Standard Model. It has been studied extensively at high-energy, in the asymptotic freedom regime, in which perturbation theory in the coupling constant can be used. At low energy the QCD coupling constant $\alpha_S$ is larger than one and perturbative expansion in $\alpha_S$ cannot be done. Weinberg proposed Chiral Perturbation Theory (ChPT) [30] to deal with this problem. More advanced calculations have been performed recently, that require adequate testing [31–33].

Pionic atom energies, however, are dominated by the electromagnetic interaction of its constituents. The effect of the strong interaction is only significant if the wave functions of the pion and the proton have a large overlap. In the ground state of the pionic hydrogen atom, the strong interaction induces a shift $\varepsilon_{1s} \approx 7$ eV and a broadening $\Gamma_{1s} \approx 1$ eV for an electromagnetic binding energy $E_{1s} = 3238$ eV. The measured quantities are connected to the hadronic scattering lengths $a^h$, which describe respectively the $\pi^- p \rightarrow \pi^- p$ and $\pi^- p \rightarrow \pi^0 n$ process, by Deser-type formulae [34,35]

$$\frac{\varepsilon_{1s}}{E_{1s}} = -\frac{4}{r_B} a^h_{\pi^- p \rightarrow \pi^- p}(1 + \delta_\varepsilon), \tag{1}$$

$$\frac{\Gamma_{1s}}{E_{1s}} = \frac{8\mathcal{Q}_0}{r_B}\left(1 + \frac{1}{\mathcal{P}}\right)\left(a^h_{\pi^- p \rightarrow \pi^0 n}(1 + \delta_\Gamma)\right)^2, \tag{2}$$

where $r_B$ is the Bohr radius of the pionic hydrogen atom ($r_B = 222.56$ fm), $\mathcal{Q}_0 = 0.142$ fm$^{-1}$ is a kinematic factor, $\mathcal{P} = (1.156 \pm 0.009)$ is the Panofsky ratio [36] and

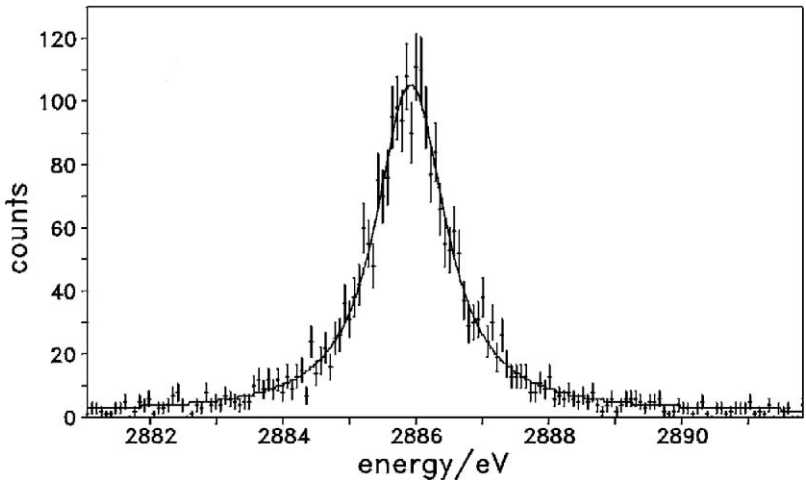


**FIGURE 11.10** Spectrum of the 3p → 1s transition in pionic hydrogen with a $H_2$ target at a pressure $P = 2$ bar and temperature $T = 20$ K (equivalent to a pressure of 28 bar at room temperature). The crystal used is a quartz $(10\bar{1})$.

$a^{\mathrm{h}}$ are the hadronic scattering lengths. The electromagnetic corrections $\delta_\varepsilon$ and $\delta_\Gamma$ have recently been calculated with a model potential with an accuracy of about 0.5% [37], and with the ChPT method [32,38].

The shift and the width of the ground state in pionic hydrogen and deuterium atoms have been determined in a recent series of experiments of the *ETHZ-Neuchâtel-PSI* collaboration by measuring the 3p → 1s transition at 2886 eV with a reflection-type crystal spectrometer [6,37]. The results improved the value for the strong interaction shift $\varepsilon_{1\mathrm{s}}$ by almost two orders of magnitude compared to earlier works. In addition, a first accurate measurement of the width $\Gamma_{1\mathrm{s}}$ was obtained. Yet, the error in the width is still almost an order of magnitude larger than the one in the shift and is strongly influenced by the poor knowledge the contributions of Doppler broadening due to the accelerations by inelastic collisions during the de-excitation of the pionic atoms [39]. This makes impossible any determinations of the isospin separated scattering lengths with a %-level relative accuracy. Since the acceleration mechanism which leads to the Doppler broadening is level-dependent, it is possible to achieve much higher accuracies, by combining measurements of several n$p$ → 1s transitions and several target pressures between 3 and 15 bar and in liquid hydrogen. The measurement of the width can be extracted from a simultaneous fit of all transitions, which lets the different Doppler broadenings vary freely, and using more advanced cascade models [40–43]. One still need however to know accurately the instrumental response function, and to exclude possible contributions from exotic hydrogen molecules radiative transitions. The instrumental response has been determined, as explained in Section 2. The high statistics that were obtained for all three n$p$ → 1s transitions, the very low background, and the detailed analysis, have lead to very consistent shifts and broadening. An example of spectrum is presented in Figure 11.10.

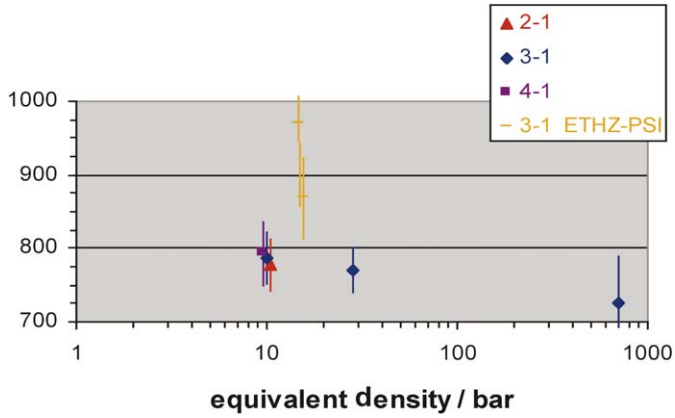


**FIGURE 11.11** The preliminary hadronic width (in meV) of the 1s state in pionic hydrogen from this work, compared to the results of Ref. [6].

The preliminary result are shown in Figure 11.11. One see that after correction for the instrumental response function and differential Doppler broadening on the different excited levels, all measurements lead to results in good agreement, that are slightly below the final results of the previous experiment [6], and much more accurate.

## 5. HIGHLY-CHARGED IONS

Contrary to the pionic nitrogen and muonic oxygen transitions, characterized by a Doppler broadening of several hundreds meV, multicharged ion transitions originating from the plasma inside an ECRIS have a typical width below 40 meV, almost 10 times smaller than the spectrometer resolution. This is due to the fact that in an ECRIS the ions are trapped in the space charge potential of the electrons that are themselves trapped by the magnetic structure of the source. The depth of this potential in only around 1 eV. For this reason, the line shape of ions X-ray line on the CCD array correspond mostly to the crystal spectrometer response function.

The Electron-Cyclotron-Resonance ion trap at the Paul Scherrer Institut was originally designed to characterize accurately the crystal spectrometer used for the study of pionic atoms. Between 2002 and summer 2005, we have obtained high-precision measurements of the X-ray spectra of argon, chlorine and sulfur, which are particularly interesting to investigate atomic physics in relatively strong Coulomb fields. These spectra have been acquired using setup with crystals of different type: silicon (111) and quartz (100) and (10$\bar{1}$). Each of them has a nominal radius of curvature of about 2985 mm. The injected microwave power was always around 200–400 W, and the total pressure in the vacuum chamber was in the range of 3 to 4 $\times$ $10^{-7}$ mbar. For any set of measurements, the ECR ion trap has been optimized on the intensity of the He-like ions 1s2s $^3S_1 \rightarrow 1s^2\ ^1S_0$ M1 transition. Each time a new crystal was inserted in the spectrometer, a focal scan was performed

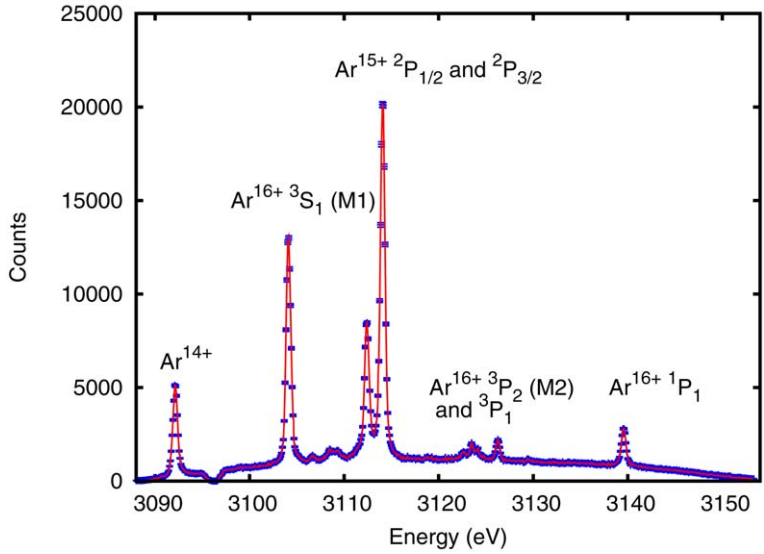


**FIGURE 11.12** He-like and Li-like argon spectrum using quartz $(10\bar{1})$ crystal. HF power injected $P = 400$ W. Argon partial pressure $p_{Ar} = 5 \times 10^{-9}$ mbar, total pressure $p_{tot} = 5 \times 10^{-7}$ mbar. This spectrum has been obtained with an integration time of 2 h. The focal position of this spectrum was in correspondence to the 1s2p $^3P_n \rightarrow 1s^2\ ^1S_0$ peak, near channel 310.

to determine precisely the position of the focal plane. The typical data acquisition time for the He-like and Li-like ions spectra was in the order of 15 min. For less intense transitions, like the He-like 1s2p $^1P_1 \rightarrow 1s^2\ ^1S_0$ and 1s2p $^3P_n \rightarrow 1s^2\ ^1S_0$ transitions, we acquired data for a period up to a maximum of 2 h. In Figures 11.12 and 11.13 we show atomic spectra near the region of the 1s2p P $\rightarrow 1s^2\ ^1S_0$ He-like argon transitions.

The transitions 1s2p P $\rightarrow 1s^2\ ^1S_0$ are principally produced by the excitation of He-like ions in the ground state due to collision with an electron: $1s^2 \rightarrow$ 1s2p. For this reason, the intensity ratio between the 1s2p $^{2S+1}P_1 \rightarrow 1s^2\ ^1S_0$ and 1s2s $^3S_1 \rightarrow 1s^2\ ^1S_0$ transitions is roughly proportional to the ratio between the number of He-like ions ($1s^2$) and the Li-like ions ($1s^2$2s) in the plasma and to the ratio between the electronic excitation cross-section, integrated over the electronic density, and the 1s ionization cross-section [9,44]. Similar selective excitation has been observed in the ESR storage ring for lithium-like uranium [45].

A single crystal spectrometer can only measure energy differences between atomic transitions. A reference is thus needed. Due to the lack of high quality reference lines in neutral atom X-ray spectra (see, e.g. [8]) we used as a reference the He-like 1s2s $^3S_1 \rightarrow 1s^2\ ^1S_0$ M1 transition. All the transition energy provided in the present work are relative to the M1 theoretical transition energy. The peaks in the spectra were fitted according to the procedure described in Section 2. The results obtained in highly-charged argon, chlorine and sulfur spectroscopy have an excellent precision, of the order of 10 meV and they agree with the previous

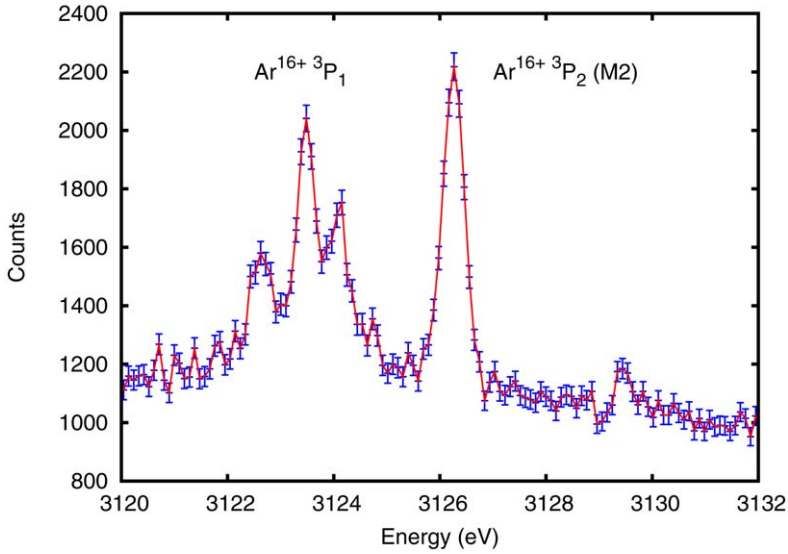


**FIGURE 11.13** Detail of the spectrum in Figure 11.12 around the $1s2p\ ^3P_n \rightarrow 1s^2\ ^1S_0$ transitions. The two lines next to the $^3P_1$ peak are due to Li-like transitions with a spectator electron in $n = 3$–5 shells (satellite lines).

**TABLE 11.1** Example of experimental determination of He-like argon transition energies in eV [11]

| Transition | $1s2p\ ^1P_1 \rightarrow 1s^2\ ^1S_0$ | $1s2p\ ^1P_1 \rightarrow 1s2s\ ^3S_1$ |
|---|---|---|
| Costa [46] (th.) | 3139.57 | 16.05 |
| Plante [47] (th.) | 3139.6236 | 16.0484 |
| Lindgren [48] (th.) | | 16.048 |
| Artemyev [49] (th.) | 3139.5821(5) | 16.0477(2) |
| Deslattes [50] (exp.) | 3139.553(36) | 16.031(72) |
| This work (preliminary results) | 3139.511(23) | 16.028(14) |

experimental values and theoretical predictions. The preliminary results for argon are presented in Table 11.1.

## 6. CONCLUSION

In this work, we have presented the present status of the pion mass measurement from light exotic atoms, and as well as preliminary results for the pionic hydrogen strong interaction shift and width measurement. We have shown that such high accuracy measurements can only be performed in conjunction with highly-charged ion measurements, that provide the necessary spectrometer characterization. As

an outstanding byproduct, we are also able to do high precision measurements of transition energy in highly charged heavy ions, providing new tests of relativistic many-body theory and QED, for medium-Z elements. A two-crystal spectrometer is being build, that will allow to do absolute measurements of the M1 transitions in He-like ions, with ppm accuracy, that should enable to have excellent tests of the relativistic many-body problems and QED effects in few-electron ions.

## ACKNOWLEDGEMENTS

The X-ray mapping of the crystals were performed with the instruments of the Quantum Metrology division at NIST. We wish to thank the late R.D. Deslattes and A. Henins for providing us access to their equipment and setting up the experiment. The suggestions and the help of D. Hitz and K. Stiebing in the preparatory phase of the experiment are warmly acknowledged. We also thank H. Reist for offering the 6.4 GHz emitter for free. Special thanks go to the Carl Zeiss Company in Oberkochen, Germany, which manufactured the Bragg crystals. We thank F. Nez for his assistance in performing the interferometric tests of the crystals, and L. Jacubowiez and T. Avignon for giving us access to the Zygo interferometer at the Institut d'Optique. Laboratoire Kastler Brossel is Unité Mixte de Recherche du CNRS n° 8552.

## REFERENCES

[1] I. Angeli, A consistent set of nuclear rms charge radii: properties of the radius surface R(N,Z), *At. Data Nucl. Data Tables* **87** (2) (2004) 185–206.
[2] L. Simons, The cyclotron trap for antiprotons, *Hyperfine Interact.* **81** (1993) 253–262.
[3] G. Fiorucci, J.-P. Bourquin, D. Bovet, E. Bovet, J.P. Egger, C. Heche, V. Nussbaum, D. Schenker, D. Varidel, J.-M. Vuillemier, CCDs as low-energy X-ray detectors, *Nucl. Instrum. Methods* **292** (1990) 141–146.
[4] D. Gotta, D.F. Anagnostopoulos, M. Augsburger, G. Borchert, C. Castelli, D. Chatellard, J.P. Egger, P. El-Khoury, H. Gorke, P. Hauser, P. Indelicato, K. Kirch, S. Lenz, T. Siems, L.M. Simons, Balmer $\alpha$ transitions in antiprotonic hydrogen and deuterium, *Nucl. Phys. A* **660** (1999) 283–321.
[5] S. Lenz, G. Borchert, H. Gorke, D. Gotta, T. Siems, D. Anagnostopoulos, M. Augsburger, D. Chatellard, J. Egger, D. Belmiloud, P. El-Khoury, P. Indelicato, M. Daum, P. Hauser, K. Kirch, L. Simons, A new determination of the mass of the charged pion, *Phys. Lett. B* **416** (1998) 50–55.
[6] H.-C. Schröder, A. Badertscher, P.F.A. Goudsmit, M. Janousch, H.J. Leisi, E. Matsinos, D. Sigg, Z.G. Zhao, D. Chatellard, J.P. Egger, K. Gabathuler, P. Hauser, L.M. Simons, A.J. Rusi El Hassani, The pion-nucleon scattering lengths from pionic hydrogen and deuterium, *Eur. Phys. J. C* **21** (2001) 473–488.
[7] N. Nelms, D.F. Anagnostopoulos, O. Ayranov, G. Borchert, J.P. Egger, D. Gotta, M. Hennebach, P. Indelicato, B. Leoni, Y.W. Liu, B. Manil, L.M. Simons, A. Wells, A large area CCD X-ray detector for exotic atom spectroscopy, *Nucl. Instrum. Methods A* **484** (1–3) (2002) 419–431.
[8] D.F. Anagnostopoulos, D. Gotta, P. Indelicato, L.M. Simons, Low-energy X-ray standards from hydrogenlike pionic atoms, *Phys. Rev. Lett.* **91** (24) (2003) 240801.
[9] G. Douysset, H. Khodja, A. Girard, J.P. Briand, Highly charged ion densities and ion confinement properties in an electron-cyclotron-resonance ion source, *Phys. Rev. E* **61** (3) (2000) 3015–3022.
[10] S. Biri, L. Simons, D. Hitz, Electron cyclotron resonance ion trap: a hybrid magnetic system with very high mirror ratio for highly charged ion production and trapping, *Rev. Sci. Instrum.* **71** (2000) 1116–1118.

[11] M. Trassinelli, S. Biri, S. Boucard, D.S. Covita, D. Gotta, B. Leoni, A. Hirtl, P. Indelicato, E.-O. Le Bigot, J.M.F. dos Santos, L.M. Simons, L. Stingelin, J.F.C.A. Veloso, A. Wasser, J. Zmeskal, High resolution He-like argon and sulfur spectra from the PSI ECRIT, in: *Electron Cyclotron Resonance Ion Sources: 16th International Workshop on ECR Ion Sources ECRIS'04,* vol. 749, AIP, Berkeley, CA (USA), 2005, pp. 81–84.
[12] M. Trassinelli, S. Boucard, D.S. Covita, D. Gotta, A. Hirtl, P. Indelicato, E.-O. Le Bigot, J.M.F. dos Santos, L.M. Simons, L. Stingelin, J.F.C.A. Veloso, A. Wasser, J. Zmeskal, He-like argon, chlorine and sulfur spectra measurement from an electron cyclotron resonance ion trap, *J. Phys.: Conf. Ser.* **58** (2007) 129–132.
[13] D.F. Anagnostopoulos, S. Biri, D. Gotta, A. Gruber, P. Indelicato, B. Leoni, H. Fuhrmann, L.M. Simons, L. Stingelin, A. Wasser, J. Zmeskal, On the characterisation of a Bragg spectrometer with X-rays from an ECR source, *Nucl. Instrum. Methods A* **545** (2005) 217.
[14] D. Gotta, Precision spectroscopy of light exotic atoms, *Prog. Part. Nucl. Phys.* **52** (1) (2004) 133–195.
[15] N. Nelms, D.F. Anagnostopoulos, M. Augsburger, G. Borchert, D. Chatellard, M. Daum, J.P. Egger, D. Gotta, P. Hauser, P. Indelicato, E. Jeannet, K. Kirch, O.W.B. Schult, T. Siems, L.M. Simons, A. Wells, Precision determination of pion mass using X-ray CCD spectroscopy, *Nucl. Instrum. Methods A* **477** (1–3) (2002) 461–468.
[16] P. Indelicato, E.-O. Le Bigot, M. Trassinelli, D. Gotta, M. Hennebach, N. Nelms, C. David, L.M. Simons, Characterization of a charge-coupled device array for Bragg spectroscopy, *Rev. Sci. Instrum.* **77** (4) (2006) 043107–043110.
[17] H.H. Johann, Die Erzeugung lichtstarker Röntgenspektren mit Hilfe von Konkavkristallen., *Z. Phys.* **69** (1931) 185.
[18] M. Sanchez del Rio, J. Dejus, XOP: Recent developments, in: *SPIE Proceedings*, 1998, p. 3448.
[19] D.W. Marquardt, An algorithm for least-squares estimation of nonlinear parameters, *J. Soc. Ind. Appl. Math.* **11** (2) (1963) 431–441.
[20] W.H. Press, S.A. Teukolsky, W.T. Vetterling, B.P. Flannery, *Numerical Recipes in Fortran 77: The Art of Scientific Computing*, Cambridge Univ. Press, New York, 2001.
[21] B. Jeckelmann, T. Nakada, W. Beer, G. de Chambrier, O. Elsenhans, K.L. Giovanetti, P.F.A. Goudsmit, H.J. Leisi, A. Ruetschi, O. Piller, W. Schiwtz, New precision determination of the $\pi^-$ mass from pionic X-rays, *Phys. Rev. Lett.* **56** (1986) 1444–1447.
[22] B. Jeckelmann, W. Beer, G. De Chambrier, O. Elsenhans, K.L. Giovanetti, P.F.A. Goudsmit, H.L. Leisi, T. Nakada, O. Piller, A. Ruetschi, W. Schwitz, New precision determination of the $\pi^-$ mass from pionic X-rays, *Nucl. Phys. A* **457** (1986) 709–730.
[23] M. Daum, R. Frosch, D. Heter, M. Janousch, P.-R. Kettle, New precision measurement of the muon momentum in pion decay at rest, *Phys. Lett. B* **265** (1991) 425–429.
[24] B. Jeckelmann, P. Goudsmit, H. Leisi, The mass of the negative pion, *Phys. Lett. B* **335** (1994) 326–329.
[25] K. Assamagan, C. Brönnimann, M. Daum, H. Forrer, R. Frosch, P. Gheno, R. Horisberger, M. Janousch, P. Kettle, T. Spirig, C. Wigger, Upper limit of the muon-neutrino mass and charged-pion mass from momentum analysis of a surface muon beam, *Phys. Rev. D* **53** (1996) 6065–6077.
[26] T. Araki, K. Eguchi, S. Enomoto, K. Furuno, K. Ichimura, H. Ikeda, K. Inoue, K. Ishihara, T. Iwamoto, T. Kawashima, Y. Kishimoto, M. Koga, Y. Koseki, T. Maeda, T. Mitsui, M. Motoki, K. Nakajima, H. Ogawa, K. Owada, J.-S. Ricol, I. Shimizu, J. Shirai, F. Suekane, A. Suzuki, K. Tada, O. Tajima, K. Tamae, Y. Tsuda, H. Watanabe, J. Busenitz, T. Classen, Z. Djurcic, G. Keefer, K. McKinny, D.-M. Mei, A. Piepke, E. Yakushev, B.E. Berger, Y.D. Chan, M.P. Decowski, D.A. Dwyer, S.J. Freedman, Y. Fu, B.K. Fujikawa, J. Goldman, F. Gray, K.M. Heeger, K.T. Lesko, K.-B. Luk, H. Murayama, A.W.P. Poon, H.M. Steiner, L.A. Winslow, G.A. Horton-Smith, C. Mauger, R.D. McKeown, P. Vogel, C.E. Lane, T. Miletic, P.W. Gorham, G. Guillian, J.G. Learned, J. Maricic, S. Matsuno, S. Pakvasa, S. Dazeley, S. Hatakeyama, A. Rojas, R. Svoboda, B.D. Dieterle, J. Detwiler, G. Gratta, K. Ishii, N. Tolich, Y. Uchida, M. Batygov, W. Bugg, Y. Efremenko, Y. Kamyshkov, A. Kozlov, Y. Nakamura, C.R. Gould, H.J. Karwowski, D.M. Markoff, J.A. Messimore, K. Nakamura, R.M. Rohm, W. Tornow, R. Wendell, A.R. Young, M.-J. Chen, Y.-F. Wang, F. Piquemal, K. Collaboration, Measurement of neutrino oscillation with KamLAND: Evidence of spectral distortion, *Phys. Rev. Lett.* **94** (8) (2005) 081801–081805.
[27] P.J. Mohr, B.N. Taylor, CODATA recommended values of the fundamental physical constants: 2002, *Rev. Mod. Phys.* **77** (1) (2005) 1–107.

[28] H.B. Bethe, E.E. Salpeter, *Quantum Mechanics of One- and Two-Electron Atoms*, first ed., Springer-Verlag, New York, 1957.
[29] D. Delker, G. Dugan, C. Wu, D.C. Lu, A. Caffrey, Y. Cheng, Y. Lee, Experimental verification of the relativistic fine-structure term of the Klein–Gordon equation in pionic titanium atoms, *Phys. Rev. Lett.* **42** (2) (1979) 89–92.
[30] S. Weinberg, Phenomenological Lagrangians, *Physica A* **96** (1–2) (1979) 327–340.
[31] V.E. Lyubovitskij, A. Rusetsky, $\pi$p atom in ChPT: Strong energy-level shift, *Phys. Lett. B* **494** (1–2) (2000) 9–18.
[32] J. Gasser, M.A. Ivanov, E. Lipartia, M. Mojzis, A. Rusetsky, Ground-state energy of pionic hydrogen to one loop, *Eur. Phys. J. C* **26** (2003) 13–34.
[33] T.E.O. Ericson, B. Loiseau, S. Wycech, A phenomenological $\pi^- p$ scattering length from pionic hydrogen, *Phys. Lett. B* **594** (2004) 76–86.
[34] S. Deser, M.L. Goldberger, K. Baumann, W. Thirring, Energy level displacements in Pi-mesonic atoms, *Phys. Rev.* **96** (3) (1954) 774776.
[35] G. Rasche, W.S. Woolcock, Connection between low-energy scattering parameters and energy shifts for pionic hydrogen, *Nucl. Phys. A* **381** (1982) 405–418.
[36] J. Spuller, D. Berghofer, M.D. Hasinoff, R. Macdonald, D.F. Measday, M. Salomon, T. Suzuki, A remeasurement of the Panofsky ratio, *Phys. Lett. B* **67** (4) (1977) 479–482.
[37] D. Sigg, A. Badertscher, P.F.A. Goudsmit, H.J. Leisi, G.C. Oades, Electromagnetic corrections to the s-wave scattering lengths in pionic hydrogen, *Nucl. Phys. A* **609** (3) (1996) 310–325.
[38] J. Zemp, Ph.D. thesis, University of Bern (2004).
[39] M. Leon, H.A. Behte, Negative meson absorption in liquid hydrogen, *Phys. Rev.* **127** (1962) 636–647.
[40] T.S. Jensen, V.E. Markushin, Collisional deexcitation of exotic hydrogen atoms in highly excited states. II. Cascade calculations, *Eur. Phys. J. D* **21** (2002) 271–283.
[41] T.S. Jensen, V.E. Markushin, Collisional deexcitation of exotic hydrogen atoms in highly excited states. I. Cross-sections, *Eur. Phys. J. D* **21** (2002) 261–270.
[42] T.S. Jensen, V.E. Markushin, Scattering of light exotic atoms in excited states, *Eur. Phys. J. D* **19** (2002) 165–181.
[43] T.S. Jensen, Kinetic energy distributions in pionic hydrogen, *Eur. Phys. J. D* **31** (1) (2004) 11–19.
[44] M.C. Martins, A.M. Costa, J.P. Santos, P. Indelicato, F. Parente, Interpretation of X-ray spectra emitted by Ar ions in an electron cyclotron resonance ion source, *J. Phys. B* **34** (2001) 533–543.
[45] J. Rzadkiewicz, T. Stohlker, D. Banas, H.F. Beyer, F. Bosch, C. Brandau, C.Z. Dong, S. Fritzsche, A. Gojska, A. Gumberidze, S. Hagmann, D.C. Ionescu, C. Kozhuharov, T. Nandi, R. Reuschl, D. Sierpowski, U. Spillmann, A. Surzhykov, S. Tashenov, M. Trassinelli, S. Trotsenko, Selective population of the 1s2s $^1S_0$ and 1s2s $^3S_1$ states of He-like uranium, *Phys. Rev. A* **74** (1) (2006) 012511–012517.
[46] A.M. Costa, M.C. Martins, F. Parente, J.P. Santos, P. Indelicato, Dirac–Fock transition energies and radiative and radiationless transition probabilities for $Ar^{9+}$ to $Ar^{16+}$ ion levels with K-shell holes, *At. Data Nucl. Data Tables* **79** (2) (2001) 223–239.
[47] D.R. Plante, W.R. Johnson, J. Sapirstein, Relativistic all-order many-body calculations of the $n = 1$ and $n = 2$ states of heliumlike ions, *Phys. Rev. A* **49** (5) (1994) 3519–3530.
[48] I. Lindgren, B. Åsén, S. Salomonson, A.-M. Mårtensson-Pendrill, QED procedure applied to the quasidegenerate fine-structure levels of He-like ions, *Phys. Rev. A* **64** (6) (2001) 062505(5).
[49] A.N. Artemyev, V.M. Shabaev, V.A. Yerokhin, G. Plunien, G. Soff, QED calculation of the $n = 1$ and $n = 2$ energy levels in He-like ions, *Phys. Rev. A* **71** (6) (2005) 062104–062126.
[50] R.D. Deslattes, H.F. Beyer, F. Folkmann, Precision X-ray wavelength measurements in heliumlike argon recoil ions, *J. Phys. B* **17** (1984) L689–L694.

CHAPTER 12

# Conceptual Problems in Phenomenological Interpretation in Searches for Variation of Constants and Violation of Various Invariances

**Savely G. Karshenboim***

Contents



* D.I. Mendeleev Institute for Metrology (VNIIM), St. Petersburg 190005, Russia and Max-Planck-Institut für Quantenoptik, 85748 Garching, Germany
E-mail: sek@mpq.mpg.de

Advances in Quantum Chemistry, Vol. 53
ISSN 0065-3276, DOI:10.1016/S0065-3276(07)53012-1

Abstract At present a number of current or proposed experiments are directed towards a search for 'new physics' by detecting variations of fundamental physical constants or violations of certain basic symmetries. Various problems related to the phenomenology of such experiments are considered here.

## 1. INTRODUCTION

Progress in precision studies and shortage of data on possible extension of the Standard Model of weak, electromagnetic and strong interactions have produced a situation where a number of experiments to search for so-called 'new physics' have been performed or planned in atomic physics. Among such experiments are a search for an electric dipole moment of an electron and a neutron, search for variation of fundamental constants and violation of Lorentz invariance, etc.

While a number of experiments are designed to check a particular theory, the others have aimed to look for 'new physics' in a 'model-independent way'. Most of such experiments involve various constraints even within a phenomenological interpretation. Such conceptual problems of new physics in phenomenological interpretation are considered in this note.

An example of such a problem is a relation of possible time or space variation of fundamental constants and a basic relativistic principle of local position/time invariance (LPI/LTI)[1]. Some scientists consider possible variation of constants as violation of LTI. However, that is not correct.

We should acknowledge that there are two basic possibilities of variations of constants. One is a result of certain violation of LPI, while the other is an observational effect of the interaction with environment, such as the bath of Cosmic Microwave Background (CMB) radiation of photons, neutrinos, gravitons, Dark Matter (DM), matter, etc.

The idea of scaling of the environment is changing once we increase accuracy. For example, we can say that the Earth gravity at accuracy better than one-ppm level is described by three forces: attraction by Earth, Sun and Moon, while the acceleration of free fall, $g$, is a parameter of the interaction with Earth only. Alternatively, we can say that the complete gravitational force is always $mg$ and it is varying in time because of the relative motion of Earth, Sun and Moon. That is not only a matter of definition. It depends on natural time scale of the experiment with respect to the periods of Earth motion and on whether we understand the planetary motion properly.

Interactions with the environment can always have a slow component, which is in a way universal. From the observational point of view a slowly changing parameter presents a kind of variation of a constant, but indeed that is not violation of LTI.

As a matter of fact, we have to acknowledge that the most popular model of evolution of the universe suggests so-called inflation [1] which is caused by

[1] Theoretically, LTI is indeed a part of LPI, but from the experimental point of view the related experiments are completely different

a phase transition. The latter is a transition between two phases of vacuum. In the former phase the electron mass was zero and the proton mass was approximately 5–10% lower than now.

Another example of conceptual problems is the electric dipole moment (EDM) of an electron. The EDM of an electron can be caused by two effects. One is some violation of the CP invariance in one or other way, which allows a correlation between directions of a vector (the EDM) and a pseudovector (the spin, $\mathbf{s}$). All experiments have been interpreted in such a way. Meanwhile, there is another opportunity due to a possible violation of the Lorentz invariance. Such a violation can deliver a preferred frame (e.g., related either to the isotropy in CMB or to the local DM motion) and a preferred direction related to our velocity $\mathbf{v}$ with respect to the preferred frame. The violation could induce a certain EDM directed with this preferred direction (along $\mathbf{v}$) or in a direction of $[\mathbf{v} \times \mathbf{s}]$. All the experiments have been treated in the former way, while their results were considered as a model-independent limitation on the electron's EDM.

## 2. VARIATION OF CONSTANTS

Here we consider various aspects of a possible interpretation of experiments on variation of constants.

### 2.1 Can constants vary?

First of all, we note that the very motto 'variation of constants' is a jargon which is not related to reality. In a sense, the constants cannot vary, because the idea of variation of the constants is based on an assumption, that we can apply conventional equations, but claim that some of their parameters are now adiabatically time- or space-dependent. That cannot be correct. We should completely change the equations.

Let us show a simple example why we should. Consider a quite unrealistic problem: a free electron at rest and the Planck constant changing in time ($\hbar = \hbar(t)$), but not in space in a particular frame. That is an isotropic situation and the angular moment $L_z$ is conserved. On the other hand, it is equal to $\pm(1/2)\hbar(t)$. Something should be changed. Applying conventional equations of quantum mechanics to physics with changing $\hbar$ produces an obvious contradiction. Another example is considered in Section 2.6.

### 2.2 Alternating the basic description

At present, we have many equivalent ways to describe quantum mechanics. Introduction of the 'varying constants' into these different descriptions produces different effects.

For example, even in classical mechanics we have equations (like Newton's) and the variational principle of the least action. If we introduced something similar to varying constants into the Lagrangian we will change the equations. Similar

dilemma exists in quantum theory, where we should decide what the fundamental description is and what its consequences are.

I believe [2] that the fundamental original description is the Feynman's continual integral in quantum field theory [3] (which is similar to the path integral in quantum mechanics).

Indeed, this integral is not well-defined, but it reproduces the very soul of the quantum physics—the interference as its backbone. When we do experiments, like the famous Young's double-slit experiment, we look for an interference pattern. When Bohr first created a theory of the hydrogen atom, he was also dealing with interference effects such as standing waves. The Schrödinger equation has taught us that relation for a photon $E = \hbar\omega$ has deep meaning and in a sense any energy (at least for a stationary problem) is certain frequency because the stationarity is supported by a classical picture with a periodic motion and a resulting standing wave. Having in mind the path integral, we see that a stationary motion survives because of constructive interference after going the same loop again and again, while for any other frequency the interference is destructive. The Bohr's orbit is a kind of a standing wave. The least action principle (the least distance Fermat principle for light) is also understood via a constructive interference—the phase around the least phase trajectory is almost not changing and that greatly enhances the classical trajectory by the summation of the huge number of very close trajectories, while far away from it the phase has no minimum and changes linearly with the variation of any parameter of the trajectory. The fast oscillating sum goes down because of destructive interference of nearby trajectories.

To my mind the most natural way to go beyond conventional physics phenomenologically is to change the phases in the continual integral (which is the action) and to derive proper equations from it.

Note, that to introduce medium into the Maxwell equation one has to change the electromagnetic Lagrangian in a relatively easy way (and that is related to a simple change in the action), while the derived equations already involve various complications such as derivatives.

## 2.3 Gradient terms

We need to emphasize that we deal with a phenomenological description and do not discuss how various time- and space-dependent factors can appear in the Lagrangian. We just like to describe a proper framework for the interpretation of the data.

Introducing time- or space-dependent factors into the Lagrangian we should expect their appearance in equations together with their gradients. In principle, some gradients could appear even in the Lagrangian. Once we have a derivative such as $\partial Y/\partial x_0$, where $x_0 = ct$ and $c = c(x)$, we have to think which of many ways should be taken to modify the derivative:

$$\frac{\partial Y}{\partial x_0} \to \frac{1}{c}\frac{\partial Y}{\partial t},$$
$$\frac{\partial Y}{\partial x_0} \to \frac{\partial Y}{\partial (ct)},$$

$$\frac{\partial Y}{\partial x_0} \to \frac{\partial 1}{\partial t}\frac{Y}{c},$$

with some of them including the derivative $\partial c/\partial t$. But even if the Lagrangian in proper variables is free of derivatives, the equations of motion derived from the Lagrangian should contain some gradients.

Indeed, we should not be surprised by appearance of the time- and/or space-gradients. We have a well-known self-consistent example of a violation of the relativistic invariance with the speed of light depending in principle on frame, location, time etc. That is electrodynamics in media with a proper medium density. When we consider it in a conventional way, four three-dimensional field vectors have to be applied: **E**, **D**, **B** and **H**. If we consider that as a theory of photons, we should introduce, instead of the four former field vectors, one four-dimensional vector $A_\mu$. When presenting all the equations in such a way, we immediately arrive at equations which contain not only two functions $\epsilon(x)$ and $\mu(x)$ (or even two tensor functions in a general case) but also their derivatives. If afterwards we will try to describe the complete interaction of two moving charges, their interaction should also include the derivatives of $\epsilon(x)$ and $\mu(x)$. That is far different from the naive expectation that it is enough to write $c(x)$ instead of $c$ for the Lorentz force.

## 2.4 Dimensional quantities

Presence of the gradient terms allows to search for possible variations related to dimensional quantities. However, even without any gradient terms present in the basic equations, a variation of dimensional quantities can be detected.

Any measurement is a comparison and we have to deal with a 'measured value' and a 'reference value' of the same dimension. However, applying some differential methods, a key comparison can be performed between two values of the same quantity, e.g., the speed of light, related to different directions. In other words, we can look for a relative change of a certain dimensional quantity.

Note that such a statement is related not only to fundamental physics, but also to practical issues. For example, the definition of the kilogram states that the mass of the prototype is exactly one kilogram. However, that does not mean that the mass of the prototype is not changing. A change in the mass of a particular object can be determined without any definition of the units. That can be done in relative units and only needs definitions of the involved quantities. Meanwhile, the definition of the kilogram fixes only the numerical value of the mass of the prototype, while the unit can change and that is detectable.

## 2.5 Three kinds of searches

Returning to possible variation of the constants, we conclude that there are three basic kinds of searches [2], which are

- a series of 'fast' measurements with 'long' separation periods;
- a 'long' monitoring experiment;
- a selectively sensitive 'gradient experiment'.

Selective 'gradient experiments' are model-dependent. They assume a certain possible effect and look for it. That may be a search for a gradient term, or a differential experiment. Indeed, to isolate a particular effect one should have a model and thus all such gradient terms are model-dependent and the dependence sometimes goes much further than expected naively. Due to the Lorentz invariance somewhat below the famous Michelson–Morley experiment is discussed as an experiment of this kind.

Most of the experiments are of a different kind: they look for certain values and check whether they change or not. However, a crucial point is duration of different phases of the experiment. In principle, there are two phases: reading the values (the measurement proper) and the accumulation of the effect of the variation (during a separation between the measurements).

The problem is that the accumulation period for a change of parameters of a system, like, e.g., the electron's mass and charge, usually does not involve any effects of the gradient terms. The latter are important only during the measurements. If the measurement[2] is fast enough, the effects of the gradients can be neglected and the most important effect is the evolution of the parameters of the system under study between the measurements, namely during the accumulation time. In this case we can consider the same equations as usually but with varying parameters and do a model-independent evaluation. A typical example of such kind of experiments is a study of the variability of the constants by means of atomic physics. Since the gradient are not involved the constraint can be achieved in such experiments only on variations of dimensionless quantities.

Another situation occurs for various space tests of general relativity and related experiments for $\partial G/\partial t$. The accumulation time and the reading-data time is essentially the same. Even if we try, similarly to atomic physics, to perform brief, say, one-day measurements every year, even that would not help. The problem is that when looking for a 'rotation' of an electron we cannot measure the phase of the rotation and deal with something related in sense of classical physics to average parameters of the orbital motion. The planetary motion allows us to look for the phase of the rotation and thus the 'coherence time' is equal to many periods of evolution. In a sense that is similar to the Ramsey method with two coherent space-separated short measurements. As a result, the effects of the gradients are of the same importance as effects of the time dependence of conventional terms. Any interpretation of the data in such a case is indeed strongly model-dependent.

Dealing with average values for planetary and atomic motion is also not the same. The atomic orbits are quantized. Their parameters do not depend on initial conditions, which determine only probability to create one or other atomic state. Planetary motion depends strongly on the initial conditions and thus even experiments on average values have a kind of history and accumulate effects from gradients.

Involvement of the gradient terms allows of constraining variations of dimensional constants.

[2] The measurements in sense of quantum mechanics is determined by the interaction time and by the coherence time. The measurement in sense of reading data consists of a session of many 'quantum measurements'. We indeed mean here the duration of the quantum measurements

## 2.6 An example

Let us illustrate the consideration above with a clear example. We consider a case of a non-relativistic classical problem of a two-body system with one mass, $M$, much heavier than the other $m$ (e.g., a Sun-planet, or planet-satellite system). We neglect all corrections in the order $m/M$ and for further simplicity suggest a circular orbit.

The main parameters of the problem are: heavy mass $M$, lighter mass $m$, gravitation constant $G$, orbital radius $R$ and orbital velocity $v$. Starting with the equation of motion in a conventional case ($G$, $M$ and $m$ do not depend on time) we find:

$$m\mathbf{a} = -\frac{GmM}{R^2}\frac{\mathbf{R}}{R} \tag{1}$$

or

$$\mathbf{a} = -\frac{GM}{R^2}\frac{\mathbf{R}}{R}, \tag{2}$$

with appropriate initial conditions for a circular orbit.

If we assume that all the constants ($G$, $M$ and $m$) depend on time, but expect that we can apply an adiabatic approximation, i.e., neglect all time derivatives, we can still use the equation of motion (1) or (2) and the lighter mass, $m$, vanishes there. That means in particular that any time dependence of $m$ is unimportant, because for slow changes it looks natural to neglect all time gradients. In particular, measuring the distance $R$ as a function of time we find

$$R = \frac{GM}{v^2}. \tag{3}$$

We note that the acceleration is orthogonal to the velocity and thus the velocity has only a tangential component ($v = v_{||}$) which is conserved. In other words, for time-depending terms we find a proportionality law

$$R(t) \sim G(t)M(t). \tag{4}$$

However, the 'adiabatic approximation' is inconsistent. Let us consider the problem adiabatically, but neglecting the time-gradients in conservation laws, not in the equation of motion. As a result we find that (3) is still correct; however, the tangential velocity is not conserved. Instead, the tangential component of the momentum

$$p_{||} = mv_{||} \tag{5}$$

is. As a result we find

$$R = \frac{GMm^2}{p_{||}^2} \tag{6}$$

and for time-depending quantities the proportionality law takes the form

$$R(t) \sim G(t)M(t)\big(m(t)\big)^2 \tag{7}$$

to be compared with (4).

The difference between (4) and (7) is caused by a gradient term $\mathbf{v}\partial m/\partial t$ to appear in the equation of motion (1). In other words, adiabatic treatment of the conservation laws suggests a non-adiabatic approximation in the equation of motion. The example shows that the gradient terms in the equation of motions may be as important as adiabatic effects—the former lead to $m^2$ in (7), while the latter are responsible there for $M$.

The equations achieved above via the conservation laws do not contains gradients directly. Still they allow to constraint dimensional quantities. Technically that appears as a consequence of presence of certain dimensional conserved quantities, such as $p_{||}$ (as we demonstrated its conservation is related to a gradient term of the equation of motion). The dimensionless combination on which the constraint is achieved contains such a conserved quantity. It originates from the initial conditions and that is why there is no analog of it in quantum theory where the atomic energy levels are determined only by the fundamental constants and not by any initial conditions.

One more point about this example is that the Eq. (7) cannot be the end of the story. In the framework given the mass should be conserved. There are two natural options to describe the time dependence of the mass and both imply further modifications of the scaling laws for $R(t)$.

The first idea is to allow a time dependence in the framework of classical non-relativistic physics. An obvious mechanism is to suggest that there is a mass in the space (e.g., dust particles) which is not observable and the very presence of this mass allows a change in the object moving through. This model is very similar to introducing, e.g., the internal (thermodynamic) energy into the mechanical consideration at the moment when it was absolutely unclear what the substance is. A similar successful idea was to suggest a neutrino to solve the problem of shortage of energy in the beta decay.

Suggesting such a mechanism solves the problem of a possible time dependence offering a mass transfer between unobservable dust and a moving body. Meanwhile, it opens a question of a possible transfer of momentum, angular momentum and kinetic energy. Any particular model of the mass transfer sets constraints on the transfers of other quantities and will produce different corrections to (7). Note also that such a description will require the introduction of some functions to describe the dust particle in continuous space, i.e. to introduce a kind of fields (cf. Section 4).

Another possibility is to change the framework. For example, we can stop here to deal with non-relativistic physics and recall that it is energy rather than mass, which is conserved. However, in this case even before discussing any mechanisms of the energy transfer (which should be somewhat similar to the previous consideration) we have to acknowledge, that we should immediately change the basic equations of both kinematics (describing a motion of objects) and dynamics (describing the gravity).

In other words, we cannot simply say that the masses are time-dependent, we should go further to create a consistent construction which allows such dependence within a certain framework.

We have not discussed here two other problems. One is related to what can be really measured. When we look for a change in the distance, we usually mean that we look for a change in its numerical value in some units. The interpretation would strongly depend on what kind of clocks we use (the measurement of the distance is usually a measurement of light-propagation time) and on our assumptions on what can happen with the value of speed of light $c$.

The other question is the gravitational constant, whether it can change or we look for a variation of the masses only. To create a 'real' variation of $G$ we need to modify theory of gravity. To make an 'observable' variation of $G$, it is sufficient either to change the units, or the masses, because we cannot observe $G$ separately from gravitating masses and separately from measuring masses and distances or related quantities in certain units.

## 2.7 Variations of the constants and violation of the Lorentz invariance or LTI

When searching for a variation of constants one has to remember about a possible connection with various symmetries related to relativity.

The simplest issue is an observational one. The variations are long-term changes in values of fundamental constants, while a violation of Lorentz invariance could produce periodic effects because of the Earth rotation and its motion around the Sun (more precisely both motions should be considered with respect to the remote stars[3]). That can be resolved experimentally.

The other issue is a reason for a variation of constants. There are basically three options.

- Variation of constants could be caused by 'long-range' environment. An example is the phase transition during the early time of the Universe. That has no relation to relativity.
- There is a certain dynamics directly in space-time continuum, which drives both: a violation of the relativity and a variation of the constants. An example could be a consideration of our 4-dimensional world as a result of compactification with the radius of compactification dynamically changing.
- An in-between option is a such kind of environment which affects some relativity issues naively understood. For instance, presence of a 'medium' does not violate the relativity once we speak about media as a non-fundamental issue added as an environment. Meanwhile, we can choose to consider theory with media as a fundamental 'quasifree' theory with broken relativity. What is important is the scale of phenomena. When we speak about the propagation of light and the interaction of classical macroscopic sources of the electric or magnetic field in a gas, we deal with a kind of fundamental electromagnetic theory

[3] Even that is not absolutely clear. There are at least two preferred frames moving with respect to each other: one is related to the local DM cluster, while the other is related to the isotropic CMB. They suggest a different distance scale and both can in principle lead to periodic variations. Any periodic effect induced by the dark-matter-determined frame has no relation to a violation of the Lorentz invariance. With the CMB that is not clear. CMB proper is a kind of 'environment'. Meanwhile, if there is any fundamental violation of the Lorentz invariance, we would expect that violation determined the frame where the Big Bang happened and thus where the CMB is isotropic. So this frame is specific because of a possible violation and because of environmental effects, related to violations of the Lorentz invariance in the remote past

with violated relativity. However, considering atomic spectra, we find that they are related to electrodynamics of vacuum and all deviations from the vacuum case happen on a certain macroscopic distance scale.

Indeed, only the second option is related to a violation of local position/time invariance.

## 3. PLANCK SCALE PHYSICS IN OUR LOW-ENERGY WORLD

### 3.1 Renormalization and Planck scale physics

A big success of quantum electrodynamics was due to the introduction of the renormalization scheme. Briefly speaking, quantum electrodynamics (QED) is in a sense not a fundamental theory, but a fundamental constraint.

A fundamental theory is such a theory that being formulated in terms of certain laws and certain parameters produces a result in terms of those fundamental parameters. Such a view on QED has failed because of divergences.

Indeed, in reality everything in physics should be finite, but we know that we possess only some knowledge on asymptotic low-energy behavior of various physical quantities. Very often applying asymptotics beyond their applicability one goes into unphysical behavior of various results and, sometimes, to divergences. To make divergences finite one has to use a complete description, not its asymptotics, with exact laws instead of their asymptotic forms.

The problem of QED is that we cannot learn anything about the 'complete description' and 'exact laws', because they are related to physics beyond our reach. Using different models for this physics (i.e. different regularizations) we arrive at different results.

Power of the renormalization procedure is in the treatment of QED as a fundamental constraint, not as a theory. We can calculate a long-range Coulomb-like interaction (which determines an observable value of the electric charge), we can study electron's kinetic (or complete) energy (which determines an observable value of the electron's mass) and we can measure a number of other properties such as the anomalous magnetic moment of an electron and the Lamb shift in the hydrogen atom. The 'constraint' means that they are correlated and we can calculate the correlation. Learning some of these values from experiment, we can predict the others.

The 'fundamental constraint' means that it is enough to learn very few values to predict all the others with an arbitrary accuracy (or more precisely—as accurate as we can treat them as pure QED values). For QED predictions, as we know, it is sufficient to measure the elementary charge and masses of each kind of particles.

The alternatives are known—to predict a value of the electric or magnetic field of a non-elementary object we have to know not only its charge and mass, but also all details of the distribution of its electric and magnetic moments (and a number of parameters beyond that). Those details should be also measured. So we need an infinite number of the parameters.

Does the renormalization mean that the Planck scale does not contribute to our experiments? No, it does not mean that. The Planck scale indeed contributes, but it does not contribute to the constraint, because it only affects values of masses and charges, however, we do not calculate, but measure them. That makes the Planck-scale effects unobservable. To observe we should compare a measurement and a calculation, but we have only results of measurements. However, there is an option when we should be able to see some effects of the Planck scale [2]. That is a case when we have certain dynamic effects at the Planck scale (e.g., a variation of some constants) or some violation of symmetries which would make our low-energy picture wrong.

For instance, if we assume that we live in a multidimensional world with a changing compactification radius, we may expect that electron's mass and charge should vary. The effects depend on the model of origin of bare masses and coupling constants. The bare values can change or, alternatively, the bare values would stand unchanged, while the renormalization term would change.

As an illustration we recall that we can see a number of consequences of special relativity and quantum mechanics in non-relativistic macroscopic phenomena. For instance, with a precision achieved in the mass spectroscopy, we can see a non-conservation of the mass because of the binding energy. Various interferometers of the macroscopic scale prove that the trajectory is not a well-defined property. And so on.

## 3.2 The classical Michelson–Morley experiment and calculability of the fine structure constant

Here, we consider as an example a possible problem with an interpretation of a classical version of the Michelson–Morley experiment. In the experiment some pieces of bulk matter were rotated. It was expected that when rotating their linear scale would not change and comparing the light propagation in different arms of the interferometer we can judge whether the speed of light is the same in different directions.

Meanwhile, there is no just 'speed of light' if we assume a violation of the relativity. There are many different effects instead. But still we can expect that non-relativistic physics would not change too much. The size of a piece of atomic bulk matter is basically determined by the non-relativistic Coulomb interaction and we can believe that comparing a non-relativistic distance and relativistic propagation of light we should have a clear signature.

However, that is not that simple. The non-relativistic size depends on the electron mass and its charge. Let us, e.g., assume that $\alpha$ is calculable and that means that elementary charge can be presented in terms of $\hbar c$. If special relativity is violated and, e.g., $c = c(x)$, we should also arrive at $e(x)$. (More precisely, we should speak not about varying electric charge $e(x)$, but about calculability of the non-relativistic long-distance interaction of two charges *ab initio*.) The Coulomb interaction, which is a pure non-relativistic effect, would nevertheless be sensitive to a violation of the special relativity. Rotating the interferometer built as a bulk

body we would deal with two effects: changes in speed of propagation of light and in a distance between the mirrors.

In other words, if the elementary charge is a fundamental quantity which is not correlated with the speed of light, the Coulomb-law energy is $E = Z_1 Z_2 e^2/r$ with possibly $e = e(x)$, while if $\alpha$ is calculable, it is $E = Z_1 Z_2 \alpha \hbar c/r$ with $\alpha = \alpha(x)$. Note, the mentioned suggested $x$-dependence in $\alpha(x)$ and $e(x)$ is of fundamental origin and does not correlate with a possible violation of the Lorentz invariance which could affect only $c$. (We remind that a real picture should be somewhat more complicated—instead of varying constants we should introduce some additional parameters and their derivatives (see above).)

In a more complicated way similar reasons can be related to masses of an electron and nucleon. The complicity is because we rather expect that $\alpha$, if calculable, is calculable in a kind of one-step action (with further renormalization), while for masses we need to go step by step. For instance, for the electron we should first understand the calculability of parameters of the Higgs sector.

That means that for a proper interpretation of a Michelson–Morley-like experiment with an interferometer built on an atomic bulk matter we need to consider a dynamic model of structure of this kind of matter with a possible violation of relativity. The latter may involve the Planck scale effects, where a certain relation on low-energy fundamental constants can be set.

### 3.3 How to violate symmetries?

There is a number of ways to violate a symmetry. The most naive way is to violate such a symmetry directly. For example, the masses of the up and down quarks, $m_{\rm u}$ and $m_{\rm d}$ violate a chiral symmetry of QCD. That is the most natural way for classical physics. In the case of quantum field theory, such a violation for the relativity and related effects can most likely take form of an external field (see Section 4 below). In particular, the spontaneous breakdown of symmetries takes the form of certain external fields.

Quantum theory also opens a number of other options (see, e.g., [2]). One of them is a so-called anomaly. The violating term is a purely quantum effect proportional to $\hbar$. It appears because of singularities in original theory. While in the classical case the theory is symmetrical under a number of transformations, it is not possible to regularize all singular operators to keep all classical symmetries. Some of them have to be violated in the quantum-field case. The most well-known example is a so-called axial anomaly, which violates chiral symmetry even for massless quarks.

A very remote analogy is conservation laws in classical and quantum physics. Description of quantum mechanics in terms of classical mechanics is not well defined, which happens because of commutativity of classical values and non-commutativity of their quantum analogs. We should regularize it and as a result part of classical symmetries may be realized in such a way that some conservation laws cannot be measured at all (e.g., conservation of the angular momentum as a vector). That example turns our attention to problem of observations.

Some effects may be a pure observational problem. We can illustrate it by comparing conservations in classical and quantum physics. We remark that we cannot check any conservation laws, but only their consequences. From the point of view of classical physics we expect that we can measure different components of angular momentum and check at some time whether they have the same values. From quantum physics we know that they would not have the same value and that we can directly check only conservation of one component of the angular momentum. Conservation of the angular momentum as a vector can be checked via some specific consequences, but not so directly.

The problem is with commutations of different components of the angular momentum. Meanwhile, it is expected that operators of coordinates can be not-commutative in the quantum gravity. That would produce certain observational effects for naive tests.

## 4. EXTERNAL FIELDS AND RELATED EFFECTS

### 4.1 External field as a violation of relativity and CPT

Even considering various violations, we basically expect that the relativity, CPT and many other would-be violated invariances are still present in a sense. Their violations used to be suggested in the form of a kind of external field of a classical (caused by matter or dark matter) or quantum (condensate) origin. We refer here to such a field as a 'violating field'. The violating field can have a certain simple form in a specific frame and the result in other frames can be found by an appropriate Lorentz transformation.

It is very natural that most of such violating fields are very similar to conventional fields such as scalar, electromagnetic, gravitational etc. That is not a surprise, because if we like to introduce both conventional and violating fields, we start from designing a certain interacting term in the Lagrangian which obeys all necessary symmetries. There are two basic differences between 'true' fields, which we used to deal with, and violating ones. The former are somewhat universally coupled to many objects and they are a result of certain sources existing in the case, or they are quantized as photons. The violating fields have no sources, they are background fields; and what is very important they are somewhat selectively coupled to other objects. We know only one kind of such a field, the Higgs field, which violates SU(2) $\times$ U(1) symmetry in the Stardard Model of the electroweak interactions. It is also not-universally coupled to the matter fields and as a result the masses of charged leptons and quarks are all very different.

Let us also remind that a violation of CPT, most wanted by experimentalists, is such a violation when mass and charge of particle and antiparticle are not the same. To provide the different charges would be a big problem, since it assumes a non-conservation of the charge by producing a pair of particle and antiparticle (the alternative is a photon with a very small but not vanishing charge which is also not good). Possessing different masses means, that while the mass of an electron is

$$m_- = m - \delta m,$$

the positron mass is

$$m_+ = m + \delta m.$$

However, the same effects can be obtained if we assume that

$$m_q = m + qeU,$$

where $q$ is charge, equal to $\mp 1$, and the electric potential $U$ is defined as $U = \delta m/e$.

Meanwhile, because of the gauge invariance we cannot observe any constant homogeneous potential since the related strength of the electric field is zero. Does it mean that such a term is not observable at all? The answer depends on how we treat different particles and what kind of problem we study. If, e.g., we consider the muon in the same way, but if two effective potentials are not the same ($U_e \neq U_\mu$), we should be able to observe their difference. The decay of muon and antimuon should have slightly different kinematics and the difference in their lifetime caused by the different phase volume of the decay product, would be proportional to $U_e - U_\mu$. To understand that we can have in mind so unrealistically large value of this difference that a muon would decay, but an antimuon would not.

If we do parametrization more rigorously and introduce $\gamma_0$, instead of $q$ (or more correctly to deal with the substitute

$$m \to m + \gamma^\mu a_\mu,$$

where $a_\mu$ is a time-like vector), the result remains the same. An observable departure from CPT should be proportional to a certain difference of parameters of two particles, involved into calculations (cf. contributions of the $a$ term in [4]).

## 4.2 'Selective' external fields and macroscopic experiments

As we could see above, the violating term is similar to the electric potential, but it is a kind of a selective field which should interact differently with different kinds of particles and only the differences can be observed.

A situation when the searched violating external fields are similar to conventional electromagnetic fields, but to selective ones, is very important from a practical point of view.

What is an electromagnetic field from a pragmatic point of view? In conventional electrodynamics an electron, a proton, a muon, etc., sees the same electric field (once we neglect motional magnetic effects). If we set a different background field for different particles, that may well serve for producing a CPT violation or violation of the Lorentz invariance. The conventional magnetic field interacts universally with moving charges and there is an additional interaction with spins or rather with related magnetic moments. Some of spin magnetic moments are calculable *ab initio* as for an electron or a muon, some should be treated phenomenologically, as for a proton or a neutron.

Meanwhile, any experimental setup involves macroscopic bodies, which can interact with the electromagnetic field, and some of them do interact. Certain substances do that in peculiar ways, when only one kind of universal interactions is involved.

For example, the solid conductors screen the 'true' electric field via a rearrangement of the electron density. With a violating field, which interacts with the electrons, added, the conductors should screen the field as seen by their electrons, i.e. they screen both 'true' electric field and the additional field interacting with electrons. As a result they leave a certain electric field inside the screened area. If the probe particle will be an electron, no field would be seen, because the remaining electric field will compensate the violating field. If the probe particle is a proton, it should see a certain effective field which is a difference of violating proton's and electron's fields.

A similar situation is with a magnetic-field-like violating field. The 'true' magnetic field interacts universally with all particles and the same field is seen by any orbital and spin magnetic moments in a consistent way. The violating field could be different for different particles and it may interact in a different way with the spin and the orbital motion. Some magnetic screening materials act via a production of certain electron currents (i.e., the orbital motion), while others via a rearrangement of the electron spins. While providing the screening, the electrons will act in such a way that they will cancel all the field, including a violating component.

These examples show that while there may be certain vacuum effects, the experiments are never done in vacuum. A certain screening is always needed to avoid residual electromagnetic fields. In the case of CPT violating fields, acting as 'selective' electromagnetic fields, a certain electron-interacting component of such a field should be compensated by an electromagnetic field created by the shielding material. That should be taken into account for interpretation of such experiments.

## 5. MICROSCOPIC AND MACROSCOPIC DESCRIPTION

While a natural microscopic picture involves an effective external field, the natural macroscopic description is rather a kind of dilute medium (e.g., for the dark matter) which weakly interacts with light etc. It is not the ether! The dilute medium obviously affects the Doppler effect, etc., and produces a signal for the Michelson–Morley experiment. The speed of light would not be a universal 'c'. However, for microscopic properties such as a value of $mc^2$ as the rest energy that would be different. Either they would have no relation to measured velocity of light in the media, or there would be different changes.

For example, considering the time dilation of the lifetime of an unstable nuclear level we should consider the nucleus which lifetime changes because of two different effects: conventional Lorentz transformation and interaction with the dilute media particle. The same should be with various ratios of different transition frequencies from the same atom.

Indeed, the particle interaction with the dilute media depends on their relative velocity but also on various other parameters. E.g., we can assume that the particle directly interacts with the (dark-matter) medium (via a heavy intermediate boson) and the interaction with light is indirect and somewhat weaker. Or on the contrary we can suggest that the dilute medium is weakly coupled to the light directly and

any interaction to the other matter is an induced effect. Indeed, with a fixed value of the light-media interaction, the effects of matter-media interaction can easily vary by orders of magnitude.

The crucial point here is a possible scale of the effects. The Michelson–Morley experiment and some others are of macroscopic nature and they can check various symmetries on a large scale with respect to atomic and particle effects scale. The latter scale could be studied via a different kind of experiments and it is not necessary that the result be consistent.

Addressing different scales of times and distances we study a part of effects and trying to generalize the results may do some model-dependent suggestions.

## 6. SUMMARY

Above we have demonstrated that looking for some new physics and in particular for possible violations of some symmetries it is hard to avoid certain model dependence which may sometimes produce a misleading interpretation. It is hard to give any general advices except for being careful.

This work was supported in part by the RFBR grant # 06-02-04018 and DFG grant GZ 436 RUS 113/769/0.

## REFERENCES

[1] A.D. Linde, *Inflation and Quantum Cosmology*, Academic Press, New York, 1990.
[2] S.G. Karshenboim, *Can. J. Phys.* **83** (2005) 767.
[3] See, e.g.:
P. Ramond, *Field Theory. A Modern Primer*, The Benjamin/Cumming, Menlo Park, CA, 1981;
C. Itzykson, J.-B. Zuber, *Quantum Field Theory*, McGraw–Hill, New York, 1985;
S. Weinberg, *The Quantum Theory of Fields*, vol. 1, Cambridge Univ. Press, Cambridge, 1995;
S. Weinberg, *The Quantum Theory of Fields*, vol. 2, Cambridge Univ. Press, Cambridge, 1996.
[4] R. Bluhm, V.A. Kostelecký, N. Russell, *Phys. Rev. Lett.* **82** (1999) 2254.

CHAPTER 13

# Extensive Calculations of High-Precision Energy Levels in Hydrogen and Deuterium Through a Least-Squares Adjustment

**Eric-Olivier Le Bigot**[*], **Ulrich D. Jentschura**[**], **Svetlana Kotochigova**[***], **Peter J. Mohr**[***] and **Barry N. Taylor**[***]

Contents



Abstract

Recent high-precision energy level calculations in atomic hydrogen and deuterium are presented. Numerical values are readily available on the web. The procedure found can provide new predictions in a relatively simple way, by relying on results obtained through the latest adjustment of the fundamental constants. The calculations are meant to yield optimal predictions.

[*] Laboratoire Kastler Brossel, Ecole Normale Supérieure, CNRS, Université Pierre et Marie Curie-Paris 6, Case 74, 4 place Jussieu, F-75252 Paris, Cedex 05, France
Corresponding author. E-mail: eric.lebigot@normalesup.org
[**] Max-Planck-Institut für Kernphysik, Saupfercheckweg 1, 69117 Heidelberg, Germany
[***] National Institute of Standards and Technology, Gaithersburg, MD 20899-8420, USA

Advances in Quantum Chemistry, Vol. 53
ISSN 0065-3276, DOI:10.1016/S0065-3276(07)53013-3

Some of the predicted transition frequencies have an uncertainty more than an order of magnitude smaller than that of the Landé factor $g$ of the electron, which was previously the most accurate prediction of quantum electrodynamics (QED). These predictions were obtained by combining accurately measured transitions in hydrogen and deuterium with recent QED calculations. A mostly non-technical overview of the relevant adjustment procedures is given in this paper.

# 1. INTRODUCTION

## 1.1 Description of the results

This paper discusses recently obtained high-precision predictions of energy levels and transition frequencies in atomic hydrogen and deuterium[1]. We also provide a mostly non-technical description of the procedures that led to these results, which complements more technical information available elsewhere ([1] and [2, App. E]).

### 1.1.1 High precision energy levels and transition frequencies

Energies were calculated for all levels of hydrogen and deuterium with principal quantum number $n$ smaller than 200. Optimally evaluated transitions frequencies between these levels are also available. All the results can be found on the web[2].

These results are among the most precise predictions ever made with QED, which is the most precise theory to date. Thus, the previously most precise predictions of QED can be considered to be the $g$-factor of the electron, with an uncertainty on the 13th digit (about $4 \times 10^{-12}$ relative [3, p. 64]). This is to be compared, for instance, to the precision on 1S–3D transition frequencies in [1, Table III], which reach about $3 \times 10^{-13}$, which is more precise by about an order of magnitude.

Compared to previous similar predictions of energy levels, the improvement in precision reaches in some cases about five additional orders of magnitude [4].

When compared to achieved experimental precision, the predictions are, as a general rule, more precise by a factor ranging from two to ten (see, e.g., Table I in [1]). For instance, the prediction of the "classic" Lamb shift (transition frequency between the 2S and $2P_{1/2}$ levels of hydrogen) is predicted with a precision five to ten times higher than the experimental determination [5,6].

### 1.1.2 Calculation procedure

The high precision obtained on hydrogen and deuterium energy levels comes essentially from matching experimental results with theoretical ones [1]. All the available information is meant to be used, including in particular correlations between experiments or between theoretical predictions [3].

[1] Hyperfine effects are not included, but their contribution can be added to the available predictions

[2] http://physics.nist.gov/hdel

Such correlations are at the root of precise predictions, as they put strong constraints on the variables[3] that are adjusted when experiments and theory are forced to match as best as possible. Thus, for example, the high experimental precision on the 1S–2S transition frequency $\nu_{\mathrm{H}}$ in hydrogen [7] puts strong constraints on some of the fundamental constants contained in the corresponding theoretical expression:

$$\nu_{\mathrm{H}} = \frac{3}{4}R_\infty\left[1 - \frac{m_{\mathrm{e}}}{m_{\mathrm{p}}} + \frac{11}{48}\alpha^2 - \frac{28}{9}\frac{\alpha^3}{\pi}\ln(\alpha^{-2}) - \frac{14}{9}\left(\frac{2\pi\alpha R_{\mathrm{p}}}{\lambda_C}\right)^2 + \cdots\right] + \delta_{2\mathrm{S}} - \delta_{1\mathrm{S}}. \quad (1)$$

The variables used in the right-hand side[4] are quantities that are adjusted so that theory and experiment coincide. In the expression above, the experimental frequency $\nu_{\mathrm{H}}$ is known to a precision similar to that of the theoretical prediction; this forces some constants to be strongly correlated: for instance, the correlation coefficient between the Rydberg constant $R_\infty$ and the proton radius $R_{\mathrm{p}}$ is 0.996. Such a correlation coefficient close to 1 essentially indicates that if the proton radius were slightly higher than its (central) recommended value, then the Rydberg constant would also be slightly higher (and by approximately the same amount relative to their respective standard errors). As a consequence, some predictions involving correlated adjusted variables can be more precise than the adjusted quantities that are used in their formal expression. This will turn out to be important for the precision of predicted energy levels and transition frequencies.

A simple example of how precise predictions can be achieved through the use of correlations is given by the expression $x - y$, where $x$ and $y$ are random variables with the same standard deviation $\sigma$, and have a correlation coefficient close to 1. In this situation, statistical fluctuations of $x$ are statistically compensated by fluctuations of $y$, and the "predicted" value of $x - y$ is much more precise than $\sigma$, as a shift of $x$ by some amount is compensated by a shift of $y$ by the same amount.

Another example, found in our calculations [1], is that the predictions of some energies is more precise than the uncertainty on the Rydberg constant $R_\infty$: in view of the fact that $R_\infty$ appears essentially as a factor in theoretical predictions [see Eq. (1)], this is a non-obvious result. It can for instance be observed in the $1\mathrm{S}–3\mathrm{D}_{3/2}$ transition frequency is predicted [1] to a relative precision of about $3 \times 10^{-13}$: this is 20 times smaller than the uncertainty on the Rydberg constant [3, p. 64].

Predictions that are meant to be optimal were thus obtained through both the constraints imposed by the matching of experiments with theory [2, App. E], and the use of correlations between the adjusted quantities (e.g., the Rydberg constant, the proton radius, etc.).

[3] A note about terminology is in order, here: physical *constants* are considered as *variables*, in the adjustment of the fundamental constants. Numerical values for the physical constants are obtained by finding optimal values for these variables [2, App. E]

[4] $R_\infty$ is the Rydberg constant; $m_{\mathrm{e}}$ and $m_{\mathrm{p}}$ are respectively the electron and proton masses; $R_{\mathrm{p}}$ is the proton charge radius, and $\lambda_C$ the Compton wavelength of the electron. $\alpha$ is the fine structure constant $e^2/(2\epsilon_0 hc)$, where $e$ is the electron charge, $\epsilon_0$ the electric constant, $c$ the speed of light, and $h$ the Planck constant. The Rydberg constant can be expressed in terms of other constants as $\alpha^2 m_{\mathrm{e}} c/(2h)$

### 1.1.3 Theoretical result: method for high-precision predictions

The method used for obtaining optimally precise predictions for energy levels in hydrogen and deuterium can take a simplified form, as shown in Ref. [1]. In fact, in order to calculate a new energy level with an optimal precision, it is possible to rely on data already calculated for the CODATA 2002 adjustment of the fundamental constants [3]. The energy of a level can thus be quite simply predicted by taking a theoretical formula for the energy, and then evaluating the statistical correlation between the non-calculated theoretical remainder and theoretical expressions used in the CODATA 2002 adjustment (these numbers are easy to calculate, as we describe below).

The adjustment of fundamental constants and other quantities—performed so that experiments match theoretical results—consists in a numerical procedure. It is to be noted, though that the energy levels obtained by such a method come from a *mix* of theory and experiments: they are not pure *ab initio* results. For instance, the "prediction" of the 1S–2S transition in Ref. [1] comes mostly from its experimental measurement [7]. On the other hand, the classic Lamb shift prediction mentioned above, which is given [1] to a precision better than that of experiments, is obviously not a pure experimental result, but nonetheless relies on the information provided by experiments.

Such a situation is common, as experiments and theories are intimately linked, when it comes to producing numerical values: relevant physical values require theory in order to be extracted from experiments, while at the same time theoretical formulas generally involve constants that require some experimental determination[5].

An important characteristics of the energy level predictions recently obtained in [1] is that they have a level of precision that goes beyond state-of-the-art *ab initio* calculations, as they were obtained by using additional, experimental information.

## 1.2 Motivations and applications

### 1.2.1 Tests of quantum electrodynamics

Constantly comparing predictions to observations contributes to testing quantum electrodynamics (QED)—and, beyond QED, the Standard Model of fundamental interactions and the quantum field theories that it uses. Comparing the predicted hydrogen and deuterium transition frequencies[6] with new *ab initio* QED results would contribute to testing QED.

The need for testing QED is illustrated by the inconsistencies currently observed in the atomic helium fine structure between experiments and theories. Obtaining predictions that match experiments is also useful for helium fine structure measurements to contribute to the determination of the fine structure constant $\alpha$ (recent work in this domain is presented in Ref. [8]). Many experiments have recently been performed on the helium fine structure: by Gabrielse in Harvard [9][7],

[5] Theoretical results that state that a given quantity is exactly zero obviously do not fall in this category; this can also be the case of results involving no units but only pure numbers

[6] Available at http://physics.nist.gov/hdel

[7] This paper contains a review of recent results

by Inguscio in Florence and De Natale in Naples [10,11], by Shiner at the University of North Texas [12] and Hessels at York University [13,14]. Recent theoretical results include work by Drake [15] and Pachucki [16]. A recent review of the situation can for instance be found in [3, p. 39].

On the purely theoretical side, recent high-precision (QED) results in hydrogen and deuterium were obtained recently, which have led to a significant reduction of the uncertainty of both one-photon and two-photon QED contributions (see, for instance, Refs. [16–20,21–26] in [1], and [17,18], and § 2.3.2.1).

### 1.2.2 Contribution to the determination of the fundamental constants

Even though the prediction of new energy levels and transition frequencies in [1] has no direct impact on the recommended values of the fundamental constants, compared to the adjustment on which the new predictions are based (CODATA 2002 [3]), they motivate new theoretical calculations, as mentioned above. In turn, such calculations can close the virtuous circle and contribute to an increased accuracy in the determination of fundamental constants.

An example of quantity which owes its current precision to precise predictions in hydrogen is the proton radius. In fact, this radius is one of the adjusted fundamental constants since the 2002 CODATA adjustment [3]; as illustrated in Figure 13.1, the current recommended value comes mainly from precise experiments and theory in hydrogen.

Another example of fundamental constant that relies on precise experiments and QED predictions in hydrogen is the Rydberg constant $R_\infty$, which is the second most precise constant, as given in CODATA 2002 [3].

### 1.2.3 Relevance of hydrogen and deuterium

Another reason for predicting levels in atomic hydrogen and deuterium is that transitions to their lower levels fall in the visible spectrum or are in close range: frequencies belonging to this domain can be measured very accurately. In particular, as much as about 15 digits can be obtained on such frequencies, with the recent frequency-comb technique: this technique provides about 100,000 equally-spaced laser lines located in the visible spectrum, whose frequency can be known to about 1 Hz (see, e.g. [7]).

Many recent experiments have yielded high-precision transition frequencies in hydrogen and deuterium. We can cite the 1S–2S transition in hydrogen [7]. The experimental precision obtained on this transition has increased by three orders of magnitude in about 10 years (see, for instance, Ref. [3, p. 15], and references therein). Other experiments involving levels with principal quantum number $n$ up to 12 were conducted in the last 10 years at MPQ in Garching, LKB in Paris, and Harvard, in particular (see, for instance, the introduction of Ref. [1]). In the microwave spectrum, precise measurements involving hydrogen levels with $n$ from 27 to 30 were performed recently at MIT [19].

Further progress in the spectroscopy of hydrogen is expected from groups currently working on improving measurement accuracy on some transitions: 1S–2S at the Max-Planck-Institut für Quantenoptik, Garching; 1S–3S at the Laboratoire

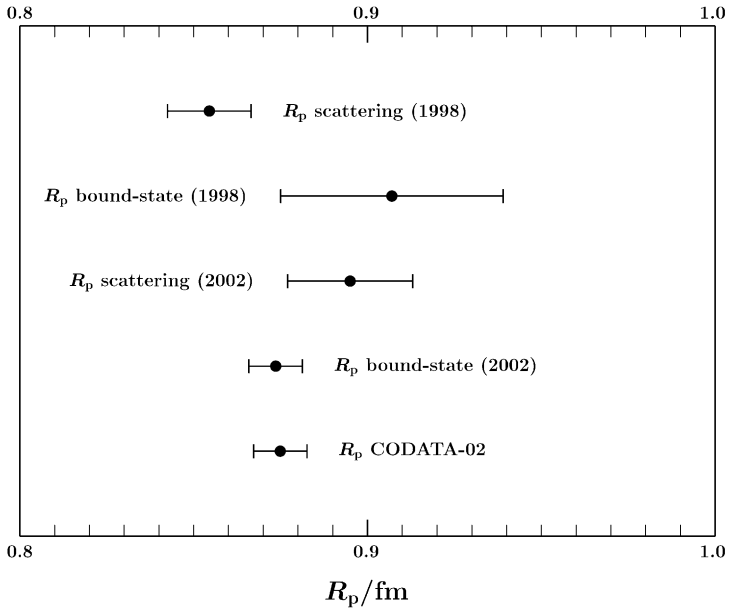


**FIGURE 13.1** Value of the proton radius, as adjusted with electron-proton scattering data, and with spectroscopic information on hydrogen. As illustrated in this graph, the current recommended value ("CODATA-02") of the proton radius [3] comes mostly from precise spectroscopy experiments in hydrogen along with precise theoretical calculations of the energy levels of hydrogen.

Kastler Brossel in Paris; and 2S to high-$n$ transitions at the National Physical Laboratory in the UK, and at MIT.

## 1.3 Outline and references

The method developed in [1] for obtaining optimal predictions in hydrogen and deuterium is discussed in this paper, along with its numerical results. We first discuss how outstanding, not yet calculated theoretical contributions $\delta$ are central both to the adjustment of the fundamental constants and to the optimal prediction of energy levels in hydrogen and deuterium. We then give a detailed overview of the adjustment of the fundamental constants, and describe the specifics of the optimal energy level prediction method in mostly non-technical terms.

More technical information about the last two fundamental constants adjustments can be found in [2,3]. Numerical results are available on the web[8].

The numerical results obtained through the fundamental constants adjustment can be used for performing optimal predictions of hydrogen and deuterium energy levels along the lines described in [1]. The resulting energies and transition

[8] http://physics.nist.gov/cuu/Constants/index.html

frequencies for all levels with principal quantum number $n$ smaller than 200 are also available on the web[9].

## 2. CALCULATION OF ENERGIES WITH AN OPTIMAL PRECISION: METHODS INVOLVED

### 2.1 Two types of adjusted quantities

The quantities adjusted in CODATA [2,3] can be divided into two classes: the group of fundamental constants chosen for the adjustment, and the group of outstanding, theoretically unknown contributions $\delta$. These quantities are involved in equations such as equation (1) above, which gives the 1S–2S transition frequency as a function of constants such as the Rydberg constant $R_\infty$, the electron mass, etc., and also of quantities denoted by $\delta_{1S}$ and $\delta_{2S}$.

#### 2.1.1 Deltas—calculation of quantities not calculated by theory

Quantities such as $\delta_{1S}$ and $\delta_{2S}$ are theoretically unknown contributions that represent the amount of energy to be added to all the calculated terms of a given level so that the total energy is *exact* (i.e., represents the full prediction of the theory used—mainly QED, in our case—, which should be consistent with any actual experimental measurement). As is customary in the literature cited here, such quantities are generically denoted by $\delta$, in this paper.

These $\delta$'s are key both to the adjustment of the fundamental constants [3] and to the optimal predictions presented here [1]; in the remainder of this paper, we often refer to these energy contributions that theory has not calculated. They are in particular useful for the evaluation of energy levels in hydrogen and deuterium: in

$$E_i = H_i(R_\infty, \alpha, \ldots) + \delta_i, \tag{2}$$

the energy $E_i$ of level $i$ is obtained as the sum of a partial theoretical prediction $H_i$ (which relies on some fundamental constants and no $\delta$), and of the non-calculated contribution $\delta_i$. The 1S–2S transition energy (1) above is thus simply $E_{2S} - E_{1S}$; part of the theoretical expression of $H_{2S} - H_{1S}$ is visible in Eq. (1). Almost all the $\delta$'s of the adjustments discussed here [1–3] come from the theory of hydrogen energy levels[10]. Both the adjustment performed for the fundamental constants [3] and for the predictions in hydrogen [1] do calculate $\delta$ values.

By definition, the $\delta$'s used in [1–3] are *not* predicted by purely theoretical calculations. Their magnitude is theoretically known, though, as calculations proceed essentially by obtaining successive perturbation terms.

This, along with theoretically-known correlations among various $\delta$'s, allows one to predict them, by combining all the relevant available information on experiments and theory.

[9] This represents about a billion numerical values (and uncertainties); they are all available at http://physics.nist.gov/hdel

[10] See http://physics.nist.gov/cuu/LSAData/zdata_a.pdf and [3, Appendices]

### 2.1.2 Overview of the adjustments

Optimal predictions of energy levels were obtained in two steps, where each of the steps involves a different set of quantities:

- In the first step, *both* fundamental constants and some $\delta$'s are adjusted. The adjusted $\delta_i$ are not yet calculated contribution to the levels $i$ that are involved in the experiments used in the adjustment [3].
- In the second step, *only* $\delta$ values are adjusted, and only for levels not already included in the first adjustment—their $\delta$'s are already known. The new $\delta_i$'s, once added to the relevant theoretical determinations $H_i$ in Eq. (2), yield the energies of the levels of interest (those with principal quantum number $n$ smaller than 200) [1].

These two steps are successively described in the remainder of this paper.

## 2.2 Adjustment of the fundamental constants

### 2.2.1 Overview

As mentioned above, the principle behind the adjustment of the fundamental constants consists in adjusting some parameters (fundamental constants and $\delta$'s) so that experiments and predictions are consistent. Mathematically, the best possible consistency is achieved by minimizing the "distance" between experimentally known values and functions of the parameters that are supposed to reproduce the known values [2, Eq. (E18)]. The minimized function can be expressed as a sum of squares, hence the term "weighted least squares" used for describing the adjustments presented here. The weights in question make a *precise* experimental measurement constrain the adjusted parameters more than a less precise measurement [20].

It is possible to not only obtain the values of the adjusted parameters that make all the available information as much consistent as possible, but to also evaluate their variances and covariances (see, e.g., Eq. (E11) in [2]).

These covariances between adjusted fundamental constants and $\delta$'s are of the utmost importance when one is interested in obtaining precise theoretical predictions through equations Eq. (2): by taking them into account, an *optimal* prediction can be extracted from the formulas, as exemplified in the introduction when discussing correlations.

### 2.2.2 Ingredients of the adjustment

Adjusting the fundamental constants requires to define both a list of parameters to be adjusted (fundamental constants and $\delta$'s), and a system of equations that constrain them.

*2.2.2.1 Adjusted parameters* The list $Z$ of the 61 variables involved in the latest adjustment of the fundamental constants (CODATA 2002 [3]) is available on the web[11].

[11] http://physics.nist.gov/cuu/LSAData/zdata_a.pdf

Among the physical constants that were adjusted and that are relevant to the theory of hydrogen and deuterium energy levels, we find, for example, the fine structure constant $\alpha$, which defines the strength of the electromagnetic force, and the Rydberg constant $R_\infty$, which is essentially the energy of the 1S level of hydrogen as predicted by the Bohr model. The proton and deuteron radii, which also enter in the theoretical predictions of the levels, were added to the list of adjusted constants in the latest CODATA [3].

*2.2.2.2 System of equations* A system of "equations" puts constraints on the adjusted parameters $Z$. As there are 105 such equations in the latest adjustment but only 61 adjusted variables (in $Z$), the system is over-constrained. Thus, all fundamental constants and $\delta$'s can be determined.

The system of equations pertaining to the kind of adjustment described here [2, App. E] has three components:

- theoretical expressions $F(Z)$, which involve only dimensionless numbers and the list of adjusted variables $Z$ ($\alpha$, $R_\infty$, $\delta$'s, ...),
- corresponding "input data" $Q$ (one value for each equation in $F$): each data is a numerical value that represents either an experimental result, or a theoretical estimate (always zero, as explained below),
- a matrix $V$ of variances and covariances that define the precision with which the numerical input data is known; equations must hold true within this precision.

Expressed in a semi-formal way, the constraints set of the list of adjusted quantities $Z$ thus take the form

$$Q \doteq F(Z) \quad \text{to a precision } V, \tag{3}$$

where $Q$ is a vector with 105 numerical quantities, $F$ a list of 105 functions of the 61 adjusted quantities $Z$, and where $V$ is a $105 \times 105$ matrix of covariances between the input values $Q$; the special symbol $\doteq$ denotes the fact that no *strict* equality is expected: both sides of the "equation" must simply be consistent within the prescribed uncertainties [3, § IV.B]. The consistency of *all* equations was carefully checked [3, p. 81]. Let's describe in more details the last three ingredients of system (3), which defines the constraints to be satisfied by the adjusted parameters $Z$.

The complete list of numerical input values $Q$ used in the latest fundamental constants adjustment is available in Tables XI and XIII in [3], and also on the web[12].

This list includes, in particular, some of the experimental results mentioned in the introduction: high-precision transition frequencies in hydrogen, between the 1S and 2S levels [7], and other measurements between levels with $n$ up to 12 (see, e.g., [21]). Other examples of included measurements are the electron $g$-factor [22], and the Josephson constant $K_J$ [3, p. 28].

As mentioned above, the physical theories used in the adjustment [3] provide some information about non-calculated terms: their magnitude can be inferred from the size of successive perturbation terms. Thus, the information available on the $\delta$'s described above (Section 2.1.1) is of the form

$$0 \pm \text{uncertainty } u = \delta, \tag{4}$$

[12] http://physics.nist.gov/cuu/LSAData/qvals.txt

where the uncertainty $u$ represents an estimate of the order of magnitude of the theoretical remainder $\delta$. Therefore, system (3) above contains equations such as (4), in the form

$$0 \doteq \delta \text{ up to some uncertainty } u,$$

and the vector $Q$ of numerical input data[13] thus contains a zero for each $\delta$.

In equation (3), the matrix of covariances $V$ sets the strength of the constraints put on the system of equations. The more precise the experiment, the most stringent the constraint put on the corresponding adjusted variables. The numerical values of $V$ used in the latest adjustment of the fundamental constants [3] are available on the web[14] (these values can be used for performing optimal predictions of energy levels, as described in Section 2.3 below). Most of the covariances between numerical input values $Q$ are zero. There are only two kinds of non-zero elements: they represent either correlations between experimental results, or between theoretical results[15]. The structure of the covariances between numerical input data $Q$ is depicted in Figure 13.2.

Non-zero covariance values in $V$, between *experimental* results from $Q$, come from experiments that are related. For instance, some contributions are common to some experiments performed with similar set-ups. An example is the set of hydrogen spectroscopy experiments performed at the Laboratoire Kastler Brossel in Paris [3, *A*2–*A*6 in Table XI, p. 49]: the transitions frequencies measured there between the 2S level and other levels are correlated, as they used the same reference laser, the same line shape analysis method, similar estimates of the Stark effect contribution to the final transition frequencies, etc. Thus, any deviation of one of the measured frequencies from its central measured value implies a correlated deviation of any of its related measured frequencies. Corresponding non-zero, non-diagonal elements in the covariance matrix $V$ quantify such correlations.

Regarding non-zero elements of $V$ between *theoretical* input data from $Q$, let's note that Eq. (4) gives the variances of each $\delta$: the corresponding diagonal elements of $V$ are essentially the order of magnitude of each $\delta$ (squared). Non-zero covariances between different $\delta$'s represent correlations such as the one that exists between $S$ states: at the current level of knowledge, the energy contribution not yet calculated by theory can be estimated as being of the order of $A/n^3$, for some common coefficient $A$ ($n$ is the principal quantum number of the $S$ state that is considered)[16]. It results from this that there are strong correlations between non-calculated contributions to the energy levels of $S$ states. The matrix $V$ in equation (3) thus takes this fact into account.

The theoretical expressions $F$ used in Eq. (3) for connecting numerical values $Q$ with adjusted variables $Z$ are of two kinds, that mirror the two kinds of input data in $Q$: theoretical expressions are either theoretical predictions of experimental

[13] http://physics.nist.gov/cuu/LSAData/qvals.txt

[14] http://physics.nist.gov/cuu/LSAData/v.txt

[15] This fact is the mathematical counterpart of a situation described further down in the text: even though some theory was used in obtaining some physical results used in $Q$, this theory is essentially independent of the theoretical expressions $F$ used by the adjustment

[16] This is for instance the case of the deltas labeled $A25$ to $A30$ and $A41$ to $A44$ in [3], Table XI, p. 49

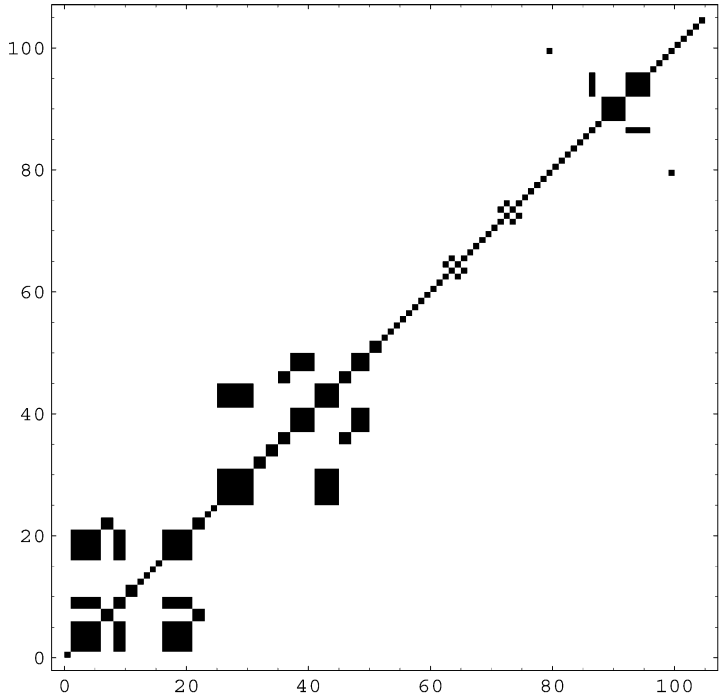


**FIGURE 13.2** Matrix of covariances and variances $V$ used in the latest adjustment of the fundamental constants [3]. The matrix contains one row and one column for each of the 105 equations of system (3), which puts constraints on the adjusted variables (physical constants and "deltas" [Section 2.1.1]). There are relatively few non-zero covariances; the corresponding elements are depicted in black. Groups of related experimental measurements or of correlated $\delta$'s can be readily be observed in this representation.

results expressed as functions of the adjusted variables $Z$, or they simply express an equation of the form (4) above[17].

It must be noted that even though *some* theory may have been used in determining the published final experimental results of the input data $Q$, this theory differs from the one expressed by the functions $F$. For example, experimentalists can theoretically take into account the contribution of some electromagnetic fields present in the apparatus, in order to deduce a specific frequency from raw data [22]; such a use of theory relies on well-tested physics that has no direct connection with *ab initio* theoretical results $F$ used in adjusting the fundamental constants.

Theoretical expressions used in the latest adjustment of the fundamental constants can be partly found in Tables XIX and XXI in [3]. Many of the expressions involved come from the theory of energy levels in hydrogen, which includes rel-

[17] Expressed formally, this means that there are equations $f_i(Z)$ in $F(Z)$ that take the form $f_i(Z) = \delta_j$ for some atomic level $j$—$\delta_j$ being one of the adjusted variables contained in the list $Z$

ativistic effects, quantum field theory effects (most notably QED effects), proton size and motion effects, etc. [3, App. A].

*2.2.2.3 Solution of the system of equations* The system of Eq. (3), whose equations combine numerical values, theoretical expressions, and covariances, can be solved for the adjusted variables $Z$: best estimates of their values can thus be calculated. The method used in [2,3] consists in using a sequence of linear approximations to system (3), around a numerical vector $\hat{Z}$ that converges toward the solution of the full, non-linear system (this is akin to Newton's method—see, e.g. [23]). Each of the successive linear approximations to system (3) is solved through the Moore–Penrose pseudo-inverse [20] (see, also, Ref. [2, App. E]). The numerical solution for $Z$ as found in CODATA 2002 can be found on the web[18]. These values are such that the equations in system (3) are satisfied, as a whole, as best as possible [3, App. E]).

This procedure yields values for the fundamental constants included in $Z$. These values are available on the web[19] and in [3, Table XXVI, p. 63]. Through this method, for instance, the proton radius is determined to a precision of about 1%, mainly through numerical constraints set by transitions in hydrogen, as shown in Figure 13.1.

The adjustment procedure also yields values for the $\delta$'s contained in $Z$. This means that by thus combining theory and experiments, one predicts theoretical energy contributions that are not yet calculated (for levels involved in some experiment exploited in CODATA 2002).

In addition to obtaining the values of the variables in $Z$ that satisfy system (3) the best, it is possible to obtain their covariance matrix $G$ (see, e.g., Ref. [3, App. E]). This matrix is also available on the web[20]. Thus, *many* numerical values of $Z$ satisfy system (3) within the imposed uncertainties $V$. This defines a set of statistically acceptable values that lie within close range of the best values; the covariance matrix of the adjusted values essentially describes the typical dimensions (in the 61-dimensional space of $Z$ (Section 2.2.2.1)) of this set of acceptable values. For instance, statistically plausible sets of numerical values for $Z$ are such that the $g$-factor of the electron (which is a component of $Z$) varies with a relative standard error of as little as $4 \times 10^{-12}$ (this incidentally makes it the most precise value determined in the latest adjustment of the fundamental constants [3]).

The covariances of the adjusted variables $Z$ can be used for calculating values with optimal uncertainties from theoretical formulas, as described in Section 1.1.2. Correlations between adjusted values (i.e., non-zero non-diagonal elements of $G$) can play an important role in the uncertainty to be associated to the calculated formula, as large correlation coefficients are observed between fundamental constants; an example is given by the values for the electron charge $e$ and the Planck constant $h$, which have a correlation coefficient of 0.999 [3, p. 69], which is very close to the maximum value of 1.

[18] The variables $Z$ listed in http://physics.nist.gov/cuu/LSAData/zdata_a.pdf were found [3], and their values are given in http://physics.nist.gov/cuu/LSAData/zvals.txt

[19] http://physics.nist.gov/cuu/LSAData/index.html

[20] http://physics.nist.gov/cuu/LSAData/g.txt

More technical presentations of the results just discussed can be found in [2, App. E] (least-squares adjustment) and [3] (CODATA 2002 adjustment of the fundamental constants). Important online resources include values of the adjusted constants[21] and data from the calculations[22] (list of adjusted variables $Z$, numerical input values $Q$, etc.).

## 2.3 Optimal predictions of energy levels

### 2.3.1 Overview of the new predictions

The method described above, which adjusts variables in order to make theory and experiments match best, was applied to the determination of fundamental constants [3]. However, fundamental constants only belong to one of the two types of adjusted variables $Z$: non-calculated energy contributions $\delta$ (Section 2.1.1) were also evaluated[23], as mentioned above in Section 2.2.2.3. It is thus possible to optimally predict the energy levels whose $\delta$-contribution was adjusted in [3], by evaluating the right-hand side of formula Eq. (2), which is exact. Their are about two dozen levels whose energy can thus be optimally evaluated; the list can be found on the web[24].

These optimal predictions were recently extended in Ref. [1] to many more levels, as all hydrogen and deuterium levels with principal quantum number $n \leqslant 200$ had their energy calculated, along with that of transitions between any pair of levels. The precision on the transitions duly includes correlations between level energies (see, e.g., Eq. (18) in [1]), so that their evaluation is optimally precise.

The principle behind the calculation of new energy levels was to adjust a list $Z_\delta$ of additional non-calculated $\delta$-contributions [1], which was added to the list of adjusted variables $Z$ (Section 2.2.2.1)—one $\delta$ for each new level of interest. Applying the adjustment procedure described in Section 2.2 then yields optimal values for the theoretical contributions ($\delta$'s); using exact predictions like (2) gives in turn energies with an optimal uncertainty. Thus, new predictions could in principle be performed by simply redoing the CODATA 2002 adjustment, but only with additional adjusted $\delta$'s.

However, it was shown [1] that the adjustment procedure used for the determination of the fundamental constants (Section 2.2) does not have to been carried out again: the full, extended adjustment thus does not represent the calculations effectively performed for the new predictions [1]. In fact, optimal predictions for additional energy levels can be obtained in a much simpler way: by combining some numerical results from the latest adjustment with covariances between a few theoretical $\delta$-contributions (see Section 2.3.3.2 below).

In order to obtain the most precise values possible, the magnitude of the newly adjusted, non-calculated $\delta$-contributions, $Z_\delta$, was minimized: the latest QED predictions were used, and some new calculations were performed (see Section 2.3.2.1 below).

[21] http://physics.nist.gov/cuu/Constants/index.html
[22] http://physics.nist.gov/cuu/LSAData/index.html
[23] http://physics.nist.gov/cuu/LSAData/zvals.txt
[24] http://physics.nist.gov/cuu/LSAData/zdata_a.pdf

### 2.3.2 System of constraints of the extended adjustment

The system of constraints used for the prediction of energy levels [1] differs a little from the one used in the latest adjustment of the fundamental constants [3]—even though it is still of the form given by Eq. (3).

*2.3.2.1 New adjusted variables; latest theoretical predictions* In order to determine the energies of all levels of hydrogen and deuterium with principal quantum number $n \leqslant 200$, about 100,000 new $\delta$'s had to be calculated[25]. These new $\delta$ variables, which form the vector $Z_\delta$, were simply appended to the list of variables $Z$ (Section 2.2.2.1) of the CODATA 2002 adjustment, thus giving an enlarged vector of adjusted variables denoted by $Z_u$ [1, Eq. (2)].

In order to obtain the best possible estimates for the chosen levels of hydrogen and deuterium, state-of-the-art theoretical calculations were used in defining the new $\delta$'s—through equation (2) above, which gives the exact energy of a level. The theory of energy levels in hydrogen and deuterium used in the latest adjustment of the fundamental constants is detailed in [3, App. A]. We performed additional theoretical calculations for the optimal predictions found on the web[26]. The (one-photon) self energy is the largest contribution of QED to the energy levels of hydrogen and deuterium; it represents the effect of the following process, where a photon (wavy line) is emitted and absorbed by the orbiting electron (double line):

A large part of the self-energy shift comes from the non-relativistic Bethe logarithm: many new values were obtained [24,25]. Higher-order corrections to the self energy used for the high-precision predictions [1] are summarized in [26]; some predictions were obtained by using the general interpolation and extrapolation method presented in the appendix of [27], applied to either new or existing self-energy numerical values. The second-largest QED contribution to the energy levels is the vacuum polarization, in which electron-positron pairs modify Coulomb's law according to the following QED diagram, which describes the interaction of the orbiting electron with such a pair (loop):

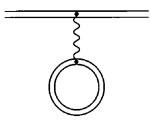

Data for this important contribution to our extended adjustment was reported in [28]. Finally, a smaller QED contribution to the hydrogen and deuterium en-

[25] These new variables are contained in the vector $Z_\delta$, in Ref. [1]

[26] http://physics.nist.gov/hdel

ergy levels is the two-photon self energy

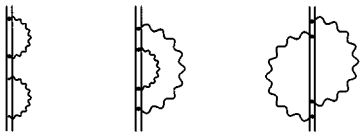

whose relevant theory and data was summarized in [29]. By using the latest QED results, for our calculation of optimal energy levels [1], we minimized the magnitudes of the new $\delta$'s introduced in the extended adjustment, thus optimizing the ultimate precision of the new predicted energies.

*2.3.2.2 Extended system of equations* The system of equations that constrains the adjusted variables $Z_u$ contains equations of a new type [1]: equations that represent a "constraint" on the energy of a level $i$:

$$0 \pm \infty = H_i(R_\infty, \alpha, \ldots) + \delta_i, \tag{5}$$

and which contains the same expression as Eq. (2)—the theoretical evaluation of the energy of level $i$. Equations of the above type have strictly no influence on the value of the adjusted variables $Z_u$, because of their infinite[27] uncertainty[28] [3].

Information about the $\delta$'s of the new levels is included [1] as in the adjustment of the fundamental constants described in Section 2.2: with equations

$$0 \pm \text{uncertainty} = \delta,$$

along with[29] theoretically known correlations[30] with other $\delta$'s. For instance, the $\delta$ of, let's say, the 30S state, has non-zero correlations with the $\delta$ of all other S states—some of which are found in the CODATA 2002 adjustment[31], while the others are from the newly studied levels, in the list $Z_\delta$ [1].

### 2.3.3 Results of the extended adjustment: numerical predictions and simple calculation method

Calculating optimal values for the variables of the extended list of adjusted quantities $Z_u$ was performed [1] along the principles described in Section 2.2.2.3; as mentioned above, it was found that the actual calculations could be carried out in a relatively simple and convenient way. Before concentrating on this efficient prediction method, let's briefly examine the numerical results.

[27] In Ref. [1], the infinite uncertainty is contained in the matrix $V_E = \lim_{u\to\infty} u \times \mathrm{Id}$, and the zero central values are the elements of the null input data vector $Q_E$

[28] The infinite uncertainty gives a zero contribution to the cost function minimized by the adjustment procedure [2, App. E]. A finite uncertainty in equation (5) would essentially not have changed this situation: the principle behind our predictions of new energies consists in using all available information that constrains the adjusted variables $Z_u$; all such information is already included in the extended adjustment [1] in the form of the equations of CODATA 2002 [3] (described in Section 2.2), and in the form of covariances involving the new $\delta$'s

[29] The zero central estimates of the new, non-calculated contributions $\delta$ are mathematically put in a null vector $Q_\delta$ [1, Eq. (2)]

[30] Numerical values for these correlations are found in matrices denoted by $S$ and $T$ in Ref. [1, Eq. (2)]

[31] http://physics.nist.gov/cuu/LSAData/zdata_a.pdf

*2.3.3.1 Numerical results* Examples of precise numerical predictions of transition energies in hydrogen and deuterium are presented in [1, Table I]. Most of these predictions are more precise than experimental measurements. This situation arises from the fact that the system of constraints satisfied by the adjustment includes all the available information on the levels of interest: consistency between many equations forces adjusted variables to take very precise values. The full list of energy levels and transition energies is available on the web site mentioned above[32].

*2.3.3.2 Simple and optimal energy prediction method* Let's now turn to the description of the theoretical results obtained [1] on the prediction of energy levels through an extended adjustment between theory and experiments. It was found that the prediction of new energies does not actually require adjusting all the variables $Z_u$ (which contain the $\delta$'s to be predicted) in the same way as done for the adjustment of the fundamental constants (Section 2.2). In fact, less calculations are actually required. This is proved in [1] through a double use of the Schur–Banachiewicz formula, which gives an expression for the inverse of a $2 \times 2$ block matrix [30,31] (the blocks separate the CODATA 2002 adjusted variables from the newly adjusted $\delta$'s; the calculation of matrix inverses allows one to calculate the Moore–Penrose least-squares inverse [3, App. E]).

One important result [1] is that the addition of new $\delta$'s to be calculated (Section 2.3.2.1) has no influence on the best estimates for the variables $Z$ initially adjusted (Section 2.2.2.1): the determinations (of fundamental constants and $\delta$'s) obtained in CODATA 2002 are not influenced by the predictions of new energy levels. This is expected, as no new information pertaining to the already adjusted quantities $Z$ (which includes $\delta_{1S}$, for instance) is added by the extension of the CODATA adjustment to new levels—no new experiment or theoretical prediction of a level used in CODATA is added by the extension (Section 2.3.2.2). One important practical gain brought forth by this result is that the linearizations (Section 2.2.2.3) of system (3) around successive values of the adjusted variables $Z$, which were done for CODATA [3], do not have to be carried out again; the linearization of system (3) around the final values $\hat{Z}$ of the CODATA variables thus directly contributes to the new predictions [1], and is readily available[33].

More generally, the prediction of both central energy values and their associated uncertainties can be obtained by combining some covariances for the new $\delta$'s with matrices and vectors that are readily available[34] and were obtained for CODATA 2002.

Thus, central values for the new high-precision energy levels of hydrogen and deuterium can be obtained by using only the covariance matrix $V$ and the linearization $A$ of system (3), along with the covariances $T$ of the new $\delta$'s with the CODATA 2002 equations [1, Eq. (16)]. Non-zero covariances with a new $\delta_i$ originate only from $\delta$'s correlated with $\delta_i$, in equations such as (1) or (4); for a given

[32] http://physics.nist.gov/hdel

[33] The linearization of system (3) is contained in the matrix $A$ in [1, Eq. (5)]. It is available at http://physics.nist.gov/cuu/LSAData/a.txt

[34] All the relevant data is available at http://physics.nist.gov/cuu/LSAData/index.html

level $i$, this represents only a few non-zero values to be calculated[35]. The fact that predicting a new energy level $i$ in hydrogen or deuterium only requires the calculation of a few *covariances* with $\delta_i$ can be understood intuitively as follows. Let's take the case of $n$S states; their non-calculated contribution is $\delta_{n\mathrm{S}} \approx A/n^3$ for some value of $A$, as mentioned above. In effect, the CODATA 2002 adjustment evaluates $A$ for each state involved (through the numerical result obtained for $\delta_{1\mathrm{S}}$, etc.); the values of $A$ found are then propagated to the new atomic level of interest $i$ through the covariance of $\delta_i$ with equations that involve $\delta_{1\mathrm{S}}$, etc. In particular, levels that have only zero covariances with the levels involved in CODATA 2002 cannot be predicted to better than what is given by their theoretical prediction: if the $T$ matrix of covariances in zero, then the adjustment yields[36] $\delta_i = 0$ (central value) for any new level $i$.

As with the CODATA 2002 adjustment of the fundamental constants, covariances between all the adjusted variables $Z_u$ can be calculated. Unlike in the calculation of central values for the new energy levels, the matrix $S$ [1, Eq. (2)] of covariances between the *new* $\delta$'s is involved in the formula that gives the covariance matrix of the new adjusted variables $Z_u$. It is indeed expected that the precision on the adjusted $\delta$'s depends on their uncertainty as predicted from theoretical considerations (through the order of magnitude of successive perturbation terms). Precise uncertainties on predicted energies and transition frequencies can then be calculated through standard propagation of uncertainties (see, e.g., Eq. (F7) in [3]), as expressed in Eqs. (17) and (18) in [1].

## 3. CONCLUSION

Numerical, optimal predictions for the energies of levels with principal quantum number $n \leqslant 200$ in hydrogen and deuterium were presented [1]. These energies, along with the corresponding transition frequencies, were made available on the web[37]. Some transition energies represent the most precise predictions obtained with Quantum Electrodynamics—with uncertainties smaller than that of the $g$-factor of the electron—reaching in some cases relative uncertainties such as $3 \times 10^{-13}$. Many predictions of transition energies are more precise than corresponding available experiments, sometimes by about an order of magnitude (Section 2.3.3.1). These predictions can be used in the future in comparisons with both experimental and theoretical calculations: as they were obtained under constraints of consistency between existing theory and experiments, they represent a combination of both theoretical and experimental work. In particular, contributions not yet calculated by theory were evaluated without calculating them *ab initio*: these so-called "deltas" (Section 2.1.1) were predicted through an adjustment of their value.

[35] Calculating the proper covariances between the new $\delta$'s and the equation $F(Z)$ of CODATA 2002 concretely requires to have the list of such equations: see Section 2.2.2.2, Tables XIX and XXI in [3], and the theory of energy levels in [3, App. A]

[36] When $T = 0$ in [1], then $D = 0$, then $Z_\delta = 0$, according to [1, Eq. (16)]

[37] http://physics.nist.gov/PhysRefData/HDEL/index.html

The high precision of the numerical energies obtained comes from using as much experimental and theoretical information as possible, and from taking advantage of known correlations between these results. Thus, the new energy predictions are obtained through a least-squares adjustment, which combines theory and experiments in an optimal way through the adjustment of variables (which include physical constants, and energy contributions $\delta$ that remain to be calculated). A mostly non-technical overview of such an adjustment was given in Section 2.2, for the latest fundamental adjustment [3], and in Section 2.3, for the adjustment of hydrogen and deuterium energy levels (where recent progress in theoretical calculations was exploited, as described in Section 2.3.2.1).

As presented in Section 2.3.3.2, we found a method that simplifies the calculation of the adjustment of new energy levels. The amount of input data and calculations required is essentially limited to calculating a few theoretical covariances for each atomic level. It is thus possible to obtain new, optimal predictions by directly using data calculated for the latest adjustment of the fundamental constant, which is also readily available on the web[38].

## REFERENCES

[1] U.D. Jentschura, S. Kotochigova, E.-O. Le Bigot, P.J. Mohr, B.N. Taylor, Precise calculation of transition frequencies of hydrogen and deuterium based on a least-squares analysis, *Phys. Rev. Lett.* **95** (16) (2005) 163003; http://link.aps.org/abstract/PRL/v95/e163003.

[2] P.J. Mohr, B.N. Taylor, CODATA recommended values of the fundamental physical constants: 1998, *Rev. Mod. Phys.* **72** (2) (2000) 351–495.

[3] P.J. Mohr, B.N. Taylor, CODATA recommended values of the fundamental physical constants: 2002, *Rev. Mod. Phys.* **77** (1) (2005) 1–107; http://link.aps.org/abstract/RMP/v77/p1.

[4] G.W. Erickson, Energy levels of one-electron atoms, *J. Phys. Chem. Ref. Data* **6** (3) (1977) 831–869.

[5] G. Newton, D.A. Andrews, P.J. Unsworth, A precision determination of the Lamb shift in hydrogen, *Philos. Trans. R. Soc. Lond. A* **290** (1373) (1979) 373–404.

[6] S.R. Lundeen, F.M. Pipkin, Separated oscillatory field measurement of the Lamb shift in H, $n = 2$, *Metrologia* **22** (1986) 9.

[7] M. Niering, R. Holzwarth, J. Reichert, P. Pokasov, T. Udem, M. Weitz, T.W. Hänsch, P. Lemonde, G. Santarelli, M. Abgrall, P. Laurent, C. Salomon, A. Clairon, Measurement of the hydrogen 1S–2S transition frequency by phase coherent comparison with a microwave cesium fountain clock, *Phys. Rev. Lett.* **84** (2000) 5496–5499.

[8] P. Cladé, E. de Mirandes, M. Cadoret, S. Guellati-Khélifa, C. Schwob, F. Nez, L. Julien, F. Biraben, Determination of the fine structure constant based on Bloch oscillations of ultracold atoms in a vertical optical lattice, *Phys. Rev. Lett.* **96** (3) (2006) 033001; http://link.aps.org/abstract/PRL/v96/e033001.

[9] T. Zelevinsky, D. Farkas, G. Gabrielse, Precision measurement of the three $2^3P_J$ helium fine structure intervals, *Phys. Rev. Lett.* **95** (20) (2005) 203001.

[10] P. Cancio Pastor, G. Giusfredi, P. De Natale, G. Hagel, C. de Mauro, M. Inguscio, Absolute frequency measurements of the $2^3S_1 \rightarrow 2^3P_{0,1,2}$ atomic helium transitions around 1083 nm, *Phys. Rev. Lett.* **92** (2) (2003) 023001.

[11] P. Cancio Pastor, G. Giusfredi, P. De Natale, G. Hagel, C. de Mauro, M. Inguscio, Erratum: Absolute frequency measurements of the $2^3S_1 \rightarrow 2^3P_{0,1,2}$ atomic helium transitions around 1083 nm, *Phys. Rev. Lett.* **92** (2004) 023001, *Phys. Rev. Lett.* **97** (13) (2006) 139903; http://arxiv.org/abs/hep-ph/0408131.

[38] http://physics.nist.gov/cuu/LSAData/index.html

[12] J. Castillega, D. Livingston, A. Sanders, D. Shiner, Precise measurement of the J = 1 to J = 2 fine structure interval in the $2^3$P state of helium, *Phys. Rev. Lett.* **84** (2000) 4321–4324.
[13] M.C. George, L.D. Lombardi, E.A. Hessels, Precision microwave measurement of the $2^3P_1$–$2\,^3P_0$ interval in atomic helium: A determination of the fine-structure constant, *Phys. Rev. Lett.* **87** (2001) 173002.
[14] C.H. Storry, M.C. George, E.A. Hessels, Precision microwave measurement of the $2^3P_1$–$2^3P_2$ interval in atomic helium, *Phys. Rev. Lett.* **84** (2000) 3274–3277.
[15] G. Drake, Progress in helium fine-structure calculations and the fine-structure constant, *Can. J. Phys.* **80** (11) (2002) 1195–1212.
[16] K. Pachucki, J. Sapirstein, Higher-order recoil corrections to helium fine structure, *J. Phys. B: At. Mol. Opt. Phys.* **36** (2003) 803–809.
[17] A. Czarnecki, U.D. Jentschura, K. Pachucki, Calculation of the one- and two-loop Lamb shift for arbitrary excited hydrogenic states, *Phys. Rev. Lett.* **95** (18) (2005) 180404; http://link.aps.org/abstract/PRL/v95/e180404.
[18] V.A. Yerokhin, P. Indelicato, V.M. Shabaev, Two-loop self-energy correction in a strong Coulomb nuclear field, *JETP* **101** (2) (2005) 280–293.
[19] J.C. De Vries, A precision millimeter-wave measurement of the Rydberg frequency, Ph.D. thesis, M.I.T. (2002); http://hdl.handle.net/1721.2/609.
[20] R. Penrose, On best approximate solution of linear matrix equations, *Proc. Cambridge Philos. Soc.* **52** (1956) 17.
[21] B. de Beauvoir, C. Schwob, O. Acef, L. Jozefowski, L. Hilico, F. Nez, L. Julien, A. Clairon, F. Biraben, Metrology of the hydrogen and deuterium atoms: Determination of the Rydberg constant and Lamb shifts, *Eur. Phys. J. D* **12** (2000) 61–93.
[22] R.S. Van Dyck Jr., P.B. Schwinberg, H.G. Dehmelt, New high-precision comparison of electron and positron $g$ factors, *Phys. Rev. Lett.* **59** (1987) 26–29.
[23] W.H. Press, B.P. Flannery, S.A. Teukolsky, W.T. Vetterling, *Numerical Recipes in C: The Art of Scientific Computing*, second ed., Cambridge Univ. Press, Cambridge, 1992.
[24] U. Jentschura, P. Mohr, Bethe logarithms for Rydberg states: Numerical values for $n \leqslant 200$, Technical note, NIST, arXiv:quant-ph/0504002 (2005); http://physics.nist.gov/PhysRefData/HDEL/PDF/bethelogs.pdf.
[25] U.D. Jentschura, P.J. Mohr, Calculation of hydrogenic Bethe logarithms for Rydberg states, *Phys. Rev. A* **72** (1) (2005) 012110; http://link.aps.org/abstract/PRA/v72/e012110.
[26] U. Jentschura, S. Kotochigova, E.-O. Le Bigot, P. Mohr, Precise theory of levels of hydrogen and deuterium: The one-photon self energy correction, Technical Note 1469, NIST (2005); http://physics.nist.gov/PhysRefData/HDEL/PDF/selfen.pdf.
[27] E.-O. Le Bigot, U.D. Jentschura, P.J. Mohr, P. Indelicato, G. Soff, Perturbation approach to the self energy of non-S hydrogenic states, *Phys. Rev. A* **68** (2003) 042101, arXiv:physics/0304068; http://link.aps.org/abstract/PRA/v68/e042101.
[28] S. Kotochigova, P. Mohr, Precise theory of levels of hydrogen and deuterium: The Coulomb vacuum polarization correction, Technical report 1468, NIST (2005); http://physics.nist.gov/PhysRefData/HDEL/PDF/vac_pol.pdf.
[29] U. Jentschura, P. Mohr, Precise theory of levels of hydrogen and deuterium: The two-photon radiative corrections, Internal report 7217, NIST (2005); http://physics.nist.gov/PhysRefData/HDEL/PDF/two_photon.pdf.
[30] I. Schur, Potenzreihen im Innern des Einheitskreises, *J. Reine Angew. Math.* **147** (1917) 205–232.
[31] T. Banachiewicz, Zum Berechnung der Determinanten, wie auch der Inversen, und zur daraut basierten Auflösung der Systeme lineärer Gleichungen, *Acta Astronom. Ser. C* **3** (1937) 41.

# SUBJECT INDEX